# FLOW PHYSICS OF STRAINED TURBULENT AXIAL VORTICES

A Thesis
Submitted to the Faculty

of

Purdue University

by

Brijesh Eshpuniyani

In Partial Fulfillment of the
Requirements for the Degree

of

Doctor of Philosophy

December 2003

For Mataji

## ACKNOWLEDGMENTS

I wish to start with thanking my research advisor Prof. Gregory A. Blaisdell. I am grateful to him at two main levels. The first one is the most obvious one - that of guiding my research work. It has been my good fortune to be able to get direct guidance from someone so knowledgeable and brilliant. And that too in such a welcoming way. His office door has always been open. He also provided me with the opportunity to participate in two conferences. This was a very good experience for me. However, above and beyond all this is the level of human-ness. Throughout my stay here I have seen the high ideals of sincerity, fairness, centeredness, patience and compassion manifest unceasingly in this gem of a human being. I have derived much inspiration from the example set by him. Thank you Professor. Knowing you has made me a better human being.

I would also like to thank Prof. Williams, Prof. Lyrintzis and Prof. Frankel for serving on my PhD committee. Your feedback has played a vital role in raising the quality of this thesis.

I wish to express my heartfelt gratitude towards my parents. They have been so patient for so long, always encouraging me to realize my goals. Papa and Mummy - Thank You for the faith you have placed in me.

To all my friends who have helped me in so many ways - thanks!!!

Finally, I would like to thank Purdue Research Foundation (PRF) for supporting me during my first two years of PhD work. The AAE department then supported me for four years with teaching assistantships. Without this financial support there is no way I could have done my PhD here at Purdue.

# TABLE OF CONTENTS

Page

# LIST OF TABLES

## LIST OF FIGURES

Figure Page

Figure Page

Figure Page

Figure Page

Figure Page

Figure Page

Figure Page

Figure Page

Figure Page

Figure Page

Figure Page

Figure Page

Figure Page

Figure Page

Figure Page

Figure Page

Figure Page

# NOMENCLATURE

## Roman symbols

| | |
|---|---|
| $\mathbf{A}$ | Mass matrix, Section 2.3.3 |
| $\widetilde{\mathbf{A}}_i$ | Effective mass matrix, Section 2.3.7 |
| $\mathbf{B}$ | Viscous matrix, Section 2.3.3 |
| $\widetilde{\mathbf{B}}_i$ | Effective viscous matrix, Section 2.3.7 |
| $C_s$ | Smagorinsky constant, Section C.5 |
| $D$ | Computational domain, Section 2.2 |
| $E^*_\gamma$ | Critical Ekman number, Section 3.4 |
| $E_{1D} = E_\theta$ | One dimensional energy spectra, Section 3.6.1 |
| $E_{2D}$ | Two dimensional energy spectra, Section 3.6.1 |
| $e$ | Strain rate, Section 3.4 |
| $e^*$ | Critical strain rate, Section 3.4 |
| $\mathbf{e_r}$ | Unit vector in the radial direction, Section 3.3 |
| $\mathbf{e}_\theta$ | Unit vector in the azimuthal direction, Section 3.3 |
| $\mathbf{F}$ | Nonlinear term, Section 2.3.3 |
| $\mathbf{f}$ | Generic function used to explain the time advance method, Section 2.3.7 |
| $f$ | Generic function used to explain the filtering concept, Section C.3 |
| $\overline{f}$ | Grid scale part of $f$ after filtering, Section C.3 |
| $f'$ | Sub grid scale part of $f$ after filtering, Section C.3 |

| | |
|---|---|
| $g_l$ | B-spline polynomial, Section 2.3.4 |
| $g_l'$ | Derivative of $g_l$, Section 2.3.4 |
| $h_i$ | Filter function in the $i^{th}$ direction, Section C.3 |
| $\mathcal{K}$ | Global turbulent kinetic energy, Section 3.5 |
| $k$ | Order of b-splines, Section 2.3.1 |
| | Turbulent kinetic energy per unit mass, Section 3.5 |
| $k_0$ | Most unstable wavenumber, Section 3.4 |
| $\overrightarrow{k}$ | Wave number vector, Section C.3 |
| $k_c$ | Cut-off wave number, Section C.3 |
| $k_z$ | Wave number in the streamwise direction, Section 2.3.2 |
| $k_\theta$ | Wave number in the azimuthal direction, Section 2.3.2 |
| $L_z$ | Length of the computational domain, Section 2.2 |
| $L(\mathbf{f})$ | Linear term in a model system of equations, Section 2.3.7 |
| $l^*$ | Smallest unstable length scale, Section 3.4 |
| $N_r$ | Number of grid points in the radial direction, Section 2.3.2 |
| $N_\theta$ | Number of Fourier modes in the azimuthal direction, Section 2.3.2 |
| $N_z$ | Number of Fourier modes in the axial direction, Section 2.3.2 |
| $N(\mathbf{f})$ | Nonlinear convective team in a model system of equations, Section 2.3.7 |
| $P$ | Modified pressure, Section 2.2 |
| | Mean pressure, Section 3.6.3.1 |
| $p$ | Pressure, Section 2.2 |
| $q$ | Swirl number, Section 1.1 |
| $q_0$ | Initial swirl number, Section 1.1 |
| $R$ | Computational domain radius, Section 2.2 |
| $R_{ij} = \overline{v_i' v_j'}$ | Reynolds stress tensor, Section 3.6.3.1 |
| $R_{sp}$ | Radial location of stagnation points, Section 3.4 |
| $Re$ | Computational Reynolds number, Section 2.2 |
| $Re_\Gamma$ | Reynolds number based on circulation, Section 3.4 |

| | |
|---|---|
| $Re^*_\Gamma$ | Critical Reynolds number, Section 3.4 |
| $r$ | Radial coordinate, Section 1.1 |
| $r_0$ | Initial vortex core size, Section 1.1 |
| $\hat{r}$ | Dimensionless radial coordinate, Section 1.1 |
| $S_{ij}$ | Strain rate tensor, Section 3.4 |
| $\overline{S}_{ij}$ | Resolved strain rate tensor, Section C.5 |
| $T$ | Mean flow time scale, Section 3.5 |
| $\overline{T}$ | Minus the divergence of the sub-grid scale stress, Section C.4 |
| $\overrightarrow{u}$ | Velocity vector, Section 2.2 |
| $\overrightarrow{u}_{\mathbf{v}}$ | That part of the velocity that does not include strain, Section 3.3 |
| $\overrightarrow{u}_{\mathbf{s}}$ | Velocity induced by the strain field, Section 3.3 |
| $\mathbf{u}_l^{\pm}$ | Vector expansion functions, Section 2.3.2 |
| $V_0$ | Initial axial velocity deficit, Section 1.1 |
| $V_r$ | Mean radial velocity section 3.6.3.1 |
| $V_\theta$ | Tangential velocity component for $q$ vortex, Section 1.1 |
| | Mean tangential velocity, Section 3.6.3.1 |
| $V_z$ | Axial velocity component for $q$ vortex, Section 1.1 |
| | Mean axial velocity, Section 3.6.3.1 |
| $\widehat{V}_r^{\,p}$, $\widehat{V}_\theta^{\,p}$, $\widehat{V}_z^{\,p}$ | Potential flow velocity components in wave space, Section 2.3.5 |
| $\overrightarrow{v}$ | Numerical approximation to $\overrightarrow{u}$, Section 2.3.2 |
| $v'_r$ | Fluctuating radial velocity component, Section 3.6.3.1 |
| $v'_\theta$ | Fluctuating azimuthal velocity component, Section 3.6.3.1 |
| $v'_z$ | Fluctuating axial velocity component, Section 3.6.3.1 |
| $\mathbf{w}_k^{\pm}$ | Vector weight function, Section 2.3.2 |
| $\mathbf{w}^1_{new}$, $\mathbf{w}^2_{new}$ | New basis weight vectors developed using boundary conditions, Section 2.3.5 |
| $x_1, x_2, x_3$ | Cartesian coordinates, Section C.3 |
| $z$ | Axial direction, Section 2.3.1 |

**Greek symbols**

| | |
|---|---|
| $\alpha_{jml}^{\pm}$ | Expansion coefficients, Section 2.3.2 |
| $\dot{\alpha}^{\pm}$ | Time derivative of expansion coefficients, Section 2.3.3 |
| $\alpha_1,\ \alpha_2,\ \alpha_3$ | Constants in the time advance scheme, Section 2.3.7 |
| $\beta^*$ | Four times strain rate to average vorticity ratio, Section 3.4 |
| $\beta_1, \beta_2, \beta_3$ | Constants in the time advance scheme, Section 2.3.7 |
| $\delta_{kl}$ | Kronecker delta, Section 2.3.3 |
| $\theta_{sp}$ | Azimuthal location of stagnation points, Section 3.4 |
| $\overrightarrow{\omega}$ | Vorticity, Section 2.2 |
| $\Omega$ | Angular velocity, Section 1.1 |
| $\Gamma$ | Vortex circulation, Section 1,1 |
| $\Gamma_\infty$ | Freestream vortex circulation, Section 3.4 |
| $\gamma$ | Constant in the initial mean velocity profile, Section 1.1 |
| | Half the vorticity, Section 3.4 |
| $\gamma_1$,$\gamma_2$,$\gamma_3$ | Constants in the time advance scheme, Section 2.3.7 |
| $\Delta$ | Effective filter width, Section C.5 |
| $\Delta_i$ | Filter width in the $i^{th}$ direction, Section C.3 |
| $\Delta t$ | Time step, Section 2.3.7 |
| $\zeta$ | Average vorticity, Section 3.4 |
| $\zeta_1, \zeta_2$ | Constants in the time advance scheme, Section 2.3.7 |
| $\nu$ | Kinematic viscosity, Section 3.4 |
| $\nu_t$ | Eddy viscosity, Section C.3 |
| $\tau_{ij}$ | Sub grid scale stress tensor, Section C.5 |
| $\overrightarrow{\xi}$ | Vector function that is divergence free and homogeneous at the boundary, Section 2.3.2 |

**Other Symbols**

| | |
|---|---|
| $\overline{(\,)}$ | Line or surface average, Section 3.7.3.1 |
| | Filtering operation, Section C.4 |
| $(\,)^{\pm}$ | Indicates the class of expansion functions. |
| $\widehat{(\,)}$ | Fourier transform. |
| $\widehat{(\,)}^{*}$ | Complex conjugate of Fourier transform. |
| $\widehat{\nabla}$ | Fourier transformed del operator. |

**Abbreviations**

| | |
|---|---|
| CDI | Core dynamics instability. |
| DNS | Direct numerical simulation. |
| FFT | Fast Fourier transform. |
| GTKE | Global turbulent kinetic energy. |
| LES | Large eddy simulation. |
| LHS | Left hand side. |
| MPI | Message passing interface. |
| ODE | Ordinary differential equation. |
| RHS | Right hand side. |
| SGS | Sub grid scale. |
| STS | Sub test scale. |
| TKE | Turbulent kinetic energy. |

## ABSTRACT

Eshpuniyani, Brijesh, Purdue University, December, 2003. Flow Physics of Strained Turbulent Axial Vortices. Major Professor: Prof. Gregory A. Blaisdell.

The flow physics of strained turbulent axial vortices has been studied using direct numerical simulations (DNS) as an investigative tool. These simulations use a b-spline/Fourier spectral method. Two specific cases have been considered. A vortex that has no axial flow in its initial laminar state is first studied (this simulation is called STRN4). This allows us to focus exclusively on the effect of the strain field. The strain field causes the streamlines to be elliptical, thereby introducing a short wavelength instability called the elliptic instability. This is followed by studying a vortex that has a wake-like axial flow profile in its initial laminar state (this simulation is called STRN2). We now have the instability due to shear in the axial flow in addition to that due to the strain field.

In both these cases the initially laminar vortex is perturbed randomly. Evolution of the overall level of turbulence is studied by computing the global turbulent kinetic energy (GTKE). In STRN4 the GTKE evolves in an "oscillatory" fashion, with periods of exponential growth followed by saturation and decay. The growth rate decreases for successive exponential GTKE rises. In STRN2 the first exponential GTKE rise occurs with a much larger growth rate than the first exponential GTKE rise for STRN4. This is due to the instability associated with the axial flow. We then observe an "oscillatory" pattern, followed by a period during which the GTKE maintains an almost uniform level, and then a final period of growth. In both the cases, the simulation had to be stopped towards the end of the final GTKE rise because the turbulence outgrows the computational domain.

Flow visualization is used to study the evolution of the vortex in terms of its structure. In STRN4 we observe the presence of left and right running helical waves along with a sinusoidal bending of the vortex along its axis. As the simulation progresses, the wavelength of this sinusoidal bending is seen to increase. This is reflected in the dominant modes found by computing the two dimensional energy spectra. The dominant modes are found to shift from $(k_\theta, k_z) = (\pm 1, 4)$ to $(\pm 1, 1)$ as the simulation progresses. In STRN2, we initially observe helical waves with positive azimuthal wavenumbers. The initially dominant modes are computed to be $(k_\theta, k_z)$ = (1,1), (2,2), (3,3), (4,4) and (5,5). As the simulation progresses, the vortex structure shows the presence of features that correspond to a varied set of dominant modes. Towards the end of the simulation $(\pm 1, 1)$ are found to be the dominant modes. Two dimensional energy spectra also give us information about how the turbulent kinetic energy is spread over different wavenumbers (length scales). In general, increases in GTKE are accompanied by the presence of more small scale structure and vice versa. In addition to the broad understanding obtained in this manner, the evolution of some mean and statistical quantities of interest is discussed.

Formulation for large eddy simulation (LES) in the context of the numerical method used in this study has been completed. The DNS code has been modified to perform large eddy simulations. Validating this code and using it to perform LES to study the vortex at higher Reynolds numbers is one of the major suggestions for future work.

# 1. INTRODUCTION

## 1.1 Motivation and Background

Kuchemann (1965) calls vortices the 'sinews and muscles of fluid motions'. Figure 1.1 is indicative of the typical structure of an axial vortex. As can be seen, an axial vortex is composed of regions that vary from being potential in nature to being highly dependent on viscosity.

Research directed towards finding some order in the seemingly chaotic phenomenon of turbulent flows has revealed the presence of organized structures in the form of vortices (Vincent and Meneguzzi (1991); Kida (1993); Cadot, Douady and Couder (1995)). These findings suggest that a clear understanding of vortical flows will enhance our understanding of turbulent flows. In a general turbulent flow we can expect to see several of these vortices, of varying sizes that span a range of length scales, deforming and interacting with each other in a complicated fashion. In order to make the problem tractable, it is of interest to understand the behavior of vortices in simplified situations. The present study is one such investigation that focuses on an axial vortex in the presence of an external strain field. The approach taken is that of direct numerical simulations (DNS).

Besides the interest in vortices purely from the scientific standpoint of wanting to further the understanding of turbulent flows, and fluid mechanics in general, there exists a need to understand vortices to make progress in being able to solve some pressing problems in the realm of day to day practical living. One such problem is known as the wake hazard problem. The wing-tip vortices behind a large aircraft threaten the stability of any following aircraft. This problem is particularly severe during take-off and landing. A need to increase the capacity of airports demands

shorter time gaps between successive landings and take-offs. Thus, how long these vortices persist becomes crucial. If we have a clear understanding of these vortices, in particular the instability mechanisms and the fully turbulent state, we may be able to hasten their breaking down, or at least their weakening in strength. This shall alleviate the danger of a following aircraft losing control, when it encounters the invisible strongly rotating flow.

Another example of situations in which the presence of vortices presents problems arises in the case of helicopters. The vortices shed by the propeller blades result in a complex and unsteady flowfield. The interaction between this flowfield and the blades result in the generation of the loud "slapping" noise commonly associated with helicopters. A good understanding of vortices might thus enable us to better understand the process of sound generation in helicopters, and possibly other situations.

Vortices are not always disadvantageous in nature though. In many situations it is of interest to have vortices in the flowfield. Coming back to aircraft, the same wing tip vortices that threaten the stability of following aircraft can also be of advantage while flying in formation. The vortices in this case have the effect of reducing the downwash for the following aircraft in the formation, thus reducing the drag. Birds can often be seen using this phenomenon to their advantage. In situations like this, a good understanding of vortices, in particular the motion of wing tip vortices, might help us design and control formations that lead to better fuel efficiency and speed for a group of aircraft flying over long distances.

Also, vortices are very adept at enhancing the process of mixing. Thus, in situations like combustion chambers, where proper mixing of the fuel and oxidizer can lead to greater efficiency, it might be of interest to have a mechanism to generate vortices in a manner (the parameters being, say, strength and frequency) that helps the combustion process reach better efficiencies. Being able to break these vortices up into a turbulent state might further enhance the mixing process.

Another motivation for the current study arises from the use of turbulence models in engineering turbulent flow calculations at the present time. The mean flow field is

solved for, with the effects of turbulence being included via a model. This is in contrast to direct numerical simulations (DNS), which while being a good research tool to study the physics of turbulent flows, are still limited to low Reynolds number flows due to their severe computational costs. A middle approach, large eddy simulations (LES), is showing promises of being used to simulate flows at realistic Reynolds numbers in the near future. DNS involves numerically solving the Navier Stokes equations, with a grid that is fine enough to resolve all the relevant scales of the flow. The number of grid points needed to meet this requirement of being able to resolve all the relevant flow scales increases rapidly with increasing Reynolds numbers, thus limiting DNS to low Reynolds number flows. LES on the other hand solves the filtered form of Navier Stokes equations (Appendix C). The scales that are larger than the filter width are simulated, while the effect of the scales that are smaller than the filter width is calculated using a model. Thus LES are economical as compared to DNS, but more expensive than turbulence modeling. Now, in order for turbulence models to have any hope of correctly reflecting the physics, and not just be ad hoc in nature (as is often the case presently), there is a need for as much turbulent flow data as possible. Data obtained in DNS and LES is of great use for this purpose. Also, within the already challenging and complex problem of being able to account for all the scales of turbulence in a model, turbulence modeling for strongly rotating flows is a particularly difficult task. The vortex is one such flow. Hence the data obtained in the current study, in addition to increasing our understanding of vortices, shall be very useful in the development of new and improved turbulence models.

The DNS carried out for the current study uses the $q$ vortex to specify the initial laminar flow field. The $q$ vortex model was proposed by Lessen, Singh and Paillet (1974) and has the following tangential and axial velocity components:

$$\frac{V_\theta}{V_0} = \frac{q_0}{\hat{r}}(1 - e^{-\hat{r}^2}) \tag{1.1}$$

$$\frac{V_z}{V_0} = (1 - e^{-\hat{r}^2})\,. \tag{1.2}$$

Here $\hat{r} = \gamma r/r_0$ is the dimensionless coordinate, $\gamma = 1.12090642$ being the root of $1 + 2\gamma^2 = e^{\gamma^2}$. $V_0$ is the initial axial velocity deficit. The initial swirl number, $q_0$, is a measure of the relative strength of the tangential velocity component to the axial velocity deficit.

Lessen et al. (1974) and Lessen and Paillet (1974) performed the first stability analysis of the $q$ vortex. They performed both inviscid and viscous calculations. They found that all the modes get stabilized, irrespective of their orientations, if the swirl parameter is increased above 1.5. Inviscid stability analysis of the $q$ vortex by Duck and Foster (1980) revealed the the presence of a continuous spectrum of unstable modes. For each combination of the swirl parameter $q$ and the axial and azimuthal wavenumbers, the spectrum was found to contain an infinite number of higher modes.

The stability characteristics of the $q$ vortex model were also studied by Leibovich and Stewartson (1983). They used asymptotic methods for their study and derived the following sufficient condition for the axial vortex to be unstable:

$$V_\theta \frac{d\Omega}{dr}\left[\frac{d\Omega}{dr}\frac{d\Gamma}{dr} + \left(\frac{dV_z}{dr}\right)\right] < 0 \tag{1.3}$$

Here $\Omega = V_\theta/r$ is the basic flow's angular velocity. This study also revealed instabilities at $q = 1.58$, albeit with very small growth rates. This study indicates that the instabilities would be strong for $q < \sqrt{2}$.

Khorrami (1991) performed a stability analysis of a trailing line vortex using the $q$ vortex model. He included viscous effects in this analysis. Two unstable modes were found with azimuthal wavenumbers 0 and 1. Evidence for the possibility of viscosity having a destabilizing effect on swirling flows was found for the first time in this study. These viscous modes have growth rates that are orders of magnitude smaller than the growth rates of the inviscid modes. These are long wavelength instabilities having an axial wavelength that scales with the vortex core radius. Results similar to Khorrami's analysis are found in experiments conducted by Singh and Uberoi (1976) and Sarpkaya and Daly (1987).

Ragab and Sreedhar (1994, 1995a, 1995b) studied turbulent axial vortices using DNS and LES. They first studied the Lamb-Oseen vortex. This is simply the $q$ vortex without the axial flow. It was found that in the absence of the axial flow, the initial disturbances are simply quenched. This is in accord with stability properties as discussed above. No axial flow corresponds to the swirl parameter being infinite. Later they included a wake like axial flow (i.e. now they studied the $q$ vortex). The axial velocity deficit is found to weaken faster than the tangential velocity. This means that the swirl number value increases and eventually becomes large enough for the turbulence to quench and the vortex relaminarizes. Qin (1998) also performed a DNS study of the Lamb-Oseen and $q$ vortices. In one of his $q$ vortex simulations, he visualized the relaminarization process by plotting sequence of vorticity magnitude isosurfaces. Helical waves with positive azimuthal wavenumbers are observed to grow initially. Eventually a quenching of the turbulence and relaminarization is observed.

Till now we have looked at instability caused by the presence of a wake like (or jet like) axial flow profile with a sufficiently large deficit (or excess). Often more than one vortex is present (for example, trailing vortices behind aircraft come in pairs). These vortices interact with each other. The physics of vortices under the influence of other vortices (such as the instability mechanisms which would cause an initially laminar vortex to transition into a turbulent state) is different from that of an isolated vortex. One way in which the vortices interact with each other is via a strain field. When this strain field is in the plane normal to the vortex axis, the streamlines become elliptical (see figure 1.2). This ellipticity of the streamlines brings into play what is known as the elliptical instability. In a recent review paper, Kerswell (2002) notes that this instability has a resonance based mechanism wherein "a normal mode, or pair of normal modes, of oscillation on the undistorted circular flow become tuned to the underlying strain field". The elliptical instability is a short wavelength instability and occupies the center-stage for much of the work presented in this thesis. We shall come back to it shortly and discuss its characteristics in detail.

Crow (1970) developed a stability theory for a pair of trailing vortices. He points out that simple diffusion is not the mechanism for the decay of trailing vortices. The vortices usually undergo a symmetric, almost sinusoidal instability, ultimately joining at intervals to form a trail of vortex rings. The most rapidly growing mode of the long wavelength instability predicted by Crow's formulation is the wavy pattern observed in practice. It is predicted that the trailing vortices distort into symmetric waves of wavelength 6.8 times the span of the aircraft. Compared with the process of vortex formation, the growth of this instability is very slow. The perturbed vortices are confined to fixed planes which are inclined at an angle of 48 degrees to the horizontal. This instability functions through the resonance between a bending Kelvin wave on the vortex filament and the external strain field from the other vortex filament.

Tsai and Widnall (1976) investigated the stability of short-wave displacements on a vortex filament of constant vorticity in a weak externally imposed strain field. For the straight filament considered by Tsai and Widnall, the cross section of the region of constant vorticity becomes an ellipse in straining flow and the velocity field is no longer tangential. The presence of strain introduces a short wavelength instability known as the Widnall instability. The maximum rate of amplification and the width of the instability zone (range of unstable wavenumbers) are proportional to the strain rate to vorticity ratio. Using numerical simulation, Robinson and Saffman (1984) extended the validity of the weak strain results (in a qualitative sense) to finite strain.

Cambon et al. (1985, 1994) studied the elliptic streamline flow using Rapid Distortion Theory (RDT). This is a homogeneous turbulent flow which combines effects of both rotation and strain. It is thus similar to the mean flow in a vortex strained in the plane perpendicular to its axis. Pierrehumbert (1986), Bayly (1986) and Waleffe (1990) studied the linear stability of the elliptical streamline flow by performing inviscid stability analyses using different methods. They reported that there are no unstable modes for circular streamlines, i.e. pure rotation. However, a band of unstable modes exists for elliptic streamlines. The growth rate of these modes is a

function of the polar angle of the wavenumber vector. Increasing the ellipticity of the streamlines has the effect of increasing the width of the band of unstable angles. The magnitude of the wavenumber vector does not affect the growth rate of the unstable modes according to the inviscid theory. Hence an instability of the basic two dimensional flow is sufficient to create arbitrarily small three-dimensional fluctuations. This was suggested by Pierrehumbert (1986) to be a possible mechanism of the cascade process in turbulence. Landman and Saffman (1987) report that viscosity modifies the growth rate of the instabilities and there is no longer an independence between the growth rate and the magnitude of the wavenumber vector. A high wavenumber cut-off exists for the instability but there is no low wave number cut-off. Arbitrarily large scales are thus unstable.

Eloy and Dizes (1999) studied the linear stability of Burgers and Lamb-Oseen vortices in the presence of a strain field in the plane normal to the vortex axis. They assumed the Reynolds numbers to be large and the strain and stretching to be small in their study. The short wavelength instability as described by Tsai and Widnall (1976) and Moore and Saffman (1975) was found to be active for both vortices. Eloy and Dizes refer to this instability as the TWMS instability. It involves the resonance of stationary helical Kelvin waves with azimuthal wavenumbers 1 and -1. The external strain amplifies these waves around critical axial wavenumbers. This instability mechanism has been extended by Eloy and Dizes to include viscous and axial stretching effects. Although the case of helical waves with azimuthal wavenumbers 1 and -1 is considered, it is pointed out that any combination of two waves with the same frequency and axial wavenumber, and azimuthal wavenumbers differing by 2, will resonate with the strain field. The growth rate of any such combination is shown to depend slightly on the azimuthal wavenumbers involved by Waleffe (1989). This similarity in the growth rates of the different combinations is suggested as a possible explanation for the rich variety of features observed in the vortex structure in experiments and numerical simulations of high Reynolds number flows. For low Reynolds

numbers though, it is expected that viscosity will strongly filter both azimuthal and axial wavenumbers.

Dizes and Laporte (2002) investigate the linear stability of a flow that is composed of a pair of parallel Gaussian vortices. They consider a general situation in which these vortices have different circulations and radii. Also, the flow is quasi-steady in a reference frame that rotates with the vortex system. They obtain the viscous growth rate of the globally unstable modes by considering the local stability in each of the vortex centers. The final formula relating the growth rate to the axial wavenumber is tested using DNS and LES. The simulations at high Reynolds numbers (greater than $10^5$) agree well with the predictions, while for small Reynolds numbers (2500-5000) the theory is found to underestimate growth rates by about 20 percent.

Blaisdell and Shariff (1994, 1996) have performed DNS for the elliptical streamline flow to examine its nonlinear development and the fully turbulent state. A principal issue they investigate is whether the instability modes grow and dominate the flow even when large initial disturbances are present. The governing parameters for the elliptic streamline flow are identified to be the aspect ratio of the elliptic streamlines (rotation rate to strain rate ratio), mean flow time scale to turbulence time scale ratio and the turbulent Reynolds number. The elliptic streamline flow is linearly unstable for all nonzero strain rates. Linear theory predicts the turbulent kinetic energy to grow exponentially. The simulation results agree with this prediction initially. At later times, the growth rate is observed to decrease. This is attributed to the growing importance of the nonlinear effects.

Leweke and Williamson (1998) experimentally investigated the three-dimensional instability of a pair of counter-rotating vortices, and provided the first clear identification of the elliptical instability manifesting in vortex cores. They observe the evolution of the short wave instabilities in the two vortices to be cooperative in nature. Using fluorescent dye flow visualization, they present pictures that show the onset of both, the long wave Crow and the short wave elliptical instabilities. It is seen that the short wave instability deforms the vortex core, in contrast to the long wave

instability which is a wavy displacement of the vortex along its length only. Leweke and Williamson note that this core deformation involves a "wavy displacement of the vortex center, the existence of a cylindrical invariant stream tube, and a radial motion of the fluid, which is in opposite directions inside and outside this tube". The cooperative nature of the short wave instabilities on the two vortices is revealed upon observing that the vortex centers, at any given axial position, get displaced in the same direction. It is also observed that the amplitude of the small scale instability is larger in regions where the two vortices have been brought together as a result of the Crow instability. This is evidence supporting the proportionality between the growth rate and the strain rate (smaller separation means larger strain rate).

Orlandi et al. (1998) reproduced results of the above experiments by Leweke and Williamson in a DNS study of trailing vortices. Taking advantage of the increased capability of DNS in obtaining and analyzing velocity and vorticity data, they could look at the non-axial vorticity components and how these lead to the cross diffusion of circulation between the vortex pair. They also looked at creating density perturbations along the vortices' axes as a possible way to initiate the cooperative instability.

Afanasyev (2002) experimentally studied the stability of a pair of vortices in a fluid which itself is in solid body rotation. One area to which this study contributes is geophysical flows. Quasi-two-dimensional vortices are found abundantly in the atmosphere as well in the oceans. Earth's rotation affects the large scale vortices while the smaller scale vortices can find themselves to be in rotating flow fields because of the presence of other vortices. Understanding the stability properties of anticyclonic columnar vortices in a rotating fluid is important with respect to such geophysical flow situations. The main non-dimensional parameter in such situations is the Rossby number ($Ro$), which is the ratio of the vorticity in the columnar vortex to the background vorticity. Afanasyev performed this study for Rossby numbers greater than unity. In these experiments Afanasyev found that the anticyclonic vortex is subject to elliptical instability when the initial ellipticity is large. The vortex filament is found

to be sinusoidally deformed in the plane of maximum stretching (symmetry plane for the vortex pair).

Coppens (1998), Qin (1998) and Blaisdell and Qin (1999) have performed DNS of axial vortices in the presence of an external strain field. Qin (1998) performed DNS of strained $q$ vortices, perturbed randomly from their initial laminar state with a specified initial turbulent kinetic energy profile. He considered cases with and without a wake like axial velocity profile over a range of Reynolds numbers. Qin (1998) and Blaisdell and Qin (1999) report success in capturing the Widnall instability for a case with a wake like axial velocity profile.

There have also been several studies of the elliptic instability in the weakly nonlinear regime. Waleffe (1989) studied a strained vortex that is bounded and uniform. In contrast, a non-bounded and nonuniform strained vortex was considered by Sipp (2000). The qualitative features of how the elliptic instability develops in both these situations are found to be similar. In both cases, it is deformations which reduce the systems' symmetry that cause the instability. Guckenheimer and Mahalov (1992) and Knobloch et al. (1994) analyze this situation of instability caused by symmetry reduction from the point of view of Hamiltonian systems. Even though fluid dynamics equations have not been explicitly used by these researchers in deriving their results, they find amplitude equations that have the same structure as found by Waleffe (1989) and Sipp (2000). Sipp analyzed in detail a case which has small amplitude initial conditions. In this analysis the linear regime is found to select a perturbation with phase angle $\pi/4$. This corresponds to the direction in which the basic flow is stretched. This selected eigenmode is found to grow exponentially till its amplitude reaches a critical value. Once this critical value is reached, the perturbation leaves the unstable direction due to the nonlinearities as well as changes to the mean field. The phase is found to now settle at $-\pi/4$. This corresponds to the direction in which the basic flow is contracted. The perturbation is now found to die out by returning its energy to the mean flow. A new linear regime, having negligible phase shift terms,

is reached. At this time it is possible that this cycle of linear instability, saturation and attenuation can start again.

This result that the elliptic instability indeed saturates seems to be in contradiction to experimental observation by Leweke and Williamson (1998) and the DNS results of Orlandi et al. (1998), both of which suggested otherwise. A similar observation was made by Malkus (1989). He performed an experimental study using a rotating elastic cylinder that is elliptically distorted. The observation in this study was that the unstable waves, after growing for some time, suddenly break down into small scale turbulence. This apparent paradox between the prediction that the elliptic instability should saturate, and experimental and numerical observations that suggest the opposite scenario, was resolved by Kerswell (1999) and Mason and Kerswell (1999). Their DNS study revealed that the above predicted saturated state was not observed because either these states were themselves made unstable by the presence of secondary instabilities, or were disrupted by other elliptical instability modes that are growing.

Lebovitz and Saldanha (1999) point out that the above mentioned studies of the short-wave instability in the weakly nonlinear regime consider only the local bifurcations of the system. They show that global bifurcations can also result from the development of the elliptic instability in the weakly nonlinear regime. Due to this reason, and due to the possibility of the weakly nonlinear saturated states themselves being unstable, one has to be careful while attempting to draw conclusions about the role played by the elliptical instability in situations such as the dispersion of wingtip vortices in the wake of an aircraft.

In contrast to the elliptical instability of bending waves, i.e. perturbations that bend the vortex axis, Pradeep and Hussain (2001) investigated the effect of strain on axial waves. These are perturbations that do not deflect the vortex axis while causing variations in the core vorticity. They consider the instability resulting from an axisymmetric variation in the core area along the axis of a vortex column, in the presence of an external strain field, and call it the core dynamics instability (CDI).

CDI results from the tilting of the column's axial vorticity. This results in a generation of radial and azimuthal vorticity components, which can undergo stretching due to the strain. They observe that the CDI leads to a more rapid transition than the bending wave instability, and suggest that this is due to the location of the self-stretching. Self stretching induced by CDI occurs near the vortex axis, a region of large vorticity magnitudes, while the self-stretching in the case of bending waves takes place in the periphery of the core, a region of low vorticity magnitudes.

Mason and Kerswell (2002) point out that although we have developed a good understanding of the linear instability of elliptical streamlines, the nonlinear evolution of this instability has still not been studied in detail. According to them efforts in this direction have faced obstacles because a natural situation that is amenable to numerical simulation is not available. They provide examples to support this claim. It is pointed out that in studying elliptical flow in a plane layer, the compromise of enforcing periodicity had to be made (Lungren and Mansour (1996)). In other DNS studies, such as that of the elliptical instability of a vortex pair by Laporte and Corjon (2000), or that involving an elliptical geometry (Mason and Kerswell (1999)), the increased computational cost placed a limitation on how much we could learn.

It is suggested by Mason and Kerswell (2002) that strained rotating flows can also be studied in the area of precessing flows. In these flows, the strain acts perpendicular to the plane of streamlines, in contrast to elliptic flows in which the strain is in the plane of streamlines. The streamlines thus remain circular in precessing flows. However the line passing through their centers does not stay perpendicular to the plane containing them. The streamlines are thus sheared across each other. However, in both these categories of flows, the instability mechanism involves the pairwise resonance of inertial waves. Although the conditions for the two waves to resonate and grow would be different in the two scenarios (Kerswell (2002)), the non linear dynamics for the two flow scenarios are expected to be similar. With this in mind, Mason and Kerswell used DNS to study the nonlinear dynamics generated by instabilities in a precessing flow situation. Multiple nonlinear states are found to co-exist. Some

of these states are chaotic. The flow seems to select what the authors call "the most efficient dissipative state". The term "efficiency" here has been loosely defined by the authors as "some ratio of total dissipation to instability kinetic energy".

## 1.2 Objectives

The present study continues the work of Blaisdell and Qin (1999). Initially the plan was to study the vortex at higher Reynolds numbers by performing LES. However, it was later discovered that the simulations by Qin were not carried out for a sufficient length of time. This resulted in an incomplete understanding of the flow physics. The focus of the current study thus shifted to revisiting Qin's simulations and obtaining a more complete and correct picture of strained turbulent axial vortices.

Two of the DNS performed by Qin (1998) have been extended further in time. One of these, labeled as STRN2 by Qin, considers a strained axial vortex with an initial wake like axial velocity profile. The other, labeled as STRN4 by Qin, considers a strained axial vortex that does not have an initial axial flow. The overall aim of this study is to study the evolution of these two vortices from their initially laminar state in detail. In order to accomplish this, we can create a list of objectives as follows:

- Study how the overall level of turbulence evolves in time by computing the global turbulent kinetic energy (defined in Section 3.5).
- Use flow visualization to study how these vortices evolve in terms of their structure.
- Compute 2-D energy spectra (defined in Section 3.6.1) to study the distribution of turbulent kinetic energy over different wavenumbers (length scales).
- Take a close look at how some mean and statistical quantities of interest (mean velocity and vorticity components, turbulent kinetic energy, Reynolds stress components and enstrophy) evolve in time.

One of the major contributions of the work presented in this thesis is in providing a detailed DNS study of how the elliptical instability behaves beyond its initial linearly unstable phase. Also, the DNS study of the strained vortex with a wake-like axial flow presented here is the first such study, wherein a flow that simultaneously contains the elliptical instability and the axial flow instability is studied in detail beyond the initial linearly unstable phase. The detailed statistics computed during these simulations are a valuable contribution to the field of turbulence modeling, particularly for strongly rotating flows.

### 1.3 Layout of Thesis

The numerical method used for performing these DNS is explained in chapter two. Chapter two also discusses the boundary conditions and how these are implemented in the context of the current numerical method. The initial conditions are explained in chapter three. This is followed by an explanation of how strain is imposed and what constraints this leads to in choosing the parameters for our simulations. We then take a close look at the results obtained in terms of the objectives listed out above. Chapter four finally draws some conclusions and makes some suggestions for future work. Appendices A and B contain details associated with the numerical method explained in chapter two. Appendix C deals with the formulation of LES, first in general and then in the context of the current numerical method. This falls in line with one of the suggestions made for future work in chapter four, which is to study the vortex at higher Reynolds numbers by performing LES.

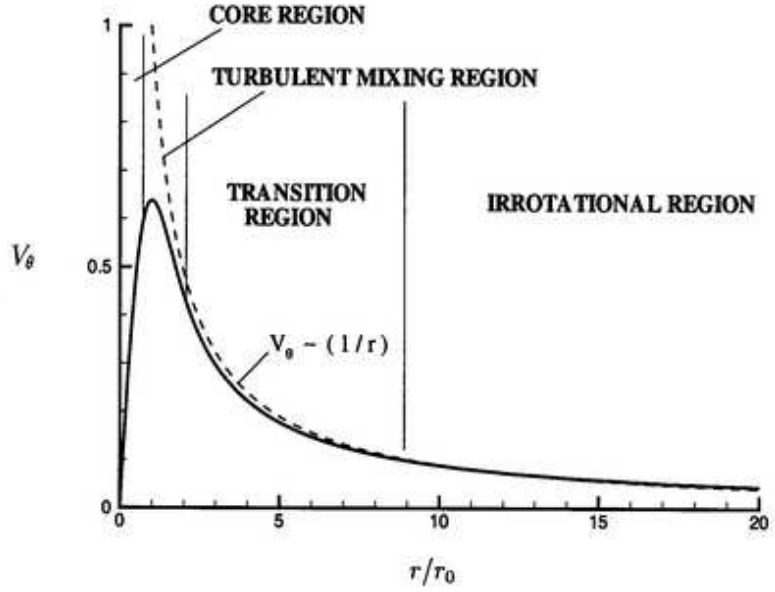


Figure 1.1 Typical axial vortex structure (Takahashi and McAlister (1987)).

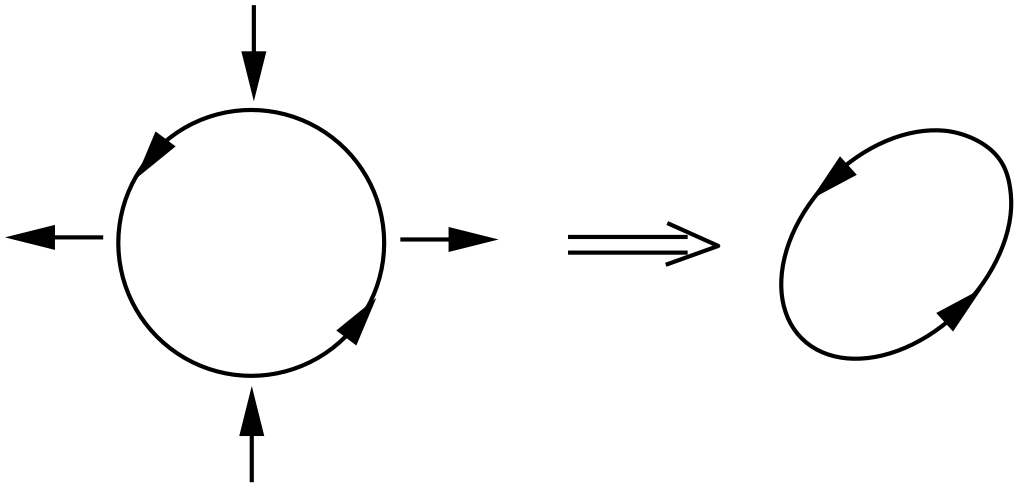

Figure 1.2 A strained vortex (Qin (1998))

# 2. DIRECT NUMERICAL SIMULATIONS I FORMULATION

## 2.1 Introduction

The turbulent flow simulation approach used in the current study assumes that the dynamics of turbulence is represented by the Navier-Stokes equations, a system of non-linear partial differential equations, obtained by applying the laws of conservation of mass, momentum and energy to a fluid, along with the continuum hypothesis. A simulation that uses a discretization fine enough to resolve all the relevant length and time scales is known as a direct numerical simulation (DNS). The disparity between the largest and the smallest scales increases rapidly with increasing Reynolds numbers. The immense computer resources required to resolve a turbulent flow well, even at moderate Reynolds numbers, make DNS a very expensive proposition for simulating real life engineering flows. For this reason most DNS are limited to low Reynolds number flows and are mainly used as an investigative tool to better understand the flow physics.

It is with this intention that a DNS study of turbulent axial vortices is being performed. This chapter develops the numerical method used in the current study.

## 2.2 Governing Equations

The incompressible Navier-Stokes equations can be written as

$$\overrightarrow{\nabla}.\overrightarrow{u} = 0 \tag{2.1}$$

$$\frac{\partial \overrightarrow{u}}{\partial t} + \overrightarrow{u}.\overrightarrow{\nabla}\overrightarrow{u} + \overrightarrow{\nabla}p = \frac{1}{Re}\overrightarrow{\nabla}.\overrightarrow{\nabla}\overrightarrow{u}, \tag{2.2}$$

where $\overrightarrow{u}$ = velocity and $p$ = pressure. Here all quantities are normalized using the radius of the computational domain (Figure 2.1), $R$, as the length scale and the initial

axial velocity deficit, $V_o = V_z(r=\infty) - V_z(r=0)$, as the velocity scale, where $V_z(r)$ is the mean axial velocity. In simulations of vortices without a wake like axial velocity profile, $V_o$ is assigned the value it would have for a corresponding case with axial flow, with the same initial swirl number (defined in section 3.2). $Re = V_o R/\nu$ is the computational Reynolds number.

Using the identity $\overrightarrow{u}.\overrightarrow{\nabla}\overrightarrow{u} = -\overrightarrow{u} \times \overrightarrow{\omega} + \frac{1}{2}\overrightarrow{\nabla}(\overrightarrow{u}.\overrightarrow{u})$ we write the momentum equation as

$$\frac{\partial \overrightarrow{u}}{\partial t} + \overrightarrow{\nabla} P = \overrightarrow{u} \times \overrightarrow{\omega} + \frac{1}{Re}\overrightarrow{\nabla}.\overrightarrow{\nabla}\overrightarrow{u}, \tag{2.3}$$

where $\overrightarrow{\omega} = \overrightarrow{\nabla} \times \overrightarrow{u}$ is the vorticity and $P = p + \frac{1}{2}\overrightarrow{u}.\overrightarrow{u}$ is the modified pressure.

## 2.3 Numerical Method

### 2.3.1 Choice of method

The vortex under consideration is time developing and, therefore, homogeneous in the axial ($z$) direction. This corresponds to a vortex far downstream, under the approximation that the flow changes slowly in the streamwise direction. Also, the azimuthal direction is naturally periodic. This enables the use of a Fourier spectral method in the streamwise and azimuthal directions. Basis spline polynomials (b-splines) are used in the radial direction. These provide spectral-like accuracy and are $C^{k-2}$ continuous, where $k$ is the order of the splines being used. In the current work, $4^{th}$ order b-splines are used. Also, since b-splines have local support on a given interval (Figure 2.2), they lead to sparse matrices that can be efficiently stored and solved.

Loulou (1996) developed a serial computer program to study turbulent pipe flow that solves the incompressible Navier-Stokes equations in cylindrical coordinates using a Galerkin formulation with a Fourier spectral method in $z$ and $\theta$ and a b-spline method in $r$. The program was modified by Qin (Qin *et al.* 1998 ) to solve the vortex problem and to run on an IBM SP2 parallel computer. Parallelization was done using the MPI message passing library. This code is used for the current work and it is further modified to perform large eddy simulations.

### 2.3.2 Weak form

Before solving the filtered Navier-Stokes equations, they are transformed to a form that is better suited to numerical computation. Let $\overrightarrow{v}$ be a numerical approximation to $\overrightarrow{u}$ that consists of a truncated expression in terms of divergence free vector functions (Moser *et al.* (1983)). Thus equation (2.1) drops out by construction. The continuity constraint results in the velocity vector having only two independent components. Hence two distinct classes of divergence free vectors are required to represent $\overrightarrow{v}$. For the current problem, since homogeneity is assumed in the streamwise direction and the azimuthal direction is periodic, $\overrightarrow{v}$ is represented as

$$\overrightarrow{v} = \sum_{jml} [\alpha^{+}_{jml}(t)\,\overrightarrow{u}^{+}_{l}(r, k_\theta, k_z) + \alpha^{-}_{jml}(t)\,\overrightarrow{u}^{-}_{l}(r, k_\theta, k_z)] e^{i(k_\theta \theta + k_z z)}, \tag{2.4}$$

where $\alpha^{\pm}$ are the expansion coefficients, $k_z = 2\pi m / L_z$ $(-N_z/2 \leq m \leq N_z/2 - 1)$ are the streamwise wave numbers, $k_\theta = j$ $(-N_\theta/2 \leq j \leq N_\theta/2 - 1)$ are the azimuthal wave numbers and $\overrightarrow{u}^{\pm}_{l}$ $(1 \leq l \leq N_r)$ are the basis expansion vectors.

Also, let $\overrightarrow{\xi}$ be any vector function representable by an additional set of divergence free vector functions such that it is homogeneous at the domain boundary. Now the standard weighted residual technique is used, with $\overrightarrow{\xi}$ as the weight function, to get the weak form of the Navier-Stokes equation

$$\left( \overrightarrow{\xi}, \frac{\partial \overrightarrow{v}}{\partial t} \right) = \frac{1}{Re} \left( \overrightarrow{\xi}, (\overrightarrow{\nabla} . \overrightarrow{\nabla}\, \overrightarrow{v}) \right) + \left( \overrightarrow{\xi}, (\overrightarrow{v} \times \overrightarrow{\omega}) \right) \tag{2.5}$$

where $(\overrightarrow{a}, \overrightarrow{b}) = \int_D \overrightarrow{a} . \overrightarrow{b}\, dV$ is an inner product. $\overrightarrow{\xi}$ being divergence free and homogeneous at the boundary results in the pressure term dropping out. The weight function $\overrightarrow{\xi}$ is chosen as

$$\xi^{\pm}_{k}(r, \theta, z; k_\theta, k_z) = \mathbf{w}^{\pm}_{k}(r, k_\theta, k_z) e^{-i(k_\theta \theta + k_z z)} \tag{2.6}$$

where $\mathbf{w}^{\pm}_{k} (1 \leq k \leq N_r)$ are the basis expansion vectors for the weight function, which are described in detail in section 2.3.4.

### 2.3.3 System of equations

Substituting equations (2.4) and (2.6) in equation (2.5) we obtain, for each Fourier mode ($k_z$ , $k_\theta$), the following system of ordinary differential equations:

$$\begin{pmatrix} \mathbf{A}^{++} & \mathbf{A}^{-+} \\ \mathbf{A}^{+-} & \mathbf{A}^{--} \end{pmatrix} \begin{pmatrix} \dot{\alpha^+} \\ \dot{\alpha^-} \end{pmatrix} = \begin{pmatrix} \mathbf{B}^{++} & \mathbf{B}^{-+} \\ \mathbf{B}^{+-} & \mathbf{B}^{--} \end{pmatrix} \begin{pmatrix} \alpha^+ \\ \alpha^- \end{pmatrix} + \begin{pmatrix} \mathbf{F}^+ \\ \mathbf{F}^- \end{pmatrix} \tag{2.7}$$

Here,

$$\mathbf{A}^{++} = \int_0^R \mathbf{w}_k^+ \cdot \mathbf{u}_l^+ r \, dr \qquad \mathbf{A}^{+-} = \int_0^R \mathbf{w}_k^- \cdot \mathbf{u}_l^+ r \, dr \tag{2.8}$$

$$\mathbf{A}^{-+} = \int_0^R \mathbf{w}_k^+ \cdot \mathbf{u}_l^- r \, dr \qquad \mathbf{A}^{--} = \int_0^R \mathbf{w}_k^- \cdot \mathbf{u}_l^- r \, dr \tag{2.9}$$

are the mass matrices,

$$\mathbf{B}^{++} = \int_0^R \mathbf{w}_k^+ \cdot (\widehat{\bigtriangledown} \cdot \widehat{\bigtriangledown} \mathbf{u}_l^+) r \, dr \qquad \mathbf{B}^{+-} = \int_0^R \mathbf{w}_k^- \cdot (\widehat{\bigtriangledown} \cdot \widehat{\bigtriangledown} \mathbf{u}_l^+) r \, dr \tag{2.10}$$

$$\mathbf{B}^{-+} = \int_0^R \mathbf{w}_k^+ \cdot (\widehat{\bigtriangledown} \cdot \widehat{\bigtriangledown} \mathbf{u}_l^-) r \, dr \qquad \mathbf{B}^{--} = \int_0^R \mathbf{w}_k^- \cdot (\widehat{\bigtriangledown} \cdot \widehat{\bigtriangledown} \mathbf{u}_l^-) r \, dr \tag{2.11}$$

where $\widehat{\bigtriangledown}$ is the del operator in wave space, are the viscous matrices, and

$$\mathbf{F}^{\pm} = \frac{1}{2\pi L_z R} \int_0^{L_z} \int_0^{2\pi} \int_0^R \mathbf{w}_k^{\pm} \cdot (\mathbf{v} \times \omega) e^{-i(k_\theta \theta + k_z z)} r \, dr \, d\theta \, dz. \tag{2.12}$$

are the nonlinear terms. $\dot{\alpha}^{\pm}$ is the time derivative of $\alpha^{\pm}$. Note that each submatrix (for the mass and viscous matrices) has the dimension $N_r$ x $N_r$, thus resulting in a $2N_r$ x $2N_r$ system.

The orthogonality property

$$\int_0^{2\pi} e^{-ik\theta} e^{il\theta} d\theta = 2\pi \delta_{kl} \tag{2.13}$$

is used to reduce the volume integrals for the mass and viscous matrices in equation (2.5) to single integrals in $r$. The row index in these matrices corresponds to $\mathbf{w}_k^{\pm}$ while the column index corresponds to $\mathbf{u}_l^{\pm}$. The basis expansion vectors for the velocity and weight functions presented in the following section are used to evaluate the expressions for the mass and viscous matrices, and the nonlinear terms. These are included in Appendix B.

### 2.3.4 Basis expansion vectors

The numerical method chosen uses divergence free vector functions to represent the velocity field. Also, in order to deal with the coordinate singularity at the origin, the basis expansion vectors for the velocity field must satisfy certain regularity conditions (Loulou 1996). These vectors are defined as follows. Note that since $\overrightarrow{v}$ is real, we have $\widehat{\overrightarrow{v}}_{-j,m,l} = \widehat{\overrightarrow{v}}^{*}_{j,m,l}$, where the superscript $*$ stands for complex conjugate. Hence, the vectors are constructed only for $k_\theta > 0$.

For $k_\theta = 0$, $k_z = 0$

$$\mathbf{u}_l^+ = \begin{pmatrix} 0 \\ g_l(r) \\ 0 \end{pmatrix} \ , \ \mathbf{u}_l^- = \begin{pmatrix} 0 \\ 0 \\ \frac{g_l(r)}{r} \end{pmatrix} \tag{2.14}$$

For $k_\theta > 0$, $k_z = 0$

$$\mathbf{u}_l^+ = \begin{pmatrix} -ik_\theta g_l(r) \\ (r g_l(r))' \\ 0 \end{pmatrix} \ , \ \mathbf{u}_l^- = \begin{pmatrix} 0 \\ 0 \\ g_l'(r) + \frac{(1-k_\theta)}{r} g_l(r) \end{pmatrix} \tag{2.15}$$

For $k_\theta = 0$, $k_z \neq 0$

$$\mathbf{u}_l^+ = \begin{pmatrix} 0 \\ k_z g_l(r) \\ 0 \end{pmatrix} \ , \ \mathbf{u}_l^- = \begin{pmatrix} -ik_z g_l(r) \\ k_z g_l(r) \\ g_l'(r) + \frac{g_l(r)}{r} \end{pmatrix} \tag{2.16}$$

For $k_\theta > 0$, $k_z \neq 0$

$$\mathbf{u}_l^+ = k_z \begin{pmatrix} -ik_\theta g_l(r) \\ (r g_l(r))' \\ 0 \end{pmatrix} \ , \ \mathbf{u}_l^- = \begin{pmatrix} -ik_z g_l(r) \\ k_z g_l(r) \\ g_l'(r) + \frac{(1-k_\theta)}{r} g_l(r) \end{pmatrix} \tag{2.17}$$

Here $g_l(r)$ is the $l^{th}$ B-spline function (Figure 2.2) and $g_l'(r)$ is the derivative of $g_l(r)$ (de Boor (1978)).

The basis expansion vectors for the weight function, $\mathbf{w}_k^\pm$, are chosen to be the complex conjugate of $\mathbf{u}_l^\pm$. Therefore this is a Galerkin formulation. However, the

requirement that $\mathbf{w}_k^{\pm}$ be homogeneous at the boundary, which is needed for the pressure term to drop out of equation 2.5, requires us to eliminate those vectors that are non-zero at the boundary. The equations corresponding to these are thus dropped from (2.7). Appropriate boundary conditions are applied to complete the system of equations.

### 2.3.5 Boundary conditions

As mentioned above, the basis vectors that are not homogeneous at the boundary are eliminated. Since this results in a loss of the corresponding equations from (2.7), appropriate boundary conditions have to be applied in order to complete the set of equations. It is known that the flow far away from the vortex core is irrotational (McCormick et al. (1968), Takahashi and McAlister (1987)). Thus we can apply potential flow boundary conditions. In the current work, constant potential flow is imposed at the boundary. Since the q-vortex or the Oseen vortex is used to specify the initial mean flow field (explained in section 3.2), the mean tangential and axial velocities obtained from these models at the boundary are imposed as the boundary condition for the velocity field.

The equations resulting for each Fourier mode are now derived. Here $\widehat{V}_r^{\,p}(R, k_\theta, k_z)$, $\widehat{V}_\theta^{\,p}(R, k_\theta, k_z)$ and $\widehat{V}_z^{\,p}(R, k_\theta, k_z)$ are the potential flow velocity components at the boundary in Fourier wave space for mode $(k_\theta, k_z)$. Since we are imposing constant potential flow at the boundary, $\widehat{V}^p_{r,\theta,z} = 0$ for all $k_\theta, k_z \neq 0$.

For $k_\theta = 0$ and $k_z = 0$, the nonhomogeneous basis weight vectors are $\mathbf{w}^+_{Nr}$ and $\mathbf{w}^-_{Nr}$. Equations corresponding to these two vectors are removed from (2.7), and the following potential flow boundary conditions are used to replace them:

$$\sum_{l=1}^{N_r} \alpha_l^+(0,0) g_l(R) = \widehat{V}_\theta^{\,p}(R, 0, 0) \tag{2.18}$$

$$\sum_{l=1}^{N_r} \alpha_l^-(0,0) \frac{g_l(R)}{R} = \widehat{V}_z^{\,p}(R, 0, 0) \tag{2.19}$$

Note that $\alpha_l^{\pm}(0,0) = \alpha_{00l}^{\pm}$, where $k_\theta = 0$ corresponds to $j = 0$ and $k_z = 0$ corresponds to $m = 0$ in $\alpha_{jml}^{\pm}$. Since $g_l(R) = 0$ for all $l$ except $l = N_r$, these give the following two equations to re-complete (2.7):

$$\alpha_{N_r}^{+}(0,0) = \widehat{V}_\theta^{\,p}(R,0,0) \tag{2.20}$$

$$\alpha_{N_r}^{-}(0,0) = R\widehat{V}_z^{\,p}(R,0,0) \tag{2.21}$$

For $k_\theta \neq 0$ and $k_z = 0$, the nonhomogeneous basis weight vectors are $\mathbf{w}_{Nr-1}^{+}$, $\mathbf{w}_{Nr}^{+}$, $\mathbf{w}_{Nr-1}^{-}$, and $\mathbf{w}_{Nr}^{-}$. Equations corresponding to these four vectors are removed from (2.7), and the following potential flow boundary conditions are used to replace three of these equations:

$$\sum_{l=1}^{N_r} -ik_\theta \alpha_l^{+}(k_\theta,0) g_l(R) = \widehat{V}_r^{\,p}(R,k_\theta,0) = 0 \tag{2.22}$$

$$\sum_{l=1}^{N_r} \alpha_l^{+}(k_\theta,0)(g_l(R) + Rg_l'(R)) = \widehat{V}_\theta^{\,p}(R,k_\theta,0) = 0 \tag{2.23}$$

$$\sum_{l=1}^{N_r} \alpha_l^{-}(k_\theta,0)\left(g_l'(R) + \frac{1-k_\theta}{R} g_l(r)\right) = \widehat{V}_z^{\,p}(R,k_\theta,0) \;\; = 0 \tag{2.24}$$

Using the properties of the b-spline functions, we get the following equations from these:

$$\alpha_{N_r-1}^{+}(k_\theta,0) = 0 \tag{2.25}$$

$$\frac{g_{Nr-1}'(R)}{g_{Nr}'(R) + \frac{1-k_\theta}{R}} \alpha_{N_r-1}^{-}(k_\theta,0) + \alpha_{N_r}^{-}(k_\theta,0) = 0 \tag{2.26}$$

$$\alpha_{N_r}^{+}(k_\theta,0) = 0 \tag{2.27}$$

The fourth constraint is developed using a new basis weight vector that is constructed from a linear combination of those vectors that were eliminated.

$$\mathbf{w}_{new}^{1}(r) = c_1\mathbf{w}_{Nr-1}^{+}(r) + c_2\mathbf{w}_{Nr}^{+}(r) + c_3\mathbf{w}_{Nr-1}^{-}(r) + c_4\mathbf{w}_{Nr}^{-}(r)\,. \tag{2.28}$$

The required homogeneity of this vector at the boundary restricts us to choosing only one coefficient arbitrarily. Choosing $c_3 = 1$ and applying the condition $\mathbf{w}_{new}^{1}(R) = 0$,

we obtain $c_1 = 0$, $c_2 = 0$, $c_3 = 1$ and $c_4 = -\frac{g'_{Nr-1}(R)}{g'_{Nr}(R)+\frac{1-k_\theta}{R}}$. We thus have a new basis weight vector

$$\mathbf{w}^1_{new}(r) = \mathbf{w}^-_{Nr-1}(r) - \frac{g'_{Nr-1}(R)}{g'_{Nr}(R) + \frac{1-k_\theta}{R}}\mathbf{w}^-_{Nr}(r). \tag{2.29}$$

The fourth equation, that now re-completes (2.7), is a linear combination of the four eliminated equations with $c_1$, $c_2$, $c_3$ and $c_4$ as the coefficients for equations corresponding to $\mathbf{w}^+_{Nr-1}(r)$, $\mathbf{w}^+_{Nr}(r)$, $\mathbf{w}^-_{Nr-1}(r)$ and $\mathbf{w}^-_{Nr}(r)$ respectively.

For modes $k_\theta = 0$ and $k_z \neq 0$, the nonhomogeneous weight vectors are $\mathbf{w}^+_{Nr}$,$\mathbf{w}^-_{Nr-1}$, and $\mathbf{w}^-_{Nr}$. Equations corresponding to these three vectors are removed from (2.7), and the following potential flow boundary conditions are used to replace these equations:

$$\sum_{l=1}^{N_r} -ik_z\alpha^-_l(0,k_z)g_l(R) = \widehat{V_r}^{\,p}(R,0,k_z) = 0 \tag{2.30}$$

$$\sum_{l=1}^{N_r} k_z g_l(R)(\alpha^+_l(0,k_z) + \alpha^-_l(0,k_z)) = \widehat{V_\theta}^{\,p}(R,0,k_z) = 0 \tag{2.31}$$

$$\sum_{l=1}^{N_r} \alpha^-_l(0,k_z)\left(g'_l(R) + \frac{g_l(r)}{R}\right) = \widehat{V_z}^{\,p}(R,0,k_z) = 0\,, \tag{2.32}$$

These give the following three equations to re-complete (2.7):

$$\alpha^-_{N_r-1}(0,k_z) = 0 \tag{2.33}$$

$$\alpha^+_{N_r}(0,k_z) = 0 \tag{2.34}$$

$$\alpha^-_{N_r}(0,k_z) = 0 \tag{2.35}$$

For $k_\theta \neq 0$ and $k_z \neq 0$, the nonhomogeneous basis weight vectors are $\mathbf{w}^+_{Nr-1}$, $\mathbf{w}^+_{Nr}$, $\mathbf{w}^-_{Nr-1}$, and $\mathbf{w}^-_{Nr}$. Equations corresponding to these four vectors are removed from (2.7), and the following potential flow boundary conditions are used to replace three of these equations:

$$\sum_{l=1}^{N_r} -ik_z g_l(R)(k_\theta\alpha^+_l(k_\theta,k_z) + \alpha^-_l(k_\theta,k_z)) = \widehat{V_r}^{\,p}(R,k_\theta,k_z) = 0 \tag{2.36}$$

$$\sum_{l=1}^{N_r} k_z\alpha^+_l(k_\theta,k_z)(g_l(R) + Rg'_l(R)) + k_z\alpha^-_l(k_\theta,k_z)g_l(R) = \widehat{V_\theta}^{\,p}(R,k_\theta,k_z) = 0 \tag{2.37}$$

$$\sum_{l=1}^{N_r} \alpha_l^-(k_\theta, k_z) \left( g_l'(R) + \frac{1-k_\theta}{R} g_l(r) \right) = \widehat{V_z}^p(R, k_\theta, k_z) = 0 \tag{2.38}$$

We get the following equations from these:

$$\frac{g'_{Nr-1}(R)}{g'_{Nr}(R) + \frac{1-k_\theta}{R}} \alpha^+_{N_r-1}(k_\theta, k_z) + \alpha^+_{N_r}(k_\theta, k_z) = 0 \tag{2.39}$$

$$\frac{g'_{Nr-1}(R)}{g'_{Nr}(R) + \frac{1-k_\theta}{R}} \alpha^-_{N_r-1}(k_\theta, k_z) + \alpha^-_{N_r}(k_\theta, k_z) = 0 \tag{2.40}$$

$$k_\theta \alpha^+_{N_r}(k_\theta, k_z) + \alpha^-_{N_r}(k_\theta, k_z) = 0 \tag{2.41}$$

The fourth constraint is developed using a new basis weight vector that is constructed from a linear combination of those vectors that were eliminated.

$$\mathbf{w}^2_{new}(r) = c_1 \mathbf{w}^+_{Nr-1}(r) + c_2 \mathbf{w}^+_{Nr}(r) + c_3 \mathbf{w}^-_{Nr-1}(r) + c_4 \mathbf{w}^-_{Nr}(r) \, . \tag{2.42}$$

The required homogeneity of this vector at the boundary restricts us to choosing only one coefficient arbitrarily. Choosing $c_1 = 1$ and applying the condition $\mathbf{w}^2_{new}(R) = 0$, we obtain $c_1 = 1$, $c_2 = -\frac{g'_{Nr-1}(R)}{g'_{Nr}(R) + \frac{1-k_\theta}{R}}$, $c_3 = -k_\theta$ and $c_4 = k_\theta \frac{g'_{Nr-1}(R)}{g'_{Nr}(R) + \frac{1-k_\theta}{R}}$. We thus have a new basis weight vector

$$\mathbf{w}^2_{new}(r) = \mathbf{w}^+_{Nr-1}(r) - \frac{g'_{Nr-1}(R)}{g'_{Nr}(R) + \frac{1-k_\theta}{R}} \mathbf{w}^+_{Nr}(r) - k_\theta \mathbf{w}^-_{Nr-1}(r) + k_\theta \frac{g'_{Nr-1}(R)}{g'_{Nr}(R) + \frac{1-k_\theta}{R}} \mathbf{w}^-_{Nr}(r) \tag{2.43}$$

The fourth equation, that now re-completes (2.7), is a linear combination of the four eliminated equations with $c_1$, $c_2$, $c_3$ and $c_4$ as the coefficients for equations corresponding to $\mathbf{w}^+_{Nr-1}(r)$, $\mathbf{w}^+_{Nr}(r)$, $\mathbf{w}^-_{Nr-1}(r)$ and $\mathbf{w}^-_{Nr}(r)$ respectively.

### 2.3.6 Nonlinear term

Taking advantage of the fact that the integral

$$\frac{1}{2\pi L_z} \int_0^{2\pi} \int_0^{L_z} \mathbf{w}^\pm_k \cdot (\mathbf{v} \times \omega) e^{-i(k_\theta \theta + k_z z)} \, d\theta \, dz \tag{2.44}$$

is indeed the definition of the inverse Fourier transform of $\mathbf{w}^\pm_k \cdot (\mathbf{v} \times \omega)$, a pseudo spectral approach is used to evaluate the non-linear terms (2.12). In this approach, fast Fourier transforms (FFT) are used to evaluate the product $\mathbf{w}^\pm_k \cdot (\mathbf{v} \times \omega)$ in physical

space. The Gauss quadrature technique is used to compute the integrals over $r$ to machine accuracy thus alleviating numerical errors in the radial direction. The inverse transform is used to go back into Fourier wave space thus obtaining the value of the non-linear term for each $(k_\theta, k_z)$ mode. De-aliasing (Orszag 1971, Canino et al. 1988) is ensured by using the 3/2 rule while performing the Fourier transforms. The pseudo spectral approach using FFTs requires $O(N\log_2 N)$ operations as compared to $O(N^2)$ required for a full spectral approach. This approach thus saves on computational cost which is a significant concern in DNS and LES. The evaluation of the nonlinear term is explained in detail in Appendix B.

### 2.3.7 Time advance

A mixed explicit-implicit method developed by Spalart, Moser and Rogers (1991) is employed to solve the system of equations (2.7). This method (also called the SMR method) computes the non-linear terms explicitly using a third order Runge-Kutta scheme, while implicitly time-marching the linear viscous term using a Crank-Nicholson scheme.

Consider a model system of equations

$$\frac{\partial \mathbf{f}}{\partial t} = L(\mathbf{f}) + N(\mathbf{f}) \,, \tag{2.45}$$

where $L(\mathbf{f})$ is the linear term consisting of the viscous term, while $N(\mathbf{f})$ is the nonlinear convective term. The SMR method advances $\mathbf{f}_n$ at time $t$ to $\mathbf{f}_{n+1}$ at time $t + \Delta t$ as follows:

$$\mathbf{f'}_n = \mathbf{f}_n + \Delta t[L(\alpha_1 \mathbf{f}_n + \beta_1 \mathbf{f'}) + \gamma_1 N(\mathbf{f}_n)] \tag{2.46}$$

$$\mathbf{f''}_n = \mathbf{f'}_n + \Delta t[L(\alpha_2 \mathbf{f'} + \beta_2 \mathbf{f''}) + \gamma_2 N(\mathbf{f'}) + \zeta_1 N(\mathbf{f}_n)] \tag{2.47}$$

$$\mathbf{f}_{n+1} = \mathbf{f''}_n + \Delta t[L(\alpha_3 \mathbf{f''} + \beta_3 \mathbf{f}_{n+1}) + \gamma_3 N(\mathbf{f''}) + \zeta_1 N(\mathbf{f'})] \tag{2.48}$$

where

$$\alpha_1 = \frac{29}{96}\,, \quad \alpha_2 = -\frac{3}{40}\,, \quad \alpha_3 = \frac{1}{6}\,, \tag{2.49}$$

$$\beta_1 = \frac{37}{160}\,, \quad \beta_2 = \frac{5}{24}\,, \quad \beta_3 = \frac{1}{6}\,, \tag{2.50}$$

$$\gamma_1 = \frac{8}{15}\,, \quad \gamma_2 = \frac{5}{12}\,, \quad \gamma_3 = \frac{3}{4}\,, \tag{2.51}$$

$$\zeta_1 = \frac{17}{60}\,, \quad \zeta_2 = \frac{5}{12}\,. \tag{2.52}$$

Upon applying this method to the system of equations (2.7), we obtain the following:

$$\widetilde{\mathbf{A}}_1\alpha' = \widetilde{\mathbf{B}}_1\alpha_n + \Delta t\gamma_1\mathbf{F}(\alpha_n) \tag{2.53}$$

$$\widetilde{\mathbf{A}}_2\alpha'' = \widetilde{\mathbf{B}}_1\alpha' + \Delta t\left[\gamma_2\mathbf{F}(\alpha') + \zeta_1\mathbf{F}(\alpha_n)\right] \tag{2.54}$$

$$\widetilde{\mathbf{A}}_3\alpha_{n+1} = \widetilde{\mathbf{B}}_1\alpha'' + \Delta t\left[\gamma_3\mathbf{F}(\alpha') + \zeta_2\mathbf{F}(\alpha')\right] \tag{2.55}$$

where

$$\mathbf{F} = \begin{pmatrix} \mathbf{F}^+ \\ \mathbf{F}^- \end{pmatrix}\,, \quad \alpha = \begin{pmatrix} \alpha^+ \\ \alpha^- \end{pmatrix}\,, \tag{2.56}$$

and $\widetilde{\mathbf{A}}_i$ and $\widetilde{\mathbf{B}}_i$ are the effective mass and viscous matrices

$$\widetilde{\mathbf{A}}_i = \begin{pmatrix} \mathbf{A}^{++} & \mathbf{A}^{-+} \\ \mathbf{A}^{+-} & \mathbf{A}^{--} \end{pmatrix} - \beta_i\Delta t \begin{pmatrix} \mathbf{B}^{++} & \mathbf{B}^{-+} \\ \mathbf{B}^{+-} & \mathbf{B}^{--} \end{pmatrix}\,, \tag{2.57}$$

$$\widetilde{\mathbf{B}}_i = \begin{pmatrix} \mathbf{A}^{++} & \mathbf{A}^{-+} \\ \mathbf{A}^{+-} & \mathbf{A}^{--} \end{pmatrix} - \alpha_i\Delta t \begin{pmatrix} \mathbf{B}^{++} & \mathbf{B}^{-+} \\ \mathbf{B}^{+-} & \mathbf{B}^{--} \end{pmatrix}\,. \tag{2.58}$$

Although the method requires three storage locations, the algorithm in table 2.1 makes it possible to implement it using only two storage locations.

As indicated by $\widetilde{\mathbf{A}}_i^{-1}$, a linear system is being solved. The parallel implementation of the algorithm is facilitated by the fact that a separate linear system is solved for each mode $(k_\theta, kz)$.

Table 2.1 SMR method using two storage locations (Loulou 1996, Qin 1998).

| Time | Location 1 | Location 2 |
|---|---|---|
| $t_n$ | $\alpha^1 = \alpha_n$ | $\alpha^2 = \alpha_n$ |
| $t_n$ | $\alpha^1 = \mathbf{F}(\alpha^1)$ | $\alpha^2 = \widetilde{\mathbf{B}}_i \alpha^2$ |
| | $\alpha^1 = \alpha^2 + \gamma_1 \Delta t \alpha^1$ | $\alpha^2 = (\alpha^2 - \alpha^1)/(\gamma_1 \Delta t)$ |
| | $\alpha^1 = \alpha' = \widetilde{\mathbf{A}}_1^{-1} \alpha^1$ | $\alpha^2 = \widetilde{\mathbf{B}}_i \alpha^1 + \zeta_1 \Delta t \alpha^2$ |
| $t_n$ | $\alpha^1 = \alpha^2 + \gamma_2 \Delta t \mathbf{F}(\alpha^1)$ | $\alpha^2 = (\alpha^2 - \alpha^1)/(\gamma_1 \Delta t)$ |
| | $\alpha^1 = \alpha'' = \widetilde{\mathbf{A}}_2^{-1} \alpha^1$ | $\alpha^2 = \widetilde{\mathbf{B}}_3 \alpha^1 + \zeta_2 \Delta t \alpha^2$ |
| $t_n$ | $\alpha^1 = \alpha^2 + \gamma_3 \Delta t \mathbf{F}(\alpha^1)$ | $\alpha^2 = \alpha^2$ |
| | $\alpha^1 = \alpha''' = \widetilde{\mathbf{A}}_3^{-1} \alpha^1$ | $\alpha^2 = \alpha^1$ |
| $t_{n+1} = t_n + \Delta t$ | $\alpha_{n+1} = \alpha'''$ | $\alpha_{n+1} = \alpha'''$ |

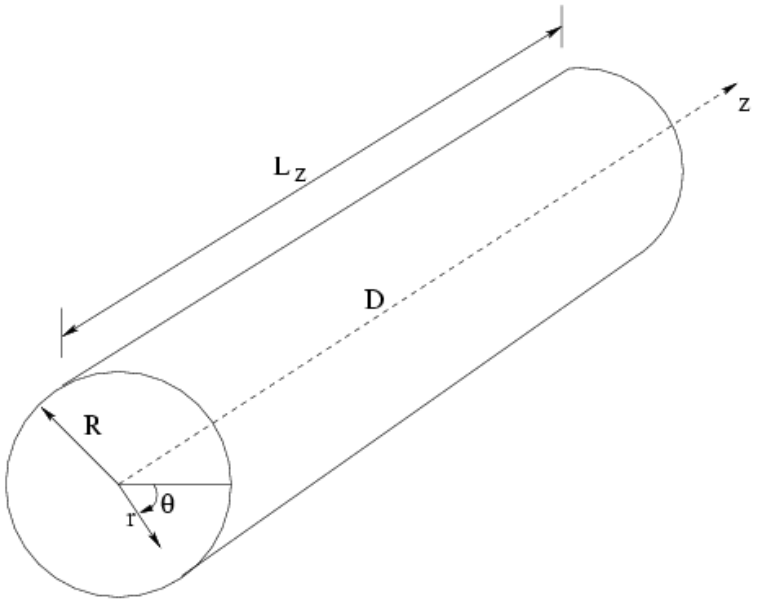


Figure 2.1 The coordinate system and the computational domain

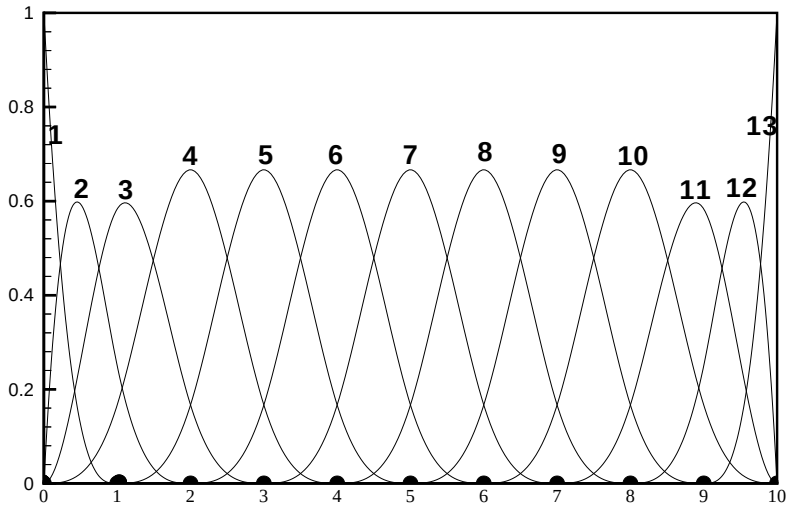


Figure 2.2 Cubic B-splines on an 11-knot uniform grid (Qin (1998))

# 3. DIRECT NUMERICAL SIMULATIONS II RESULTS AND DISCUSSION

## 3.1 Introduction

Qin (1998) performed a series of direct numerical simulations (DNS) of a strained turbulent axial vortex using the B-spline spectral method. Using a $q$ vortex with an imposed steady and irrotational external strain field as the initial state, Qin simulated cases both with and without an axial flow. For cases without an axial flow, he reports an eventual decay of the global turbulent kinetic energy (GTKE) (defined in Section 3.5). The reason suggested by Qin for not being able to capture the Widnall instability is the local stability of most regions inside the vortex core. Of the two cases with axial flow considered by him, Qin reports an unbounded growth of GTKE for the case with the higher Reynolds number, indicating a complete capture of the Widnall instability. The current study started with an aim to complete a DNS database for a thorough parametric study, which would hopefully aid in more clearly understanding the factors that enabled the capture of the Widnall instability. It was later discovered that the simulations by Qin were not carried out for a sufficient length of time thus resulting in an incomplete understanding of the flow physics. The focus of the current study shifted to revisiting Qin's simulations and obtaining a more complete and correct picture of strained axial vortices.

## 3.2 Initial Conditions

The initial mean flowfield (see figure 3.1) corresponds to that of a $q$ vortex. The tangential and axial velocity components are given by

$$\frac{V_\theta}{V_0} = \frac{q_0}{\hat{r}}(1 - e^{-\hat{r}^2}) \tag{3.1}$$

$$\frac{V_z}{V_0} = (1 - e^{-\hat{r}^2}) \,. \tag{3.2}$$

Here $\hat{r} = \gamma r/r_0$ is the dimensionless coordinate, $\gamma = 1.12090642$ being the root of $1 + 2\gamma^2 = e^{\gamma^2}$. $V_0$ is the initial axial velocity deficit. The initial swirl number, $q_0$, is a measure of the relative strength of the tangential velocity component to the axial velocity deficit. For simulations without axial flow, $V_z$ is set to 0. As mentioned in section 2.2, for cases without axial flow, $V_o$ is assigned the value it would have for a corresponding case with axial flow, with the same initial swirl number. $q_0$ is set to 1 in all our simulations.

The initial mean velocity field has to be converted from physical space (as given above in equations 3.1 and 3.2) to the expansion coefficients (see section 2.3). This is accomplished using the procedure described in Appendix A. The mean velocity field corresponds to $k_\theta = k_z = 0$ in the wave space. In order to provide initial turbulent fluctuations, the expansion coefficients for the non zero wave numbers are perturbed randomly. A power spectrum is specified to generate the desired initial turbulent kinetic energy (TKE) profile in the physical space (see figure 3.2).

### 3.3 Imposing Strain

An external strain field is imposed by decomposing the velocity into two parts

$$\overrightarrow{v} = \overrightarrow{\mathbf{u_v}} + \overrightarrow{\mathbf{u_s}} \tag{3.3}$$

where $\overrightarrow{\mathbf{u_s}}$ is the velocity induced by the strain field, while $\overrightarrow{\mathbf{u_v}}$ is that part of the velocity which does not include the strain. $\overrightarrow{\mathbf{u_s}}$ is given by

$$\overrightarrow{\mathbf{u_s}} = e\cos(2\theta)\mathbf{e_r} - e\sin(2\theta)\mathbf{e}_\theta \tag{3.4}$$

where $e$ is the strain rate (defined in section 3.4), while $\mathbf{e_r}$ and $\mathbf{e}_\theta$ are the unit vectors in the radial and azimuthal directions respectively. The external strain field applied is both steady and irrotational.

$$\frac{\partial \overrightarrow{\mathbf{u_s}}}{\partial t} = 0 \quad \text{and} \quad \bigtriangledown \times \overrightarrow{\mathbf{u_s}} = 0 \tag{3.5}$$

Substituting equations 3.3 and 3.5 into equation 2.5 results in the following equation

$$(\overrightarrow{\xi}, \frac{\partial \overrightarrow{\mathbf{u_v}}}{\partial t}) = \frac{1}{Re}(\overrightarrow{\xi}, (\overrightarrow{\nabla}.\overrightarrow{\nabla}\overrightarrow{\mathbf{u_v}})) + (\overrightarrow{\xi}, ((\overrightarrow{\mathbf{u_v}} + \overrightarrow{\mathbf{u_s}}) \times \overrightarrow{\omega})) \tag{3.6}$$

where where $\overrightarrow{\omega} = \overrightarrow{\bigtriangledown} \times (\overrightarrow{\mathbf{u_v}} + \overrightarrow{\mathbf{u_s}}) = \overrightarrow{\bigtriangledown} \times \overrightarrow{\mathbf{u_v}}$ is the vorticity. Thus we see that only the nonlinear term needs to be modified if one solves for $\overrightarrow{\mathbf{u_v}}$ instead of $\overrightarrow{v}$. Note that the strain enters the formulation only through modes $k_z = 0$ and $k_\theta = \pm 2$ (see equation 3.4).

### 3.4 Constraints

The parameters that form the framework within which the current numerical simulations are carried out are the initial core radius to computational domain radius ratio, $r_0/R$, the non-dimensional strain rate, $e/e^*$ ($e^*$ defined later), and the Reynolds number, $Re_\Gamma = \Gamma_\infty/\nu$. Certain features of the flowfield, in particular the presence of stagnation points, the boundary conditions, and the magnitude and orientation of the unstable wave vectors, lead to constraints within which these parameters can be chosen.

As can be seen in figure 3.3, the flow field for a vortex with an externally imposed uniform strain field contains stagnation points. The computational domain cannot contain these stagnation points, as their presence will cause undesired instability. In reality, the strain field of a pair of vortices is not uniform, and the stagnation points do not correspond to the wake vortex problem we are trying to better understand. Solving the potential flow obtained by combining a point vortex and linear strain gives us the location of these stagnation points

$$R_{sp} = \sqrt{\frac{\Gamma_\infty}{2\pi e}}\,, \quad \text{and} \quad \theta_{sp} = \frac{\pi}{4} \; or \; \frac{3\pi}{4}\,, \tag{3.7}$$

where $R_{sp}$ and $\theta_{sp}$ are the radius and azimuthal angle of the stagnation points, and e is the strain rate defined as

$$S_{rr} = \frac{\partial V_r}{\partial r} = e\cos 2\theta \quad \text{and} \quad S_{\theta\theta} = \frac{1}{r}\frac{\partial V_\theta}{\partial \theta} + \frac{V_r}{r} = -e\cos 2\theta\,. \tag{3.8}$$

Since we are using potential flow boundary conditions, the radius of the computational domain has to be sufficiently larger than the core radius to ensure irrotationality of the flow at the boundary. For the current simulations the ratio of the initial core radius to the computational domain radius is kept less than or equal to 0.15 (see table 3.1). For a given computational domain radius, R, and $\Gamma_\infty$, equation 3.7 places an upper limit on the strain rate we can impose

$$e \leq e^* = \frac{\Gamma_\infty}{2\pi R^2} \,. \tag{3.9}$$

where $e^*$ is the critical strain rate.

As discussed in chapter one, the presence of strain introduces a short wavelength instability (Widnall instability). If we are to capture this instability in our simulations, we need to make sure that the core size of our vortex is greater than the smallest (in terms of length scale) instability mode. The strained vortex is related to the so called elliptic streamline flow in matters of stability. This flow is a combination of solid body rotation and uniform strain. It is a homogeneous turbulent flow, and as the name suggests, it has elliptic streamlines. Linear stability analysis reveals the following to be the smallest unstable length scale for this flow (Landman and Saffman (1987))

$$l^* = (2\pi)^{\frac{3}{2}} \sqrt{\frac{\nu}{\gamma E^*_\gamma}} \,, \tag{3.10}$$

where $\nu$ and $\gamma$ are the kinematic viscosity and half the vorticity respectively. $E^*_\gamma$ is the critical Ekman number

$$E^*_\gamma = \frac{2\pi\nu k_0^2}{\gamma} \,, \tag{3.11}$$

where $k_0$ is the wave number of the most amplified perturbation. Shariff, Verzico and Orlandi (1994) showed that the above result can be used to determine the smallest unstable length scale of a strained vortex, if one replaces the vorticity, $2\gamma$, by an average vorticity (the vorticity inside the core of our $q$ vortex is not constant, as opposed to the situation in an elliptic streamline flow) defined as

$$\zeta = 2\gamma = \frac{\Gamma_\infty}{\pi r_0^2} \,, \tag{3.12}$$

Substituting this in equation 3.10 gives us the smallest unstable length scale for our strained vortex

$$l^* = \frac{4\pi^2 r_0}{\sqrt{Re_\Gamma E^*_\gamma}}\,, \tag{3.13}$$

The requirement that the minimum unstable length scale $l^*$ be less than the core size $r_0$ of the vortex establishes a lower limit on the Reynolds number which can be deduced from equation 3.13 by setting $l^* = r_0$

$$Re^*_\Gamma = \frac{16\pi^4}{E^*_\gamma}\,, \tag{3.14}$$

Thus we hope to capture the Widnall instability only for Reynolds numbers that are greater than this critical Reynolds number $Re^*_\Gamma$. It is desirable to express $Re^*_\Gamma$ in terms of the strain rate. This is achieved by using the following approximation for $E^*_\gamma$ (Shariff et al. (1994)) for small strain rates

$$E^*_\gamma \approx 3.25\beta^* - c_1\beta^{*2} + O(\beta^{*3})\,, \tag{3.15}$$

where $\beta^* = 4e/\zeta$ and $c_1$ is a constant. Since we are only applying small strain rates to our vortex, and thus are dealing only with small values of $\beta^*$, we can neglect the second order term in the above equation to get

$$E^*_\gamma \approx 3.25\beta^* + O(\beta^{*2}) \tag{3.16}$$

Substituting equations 3.16, 3.12 and 3.9 in equation 3.14, we get

$$Re^*_\Gamma = \frac{8\pi^4}{3.25}\left(\frac{e^*}{e}\right)\left(\frac{R}{r_0}\right)^2\,, \tag{3.17}$$

Table 3.1 reflects the use of this result in setting up the parameters for the various DNS.

### 3.5 Revisiting Qin's DNS

Qin (1998) presented four direct numerical simulations of a strained turbulent axial vortex (see table 3.1). STRN1 and STRN2 included a wake like axial velocity profile, while STRN3 and STRN4 considered a vortex without any axial flow. Qin observed

an unbounded monotonic growth of the global turbulent kinetic energy (GTKE) in STRN2, while GTKE showed eventual decay for the other cases. Here GTKE is the non dimensionalized volume averaged turbulent kinetic energy defined as

$$\mathcal{K} = \frac{1}{\pi R^2 L_z {V_0}^2} \int_0^R \int_0^{2\pi} \int_0^{L_z} k r dz d\theta dr \,, \tag{3.18}$$

where $R$ is the radius of the computational domain, $L_z$ is the length of the computational domain in the streamwise direction, and $k$ is the local turbulent kinetic energy per unit mass.

Upon continuing the simulation STRN2 further in time, it was discovered that the GTKE eventually decays in a manner similar to the DNS at a lower Reynolds number (STRN1). This indicated that the Widnall instability may not have been captured (see figure 3.4), contrary to the conclusion drawn earlier based on a DNS that was not extended far enough in time. Note that the non-dimensional time, $t$, is being scaled by the mean flow time scale defined as $T = 2\pi r_0 / V_\theta^{max}(t = 0)$. This scaling has been done while plotting the temporal evolution of any quantity in this study. This led to a fresh look at the DNS results by Qin and an inquiry into the possible reasons behind the perceived lack of success in capturing the Widnall instability. As this instability is introduced by the external strain field, the simulations of the strained vortex without an axial wake (STRN3 and STRN4) were revisited in order to study the effect of the strain field without any possible interference from the axial flowfield during the simulation.

The fact that these DNS were carried out at low Reynolds numbers was considered as a possible reason for not capturing the Widnall instability. Hence, DNS of a strained vortex at higher Reynolds numbers were performed. However, eventual decay of GTKE was observed in all these simulations (see figure 3.5). Here $Re = V_0 R/\nu$ is the computational Reynolds number. Although the DNS performed at these high Reynolds numbers are expected to be severely under-resolved, this was the best attempt possible at the time in seeing if the flow becomes unstable as the Reynolds number is increased.

Shariff et al. (1994) present the evolution of modal energies for a three-dimensional vortex ring simulation. The evolution of all but a few unstable modes show a striking resemblance to the GTKE behavior in figure 3.5. However, after a long period of time the initially stable modes also show unbounded growth. Since a strained vortex has the same short wavelength instability as a vortex ring (Widnall et al.), the possibility of a similar phenomenon occurring in the current DNS was explored by extending the DNS at the largest Reynolds number considered to a longer period of time. It is observed that the GTKE begins to grow exponentially after a long period of decay (see figure 3.6).

Upon this observation, STRN4 was extended in time to see if the Widnall instability can indeed be captured at the Reynolds numbers considered by Qin. It is observed that the GTKE does grow exponentially after a long period of decay (see figure 3.7). However, we do not observe an unbounded growth of GTKE. Instead the GTKE reaches a peak value and begins to decay again. An "oscillatory" behavior is observed for some time. We shall see later that eventually the domain size becomes a constraint in the current simulation. The simulation cannot be carried further in time, thus prohibiting us from finding out the eventual behavior of the vortex.

STRN2 was also revisited to include the effect of a wake-like initial axial velocity profile. Upon extending STRN2 further in time (see figure 3.8), it was observed that GTKE seems to settle down at a level which is higher than the initial GTKE after a period of oscillatory behavior. There seems to be some sort of an "equilibrium" turbulent state that the vortex has reached. After maintaining this state for a long period of time, the GTKE begins to grow again. Taking a cue from STRN4, this simulation has also been carried out till we encounter the domain size limitation. This will be explained while discussing STRN2 in detail.

### 3.6 STRN4 - A Close Look

Let us first look at STRN4 closely as it does not have any axial flow, thus allowing us to focus exclusively on the effects of the applied strain field. In order to study the

flow in sufficient detail, in a systematic and convenient manner, the simulation has been divided into four different time periods. These time periods have been defined using the time history of GTKE as a guideline. See figure 3.7 for the definitions of the terms "1st ebb", "1st peak", etc. These terms shall now be used to define the four time periods. The first time period is from the initial state till the "2nd ebb". The time period from the "2nd ebb" till the "2nd peak" forms our second time period. The third time period is from the "2nd peak" till the "4th ebb", and the time period from the "4th ebb" till the end of the simulation forms our fourth time period. In each of the time periods, the flow has been closely studied at several locations. These locations have been marked by circles in figure 3.7.

Note that during the discussion, some loosely defined terms such as "interior of the vortex", "outer regions of the vortex", etc. have been repeatedly used. This has made it easier to present a physical picture of how the vortex evolves in time. The meaning of these terms at any given time is clear when one looks at the appropriate figures that have been referred to during the discussion. Also, the term "core" has been used to mean the region from the centerline to the initial core radius ($r/r_0 = 1$) although the vortex core changes in size as the vortex evolves.

### 3.6.1 Checking Resolution

Before we proceed to take a close look at the results obtained, we need to see how well our simulation is resolved. One way to do this is by computing the 1-D energy spectra defined as follows:

$$\begin{aligned} E_{1D}(r,k_\theta) = E_\theta(r,k_\theta) = \int_{k_z} [ \quad & \widehat{u_r} \quad (r,k_\theta,k_z)\widehat{u_r}^*(r,k_\theta,k_z) \\ + \quad & \widehat{u_\theta} \quad (r,k_\theta,k_z)\widehat{u_\theta}^*(r,k_\theta,k_z) \\ + \quad & \widehat{u_z} \quad (r,k_\theta,k_z)\widehat{u_z}^*(r,k_\theta,k_z)]dk_z \end{aligned} \tag{3.19}$$

This 1-D energy spectra is a measure of the turbulent kinetic energy contained in the different azimuthal modes $k_\theta$. Integration over the axial wavenumbers $k_z$ is possible since we have assumed homogeneity in the axial direction. In a well resolved simulation we expect to see the following two principal features:

- A drop in $E_{1D}$ by at least about 2 orders of magnitude as we go from $k_\theta = 0$ to higher values of $k_\theta$.
- Absence of any significant pile up of energy in the higher wavenumbers.

The 1-D energy spectra has been computed at times which correspond to the flow being highly turbulent (as indicated by peaks in the GTKE evolution). It is at these times that the our simulation faces the highest challenge of being well resolved. Figure 3.9 shows the 1-D energy spectra at t/T = 45.12 (just after GTKE reaches the 2nd peak). Three different radial locations have been considered as the level of turbulence varies with distance from the vortex axis (this will be looked at later). The features mentioned above are indeed observed. We do observe a small pile up of energy at higher wavenumbers. This indicates a slight lack of resolution. This pile up is larger at $r/r_0 = 2$. Note that the same computational azimuthal wavenumbers correspond to larger physical wavelengths as we move away from the center. This is the reason why resolution of smaller scales is poorer at a greater distance from the center. However, the pile up is not significant and we can consider the results to be of a reasonable quality in terms of resolution. Figures 3.10, 3.11 and 3.12 show the 1-D energy spectra at t/T = 72.01 (3rd peak of GTKE), 107.57 (4th peak of GTKE) and 127.08 (last location at which flow is closely looked at) respectively. We see the presence of the above features at all these times. This gives us confidence in the results we have obtained and we can now take a close look at them to enhance our understanding of the flow.

Let us also define a 2-D energy spectra as follows:

$$\begin{aligned} E_{2D}(r,k_\theta,k_z) = &\ \widehat{u_r}\ (r,k_\theta,k_z)\widehat{u_r}^*(r,k_\theta,k_z) \\ + &\ \widehat{u_\theta}\ (r,k_\theta,k_z)\widehat{u_\theta}^*(r,k_\theta,k_z) \\ + &\ \widehat{u_z}\ (r,k_\theta,k_z)\widehat{u_z}^*(r,k_\theta,k_z) \end{aligned} \tag{3.20}$$

This 2-D energy spectra gives us information regarding the spread of energy over various length scales (higher wavenumbers correspond to smaller length scales). Also, during periods of GTKE growth (particularly when we have exponential growth of GTKE), it is of interest to know which modes contain most of the energy. These are the unstable modes responsible for the flow becoming turbulent. This information can be obtained from the above defined 2-D energy spectra.

### 3.6.2 The Broad Picture

In this section we obtain a broad vision of the flow. Flow visualization is used to study the evolution of the vortex in term of its structure. This is done by plotting vorticity magnitude isosurfaces at several locations along the evolution of GTKE. Along with visualizing the flow in this manner, we get a quantitative feel of the range of length scales present in the flow by computing the 2-D energy spectra. As mentioned above, the 2-D energy spectra also gives us information about the unstable modes during the periods of GTKE growth. After confirming that the GTKE is growing exponentially, the growth rate (defined later) of GTKE is computed to know how fast these unstable modes grow.

During the first period (initial state to 2nd ebb), we essentially have a decrease in the overall level of turbulence. The vortex structure does not vary much in this time period. Let us move directly into the second time period as it is here that the vortex begins to deform.

#### 3.6.2.1 Second Time Period

This is a period of exponential growth of GTKE. When the GTKE grows exponentially, we can define its growth rate as $\sigma = \frac{d}{d(t/T)}(ln(GTKE))$. For this first exponential ascent of GTKE, the growth rate is computed to be 0.44. Figure 3.13 shows vorticity magnitude isosurfaces at $t/T = 35.27$. Parts (a) through (d) of this figure correspond to 0.1, 0.25, 0.5 and 0.75 times the peak vorticity magnitude at this time respectively. Lower vorticity magnitudes correspond to the outer regions of the vortex, while with increasing vorticity magnitudes we move to the inner regions. We observe that the vortex has a sinusoidal structure which would correspond to a bending wave instability mode. In part (d) of this figure, which corresponds to the inner structure of the vortex, we see a helical structure in addition to the sinusoidal structure observed in the outer regions. Figure 3.14 presents the 2-D energy spectra at this time. We have contour plots of $log_{10}(E_{2D})$ at $r/r_0 = 0.5$, 1.0 and 2.0 in parts (a), (b) and (c) of this figure (and the subsequent 2-D energy spectra plots) respectively. We can see that the unstable modes are $(k_\theta, k_z) = (\pm 1, 4)$. We also see that as we move outwards the energy contained in these unstable modes becomes lower. This indicates that the onset of this instability is inside the core. Recall from chapter one that the predicted unstable azimuthal wavenumbers for the elliptical instability are $\pm 1$ (Eloy and Dizes (1999)). Also, it was pointed out that this instability has been observed to involve a deformation of the vortex core. Leweke and Williamson (1998) have observed a "wavy displacement of the vortex center" in their experiments. Figure 3.15 shows the perturbation velocity vectors in a cross-sectional plane at this time. As we can see in this picture, there exists a circular region within which the perturbation velocity has a direction opposite to that outside the region. This feature is a typical characteristic of the elliptical/Widnall instability (Coppens (1998)). The observation of these features in our current study assures us that we are indeed capturing the elliptical instability. Note that $k_\theta = \pm 1$ indicates the presence of left and right running helical waves. These are not clearly observable in the isosurface

plots at this time step. However we clearly see the presence of these helical waves at $t/T = 40$.

Parts (a), (b) and (c) of figure 3.16 show vorticity magnitude isosurfaces corresponding to vorticity magnitudes that are 0.1, 0.25 and 0.5 times the peak vorticity magnitude at $t/T = 40$. We observe an increase in the amplitude of the sinusoidal bending of the vortex. We also observe the presence of the helical structure in the outer regions of the vortex now. Note that both left and right handed helical structures are seen here. Part (c), which corresponds to the high vorticity magnitude internal structure of the vortex, shows that small scale structure is beginning to form in the interior regions. These features are reflected in the 2-D energy spectra shown in figure 3.17. In part (a) of this figure we see that the turbulent kinetic energy is spread over a wider range of wavenumbers (higher wavenumbers correspond to smaller length scales). This range of wavenumbers becomes smaller as we move outwards. The magnitude of energy contained in the unstable modes also decreases as we move outwards. However this magnitude is higher than before at all the three locations. We can also see more of the vortex becoming turbulent (meaning more presence of small scale structure). Another piece of information obtained from part (c) of figure 3.16 is that the peak vorticity magnitude no longer lies at the centerline of the vortex. A plot of the vorticity magnitude isosurface corresponding to 0.75 times the peak vorticity magnitude is not included for this and subsequent times. This is so because no definite structure is observable at high levels of vorticity magnitude from here on. Also, from here on, parts (a), (b) and (c) of all the figures showing vorticity magnitude isosurfaces will correspond to 0.1, 0.25 and 0.5 times the peak vorticity magnitude at those times.

Figure 3.18 looks at the vortex structure at $t/T = 42.98$. We are now approaching the end of the 2nd time period. The GTKE has been growing exponentially and is now nearing the 2nd peak. The outer portions of the vortex are also now beginning to show a substantial presence of small scale structure. We look at the vortex just after the GTKE peak ("2nd peak") in figure 3.19 ($t/T = 45.12$). Although we have

fine scale turbulence in the outer regions of the vortex also, the sinusoidal and helical structure is still preserved. This is reflected in the 2-D energy spectra presented in figure 3.20. The turbulent kinetic energy is spread over a large range of wavenumbers now, especially in the inner regions of the vortex. The outer region is also showing lots of fine scale structure now. However, we can still clearly pick out $(k_\theta, k_z) = (\pm 1, 4)$ as the most energetic modes.

#### 3.6.2.2 Third Time Period

This period starts with a decay in the GTKE. Figures 3.21 and 3.22 present pictures of vortex structure in terms of vorticity magnitude isosurfaces during this descent of GTKE. Figure 3.21 corresponds to $t/T = 49.01$ and shows the vortex to be still quite turbulent with a lot of fine scale structure. However, figure 3.22 which corresponds to $t/T = 56.83$, just after the GTKE reaches an ebb, shows a consolidation of the vortex. We still observe the presence of the sinusoidal and helical structures, though now much less pronounced. In figure 3.23 note the drop in the peak values of the 2-D energy spectra. We also notice that the most energetic modes are no longer $(k_\theta, k_z) = (\pm 1, 4)$. In the inner regions of the vortex, $(k_\theta, k_z) = (0, 1)$ and $(k_\theta, k_z) = (1, 3)$ dominate. In the outer regions the dominant modes are $(k_\theta, k_z) = (\pm 1, 3)$. This shift in the wavenumber of the sinusoidal unstable mode from $k_z = 4$ to $k_z = 3$ means that a larger length scale is now becoming unstable.

We now follow the next ascent of GTKE. Figure 3.24 presents the vortex structure at $t/T = 67.56$. The vortex is again displaying the growth of sinusoidal and helical waves. The outer regions of the vortex once again show pronounced left handed and right handed helical structures. We also observe a slightly sinusoidal bending of the vortex along its axis. As we move into the interior of the vortex, we observe this sinusoidal bending and helical twisting of the vortex much more clearly. However the sinusoidal wave has a larger wavelength now as compared to the first GTKE ascent. This is in accordance with the new unstable wavenumbers $(k_\theta, k_z) = (\pm 1, 3)$. These can be picked out in the 2-D energy spectra presented in figure 3.25. We

do not see a significant increase in the range of wavenumbers containing substantial levels of turbulent kinetic energy. On the contrary, in the outer regions of the vortex, a smaller range of energy containing wavenumbers (and hence length scales) is observed. However, the level of energy contained in unstable modes has increased significantly. Note that the process of larger scales breaking down to smaller scales again begins in the interior as can be seen in part (c) of figure 3.24. As the GTKE peaks again at $t/T = 72.01$, we once again observe the presence of fine scale structure (see figure 3.26). Small scale structure is present all the way to the outer regions of the vortex. Note that a strong helical, and not so strong sinusoidal, structure is still maintained. This corresponds to the dominant modes being $(k_\theta, k_z) = (\pm 1, 3)$. These can be identified in figure 3.27. We observe a large range of energy containing length scales (wavenumbers) now. This corresponds to the fine scale structure observed in the vorticity magnitude isosurface plots. This exponential rise of GTKE occurred at a growth rate of 0.26. Thus while the unstable axial wavelength has increased, the rate at which this mode is growing has decreased.

We now follow the descent of GTKE till the 4th ebb (end of third period). Figure 3.28 shows the vortex structure during this descent at $t/T = 78.51$, followed by figure 3.29 at at the 4th ebb ($t/T = 90.14$). We do observe some consolidation (meaning lesser fine scale structure), particularly in the inner regions of the vortex. However, the reduction in the amount of fine scale structure is not as much as the earlier descent in this time period. This is reflected in the 2-D energy spectra presented in figure 3.30. We still have a lot of fine scale turbulence though containing lesser energy (as is expected with a decrease in GTKE). Note that modes $(k_\theta, k_z) = (-1, 2)$, $(k_\theta, k_z) = (0, 1)$ and $(k_\theta, k_z) = (1, 3)$ are the dominant energy containing modes inside the core now. At $r/r_0 = 1$, $(k_\theta, k_z) = (\pm 1, 3)$, $(k_\theta, k_z) = (-1, 2)$, $(k_\theta, k_z) = (0, 1)$ and $(k_\theta, k_z) = (1, 1)$ are the dominant modes. Further out, the dominant modes are observed to be $(k_\theta, k_z) = (\pm 1, 3)$ and $(k_\theta, k_z) = (\pm 1, 2)$. The unstable modes once again seem to be shifting to smaller axial wavenumbers (larger axial length scales).

As noted earlier, having larger unstable length scales is indicative of the vortex as a whole becoming more unstable.

#### 3.6.2.3 Fourth Time Period

The GTKE now begins to ascend again. Figure 3.31 shows that helical and sinusoidal modes again begin to grow. Looking at the 2-D energy spectra at this time ($t/T = 100.78$) shows that the unstable modes are now $(k_\theta, k_z) = (\pm 1, 2)$ (see figure 3.32). So, the unstable modes have shifted from being $(k_\theta, k_z) = (\pm 1, 4)$ in the first ascent of GTKE, to $(k_\theta, k_z) = (\pm 1, 3)$ in the second GTKE ascent, to $(k_\theta, k_z) = (\pm 1, 2)$ in this third and final GTKE ascent in our simulation. In the inner regions of the vortex, the mode $(k_\theta, k_z) = (0, 1)$ is also seen to have a substantial level of energy. At $t/T = 104.37$, which is further along this GTKE ascent, the same trend continues. Figure Figure 3.33 shows an increased presence of fine scale structure in the outer regions of the vortex. The unstable modes are more pronounced, especially the helical waves. This is reflected in the 2-D energy spectra presented in figure 3.34. The range of energy containing wavenumbers shows a marked increase in the outer region of the vortex. The energy carried by the unstable modes also increases substantially in the outer region of the vortex. At $r/r_0 = 0.5$ however, the opposite is observed with the peak value of the 2-D energy spectra decreasing. The GTKE is growing exponentially in this period of ascent with a growth rate of 0.16. The trend of increasing unstable axial wavelengths and decreasing exponential growth rates has continued.

Figure 3.35 presents the vortex structure at the 4th peak of GTKE ($t/T = 107.57$). The helical waves are very pronounced in the outer regions. In the 2-D energy spectra (see figure 3.36), the peak value of the energy spectra in the interior regions of the vortex (now at $r/r_0 = 0.5$ and $r/r_0 = 1$) has decreased substantially. The peak value at $r/r_0 = 2$ has also slightly decreased. However, the energy is spreading out into larger wavenumbers (smaller length scales). This can be seen if we look at the increased spread of energy around the unstable modes. It seems that the vortex is headed towards having more and more fine scale structure. Also the turbulence seems

to be spreading outwards towards the boundary of our domain. This is confirmed in figure 3.37. Here vorticity magnitude isosurfaces are presented at $t/T = 127.08$. We see fine scale structure present in a much larger portion of the vortex. In fact substantial level of vorticity magnitude has now reached the boundary. This is in conflict with our potential flow boundary condition. Hence the simulation has to be stopped now. We would need a larger computational domain size to be able to study the vortex further. Although we cannot make a definite statement about what the vortex would do next, it seems that we now have an unbounded growth of turbulence. The 2-D energy spectra at this time (see figure 3.38) shows that in the interior regions of the vortex the dominant modes have further shifted to $(k_\theta, k_z) = (\pm 1, 1)$. The peak value at all the three radial locations has decreased. It thus seems that the turbulent kinetic energy is being passed on to smaller length scales.

### 3.6.3 Mean and Statistical quantities

Now that we have a physical feel of how the vortex evolves in time, let us look at the evolution of some mean and statistical turbulent quantities of interest (mean velocity components, mean vorticity components, Reynolds stresses, turbulent kinetic energy and enstrophy). Since the applied strain field makes the streamlines elliptical, the flow is no longer axisymmetric. We thus have to be careful not to miss the azimuthal variation of the mean and statistical quantities being studied. Here we look at how the above mentioned quantities evolve in time at the angular locations of $\theta = 45^o$ and $\theta = 135^o$. These correspond to the major and minor axes of the elliptical streamlines. Note that the mean flow is symmetric about the major and minor axes of the elliptical streamlines. Also, $\theta = 45^o$ corresponds to the direction in which the vortex is most stretched while $\theta = 135^o$ corresponds to the direction in which the vortex is most compressed. Hence the evolution of mean and statistical quantities in these two directions will be representative of their evolution in the stretched and compressed regions of the vortex.

#### 3.6.3.1 First time period

Let us turn our attention to the first time period. We first look at the evolution of turbulence. Figure 3.39 shows how the turbulent kinetic energy (henceforth referred to as TKE) evolves in time. The initially laminar vortex is perturbed in such a way that the TKE peaks at the core radius at the beginning of the simulation. As the simulation progresses in time, the peak value of TKE increases and moves to the center. The peak then stays at the center but decreases in value till the 2nd ebb of GTKE is reached.

Before we start looking at the mean velocity field, let us write down the equations governing the evolution of the three mean velocity components:

$$\frac{\partial V_r}{\partial t} + V_r\frac{\partial V_r}{\partial r} + \frac{V_\theta}{r}\frac{\partial V_r}{\partial \theta} + V_z\frac{\partial V_r}{\partial z} - \frac{V_\theta^2}{r} = -\frac{\partial P}{\partial r} + \frac{1}{Re}(\nabla^2 V_r - \frac{2}{r^2}\frac{\partial V_\theta}{\partial \theta} - \frac{V_r}{r^2}) \\ -(\frac{1}{r}\frac{\partial}{\partial r}(r\overline{v_r'^2}) + \frac{1}{r}\frac{\partial}{\partial \theta}\overline{v_r'v_\theta'} + \frac{\partial}{\partial z}\overline{v_r'v_z'} - \frac{\overline{v_\theta'^2}}{r}) \quad (3.21)$$

$$\frac{\partial V_\theta}{\partial t} + V_r\frac{\partial V_\theta}{\partial r} + \frac{V_\theta}{r}\frac{\partial V_\theta}{\partial \theta} + V_z\frac{\partial V_\theta}{\partial z} + \frac{V_rV_\theta}{r} = -\frac{1}{r}\frac{\partial P}{\partial \theta} + \frac{1}{Re}(\nabla^2 V_\theta + \frac{2}{r^2}\frac{\partial V_r}{\partial \theta} - \frac{V_\theta}{r^2}) \\ -(\frac{1}{r}\frac{\partial}{\partial r}(r\overline{v_r'v_\theta'}) + \frac{1}{r}\frac{\partial}{\partial \theta}\overline{v_\theta'^2} + \frac{\partial}{\partial z}\overline{v_\theta'v_z'} + \frac{\overline{v_r'v_\theta'}}{r}) \quad (3.22)$$

$$\frac{\partial V_z}{\partial t} + V_r\frac{\partial V_z}{\partial r} + \frac{V_\theta}{r}\frac{\partial V_z}{\partial \theta} + V_z\frac{\partial V_z}{\partial z} + \frac{V_rV_\theta}{r} = -\frac{\partial P}{\partial z} + \frac{1}{Re}\nabla^2 V_z \\ -(\frac{1}{r}\frac{\partial}{\partial r}(r\overline{v_r'v_z'}) + \frac{1}{r}\frac{\partial}{\partial \theta}\overline{v_\theta'v_z'} + \frac{\partial}{\partial z}\overline{v_z'^2}) \quad (3.23)$$

Note that since we are assuming axial homogeneity, the mean and statistical quantities do not vary axially. Hence the $\partial/\partial z$ terms in the above equations are zero.

Figure 3.40 shows the evolution of the mean tangential velocity. We observe a gradual diffusion of the mean tangential velocity. The peak value decreases and moves outwards. Note that the peak value of $V_\theta$ is higher at $\theta = 135^o$. This is a consequence of the strain field. Since we do not have any axial flow to start with, equation 3.23 tells us that $V_z$ will stay zero throughout the simulation. Figure 3.41 confirms this as

the values observed are very small. The non-zero values are simply due to limitations in the sampling space while computing mean and statistical quantities. The evolution of mean radial velocity is presented in figure 3.42. Although the presence of strain makes the radial flow non-zero in the mean, we expect it to stay small intuitively. This is indeed the case in this and subsequent time periods. For the remaining periods, only the tangential mean velocity shall be looked at, as it is the only component that is relevant to understanding the flow better.

Let us now look at the three mean vorticity components. Figure 3.43 shows the evolution of the mean axial vorticity. We have a gradual diffusion of the mean axial vorticity (this corresponds with the gradual diffusion of the mean tangential velocity observed). The peak value stays at the centerline and decreases slowly. Within the core the mean axial vorticity decreases, while it increases outside the core. The vorticity is thus diffusing outward. The evolutions of the mean tangential vorticity and the mean radial vorticity are presented in figures 3.44 and 3.45. Once again, in the absence of any axial flow, these components of mean vorticity are expected to be zero. The small non-zero values observed are a reflection of the limitations in sampling space. For the remaining time periods, we shall not look at these mean vorticity components.

The turbulence affects the mean velocity via the Reynolds stresses $R_{ij} = \overline{v_i' v_j'}$ as can be seen in equations 3.21, 3.22 and 3.23. The Reynolds stresses can be interpreted as being responsible for momentum transfer via the motion of eddies in a turbulent flow, analogous to viscous stresses which account for momentum transfer via molecular motion. Although we have identified the mean tangential velocity to be the only component that is relevant to understanding the flow better, we will also look the Reynolds stress components that affect the radial and axial components of the mean velocity. Besides ensuring completeness in studying the flow, with regards to Reynolds stresses, this will also add to the information available for development of new and improved turbulence models for strongly rotating flows.

The turbulence affects the mean tangential velocity via the Reynolds stress components $R_{\theta\theta} = \overline{v_\theta'^2}$, $R_{r\theta} = \overline{v_r' v_\theta'}$ and $R_{\theta z} = \overline{v_\theta' v_z'}$ (see equation 3.22). Figures 3.46, 3.47 and 3.48 show the evolution of these Reynolds stress components. $R_{\theta\theta}$ exhibits essentially the same behavior as the TKE. However at $\theta = 45^o$, the peak value, instead of settling at the center, establishes itself very close to the center. At $\theta = 45^o$ the peak value of $R_{r\theta}$ also increases initially and moves to the center, and then decreases in value while staying at the center. Note that the values of $R_{r\theta}$ at the two angular locations considered are in general of opposite signs and similar magnitudes. In the absence of axial flow we expect $R_{\theta z}$ to be zero. The non-zero values observed in figure 3.48 are a result of insufficient sampling space in the homogeneous axial direction.

The Reynolds stress components responsible for the effect of turbulence on the mean axial flow are $R_{zz} = \overline{v_z'^2}$, $R_{rz} = \overline{v_r' v_z'}$ and $R_{\theta z} = \overline{v_\theta' v_z'}$ (see equation 3.23). Figure 3.49 shows the evolution of $R_{zz}$. We observe that $R_{zz}$ attains a value at the centerline very early in the simulation and maintains this value as the simulation progresses. This becomes it's peak value towards the end of the first time period. The magnitudes of $R_{zz}$ values are found to be comparable at the two locations. Evolution of $R_{rz}$ is presented in figure 3.50. Again, in the absence of axial flow we expect $R_{rz}$ to be zero. Insufficient sampling space while calculating the statistics results in non-zero values observed.

The turbulence affects the mean radial velocity via the Reynolds stress components $R_{rr} = \overline{v_r'^2}$, $R_{r\theta} = \overline{v_r' v_\theta'}$, $R_{rz} = \overline{v_r' v_z'}$ and $R_{\theta\theta} = \overline{v_\theta'^2}$ (see equation 3.21). We observe that $R_{rr}$ evolves (see figure 3.51) in a manner similar to the TKE. The peak value initially increases and moves to the center, and then decreases in value while staying at the center. The evolutions of $R_{r\theta}$, $R_{rz}$ and $R_{\theta\theta}$ during this time period have already been discussed above.

For the remaining time periods, evolutions of $R_{rz}$ and $R_{\theta z}$ will not be looked at. As has been pointed out above, we expect these values to be zero in the absence of any axial flow. Small non-zero values have been observed throughout the simulation. This has simply been a result of limitation in the sampling size.

Finally we look at the evolution of enstrophy (see figure 3.52) to get a measure of the level of vorticity fluctuations. Initially the enstrophy has its peak at the core radius. As we move through this time period, the level of enstrophy decreases rapidly. At the end of this time period, the peak has moved to the centerline.

#### 3.6.3.2 Second time period

We now move on to the second time period, i.e., till the 2nd peak of GTKE. We again start by looking at the behavior of turbulence. Figure 3.53 shows the evolution of TKE. As the simulation progresses, the peak value of TKE stays at the center and increases in value. The TKE profile also becomes fuller which shows that a large portion of the vortex becomes turbulent. At the beginning of this time period all the turbulence was essentially within the vortex core. This changes as the simulation progresses and we observe substantial turbulence up to more than twice the core radius. At the 2nd peak of GTKE, the TKE peak seems to begin to move away from the center.

Figure 3.54 shows the evolution of the mean tangential velocity. As the simulation progresses through this time period, initially the mean tangential velocity continues to diffuse slowly in the same way as the first time period. However as the GTKE approaches it's peak (i.e. towards the end of this time period), the tangential velocity starts decreasing rapidly in the interior of the core (from $r/r_0 = 0$ till about $r/r_0 = 0.8$) and outside the core. However, the peak which was moving slowly outward and falling in value, moves inward and stays approximately around $r/r_0 = 0.8$. It also increases in value for some time (this is clearly visible at $\theta = 45^o$) but eventually decreases. We observe a reversal in the curvature of the $V_\theta$ profile as we move from the centerline to the peak and then from the peak to the edge of the core. We will come back to this point when we look at the Reynolds stresses.

Figure 3.55 shows the evolution of the mean axial vorticity. Recall that we observed a gradual diffusion of the mean axial vorticity in the first time period. That behavior continues for some time in this time period as well. However, we observe

a sudden drop in the centerline value at one stage and a reversal in trend inside the core. $\Omega_z$ increases from the centerline till approximately the core edge and then drops steeply and settles into a slow decay to zero as we approach the boundary. Note that this corresponds to 3.16 (c) where we observed that the vorticity maximum has left the center.

Figures 3.56 and 3.57 and show the evolution of $R_{\theta\theta}$ and $R_{r\theta}$ during this time period. We observe that the regions of rapid decrease in the mean tangential velocity show high levels of $R_{\theta\theta}$ and $R_{r\theta}$. This could be a reflection of a high level of momentum transfer via turbulent eddies into the annular region approximately between $r/r_0 = 0.8$ and $r/r_0 = 1$ from both the sides. Note that $R_{\theta\theta}$ values at $\theta = 45^o$ reach about twice the magnitude of those at $\theta = 135^o$ towards the end of this time period. $R_{r\theta}$ values are in general of the same magnitude but opposite signs at the two angular locations considered. Figure 3.58 shows the evolution of $R_{zz}$. In contrast to $R_{\theta\theta}$, $R_{zz}$ has low values at the centerline. As we move outwards, the level of $R_{zz}$ increases steeply and after reaching a peak, decreases steeply. A much smaller peak is formed as we move further out and eventually the value decays to zero as we approach the boundary. We observe that $R_{rr}$ behaves in a manner similar to $R_{\theta\theta}$ in terms of the profile shape (see figure 3.59). However, as opposed to $R_{\theta\theta}$, here we have higher values of $R_{rr}$ at $\theta = 135^o$ towards the end of this time period.

Figure 3.60 shows an increase in the level of vorticity fluctuations as we approach the 2nd peak in the GTKE profile. We also observe the development of a peak in enstrophy at roughly the same location to which the peak in $\Omega_z$ shifted from the centerline. The values of enstrophy at the two angular locations have the same order of magnitude.

#### 3.6.3.3 Third time period

Continuing the trend established above, we start by looking at the distribution of TKE (figure 3.61). Throughout the third time period, the TKE profile maintains its trend of peaking at the center and decaying as we move outwards. The third period

starts with the GTKE decaying from the 2nd peak. The GTKE then goes through an ebb and another peak, and the end of this time period coincides with the GTKE reaching the fourth ebb. The peak value of the TKE follows the GTKE in its trend. It falls as we move from the 2nd peak to the 3rd ebb, then increases in value as the GTKE grows till the 3rd peak, and then falls again as the GTKE goes from the 3rd peak to the 4th ebb.

Figure 3.62 presents the evolution of tangential velocity in the third time period. As the GTKE moves from the 2nd peak to the 3rd ebb, the peak drops in value and moves outward. As we reach the 3rd ebb we observe an increase in $V_\theta$ in the interior of the core (approximately between $r/r_0 = 0$ to $r/r_0 = 0.8$). We need to compute eddy viscosity to see if this is a result of anti-diffusion. As we move from the 3rd ebb to the 3rd peak, we see a behavior similar to that observed during the approach to the 2nd peak in the previous time period. A rapid decrease in $V_\theta$ is observed in regions to the left and the right of the peak for some time. As we reach the 3rd peak, we observe that the peak value is again beginning to decrease and move outward. The final portion of this time period, i.e. the fall of the GTKE from the 3rd peak to the 4th ebb, displays a behavior of $V_\theta$ that is similar to the first part of this time period, i.e. the decay of GTKE from the 2nd peak to the 3rd ebb. The peak value falls and moves outward at a considerable rate, thus showing a highly diffusive process. However, once again in the interior of the core, we see an increase in the value of $V_\theta$. Whether this is a result of anti-diffusion or not has to be determined by computing the eddy viscosity.

We now look at how the mean axial vorticity evolves in this time period (figure 3.63). The limitation in the sampling space available results in the noise observed in the profiles for $\Omega_z$. Due to this noise it is difficult to make a statement about the shape of the profile . However a rough impression obtained is that the shape taken by the profile towards the end of the 2nd time period is maintained.

The Reynolds stresses that account for the effect of turbulence on the mean tangential velocity, namely $R_{\theta\theta}$ and $R_{r\theta}$, are plotted in figures 3.64 and 3.65. As the

GTKE falls from the 2nd peak to the 3rd ebb, the value of $R_{\theta\theta}$ inside the core falls rapidly, while about the same level is maintained outside the core. The peak value stays established at the center. As the 3rd ebb is reached, the peak value shows an increase, but is accompanied by a steep drop as we move away from the centerline. At $\theta = 45^o$, $R_{r\theta}$ starts with a positive value in the interior of the core as the GTKE begins it's descent. As the simulation progresses through the 3rd time period, we observe a reversal in this trend. The peak value at the centerline becomes negative. $R_{r\theta}$ in the interior of the core is now negative and we have mixed regions of positive and negative values as we move outward. This reversal in sign is another indication that we may have anti-diffusion. However, as mentioned before, eddy viscosity needs to be computed to confirm that. At $\theta = 135^o$, $R_{r\theta}$ values are opposite in sign to the values at $\theta = 45^o$ while having comparable magnitudes. As the GTKE now increases from the 3rd ebb to the 3rd peak, both $R_{\theta\theta}$ and $R_{r\theta}$ profiles show a trend that is similar to what was observed in the 2nd time period. This is in accord with the similarity in the $V_\theta$ profiles for these two ascents of the GTKE. As the GTKE now descends from the 3rd peak to the 4th ebb, similar trends are observed in the $R_{\theta\theta}$ and $R_{r\theta}$ profiles as in the descent from the 2nd peak to the 3rd ebb. The shift from positive to negative values of $R_{r\theta}$ at $\theta = 45^o$ (and from negative to positive at $\theta = 135^o$ in the interior of the core is delayed and less pronounced. Nevertheless we once again have indications of the presence of anti-diffusion in our flow. Note that during this time period, $R_{\theta\theta}$ values at the $\theta = 135^o$ location are about twice those at $\theta = 45^o$. This is opposite of what was observed in the second time period.

Let us take a look at how $R_{zz}$ evolves during this period (see figure 3.66). $R_{zz}$ decays rapidly as the GTKE decreases from the 2nd peak to the 3rd ebb. During the increase of GTKE from the 3rd ebb to the 4th peak, the $R_{zz}$ profiles are similar in trend to the 2nd time period - an increase from the centerline value, a peak, and then a steep fall followed by a gradual decay to zero as we approach the boundary. The second small peak that was observed clearly during the second time period seems to be absent now. After this as the GTKE decreases from the 3rd peak to the 4th

ebb, $R_{zz}$ again decreases rapidly in a manner similar to the descent of GTKE from the 2nd peak to the 3rd ebb. $R_{rr}$ at $\theta = 45^o$ behaves in a manner similar to $R_{\theta\theta}$ at $\theta = 135^o$ (and vice versa) in this time period (see figure 3.67). Note that during this time period, $R_{rr}$ values at the $\theta = 45^o$ location are about twice those at $\theta = 135^o$. This is opposite of what was observed in the second time period.

Finally we look at the evolution of enstrophy during this time period (see figure 3.68). The peak value stays at the centerline throughout this period. The core contains the most significant level of enstrophy at any time. As we move away from the core radius (approximately $r/r_0 = 1$), the enstrophy level falls rapidly. The enstrophy level follows the GTKE pattern. As the GTKE descends to the 3rd ebb, the enstrophy level also falls. It then increases as the GTKE ascends to the 3rd peak and falls as the GTKE descends to the 4th ebb at the end of this time period. This is intuitively expected as a higher level of vorticity fluctuations should correspond to the presence of more small scale turbulence and vice versa. The enstrophy level is of the same order of magnitude at both the angular locations considered.

#### 3.6.3.4 Fourth time period

We now enter the fourth and final time period of STRN4. During this time period the GTKE ascends from the 4th ebb and after peaking enters a state in which it seems to have some random oscillations before beginning a steep plunge. As mentioned in the discussion of the vortex structure, the simulation has to be stopped at this time as we have a substantial level of vorticity at the boundary which is in conflict with our potential flow boundary conditions. The peak just before the final GTKE oscillations is thus taken to be the last meaningful point in the simulation.

As before, we start by looking at evolution of TKE (see figure 3.69) As the GTKE grows, we observe an increase in TKE all the way from the centerline to the outer regions of the vortex. The peak value stays at the center and increases rapidly. As we reach the final GTKE peak (just before GTKE starts showing random oscillations) the peak TKE value at the center falls. However the TKE in the outer regions of

the vortex shows a significant increase. This trend continues as we enter the final oscillatory part of the GTKE evolution. We now observe a substantial level of TKE all the way to the vortex boundary. The profiles at $\theta = 45^o$ are some what fuller than the profiles at $\theta = 135^o$.

Let us now look at the evolution of the mean tangential velocity in this final period of the simulation (see figure 3.70). As the GTKE begins to ascend, we see trends similar to the later part of the 2nd period and ascends during the 3rd period. There is a rapid decrease in regions to the left and and right of the peak. Initially during this ascent the peak shows a movement to the left but then reverts back to its outward movement. For $\theta = 135^o$, this initial rapid decrease to the right of the peak (and the initial leftward movement of the peak) is not observed. As we reach the peak, we observe the beginning of a collapse of the profile. The peak value falls drastically. As we move into the final oscillatory part of the GTKE evolution, the profile essentially flattens out. There is a great deal of diffusion. Insufficiency of computational domain size towards the end of the simulation is observed as we observe significant diffusion close to the boundary.

The evolution of mean axial vorticity during this period is presented in figure 3.71. The amount of noise in the profiles due to the limitations in the sampling space make it difficult to recognize trends. The one thing we can notice though is that towards the end of this time period, mean axial vorticity is becoming non-zero as we approach the boundary. This is in conflict with our boundary conditions which require the flow to be potential (irrotational) at the boundary. As noted already, it is because of this reason that the simulation cannot be continued further with our current domain size.

Figures 3.72 and 3.73 show the evolution of $R_{\theta\theta}$ and $R_{r\theta}$ during this period. As the GTKE rises, trends similar to the 2nd time period and ascents during the 3rd period get established. At $\theta = 45^o$, the peak value at the centerline begins to rise. The value falls from the centerline, goes through an ebb and then another smaller peak before finally decaying to zero as we approach the boundary. For $R_{\theta\theta}$, the behavior is similar at $\theta = 135^o$ except for the $R_{\theta\theta}$ levels being about half of what they are at $\theta = 45^o$.

For $R_{r\theta}$, the major difference between the two angular locations is again the reversal of sign. As we approach the peak in GTKE, the trend begins to change for $R_{\theta\theta}$ with the centerline value starting to decrease. At the GTKE peak, the profile shape changes to being flatter. In the final GTKE oscillations, the value of $R_{\theta\theta}$ decreases in the inner portions of the domain while increasing as we move outwards, tending to a somewhat uniform value throughout the domain. For $R_{r\theta}$ this change in trend, with the centerline value beginning to decrease, starts at the location of the GTKE peak. The flattening out of the profile is more gradual as compared to $R_{\theta\theta}$.

Figure 3.74 shows the evolution of $R_{zz}$ in this time period. As the GTKE increases, the level of $R_{zz}$ begins to increase. Initially the centerline value does not show much variation, the increase in level happening mostly in the region approximately between $r/r_0 = 0.5$ and $r/r_0 = 2$. However later on the centerline value does increase significantly before beginning to fall again. Towards the end of this time period, the level of $R_{zz}$ decreases in the interior of the vortex while increasing as we move towards the boundary. We can see how $R_{rr}$ evolves during this time period in figure 3.75. Initially the level increases rapidly inside the core. Again, the levels at $\theta = 135^o$ are about twice the levels at $\theta = 45^o$ during the initial part of this time period. At $\theta = 45^o$, the level inside the core seems to saturate after some time and the level in the outer regions begins to rise. Towards the end, $R_{rr}$ seems to approach a somewhat uniform level throughout. This saturation is not observed at $\theta = 135^o$. The level in the interior keeps increasing for most of this time period. Towards the end, the value in the interior drops to about the same level as at $\theta = 45^o$ and here we see a somewhat uniform level throughout the domain.

Finally let us look at how the enstrophy evolve during this time period. This is presented in figure 3.76. As expected, we observe an increase in enstrophy as the flow becomes more turbulent. Towards the end of this time period the level falls though and levels out to a somewhat uniform value throughout the domain. We have a significant level of vorticity fluctuations near the boundary. As pointed out

earlier, this is not compatible with the potential flow boundary conditions, and the simulation is thus stopped.

### 3.7 STRN2 - A Close Look

We now turn to study STRN2 in detail. This simulation considers a strained vortex which has a wake-like axial velocity profile in the initial conditions. In the absence of the external strain field, the instability introduced by the axial flow is observed to be quenched as the vortex eventually re-laminarizes. This was observed by Qin (1998) in his isolated vortex simulations (the term isolated implying the absence of an external strain field).

Just as in the above study of STRN4, we divide the simulation into different time periods using the time history of GTKE as a guideline. See figure 3.8 for the definitions of the terms "1st peak", "1st ebb", "2nd peak", etc. The first time period for STRN2 is from the initial state to the "1st peak". The time period from the "1st peak" till the "1st ebb" forms the second time period. The third time period is from the "1st ebb" till the "2nd" ebb. After this point the flow enters a kind of a "steady state" in terms of the GTKE. This period lasting from the "2nd" ebb till the end of this GTKE "steady state" (this location labeled as "3rd ebb") is our fourth time period. From the "3rd ebb" to the "4th peak" is our fifth time period. The sixth time period is from the "4th peak" to the "5th peak" and from the "5th peak" till the end of the simulation is our seventh and last time period. Note that the terms "3rd ebb", "3rd peak", "4th peak", "5th peak" and "6th peak" are simply being used to mark locations of interest along the GTKE evolution, and do not mean peaks and ebbs in a strict sense. The flow has been studied closely at several locations in each of these time periods. These locations are marked by circles in figure 3.8.

Similar to the STRN4 discussion, some loosely defined terms such as "interior of the vortex", "outer regions of the vortex", etc. have been repeatedly used. This has made it easier to present a physical picture of how the vortex evolves in time. The meaning of these terms at any given time is clear when one looks at the appropriate

figures that have been referred to during the discussion. Also, the term "core" has been used to mean the region from the centerline to the initial core radius ($r/r_0 = 1$) although the vortex core changes in size as the vortex evolves.

### 3.7.1 Checking Resolution

Let us first check if our simulation is well resolved. Figures 3.77, 3.78, 3.79 and 3.80 present the 1-D energy spectra (equation 3.19) at the 1st peak, 2nd peak, 5th peak and 6th peak of the GTKE respectively. These are the times when we have high levels of turbulence challenging the resolution of our simulation. As can be seen, the two criterion for a well resolved simulation listed in section 3.6.1 are met. We thus have confidence in our simulation with regards to how well it has been able to resolve the various scales of motion. Let us now go ahead and study the flow closely.

### 3.7.2 The Broad Picture

As in STRN4, we start with obtaining a broad vision of the flow. In this section we will use flow visualization to study the evolution of the vortex in terms of its structure. Vorticity magnitude isosurfaces at several locations along the GTKE evolution will be looked at. Along with visualizing the flow in this manner, we will obtain a quantitative feel of the length scales present in the flow by computing the 2-D energy spectra (equation 3.20). This will also give us information regarding the unstable modes during the periods of GTKE growth. After confirming the exponential nature of GTKE growth, we shall compute the growth rate to know how fast these unstable modes grow.

#### 3.7.2.1 First Time Period

This is a period of exponential growth of GTKE. The growth rate, as defined in section 3.6.2.1, is computed to be 3.71. Figure 3.81 shows vorticity magnitude isosurfaces at $t/T = 2.53$. Parts (a) through (d) of this figure correspond to 0.1, 0.25, 0.5

and 0.75 times the peak vorticity magnitude at this time respectively. Lower vorticity magnitudes correspond to the outer regions of the vortex, while with increasing vorticity magnitudes we move to the inner regions. We observe the presence of left running helical waves along the vortex. Note that we have multiple helical waves present. Figure 3.82 presents the 2-D energy spectra at this time step. Contour plots of $log_{10}(E_{2D})$ are presented here at $r/r_0 = 0.5$, 1.0 and 2.0 in parts (a), (b) and (c) of this figure (and the subsequent 2-D energy spectra plots) respectively. We can pick out $(k_\theta, k_z)$ = (1,1), (2,2), (3,3), (4,4) and (5,5) to be the modes carrying a significant amount of energy in the inner regions of the vortex. This presence of multiple energy carrying modes corresponds to the presence of a family of helical waves. However, in the outer region we see that $(k_\theta, k_z)$ = (2,2) is the dominant mode. Recall from chapter one that the presence of a wake-like axial velocity profile introduces multiple unstable modes. Also, the helical waves seen here are similar to those seen by Qin (1998) in his study of isolated vortices with a wake-like axial flow. Qin had also observed that, when an initial wake-like axial velocity profile is included, the initial exponential growth of GTKE is similar for both isolated and strained vortices. These observations tell us that the instability caused by the axial flow is dominating in this time period.

Figure 3.83 shows us the vortex structure at $t/T = 3.07$. The outer region of the vortex is now showing the helical wave to be more developed. Fine scale structure is beginning to develop in the inner region. Note that here (and in the remaining vorticity magnitude isosurface plots), we no longer have part (d) that corresponded to 0.75 times the peak vorticity magnitude. This is so because no definite structure can be observed at that vorticity magnitude level. Figure 3.84 presents the 2-D energy spectra at this time. We can see that in the inner regions energy is spread over a wider range of wave numbers now (higher wavenumbers means smaller length scales). The outer region (part (c)) now shows that modes $(k_\theta, k_z)$ = (2,3), (3,4) and (4,6) are also beginning to become energetic.

We continue with looking at the vortex structure at $t/T = 3.91$ (see figure 3.85). The outer region of the vortex is also becoming turbulent as can be seen by the presence of fine scale structure. The family of left running helical waves can still be clearly seen as being the large scale structure. If we look at the 2-D energy spectra at this location (see figure 3.86) we can see that the dominant modes are shifting in terms of their $k_z$ value. $(k_\theta, k_z)$ = (1,1), (2,3) and (3,4) are the dominant modes in the inner region (part (a) of this figure). As we move outwards to $r/r_0 = 1$ (part (b)) we observe $(k_\theta, k_z)$ = (1,1), (2,1), (2,3) and (3,3) to be more energetic modes. In the outer region (part (c)), $(k_\theta, k_z)$ = (2,2), (2,3), (3,2) and (3,5) are the energetic modes. Note that higher values of $k_z$ correspond to the helical waves going around the vortex more number of times.

We now look at the vortex structure at the end of this time period, i.e. when the GTKE has reached the 1st peak. As would be expected in a more turbulent state, we observe more fine scale structure (see figure 3.87). The large scale structure of left traveling helical waves is still very much present though. In the 2-D spectra corresponding to this time (figure 3.88) we see the energy distributed over a wide range of wavenumbers (more fine scale structure). In part (a) of this figure, we see that $(k_\theta, k_z)$ = (-1,1) is one of the energy containing modes. A negative azimuthal wavenumber corresponds to a right running helical wave. Recall that $k_\theta = -1$ was present throughout STRN4 in one of the unstable modes. It is possible that till now the axial flow instability has been dominating and we are now beginning to see the effect of the strain. We also see several other modes carrying a substantial amount of energy in the interior of the vortex. As we move outwards, the number of energy containing modes is smaller. Also these do not have a negative azimuthal wavenumber. Remember that the elliptic instability gets initiated inside the vortex core. This may be the reason we are seeing the appearance of negative $k_\theta$ in the interior of the vortex only.

#### 3.7.2.2 Second Time Period

The GTKE now begins to decrease. Figure 3.89 shows the vortex structure at $t/T = 7.61$. We still have lot of final scale structure in the outer portion of the vortex. However the inner portion of the vortex begins to re-consolidate. This trend is seen to be continuing in figure 3.90 which presents the vortex structure at $t/T = 11.43$. In particular, note the formation of a central filament in part (b) of this figure. We can also see both left and right running helical waves around this filament. This is further indication that we are beginning to see the strain field in action. In part (b) of figure 3.91 (here we are seeing the vortex structure at $t/T = 16.22$) this process of re-consolidation is observed to have moved along further. It seems that the cross-sectional area of the vortex is increasing and decreasing as we move along the vortex length. If this is so, we might be observing the presence of the core dynamics (CDI) instability (Pradeep and Hussain (2001)). In figure 3.92 we are looking at the vortex structure at the end of this time period. The GTKE has now reached the 1st ebb. As would be expected in low turbulence situation , we see lesser fine scale structure. In part (b) of this figure we observe both a sinusoidal bending along the vortex axis and a periodic core area variation along the vortex axis. That all these features are indeed present is confirmed by picking out the dominant modes in the 2-D energy spectra plots presented in figure 3.93. In the inner regions of the vortex (parts (a) and (b) of this figure) we observe that $(k_\theta, k_z) = (\pm 1, 1)$, (0,3) and (2,3) to be the dominant modes. In the outer portion (part (c)) we have $(k_\theta, k_z) =$ (0,1) and (2,3) to be the dominant modes.

#### 3.7.2.3 Third Time Period

We observed at the end of the last time period that modes corresponding to different kinds of instabilities are present simultaneously. We expect to see a rich variety of features in terms of the vortex structure as the GTKE begins to grow again. The GTKE now grows exponentially with a growth rate of 0.13. Note the dramatic drop in the growth rate when compared with the first period. Figure 3.94

shows the vortex structure at $t/T = 22.07$ during this second GTKE ascent. Figure 3.95 presents the 2-D energy spectra at this time. We have $(k_\theta, k_z)$ = (0,3) as one of the energy carrying modes. This would correspond to a periodic variation in the cross-sectional area as we move along the vortex axis. This can indeed be observed, most prominently in figure 3.94 (a). We also have $(k_\theta, k_z)$ = (-1,2) and (2,3) as dominant modes. This corresponds to left and right running helical waves. These are also observed in figure 3.94 (a). We continue to see this rich structure in figure 3.96. Here the vortex structure is shown at $t/T = 23.58$ which is still during this second GTKE ascent. Figure 3.97 gives us information about the dominant modes at this time. $(k_\theta, k_z)$ = (1,1) is also present now. Also, $(k_\theta, k_z)$ = (-1,2) and (2,3) and (0,3) are observed at all three radial locations now. This was not the case at $t/T = 22.07$ where the dominant modes at $r/r_0 = 2$ were different and much less energetic than the other two radial locations. Figure 3.98 presents the vortex structure at $t/T = 25.61$ which corresponds to the 2nd peak of GTKE. The vortex has "tightened" (meaning that most of the vorticity is now contained in a very small annular region). We still have $(k_\theta, k_z)$ = (-1,2), (0,3) and (2,3) as energetic modes. We also note the presence of (1,1) as a dominant mode. This mode was present with a small amount of energy at $t/T = 22.07$ $r/r_0 = 2$. At this second peak of GTKE, we also see (2,2) to be one of the dominant modes.

Figure 3.100 shows the vortex structure at $t/T = 32.01$. The GTKE is now decaying again. The vortex is "loosening up" again. The structure looks similar to when the GTKE was on its way up. We see a very consolidated vortex at $t/T = 40.01$ (see figure 3.101). The vortex structure now looks much like the structure at the 1st ebb of GTKE. We reach the 2nd ebb of GTKE (and the end of this time period) at $t/T = 51.48$. Figure 3.102 shows the vortex structure just after the 2nd GTKE ebb is reached. Small scale structure is almost absent. This is also reflected in the 2-D energy spectra plots presented in figure 3.103. The dominant modes at this time are $(k_\theta, k_z)$ = (0,1), (0,3) and (-1,2). The energy levels in the outer regions (see figure 3.103 (c)) is much lower.

#### 3.7.2.4 Fourth Time Period

This time period is characterized by the fact that the GTKE evolution maintains a sort of a steady state. Figure 3.104 shows the vortex structure at $t/T = 56.01$. As expected we don't see much difference, in terms of how much small scale structure is present, as compared to the situation just after the 2nd ebb of GTKE. Left running helical waves are still prominently visible. At $t/T = 62$ (see figure 3.105), in addition to the left running waves, a sinusoidal bending along the vortex axis is also clearly visible. The same is the case at $t/T = 68.08$ (see figure 3.106). Dominant modes at this time can be picked up in the 2-D energy spectra plots presented in figure 3.107. We find that $(k_\theta, k_z)$ = (-1,1), is the most dominant mode at this time. Another modes that is carrying a significant amount of energy is (0,1). Note that dominant modes have shifted since the beginning of this period. Although, the overall level of turbulence (as measured by GTKE) is not varying much during this time period, turbulent kinetic energy is being transferred between different modes. This could indicate that selection is being made for an instability mechanism to take over. As we move on to a later location ($t/T = 74.04$) during this time period, we continue to see the presence of left running helical waves and a sinusoidal bending along the vortex axis (see figure 3.108). Let us now take a look at the vortex structure just after this time period ends. Figure 3.109 presents the structure of the vortex at $t/T = 80.52$. The vortex has "tightened" up considerably. We see the presence of left running helical waves and a sinusoidal bending along the vortex axis. Let us pick out the dominant modes at this time and contrast them with what modes dominated just at the beginning of this time period. Figure 3.110 presents the 2-D energy spectra at this time. The dominating modes are (-1,1), (0,1) and (0,2). These are different from the modes dominated as we entered this time period.

#### 3.7.2.5 Fifth Time Period

The GTKE now begins to climb again. Here the GTKE grows exponentially with a growth rate of 0.11. Figure 3.111 presents the vortex structure at $t/T = 83.51$.

The helical waves and the sinusoidal bending are more prominent. At $t/T = 85.45$, the vortex has "tightened up" as can be seen in figure 3.112 The 2-D energy spectra at this time, shown in figure 3.113, shows that in the interior regions of the vortex, turbulent kinetic energy is now spread over a large range of wavenumbers. The dominant wavenumbers are $(k_\theta, k_z) = (\pm 1, 1)$, (0,1), (0,2) and (2,2). The GTKE now reaches what we have termed to be its 3rd peak (though this is not really a peak in the strict sense of the word). At this time, the vortex is in a "tightened" state. The structure shows the presence of various deformations corresponding to different dominant modes (see figure 3.114). This is substantiated by the continued observance of the above dominant wavenumbers in the 2-D energy spectra presented in figure 3.115.

The GTKE still continues to increase though at a reduced rate. Figure 3.116 shows the vortex structure at $t/T = 90.92$. The vortex continues to be in what we have been calling a tightened state. The structure still shows the presence of deformations corresponding to a varied range of dominant modes. At the end of this time period (we have called this stage the 4th peak of the GTKE, though once again we are not really at a peak in the strict sense of the word), the vortex is still in a tightened state. We are still seeing features that correspond to various dominant modes (see figure 3.117). This is substantiated by 2-D energy spectra for this location, presented in figure 3.118. The dominant modes at this time are found to be $(\pm 1, 1)$. There are other modes that contain a significant amount of energy. However, the fact that peaks are at $(\pm 1, 1)$ could be of particular significance since these were the dominant modes towards the end of STRN4, and we are now entering the final ascent of GTKE in STRN2.

#### 3.7.2.6 Sixth Time Period

The GTKE now begins what could be called its final ascent in this simulation. The GTKE grows exponentially with a growth rate of 0.11. This is the same growth rate as for the GTKE ascent from the 3rd ebb to the 3rd peak. Note that the growth

rates presented in this thesis are truncated at the second decimal place. If more significant digits are used, we will see that the growth rate in this final GTKE ascent is slightly smaller than that for the GTKE ascent from the 3rd ebb to the 3rd peak. Figure 3.119 shows the vortex structure at $t/T = 96.77$. The vortex still continues to be in its tightened state and displays features that show the presence of various modes carrying a substantial amount of energy. However, as pointed out above, of particular interest is the sinusoidal bending accompanied by left and right running helical waves that would correspond to $(\pm 1, 1)$. Vortex structure at $t/T = 98.45$ is shown in figure 3.120. The vortex seems to tighten up even further. The 2-D energy spectra for this time, shown in figure 3.121 reveal (0,2) and (2,2) to be carrying a significant amount of energy in addition to $(\pm 1, 1)$. This substantiates the observation of a varied set of features in the vortex structure at this time.

At $t/T = 100.29$, the vortex seems to be beginning to loosen up (see figure 3.122) We are still seeing a range of flow features that would correspond to several significantly energetic modes. The vortex structure at $t/T = 101.34$, shown in figure 3.123, is along the same lines. The 2-D energy spectra at this time, shown in figure 3.124 shows us that the dominant modes are still $(\pm 1, 1)$, (0,2) and (2,2). In figure 3.125 we see the vortex structure at $t/T = 103.05$. Both left and right running helical waves and a sinusoidal bending along the vortex axis are prominent. This is also the case in figure 3.126. This is the situation just after the so called 5th peak of GTKE is reached. The dominant modes are still $(\pm 1, 1)$, (0,2) and (2,2) as can be seen in figure 3.127. Through this time period, the dominant modes have stayed the same.

#### 3.7.2.7 Seventh Time Period

We now enter the final time period of this simulation. The GTKE is still rising. Figure 3.128 shows the vortex structure at $t/T = 106.41$. We are now beginning to see a substantial presence of small scale structure. Figures 3.129, 3.130 and 3.131 show the vortex structure at times $t/T = 108.55$, 109.52 and 111.27 respectively. We are beginning to see the presence of a significant level of vorticity near the domain

boundary. At $t/T = 111.27$ we have arrived at the last GTKE peak in this simulation. The 2-D energy spectra at this time (see figure 3.132) shows $(\pm 1, 1)$ and $(0, 2)$ to be the dominant modes.

The GTKE now plunges, and as can be seen in figures 3.133 and 3.134, we have a substantial level of vorticity at the domain boundary. This is in conflict with the use of potential flow boundary conditions. The simulation has to be thus stopped. The 2-D energy spectra at $t/T = 113.93$ presented in figure 3.135 shows that $(k_\theta, k_z) = (\pm 1, 1)$ are the dominant modes. These were also the dominant modes at the end of the STRN4 simulation. Also the growth rate for the final ascent of GTKE in STRN4 was 0.16. This value is comparable to the growth rate in the final GTKE ascent for STRN2 which was 0.11. It thus seems that the same instability mechanism has eventually dominated in both the simulations.

### 3.7.3 Mean and Statistical quantities

Following the trend established in the discussion for STRN4 above, we now take a look at the evolution of some mean and statistical turbulent quantities of interest (mean velocity components, mean vorticity components, Reynolds stresses, turbulent kinetic energy and enstrophy) during each of these time periods. Once again, the flow is not axisymmetric. We thus have to be careful not to miss the azimuthal variation of the mean and statistical quantities being studied. Here we look at how the above mentioned quantities evolve in time at the angular locations of $\theta = 45^o$ and $\theta = 135^o$. These correspond to the major and minor axes of the elliptical streamlines. Note that the mean flow is symmetric about the major and minor axes of the elliptical streamlines. Also, $\theta = 45^o$ corresponds to the direction in which the vortex is most stretched while $\theta = 135^o$ corresponds to the direction in which the vortex is most compressed. Hence the evolution of mean and statistical quantities in these two directions will be representative of their evolution in the stretched and compressed regions of the vortex.

#### 3.7.3.1 First time period

As before we start by looking at the evolution of turbulence. Figure 3.136 shows how the TKE evolves in time. As was the case in STRN4, the initially laminar vortex in STRN2 is perturbed in such a way that the TKE peaks at the core radius at the beginning of the simulation. Let us first consider the situation at $\theta = 45^o$. In the early stages of the simulation, as the level of TKE grows, the peak location moves just inside the core radius. As the GTKE approaches the "1st peak", the location of the TKE peak oscillates between moving inwards to the centerline, then outwards to the core radius and then finally, as the GTKE reaches the "1st peak", moving inwards again. Towards the end of the first period, we notice that the peak value of the TKE does not vary much. However the value in the outer regions of the vortex increases, indicating a larger portion of the vortex to be turbulent. At $\theta = 135^o$ also the peak seems to oscillate during this time period. However, it seems that this peak's oscillations are out of phase with the oscillations of the peak at $\theta = 45^o$. Also, towards the end of this time period, the amount of increase in turbulence in the outer regions is less as compared to the situation at $\theta = 45^o$.

We now turn our attention to the evolution of the mean flow. Figure 3.137 shows how the mean tangential velocity evolves in time. Initially as the GTKE grows, $V_\theta$ does not show much variation. In the later stages of this period, we observe rapid diffusion, with the peak decreasing in value and moving outwards. Slightly before the onset of rapid diffusion, a small increase in the $V_\theta$ value is observed in the region just to the left of the peak. Also, in this simulation, due to the initial wake like axial velocity profile, the evolution of the mean axial velocity becomes significant in addition to the mean tangential velocity. This is shown in figure 3.138. Here also we see a trend similar to the $V_\theta$ profile, with a slow variation of the profile in the early stages, followed by a rapid diffusion as the GTKE approaches the 1st peak. In both tangential and axial velocity profiles, we notice that by the end of this time period, the changes in the flowfield have reached outer regions of the vortex. Just

as in STRN4, we have a mean radial flow due to the ellipticity of the streamlines. However, the mean radial flow is relatively much smaller than the mean tangential and axial flows (see figure 3.139). It is not seen as being significant to understanding the overall flow, and hence is not included in the discussion for the rest of the time periods.

Let us now look at how the mean vorticity evolves in time. Figure 3.140 shows the evolution of mean axial vorticity. In accordance with how the mean velocity field changes in time, the mean axial vorticity, after not showing much change in the initial stages, shows a relatively rapid diffusion as the GTKE approaches the "1st peak". The peak value stays at the centerline and falls in value. $\Omega_z$ within the core decreases in value while an increase is observed outside the core. Note that contrary to STRN4, there is no shift of the peak away from the centerline. Since we also have a mean axial flow in this simulation, the axial component of the mean vorticity is not the only non-zero component. Figure 3.141 shows how the mean tangential vorticity evolves in time. Once again the pattern observed is similar, a gradual change in the earlier stages followed by a relatively rapid diffusion as we approach the first GTKE peak. Note that both the axial and tangential mean vorticity profiles become noisy within the first period itself. This is a reflection of the limited sampling space available to compute mean and statistical quantities. This effect is seen in the mean radial vorticity profiles also (see figure 3.142) which display a noisy behavior about zero instead of remaining identically zero as would be expected.

Now that we have looked at the evolution of the mean flow, let us take a look at how the Reynolds stresses behave. Let us first consider $R_{\theta\theta}$, $R_{r\theta}$ and $R_{\theta z}$ as the turbulence affects the mean tangential velocity via these components, as can be seen in equation 3.22. Figure 3.143 shows how $R_{\theta\theta}$ evolves in time. Right from very early stages in the simulation, we observe the onset of a twin peak structure to the profile. The locations of these twin peaks for the two angular locations seem to be out of phase. A significant level of $R_{\theta\theta}$ is observed till about a distance of about 1.5 times the core radius from the centerline (highest levels being within the core itself). The

spread is lesser at $\theta = 135^o$. This could be the reason for the different locations of the twin peaks.

Figures 3.144 and 3.145 show the evolution of $R_{r\theta}$ and $R_{\theta z}$ during this time period. Note that very low levels are present for both these Reynolds stress components. This makes it difficult for us to differentiate between any patterns that may be present in the $R_{\theta\theta}$ profile from the presence of noise due to the limited sampling space available for the computation of mean and statistical quantities. However, with this cautionary note in mind, we will proceed with identifying any patterns that $R_{r\theta}$ and $R_{\theta z}$ might be following. We observe a very noisy profile in both cases. It seems as if $R_{r\theta}$ values at the two angular locations differ in sign while being similar in magnitude. In contrast to this $R_{\theta z}$ values at both locations are of the same sign (positive) and are similar in magnitude.

The Reynolds stresses that affect the mean axial velocity are $R_{zz}$, $R_{rz}$ and $R_{\theta z}$ (see equation 3.23). We have already looked at the evolution of $R_{\theta z}$ above. Let us take a look at how $R_{zz}$ evolves in time (see figure 3.146). As the GTKE grows, the $R_{zz}$ profile is found to peak just inside the core radius. As we move through this time period, the profile shape changes. Instead of growing from a near zero value at the centerline and going through the above mentioned peak, the profile shape shows an almost uniform level from the centerline till about 1.5 times the core radius at the $\theta = 45^o$ location. At the $\theta = 135^o$ location, this uniform level is seen to extend till about 2 times the core radius. At the $\theta = 45^o$ location, we observe the presence of non zero values of $R_{zz}$ further out. Figure 3.147 presents the evolution of $R_{rz}$ during this time period. Initially we see the development of a profile shape in which $R_{rz}$ has near zero values at the centerline, decreases as we move outwards, goes through an ebb (a negative peak) within the core and then increases again to reach near zero values just outside the core. Later on in this time period, as the GTKE keeps increasing, the profile flattens out with a decrease in the peak value. The single ebb structure is eventually lost at the end of this time period we see a noisy profile with

very low values. This noisiness of the profile may just be the effect of limitations in the sampling space.

Let us now look at $R_{rr}$, the sixth and final independent Reynolds stress tensor component. $R_{rr}$ along with $R_{r\theta}$, $R_{rz}$ and $R_{\theta\theta}$ (these three components have been looked at above) bring the effect of the turbulence in the evolution of the mean radial velocity. This can be seen in equation 3.21. Figure 3.148 shows the evolution of $R_{rr}$ in the first time period. We observe that the variation of the $R_{rr}$ profile in time is similar in behavior to the evolution of TKE in this time period. In the early stages of the simulation, the peak location moves just inside the core radius. At $\theta = 45^o$, as the GTKE approaches the "1st peak", the location of the TKE peak oscillates between moving inwards to the centerline , then outwards to the core radius and then finally, as the GTKE reaches the "1st peak", moving inwards again. We see this oscillatory behavior at $\theta = 135^o$ also. However, the peak locations seem to be out of phase. Towards the end of the first period, we notice that the peak value does not vary much. However the value in the outer regions of the vortex increases.

Finally we take a look at the evolution of enstrophy, to see how the level of vorticity fluctuations vary in time. The simulation starts with the enstrophy decreasing from it's initial level (see figure 3.149) and then begins to rise as the simulation progresses. This rise is initially gradual but becomes significantly faster as the GTKE approaches the "1st peak". The level of enstrophy within the vortex core is significantly higher than outside. However, we do observe the presence of a significant level of fluctuating vorticity in the outer regions of the vortex towards the end of this time period. Just as was the case with TKE and the Reynolds stress components, at $\theta = 135^o$, the spread outwards is lesser than that at $\theta = 45^o$. The enstrophy levels for both angular locations are of the same order of magnitude.

#### 3.7.3.2 Second time period

As the GTKE decreases during this time period, the TKE profile shows a significant change in shape. (see figure 3.150). The peak moves to the center and decreases

in value. Right at the end of this time period, we see a small increase in the peak value at $\theta = 45^o$. At $\theta = 135^o$, a small increase is observed in the level of turbulence even as we go away from the centerline (at the end of this time period).

In figure 3.151 we observe that the mean tangential velocity continues to diffuse in the outer regions of the vortex, though the rate at which this diffusion takes place is considerably reduced as compared to the later half of the first time period. This is reasonable as the GTKE is now decreasing and as the flow becomes less turbulent, we expect a slower diffusive process. At the $\theta = 45^o$ location, we observe an increase in $V_\theta$ in the region to the left of the peak. This could be an indication of the presence of anti-diffusion, which has to be confirmed by computing the eddy viscosity. Slow diffusion is also observed in the mean axial velocity (see figure 3.152).

The mean axial vorticity, $\Omega_z$ continues to diffuse as we enter this time period (see figure 3.153). However, a shift is observed in this trend with the peak value actually increasing at the centerline for some time. The diffusive process then starts again. One thing to be remembered is that we have a certain amount of noise in our profiles for mean and statistical quantities. Hence some of the small "shifts in trends" could be false. Figure 3.154 shows the variation of the mean tangential vorticity during this time period. We observe a continuation of the diffusive process. The noisy behavior of the profiles makes it difficult to notice trends.

The variation of $R_{\theta\theta}$ in the second time period is shown in figure 3.155. We see the emergence of a profile shape which has a peak at the center, a rapid decay reaching a low level as we reach the core edge, and then a leveling out. Towards the end of this time period, this trend shifts at the $\theta = 45^o$ location, and the profile shape seems to be going back to a multi peaked structure.

Figure 3.156 shows the variation of $R_{r\theta}$ during this time period. We observe that the sign of $R_{r\theta}$ flips repeatedly as the GTKE decreases (this is true at both the angular locations). This indicates that the eddy viscosity might be switching between being positive and being negative. A negative value of eddy viscosity points to the presence of anti-diffusion. The profiles at both the angular locations approach

limiting profiles as we approach the end of this time period. The limiting profiles at $\theta = 45^o$ and $\theta = 135^o$ have the characteristic of $R_{r\theta}$ being of opposite signs and similar magnitudes at the two angular locations (can be considered approximately "flipped" over). These limiting profiles start from near zero values at the centerline and after passing through a peak (positive at $\theta = 45^o$ and negative at $\theta = 135^o$) at about the center of the core, decay to zero as we move further outwards. This decay is seen to be pretty much complete at about the core radius.

The variation of $R_{\theta z}$ during the second time period is shown in figure 3.157. It is difficult to identify any pattern that might exist in the $R_{\theta z}$ profiles. This is particularly true at the $\theta = 45^o$ location where the levels become very low as we move through this time period. However at the $\theta = 135^o$ location, at the end of this time period, the profile shape is similar to that finally attained by $R_{r\theta}$ at this location.

The variation of $R_{zz}$ during the second time period is shown in figure 3.158. As the GTKE decreases, the level of $R_{rr}$ falls. This fall in the level is most pronounced in the region outside the core. From a multi peaked broad shape, the profile changes to having its peak at or near the centerline, followed by a rapid decay to a low level by the time we reach the core edge.

The variation of $R_{rz}$ in this time period is shown in figure 3.159. At the $\theta = 45^o$ location, no particular pattern in the profile shape seems to emerge during this time period. The noisiness in the profile could just be a reflection of the limited sampling space available for computing the statistical quantities. At the $\theta = 135^o$ location the situation is different. Although the values are still very low, we do identify a trend in the profile shape. A small positive peak inside the core is formed. Towards the end of this time period, the centerline value is observed to consistently increase.

Figure 3.160 shows the variation of $R_{rr}$ during the second time period. The profile shape changes from a multi peaked broad shape to one which peaks at the center and decays rapidly as move outward. Once it decays to a low value, the profile flattens out as one goes into the outer regions of the vortex. This is very similar to the variation

of TKE during this time period. At the end of this time period, the profile seems to be again moving towards a multi peak structure at the $\theta = 135^o$ location.

Figure 3.161 shows the variation of enstrophy during this time period. As expected, the level of vorticity fluctuations decreases significantly as the flow becomes less turbulent during this time period.

#### 3.7.3.3 Third time period

As the GTKE begins to rise in this time period, the peak value of TKE also rises (see figure 3.162). At $\theta = 45^o$, the peak value during this ascent of GTKE moves a little away from the centerline and returns there. Also, at the end of the GTKE ascent, the TKE profile becomes a little fuller in the outer half of the core. At $\theta = 135^o$, this fullness of profile is observed closer to the centerline. Also, the level of turbulence is observed to be higher. This might indicate a tendency to return to the profile shape during the earlier GTKE ascent (1st time period). Then as the GTKE begins its descent to the 2nd ebb, the profile becomes similar to what was observed in the 2nd time period. The above mentioned fullness goes away. The peak value falls rapidly. The variation in TKE is most significant in the inner portion of the core.

The behavior of the mean tangential velocity as the GTKE ascends (see figure 3.163) is similar to the later part of the first time period (GTKE was also increasing then). We observe a rapid diffusion. Later on as the GTKE is decreasing again towards the 2nd ebb, the rate at which $V_\theta$ is diffusing becomes smaller. We also observe indications of what may be a possible anti-diffusion to the left of the peak. There are instances of $V_\theta$ increasing in this region. At $\theta = 45^o$, the mean axial velocity (see figure 3.164) does not show much decrease during the GTKE ascent. However, as the GTKE begins to decrease there is a quick decrease within the core and then again the change in $V_z$ for the remaining portion of this time period is minimal. In contrast, at $\theta = 135^o$, the diffusion of $V_z$ is more uniform. Note that right towards the end of this time period, close to the centerline the $V_z$ profile is departing from its initial wake-like shape.

Figure 3.165 shows the variation of the mean axial vorticity during this time period. Although we observe a substantial oscillation at the centerline, it seems that $\Omega_z$ does not show much variation in most of the domain. There are indications of switches between diffusive and anti-diffusive processes inside the core (close to the centerline) with $\Omega_z$ switching between falling and rising in value. While looking at the mean tangential vorticity evolution (see figure 3.166), the noisiness of the profiles makes it difficult to identify detailed trends. However the overall behavior of $\Omega_\theta$ during this time period has been to decrease. The peak seems to have become less negative and has moved outwards. We might also be observing a change in the shape of the profile close to the centerline. This would correspond to the change in the $V_z$ profile shape.

The variation of $R_{\theta\theta}$ during the third time period is shown in figure 3.167. The principle observation is that $R_{\theta\theta}$ during this time period is essentially contained within the region which extend to about 1.2 times the core radius. At $\theta = 135^o$, $R_{\theta\theta}$ is seen to be contained closer to the centerline as compared to $\theta = 45^o$.

Figure 3.168 shows the variation of $R_{r\theta}$ in the third time period. As the GTKE grows, the profiles at the two angular locations leave the shape they had achieved at the end of the last time period. At the $\theta = 45^o$ location, $R_{r\theta}$ profile is observed to repeatedly flip over (change sign) as we progress through this time period. A typical profile shape in the initial stages of this time period has $R_{r\theta}$ peaking at or near the centerline, decaying rapidly as we move outward, crossing the $R_{r\theta} = 0$ axis at about halfway through the core, going through a negative peak just inside the core radius and then increasing again to zero as we continue moving outward. When the profile flips, the above description with the signs changed holds true. Later on the profile decays and the above mentioned shape is lost. At the $\theta = 135^o$ location, the profile initially develops a shape that has a peak negative value at the centerline, a quick increase to a near-zero peak near the centerline, followed by a decrease again to a negative peak (less negative than the centerline value) just inside the core radius.

Later the profile leaves this shape and eventually the level of $R_{r\theta}$ falls and we have a noisy profile about the $R_{r\theta} = 0$ axis.

The variation of $R_{\theta z}$ in the third time period is shown in figure 3.169. At the $\theta = 45^o$ location, in the early parts of this time period the profile shape has negative $R_{\theta z}$ values near the centerline. This changes and in the later part of this period, we have near zero values at the centerline, an increase as we move outward till a peak is reached, followed by a decay back to zero as we move further out. As we have come through this time period, a small positive peak has been established at about 0.6 times the core radius. At the $\theta = 135^o$ location, in the initial part of this time period, $R_{\theta z}$ becomes increasingly negative in the inner portion of the vortex core. This trend stops as we move on through this time period. There are instances of $R_{\theta z}$ being positive very close to the centerline and decaying to zero rapidly. Eventually have a noisy profile with very small values.

The variation of $R_{zz}$ during the third time period is shown in figure 3.170. The profile shape obtained towards the end of the last time period is essentially maintained as we go through a rise and decay of GTKE during this time period. Although the centerline value does show rises and falls, the level of $R_{zz}$ does not vary much elsewhere. When the GTKE peaks, at the $\theta = 45^o$ location we do observe a slight increase in the level at about the core radius. In contrast, at $\theta = 135^o$ a high level of $R_{zz}$ is observed inside the core at this GTKE peak. As the GTKE begins to decrease, these go away, and the level is approximately sustained till we approach the end of the time period. At this time period comes to an end we observe that the level in the region close to the centerline has decreased substantially.

Figure 3.171 shows the variation of $R_{rz}$ during this time period. In the previous time periods, the level of $R_{rz}$ had stayed considerably low. This changes now and within the core there is a significant level. At the $\theta = 45^o$ location during the descent of GTKE, the level fluctuates between being significantly negative and being slightly positive or nearly zero. The main difference at the $\theta = 135^o$ location seems to be the

containment of the negative value region nearer the centerline and a more pronounced presence of a positive value region in the outer part of the core.

The evolution of $R_{rr}$ during this time period is presented in figure 3.172. Let us first look at the $\theta = 45^o$ location. Note that the inner part of the vortex core is the region where substantial activity takes place. As the GTKE increases, we see an increase in the level of $R_{rr}$ also. At the 2nd peak, we see a bulge in the profile in the outer half of the core. This bulge goes away as the GTKE starts decreasing again. The centerline value increases for some time even during the GTKE decay. However, eventually it falls and as this time period comes to an end the profile has decayed substantially with $R_{rr}$ being of about the same level as in the initial part of this time period. At the $\theta = 135^o$ location, there is much lesser variation in the centerline value in terms of magnitude. However it rises and falls more frequently. During the GTKE decay, the $R_{rr}$ profile shows rises and falls instead of a consistent decay as was the case at $\theta = 45^o$. Also, the profiles are in general fuller as compared to the the $\theta = 45^o$ location.

Figure 3.173 shows the variation of enstrophy in this time period. In the earlier time periods we had observed the presence of a significant amount of enstrophy outside the core. This is not the case any more. Although the level of enstrophy rises and falls along with the rise and fall of GTKE, most of it is contained within the core during this time period. When GTKE reaches the 2nd peak, the enstrophy profile is fuller (and the level is somewhat higher) for $\theta = 135^o$. This corresponds to the TKE profile behaving the same way at this angular location. More turbulence would generally mean a higher level of vorticity fluctuations.

#### 3.7.3.4 Fourth time period

Figure 3.174 shows the variation of TKE in the fourth time period. As the GTKE maintains a sort of a "steady" state in this time period, the TKE profile also does not show much variation. The level of turbulence in the vortex shows small rises and falls (this is most easily seen in the behaviors of the peak value which is located at

or near the center). This is consistent with the behavior of GTKE. Although there are small level fluctuations, the overall behavior is that of a "steady" type. Note that at $\theta = 135^o$, as we move away from the centerline, the TKE level falls faster than at $\theta = 45^o$.

As the GTKE level maintains a sort of a steady value, the mean tangential velocity continues to diffuse (see figure 3.175). through this time period. As would be expected in the absence of significant GTKE increases or decreases, the rate at which $V_\theta$ diffuses also does not vary much. Not only has the peak been decreasing in value and moving out, the profile also seems to be becoming flatter. There are instances of $V_\theta$ increasing slightly in the region to the left of the peak. This could be because of the presence of anti-diffusion. As mentioned before this has to be confirmed by computing eddy viscosity. Within the core, the mean axial velocity decreases quite a bit (see figure 3.176). Note that the centerline value itself doesn't show much of a shift. Similar to the $V_\theta$ profile, the $V_z$ profile is also becoming flatter. The profile shape inside the core is no longer maintaining a wake-like shape.

The mean axial vorticity shows a rapid decrease inside the core region as we go through this time period (see figure 3.177). However right at the end of this time period, the centerline value has shown a substantial jump. In regions outside the core, the change is not significant. We observe that the mean tangential vorticity is now significantly lower (see figure 3.178). Despite the noisy profiles, the overall impression obtained is of a continuation of the diffusive process during this time period. Also note the change in the profile shape inside the core region. This corresponds to the departure from the wake-like shape of the axial velocity profile.

The variation of $R_{\theta\theta}$ during the fourth period is shown in figure 3.179. We observe slight rises and falls of the $R_{\theta\theta}$ level during this time period, consistent with the small variations if GTKE. At the angular location of $\theta = 135^o$, $R_{\theta\theta}$ is contained closer to the centerline while having higher values, as compared to the angular location of $\theta = 45^o$.

Figure 3.180 shows the variation of $R_{r\theta}$ during the fourth time period. Let us first look at the $\theta = 45^o$ location. Note that the magnitude of $R_{r\theta}$ during this time period

does not vary much. This is consistent with the level of turbulence (as indicated by GTKE) does not vary much. However, the sign flips repeatedly. This might be due to the eddy viscosity becoming negative, which would signify the presence of anti-diffusion. At the $\theta = 135^o$ location, the profile seems to be getting damped. As the magnitude of $R_{r\theta}$ decreases, the sign is observed to change repeatedly. Hence we might be observing anti-diffusion in the compressive part of the vortex also. However, $R_{r\theta}$ values at the two angular locations, at any particular time, do not have opposite signs.

The evolution of $R_{\theta z}$ during the fourth time period is shown in figure 3.181. At $\theta = 45^o$ we observe that the profiles seem to be getting damped as we move through this time period. As the magnitude of $R_{\theta z}$ decreases, the sign is observed to change repeatedly. Note that similar behavior was observed for $R_{\theta z}$ at the $\theta = 135^o$ location. The evolution of $R_{\theta z}$ at the $\theta = 135^o$ location is similar to that of $R_{r\theta}$ at $\theta = 45^o$. The magnitude does not vary much while the sign flips repeatedly. Thus the behavior of $R_{r\theta}$ in the stretched part of the vortex is similar to the behavior of $R_{\theta z}$ in the compressed part of the vortex, and vice versa. Although the evolution of $R_{r\theta}$ at $\theta = 45^0$ is similar to that of $R_{\theta z}$ at $\theta = 135^o$ in the above mentioned way, they have opposite signs at any of the times considered during this time period.

Figure 3.182 shows the variation of $R_{zz}$ during this time period. The level near the centerline has increased again (we had observed a substantial decrease at the end of the last time period). The profile shape is essentially the same as before. $R_{zz}$ has its peak at or near the centerline. It then decays rapidly to a very low value by the time we reach the core radius. $R_{zz}$ is contained closer to the centerline at the $\theta = 135^o$ location. Overall we do not observe significant variations in the level of $R_{zz}$. This is in accord with the GTKE level staying nearly uniform through this time period. There are some rises and falls though, particularly near the centerline.

The variation of $R_{rz}$ during this time period is shown in figure 3.183. At the $\theta = 45^o$ location, the level stays about the same as we go through this time period. This is consistent with the GTKE not showing much variation. However the sign

repeatedly flips. This indicates that the eddy viscosity might be changing its sign which would signify that both diffusive and anti-diffusive processes are present. At the $\theta = 135^o$ location, we observe a dampening of the profile. As the magnitude of $R_{rz}$ decreases, the sign is observed to change repeatedly. Hence we might be observing anti-diffusion in the compressive part of the vortex also. Note that these observations are similar to those made for $R_{r\theta}$ in this time period. The one difference is that $R_{rz}$ seems to have opposite signs at the two locations for the same plotting time, especially during the early part of this time period.

Figure 3.184 shows the evolution of $R_{rr}$ during this time period. The profile shape is similar to that of TKE. The level of $R_{rr}$ does not show significant rises and falls. This is consistent with the almost uniform level of GTKE during this time period. Note that the level is lower at the $\theta = 135^o$ location.

Figure 3.185 shows the variation of enstrophy in this time period. The containment of enstrophy within the core observed in the last time period continues here. Although there are rises and falls, we notice that the enstrophy level stays within the same order of magnitude. This is different from previous time periods, where there was a much larger variation. This is consistent with the small variations of GTKE during this time period.

#### 3.7.3.5 Fifth Time Period

Although the GTKE rises in this time period, we do not observe a significant increase in the peak value of TKE (see figure 3.186). The TKE peak stays at or near the centerline while displaying small oscillations in its value. We also observe some oscillation in how full the TKE profile is near the center. Note that at $\theta = 135^o$, there is hardly any variation in how far away from the centerline the turbulence reaches.

The process of $V_\theta$ diffusion (see figure 3.187) (in terms of the peak decreasing in value and moving outwards) continues. At $\theta = 45^o$, to the left of the peak value (inside the core) there is a significant amount of diffusion by the time we reach the end of this time period. However, it has not been a smooth diffusive process. On

the contrary we observe rises and falls in the value of $V_\theta$ indicating the presence of anti-diffusion at certain times. In fact we even observe the peak value increasing at a certain stage before continuing to fall again. Towards the end of this time period, we observe an instance of the value in the outer regions decreasing. At $\theta = 135^o$ we see rises and falls in the value of $V_\theta$ to the left of the peak. This is again an indication that we may have the presence of anti-diffusion in our flow. In the interior of the vortex, the mean axial velocity profile also varies significantly during this time period (see figure 3.188). We observe that a significant amount of diffusion of $V_z$ has taken place by the end of this time period inside the core. Outside the core however, the change is much lesser. Another feature of interest that the profile shape inside the core is much different by the time we end this time period. The classical wake like shape is not maintained anymore. At $\theta = 45^o$, the profile shape inside the core actually resembles a jet. The profile seems to be tending to this shape at $\theta = 135^o$ also.

We once again observe the core region to be very active when we look at the evolution of mean axial vorticity (see figure 3.189). The level of mean axial vorticity close to the centerline has fallen dramatically by the time we reach the end of this time period. The diffusion of $\Omega_z$ reaches out further at $\theta = 45^o$. Note that at $\theta = 45^o$, the profile shape of the mean tangential vorticity (see figure 3.190) changes significantly inside the core. This is consistent with the change in profile shape for $V_z$.

The evolution of $R_{\theta\theta}$ during this time period is shown in figure 3.191. The trend of $R_{\theta\theta}$ being contained closer to the centerline, while having larger values, at the $\theta = 135^o$ location continues in this time period. Also, the $R_{\theta\theta}$ profile at this location does not show much variation as we move through this time period. While moving from the 3rd to the 4th peak, we do observe an increase in the peak value, but this value then falls again. However, the $\theta = 45^o$ location is one of a higher amount of activity. At this location, as we move into this time period, we observe the peak of $R_{\theta\theta}$ to be near the centerline. Initially the profile does not show much variation. As we reach the 3rd peak, we observe that the peak moves away from the centerline

and increases in value. We then observe some thing rather interesting. The profile changes its shape inside the core. $R_{\theta\theta}$ decreases in value as we move away from the centerline and goes through an ebb at about the same location where the peak had moved to earlier. The value then rises and after going through a peak at about the core radius falls away gradually. At the end of this time period, we observe that the profile has again changed its shape. We again have a peak some distance away from the centerline. The value then gradually decays.

We now look at how $R_{r\theta}$ evolves during this time period (see figure 3.192). At the $\theta = 45^o$ location, $R_{r\theta}$ attains its minimum value at or near the centerline, increases as we move outwards, becomes positive at about the core radius, and after going through a small peak decays to zero as we approach the boundary. At $\theta = 135^o$ we observe exactly the opposite scenario. $R_{r\theta}$ at the two angular locations thus has opposite signs while being similar in magnitude. Note that as we go through this time period, $R_{r\theta}$ does not rise or fall significantly at either angular location.

The evolution of $R_{\theta z}$ in the fifth time period is shown in figure 3.193. At $\theta = 45^o$, the general trend exhibited by the $R_{\theta z}$ profiles is to decrease from a near zero value at the centerline as we move outward, go through a negative peak, become positive again at about the core radius and then after going through a small positive peak decay to zero as we approach the boundary. In some ways this is similar to the general profile shape of $R_{r\theta}$ at this angular location. The main difference is in the value of the negative peak. $R_{r\theta}$ has a more negative peak. Also, the negative peak for $R_{r\theta}$ is closer to or at the centerline. At $\theta = 135^o$, the manner of evolution has similarities to the last time period. Close to the centerline, there is a shifting in the sign. However, instead of rapid flipping of the sign, we now see a gradual shift from positive to negative values. At the end of the time period the sign has again become positive in the interior of the vortex. A small positive peak develops just outside the core radius.

Figure 3.194 shows the evolution of $R_{zz}$ during this time period. The profile shape continues to be the same as the last period. We observe large fluctuations in the level of $R_{zz}$ inside the core region, particularly at the $\theta = 45^o$ location.

The evolution of $R_{rz}$ during this time period is presented in figure 3.195. Let us look at the $\theta = 45^o$ location first. In the early part of this time period, we observe a near zero level of $R_{rz}$ all the way from the centerline to the outer region. As we move on, an ebb (negative peak) develops about halfway through the core. This flips over and becomes a positive peak as we move further along. Note that the centerline value repeatedly switches between being positive and negative. At the $\theta = 135^o$ location, the profile shape in the early stage of this time period starts from near zero values at the centerline, goes through a small positive peak, decreases and becomes negative, goes through a small negative peak, and then increases again to near zero values as we move further out. Both the positive and negative peaks are within the core. As we move further along, the profile shape changes into one that has a negative peak about halfway through the core. At the end of the time period the profile reverts back to the earlier shape with a positive peak and a negative peak inside the core.

Let us now look at how $R_{rr}$ evolves during this time period (see figure 3.196). The profile shape of $R_{rr}$ is very similar to that of TKE. The peak value stays at or near the center. We do observe significant fluctuations in the peak/centerline value. Note that the levels at $\theta = 135^o$ are lower. The centerline value at this location also does not fluctuate as much as at $\theta = 45^o$.

The enstrophy is mostly contained within the core region (see figure 3.197). Let us first look at the $\theta = 45^o$ location. As the GTKE increases from the 3rd ebb to the 3rd peak, we observe an increase in the level of enstrophy (as expected). We start with the peak being at the center and the value falling rapidly as we move away from the centerline. At the 3rd peak, we have a much fuller profile, and instead of seeing a peak at the centerline, we observe a near uniform level of enstrophy throughout the core. This again changes as we move on from the 3rd peak, with the profile shape reverting back to a quick decay as we move away from the centerline. We also have a

drop in the peak value. At the 4th peak however, we again have a near uniform level of enstrophy within the core. The enstrophy level at the fourth peak is considerably lesser than that at the 3rd peak. At $\theta = 135^o$ the variation is not that much. Also, at the 4th peak, instead of a near uniform level within the core, we have the peak at the center with a decay as we move away.

#### 3.7.3.6 Sixth Time Period

As the GTKE begins what we can consider to be its final ascent during this simulation, the TKE profile at the $\theta = 45^o$ location becomes fuller (see figure 3.198). The peak value does not show an increase along with the increase in GTKE. It stays almost constant for most of this time period. The fact that more and more of the vortex is becoming turbulent (as can be see by the increasing fullness of the TKE profile) is reflected in the increasing value of GTKE. In fact towards the end of this time period, we notice that the peak value actually drops and there is a dramatic increase in the fullness of the profile. The level of turbulence instead of decreasing quickly as we move away from the centerline, now stays about the same for increasing distances from the centerline. This behavior is not seen at the $\theta = 135^o$ location. Here the profile almost tends to maintain itself. It seems that more and more of the vortex in direction of its stretching is getting turbulent, whereas in the direction of its compression, turbulence is still staying confined to short distances from the center.

More of the vortex becoming turbulent would lead us to expect that our mean velocity would diffuse in a larger portion of the vortex. This is indeed the case (see figure 3.199). At the $\theta = 45^o$ location, as we move through this time period, we initially see a rapid diffusion inside the core. Towards the end of this time period, significant diffusion is observed up to about 2 core radii from the center. In some regions (particularly just to the left of the vortex peak) we observe increases in the value of $V_\theta$ followed by a continuation of decrease in value. This could indicate the presence of anti-diffusion. However, since the GTKE is increasing, we have the flow becoming more and more turbulent. Anti-diffusion is not really expected when

we have increasing turbulence. In accordance with the turbulence being confined to shorter distances from the center at the $\theta = 135^o$ location, the mean tangential velocity does not diffuse as rapidly and far-reachingly as at the $\theta = 45^o$ location.

At the $\theta = 45^o$ location, we also observe a significant variation in the profile shape of $V_z$ in the interior of the vortex (see figure 3.200). We had observed at the end of the last time period that the profile was no longer of a classical wake shape. Instead in the interior we had a jet shaped profile. During this period, the profile inside the vortex core changes shape again. There does not seem to be a consistent shape it adheres too. In fact near the end of this time period, we actually observe a wake like shape to start with, and then as we move further away from the centerline, the we observe a jet like bulge just outside the core and then again a continuation of the wake like approach to free stream velocity. At the end of this time period though we again have a proper wake like profile. Within the core region the value of $V_z$ does not change much as compared to the previous time period. However, variations in $V_z$ extend further away from the centerline now. Such dramatic variations in the $V_z$ profile shape are not observed at the $\theta = 135^o$ location. Again, this is to be expected since it is along the stretching direction that the vortex is becoming more turbulent.

By the end of this time period, we observe the mean axial vorticity to have reduced considerably in the interior of the vortex (see figure 3.201). During the time period, we observe fluctuations in the value of $\Omega_z$ close to the centerline. Once again, in accordance with the above observations, diffusion of $\Omega_z$ extends further at the $\theta = 45^o$ location. Now let us look at the evolution of the mean tangential vorticity (see figure 3.202) during this time period. At the $\theta = 45^o$ location, although the profile shape in the outer regions corresponds to what would be expected for a wake like axial velocity profile, in the interior the profile shape varies. This is expected since the mean axial velocity profile was also varying. Also variations in the profile seem to have extended further out than before. This corresponds to variations in mean axial velocity extending further out. At the $\theta = 135^o$ location, the profile shape does

not depart much from the expected shape for a wake-like axial velocity profile (as expected).

Figure 3.203 presents the evolution of $R_{\theta\theta}$ during this time period. At the $\theta = 45^o$ location the level of $R_{\theta\theta}$ in the interior of the vortex (close to the centerline) does not vary much as we go through this time period. There is an increase in the level as compared to the last time period though. In the region from about $r/r_0 = 1$ to $r/r_0 = 2$, the profile is fuller. At the $\theta = 135^o$, the main difference as compared to the last time period is an increase in the fullness of the profile.

Let us now take a look at how $R_{r\theta}$ evolves during this time period (see figure 3.204). The profiles at the two angular locations keep the shape they attained during the last time period. During the later stages of this time period, the magnitude at the centerline decreases. Also, as we go through this time period the small peak (positive at $\theta = 45^o$ and negative at $\theta = 135^o$) right outside the core radius is seen to change in value and position. The net change observed at the end of this time period is these peaks have moved outwards while increasing in value. This overall behavior of $R_{r\theta}$ during this time period reflects an outward movement of turbulence in the vortex.

Figure 3.205 shows the evolution of $R_{\theta z}$ in this time period. At the $\theta = 45^o$ location, the overall behavior observed is a dampening of the profile. Non zero values of $R_{\theta z}$ are observed for longer distances from the centerline though. At $\theta = 135^o$, we see rises and falls in the peak value. The peak position also shifts between being close to the centerline and being further out. However, $R_{\theta z}$ stays positive (except for some excursions into being negative very close to the centerline).

The evolution of $R_{zz}$ during this time period is presented in figure 3.206. At the $\theta = 45^o$ location, the profile shape essentially remains unchanged. We observe rises and falls in the levels. Also, significant levels of $R_{zz}$ are observed further out from the centerline as we go through this time period. The situation at the $\theta = 135^o$ locations is different though. The profile shape switches between two possibilities. One of these is the shape maintained by the profile all the way from the second time period to the end of the last time period. In the other shape, $R_{zz}$ increases in value as we move

away from the centerline, goes through a peak about halfway through the core and then decays rapidly again till we reach about the core radius.

Figure 3.207 shows the evolution of $R_{rz}$ during this time period. At the $\theta = 45^o$ location, we observe an oscillation of the profile about the $R_{rz} = 0$ axis. During the initial stages of this period, a change in the sign of $R_{rz}$ is observed all the way from the centerline to about 2 times the core radius. Later on, $R_{rz}$ starts with a near-zero value at the centerline and decreases in value till a small negative peak is reached. This trend gets well established and values beyond this small negative peak change sign repeatedly. Repeated changing of sign is also observed at the $\theta = 135^o$ location.

The evolution of $R_{rr}$ during this time period is presented in figure 3.208. At the $\theta = 45^o$ the profile shape changes as we go through this period. The centerline value drops while the peak moves outwards. At the $\theta = 135^o$ location, this change in the profile shape is not observed. $R_{rr}$ at this location still peaks at or near the centerline and decays as we move outwards. However this peak centerline value is higher than the last time period. We do observe small rises and falls in the centerline value as the GTKE grows through this time period.

Finally we look at the evolution of enstrophy during this final ascent of GTKE (figure 3.209). The principal observation is the spreading out of enstrophy at $\theta = 45^o$ and the containment of enstrophy at $\theta = 135^o$. The level does not increase much (we have observed variations over orders of magnitude before). At $\theta = 45^o$, the spreading out starts with the peak moving away from the centerline. Once the peak reaches to about the core radius, it drops in value. We don't really observe the presence of a definite peak after that - an almost uniform level is observed up till about $r/r_0 = 1.4$ The value then drops steeply. This seems to correspond well with how much of the vortex is turbulent.

#### 3.7.3.7 Seventh Time Period

As we move into this time period, the GTKE is still increasing in value. Most of the vortex is now turbulent (see figure 3.210). As we approach the sixth peak of

GTKE, the TKE peak shows a sudden increase and moves away from the center. It however returns to the centerline and falls in value again. Note that we now have a significant level of turbulence near the boundary of the domain. This reflects the fact that the computational domain size is now no longer large enough to give meaningful results.

The diffusion of the mean tangential velocity is very rapid in this last period (see figure 3.211). As always we are looking at the $V_\theta$ profiles at a series of different times during this period. At the $\theta = 45^o$ location, the variations in the profile, say in terms of where the peak is located, from one such plotting time to the next is substantial. This could be a reflection of the limitation is sampling space while computing the mean quantities. Or maybe there is the presence of anti-diffusion. That has to be checked by computing the eddy viscosity. The $\theta = 135^o$ location does not show such substantial oscillations. The process of diffusion seems to continue in a rather smooth way. At the end of this time period, the peak has moved far out towards the boundary and has dropped significantly in value. The peak value is now about 0.2 compared to about 0.7 at the beginning of the simulation. We observe a significant amount of diffusion in the axial velocity profile also (see figure 3.212). At the end of this time period, the wake has all but dissapeared.

The noisiness of the mean axial vorticity profiles (see figure 3.213), due to limitations in the sampling space, make it difficult to see how the profile changes from one plotting time to the next. However it can be seen that areas of the vortex close to the boundary are also beginning to have non-zero values. This corresponds well with the extensive diffusion of mean tangential velocity. Non zero values of mean tangential vorticity (see figure 3.214) near the boundary can also be observed. We also see that $\Omega_\theta$ has reduced significantly in value (since the wake like axial flow is all but gone). Non zero values of mean vorticity near the boundary is further indication that the simulation has to be stopped. We would need a bigger computational domain to be able to continue having meaningful simulation results.

Figure 3.215 shows the evolution of $R_{\theta\theta}$ during this time period. The main difference from the last time period is the increased fullness of the profiles at both the angular locations. As has been the case throughout this simulation, the spread of $R_{\theta\theta}$ is further out the $\theta = 45^o$ location. In fact towards the end of this time period, we find a substantial level of $R_\theta\theta$ close to the boundary at this angular location.

Let us now take a look at the evolution of $R_{r\theta}$ during this time period (see figure 3.216). The profile shape observed during the last two periods is maintained. The trend of $R_{r\theta}$ decreasing in magnitude in the inner regions of the vortex while spreading further out and increasing in level in the outer regions continues through this time period. At the $\theta = 45^o$ location, a substantial level $R_{r\theta}$ is observed near the boundary at the end of this time period.

Figure 3.217 shows the evolution of $R_{\theta z}$ during this time period. At the $\theta = 45^o$ location, no particular pattern is observed. The profile has a noisy/oscillatory character. The main observation is that significant levels are observed near the boundary as we approach the end of this time period. The situation at the $\theta = 135^o$ location is similar. The main difference observed is that $R_{\theta z}$ is contained closer to the centerline.

The evolution of $R_{zz}$ in this final time period is presented in figure 3.218. At the $\theta = 45^o$ location, the profile has departed from the shape it had maintained for the last 5 time periods. Instead of seeing a peak at or near the centerline followed by a decay as we move outwards, we now see a nearly uniform level till about twice the core radius. The value then decays as we move further out. Note that we have significant levels near the boundary. At $\theta = 135^o$, instead of the level being approximately uniform as we move away from the centerline, we observe an increase. The level goes through a peak and then decays again. The location of this peak shifts between being just inside the core and being outside the core. Also, there are instances of multiple peaks. The distance from the centerline till which a significant level of $R_{zz}$ is observed is lesser at this location as compared to the $\theta = 45^o$ location.

Figure 3.219 shows the evolution of $R_{rz}$ during this time period. The main observation is the presence of significant levels of $R_{rz}$ in regions further away from the

Table 3.1 Case parameters for the strained vortex (Qin(1998))

| Case | $r_0/R$ | $e/e^*$ | $\beta^*$ | $Re_\Gamma$ | $l^*/r_0$ | Axial flow | Domain size |
|---|---|---|---|---|---|---|---|
| STRN1 | 0.125 | 0.8967 | 0.0281 | 19268 | 0.942 | wake | $R = 8.0r_0$ |
| STRN2 | 0.15 | 0.8967 | 0.0404 | 29428 | 0.635 | wake | $R = 6.67r_0$ |
| STRN3 | 0.15 | 0.8967 | 0.0404 | 29428 | 0.635 | none | $R = 6.67r_0$ |
| STRN4 | 0.15 | 0.8967 | 0.0404 | 58836 | 0.449 | none | $R = 6.67r_0$ |

centerline. This spreading of $R_{rz}$ extends further out at the $\theta = 45^o$ location. The values are predominantly negative. There are occurances of changes in the sign.

The evolution of $R_{rr}$ during this time period is presented in figure 3.220. At $\theta = 45^o$ the outward spreading of $R_{rr}$ that started in the last time period continues. No adherence to any particular profile shape is observed. Note that a significant level of $R_{rr}$ is now present close to the boundary. At the $\theta = 135^o$ location, the general profile shape still has a peak at or near the centerline. $R_{rr}$ then decays as we move outwards. However, the profiles have become much fuller in this time period. The outward spread of $R_{rr}$ corresponds well with outer regions of the vortex becoming more turbulent.

The level of enstrophy does not vary much during this time period (see figure 3.221). At the $\theta = 45^o$ location, we are seeing a substantial level of enstrophy near the boundary. This is of course in conflict with our use of potential flow boundary conditions.

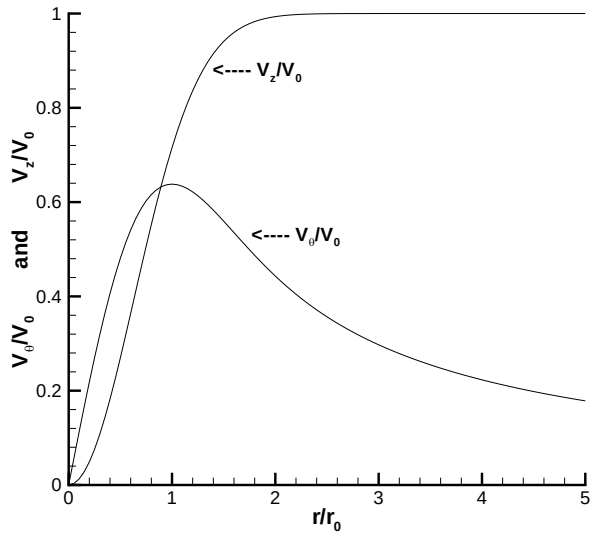


Figure 3.1 The initial mean velocity profiles

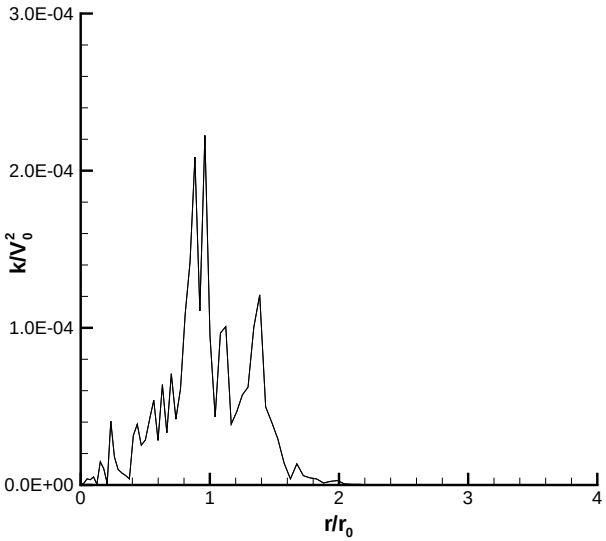


Figure 3.2 A typical initial TKE profile at an arbitrary azimuthal location

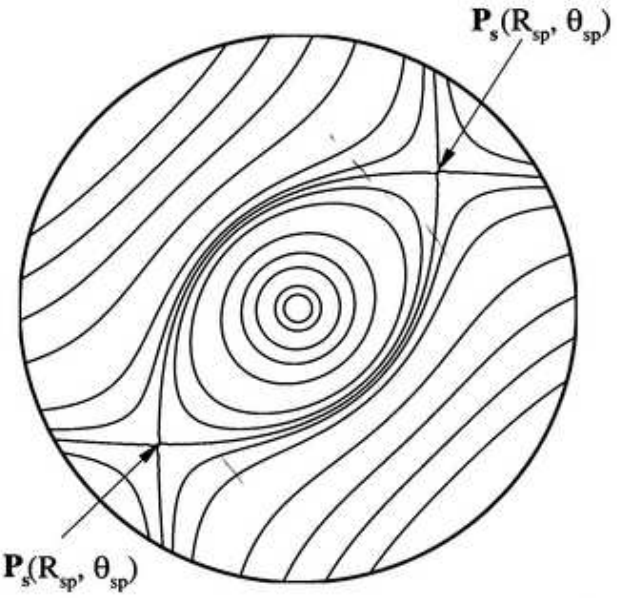


Figure 3.3 Streamlines for a strained vortex - cross-sectional view (Qin (1998))

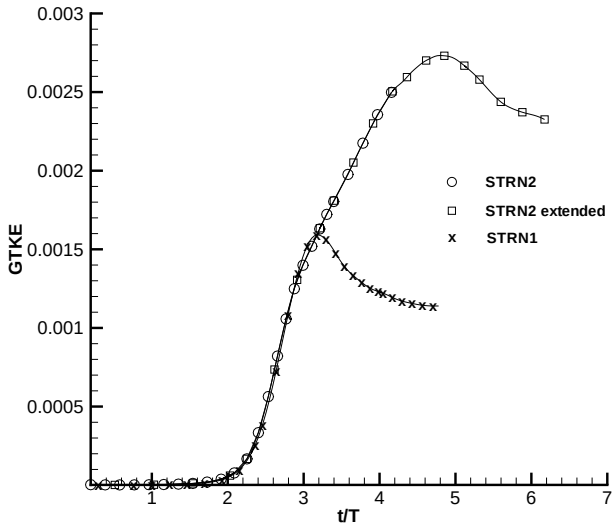


Figure 3.4 Global turbulent kinetic energy history for STRN 2 by Qin(1998) extended in time

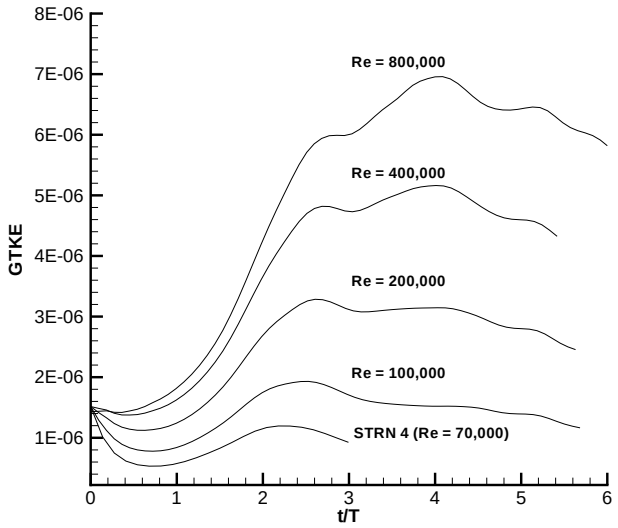


Figure 3.5 Global turbulent kinetic energy history for a strained vortex without axial flow at higher Reynolds numbers

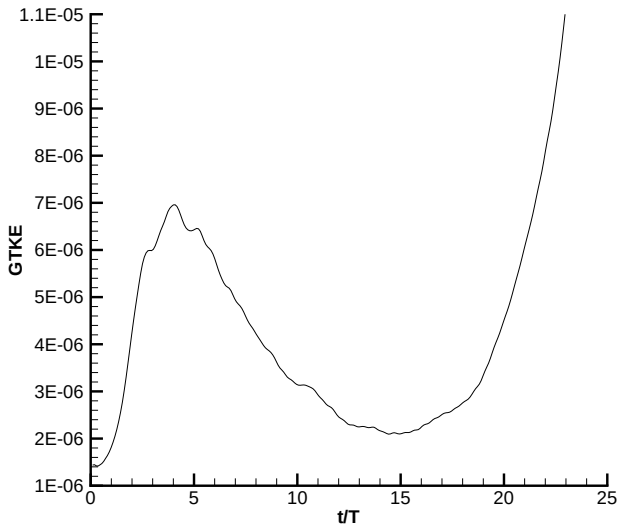


Figure 3.6 Global turbulent kinetic energy history for a strained vortex without axial flow at Re = 800,000 extended in time

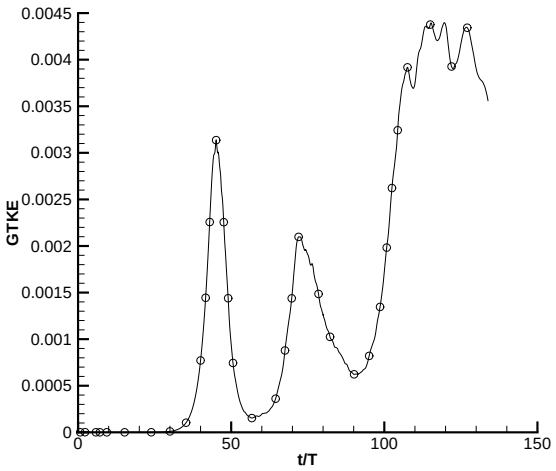


(a)

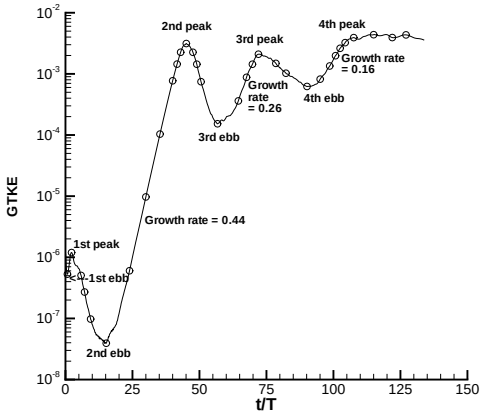


(b)

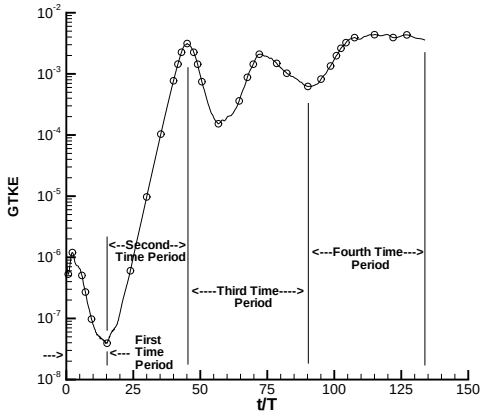


(c)

Figure 3.7 Global turbulent kinetic energy history for STRN4 extended in time; (a) linear scale; (b) log scale; (c) defining periods

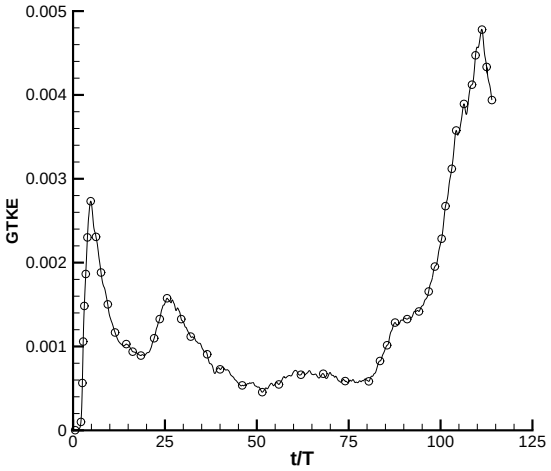


(a)

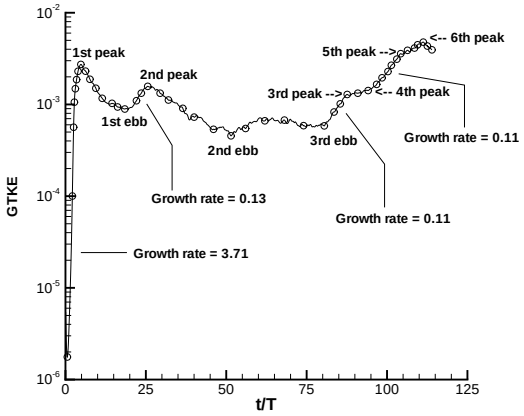


(b)

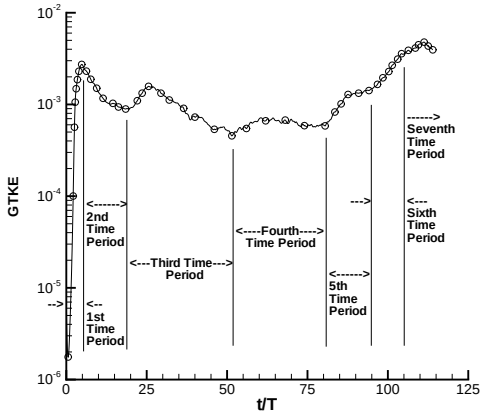


(c)

Figure 3.8 Global turbulent kinetic energy history for STRN2 extended in time; (a) linear scale; (b) log scale; (c) defining periods

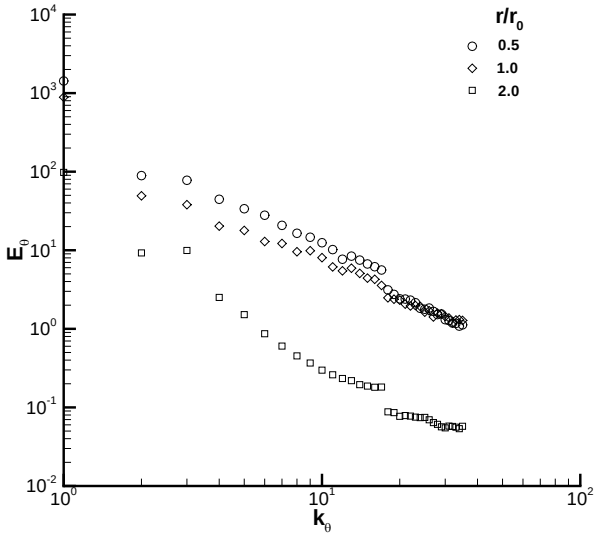


Figure 3.9 1-D energy spectra for STRN4 at t/T = 45.12

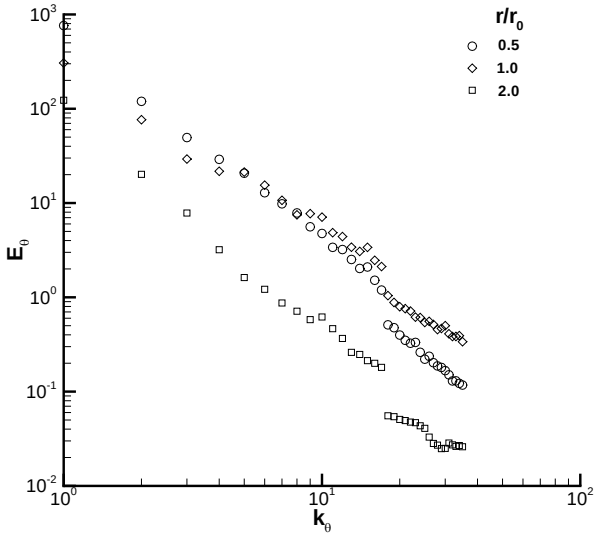


Figure 3.10 1-D energy spectra for STRN4 at t/T = 72.01

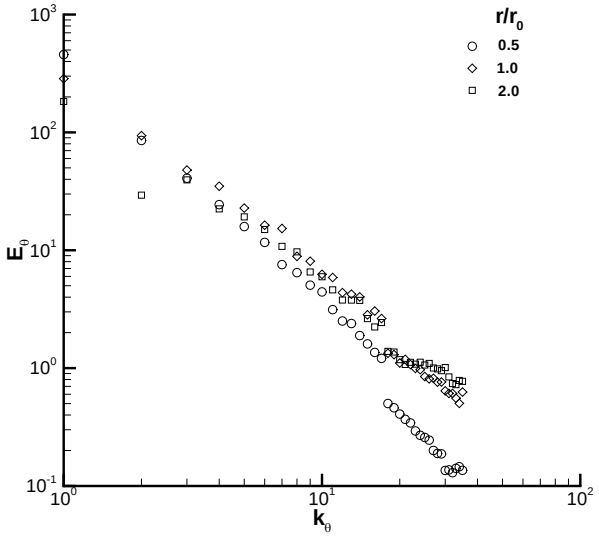


Figure 3.11 1-D energy spectra for STRN4 at t/T = 107.57

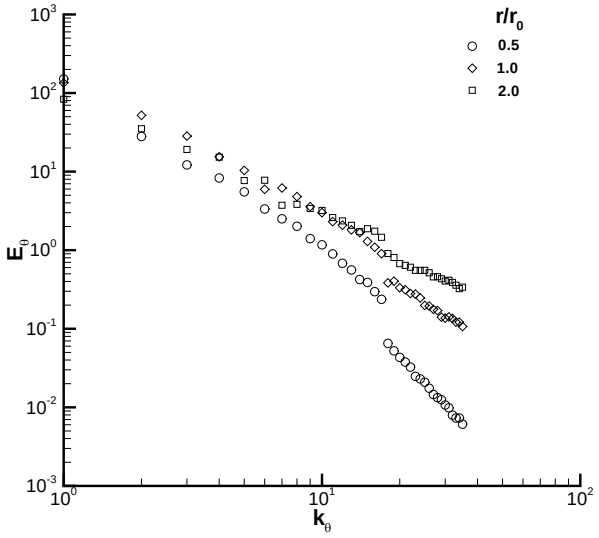


Figure 3.12 1-D energy spectra for STRN4 at t/T = 127.08

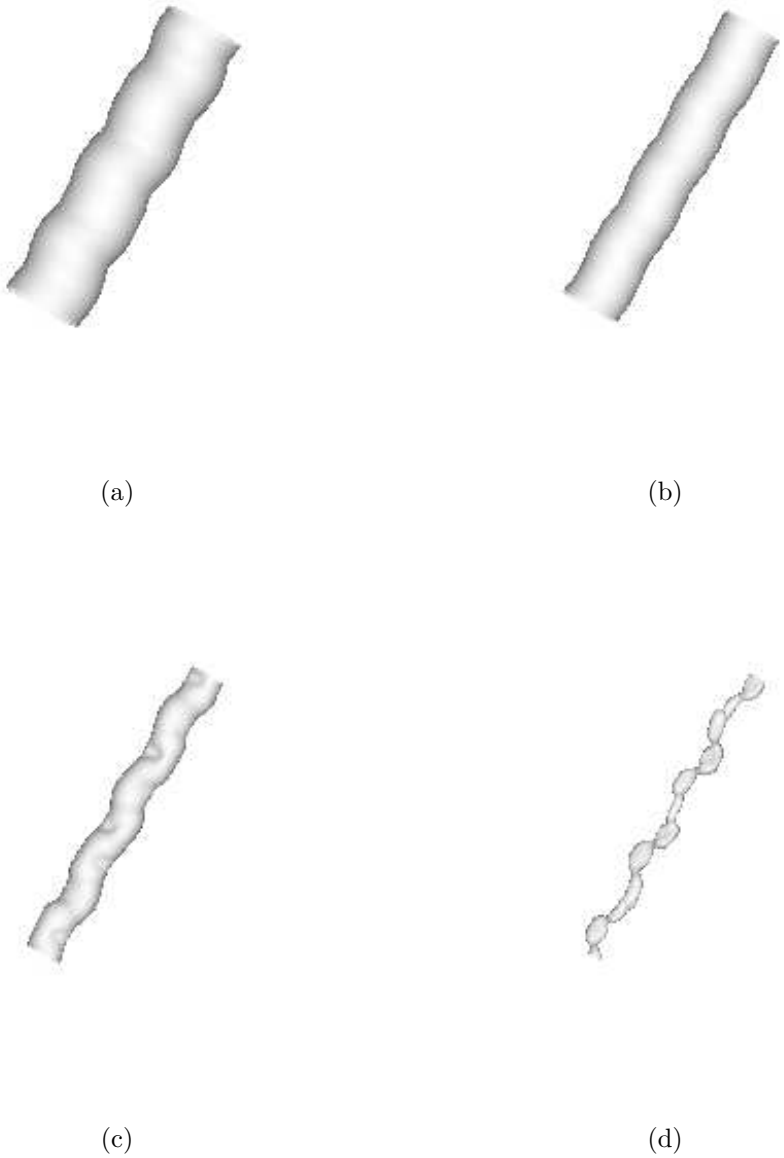

(a) (b)

(c) (d)

Figure 3.13 Vorticity magnitude isosurfaces for STRN4 at t/T = 35.27; (a), (b), (c) and (d) correspond to 0.1, 0.25, 0.5 and 0.75 times the peak vorticity magnitude respectively

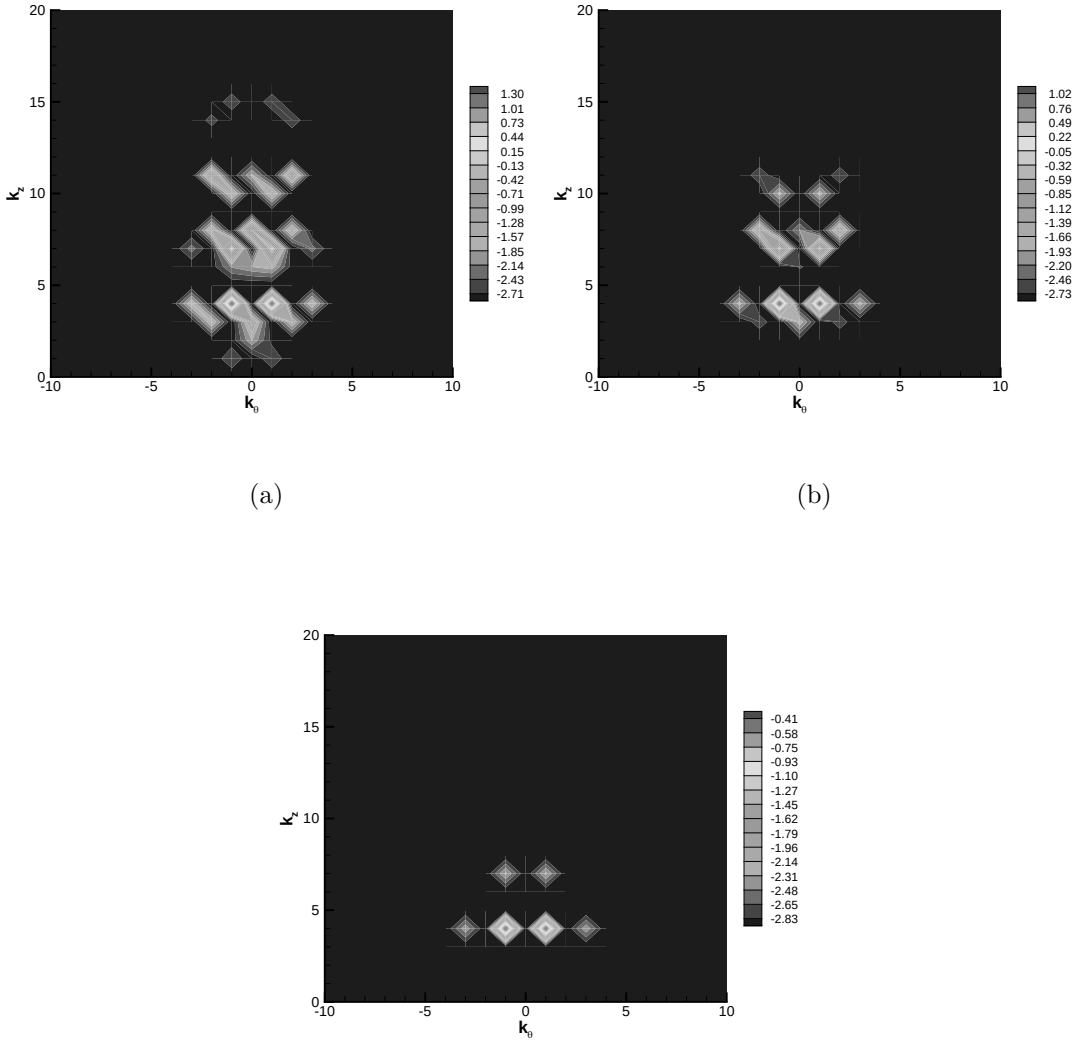


(a) (b)

(c)

Figure 3.14 2-D Energy spectra for STRN4 at $t/T = 35.27$; Contours of $log_{10}(E_{2D})$; (a), (b) and (c) correspond to $r/r_0 = 0.5$, 1.0 and 2.0 respectively

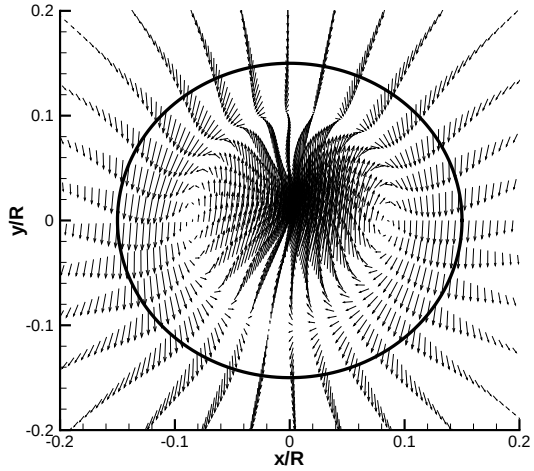


(a)

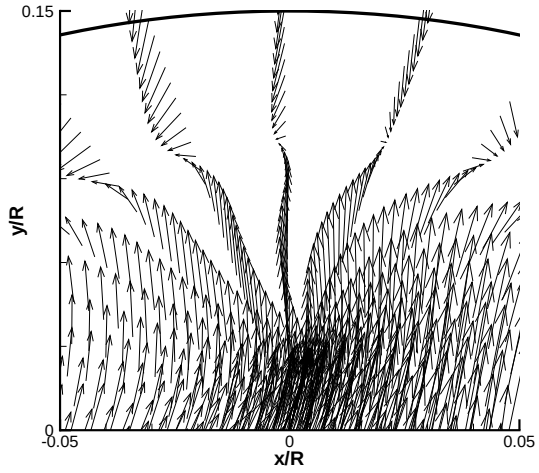


(b)

Figure 3.15 (a) Perturbation velocity vectors in a cross-sectional plane at $t/T = 35.27$, (b) Zoomed view

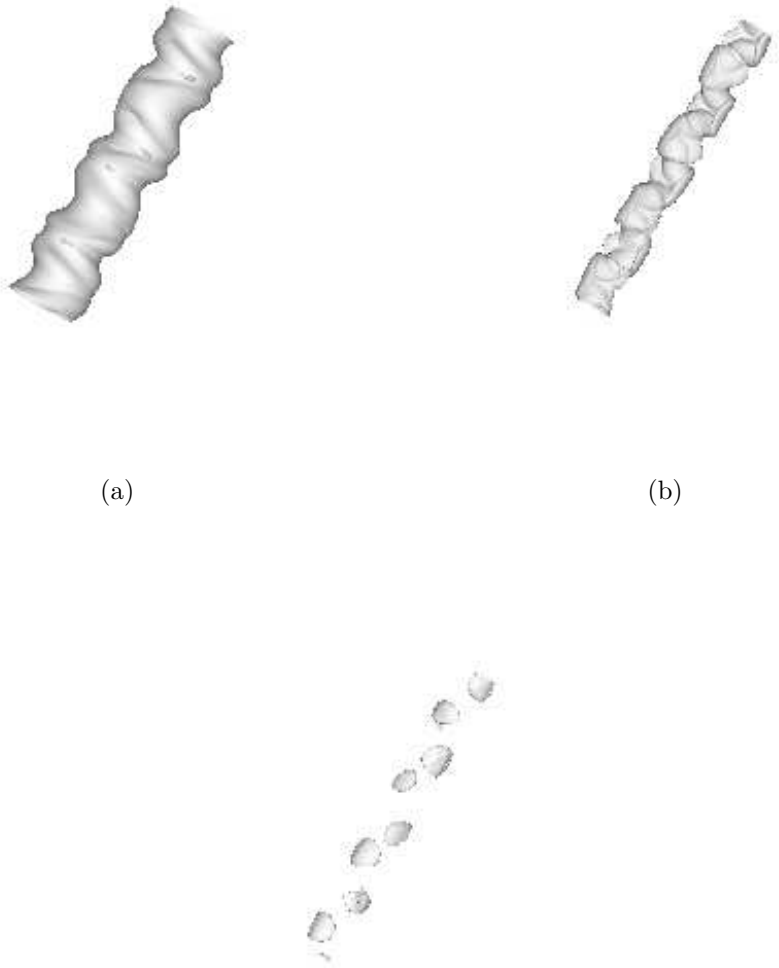

(a) (b)

(c)

Figure 3.16 Vorticity magnitude isosurfaces for STRN4 at t/T = 40; (a), (b), and (c) correspond to 0.1, 0.25 and 0.5 times the peak vorticity magnitude respectively

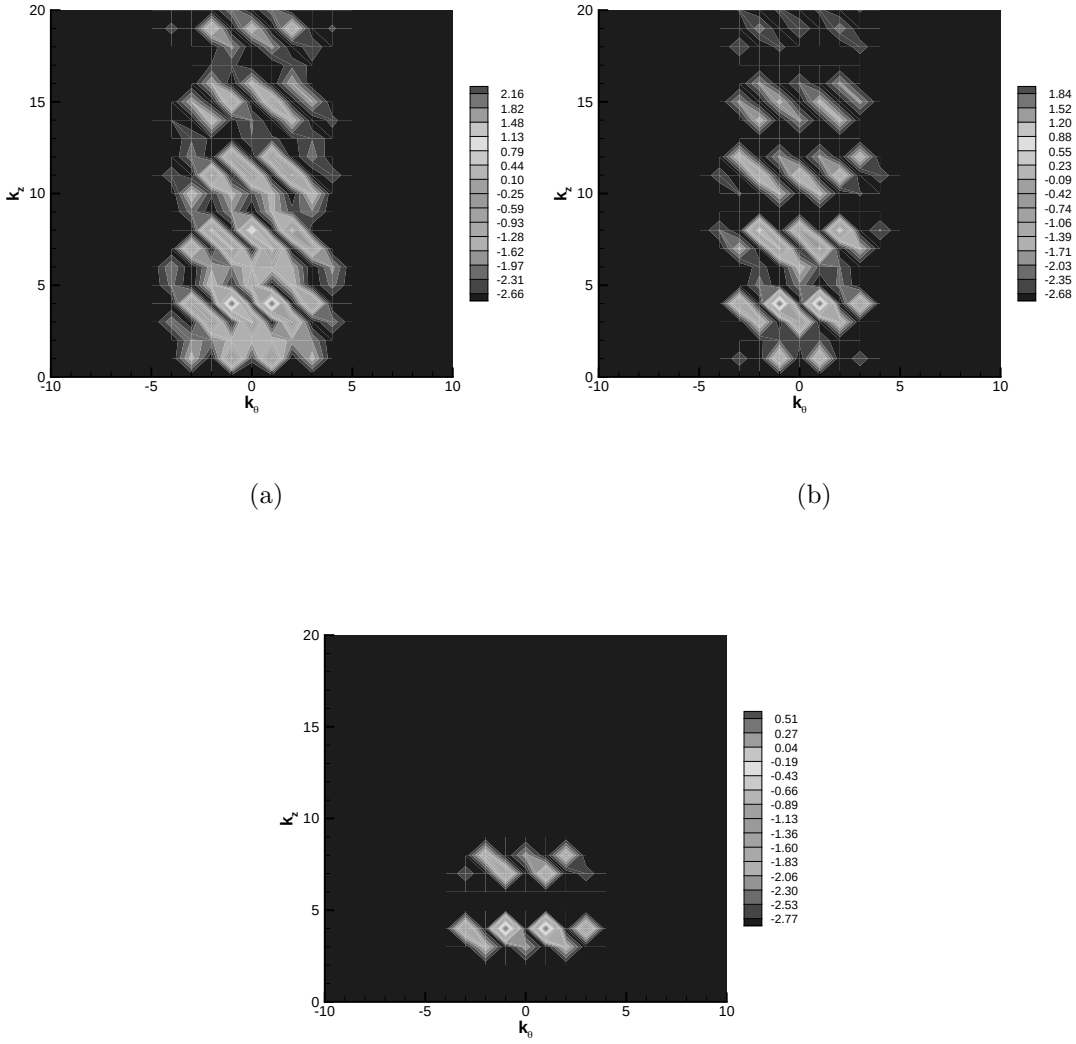


(a) (b)

(c)

Figure 3.17 2-D Energy spectra for STRN4 at $t/T = 40$; Contours of $log_{10}(E_{2D})$; (a), (b) and (c) correspond to $r/r_0 = 0.5$, 1.0 and 2.0 respectively

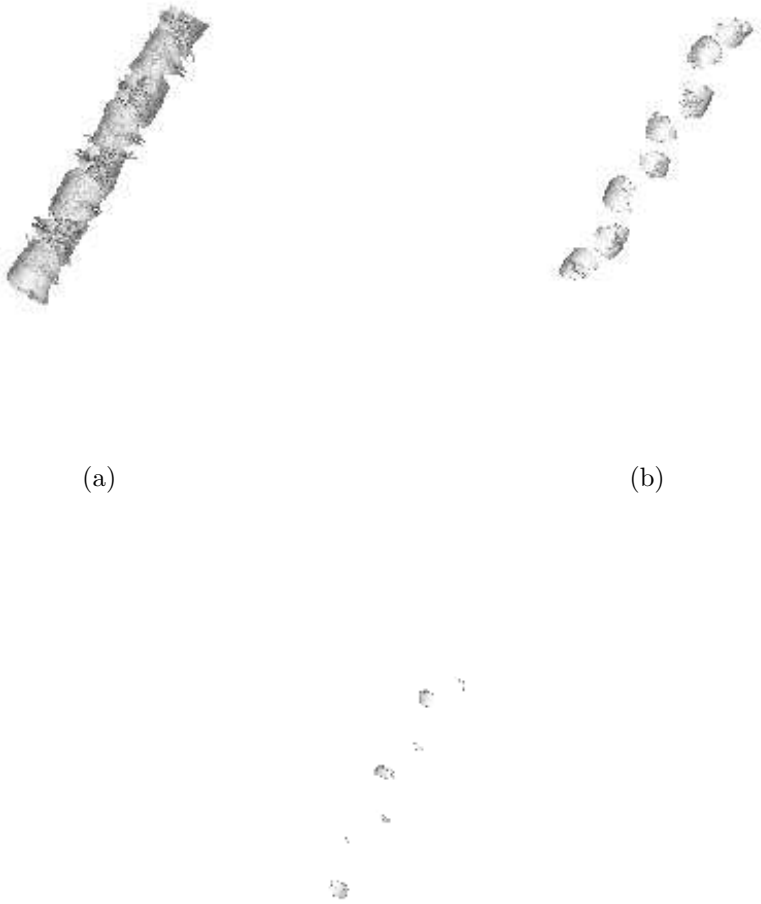

(a) (b)

(c)

Figure 3.18 Vorticity magnitude isosurfaces for STRN4 at t/T = 42.98; (a), (b), and (c) correspond to 0.1, 0.25, and 0.5 times the peak vorticity magnitude respectively

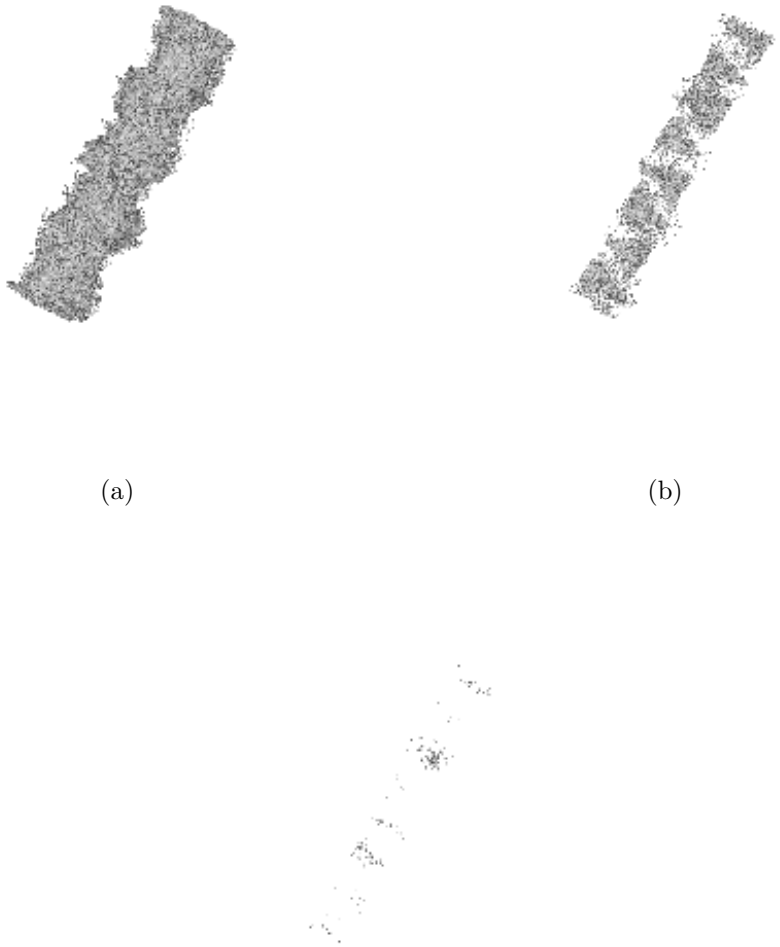

(a) (b)

(c)

Figure 3.19 Vorticity magnitude isosurfaces for STRN4 at t/T = 45.12; (a), (b), and (c) correspond to 0.1, 0.25, and 0.5 times the peak vorticity magnitude respectively

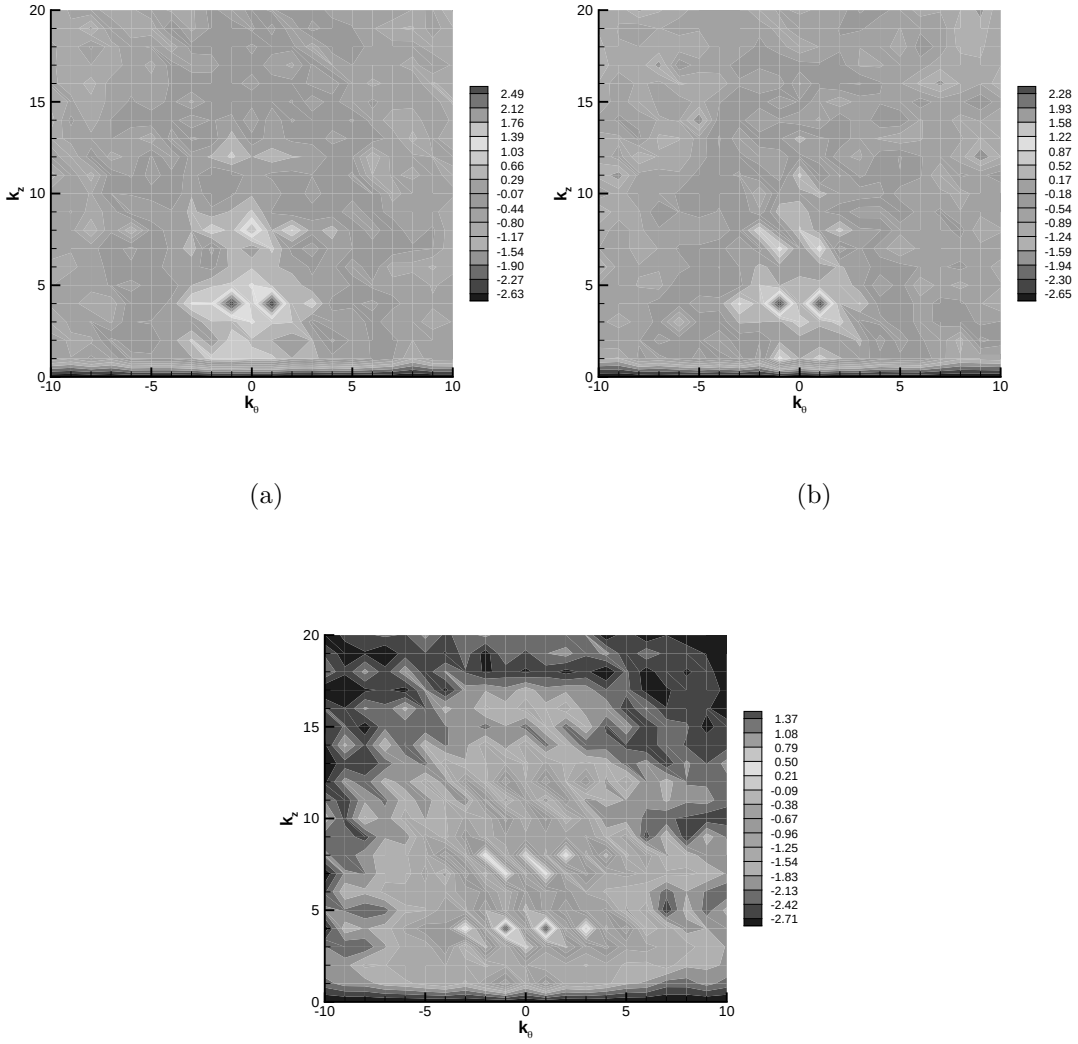


(a) (b)

(c)

Figure 3.20 2-D Energy spectra for STRN4 at $t/T = 45.12$; Contours of $log_{10}(E_{2D})$; (a), (b) and (c) correspond to $r/r_0 = 0.5$, 1.0 and 2.0 respectively

(a) (b)

(c)

Figure 3.21 Vorticity magnitude isosurfaces for STRN4 at t/T = 49.01; (a), (b), and (c) correspond to 0.1, 0.25, 0.5 times the peak vorticity magnitude respectively

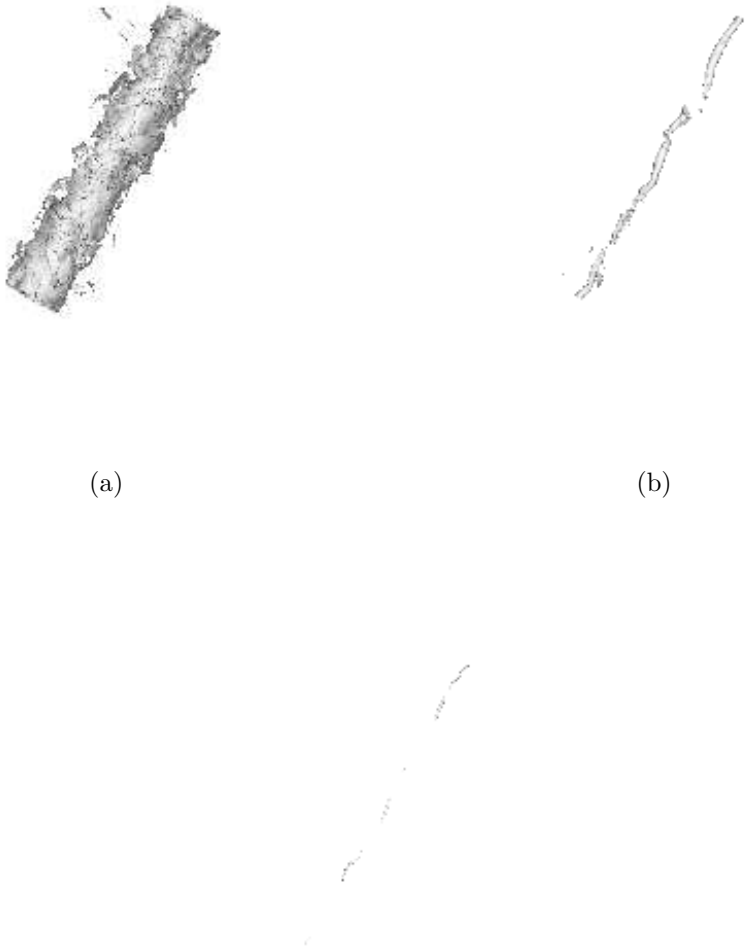

(a) (b)

(c)

Figure 3.22 Vorticity magnitude isosurfaces for STRN4 at t/T = 56.83; (a), (b), and (c) correspond to 0.1, 0.25, and 0.5 times the peak vorticity magnitude respectively

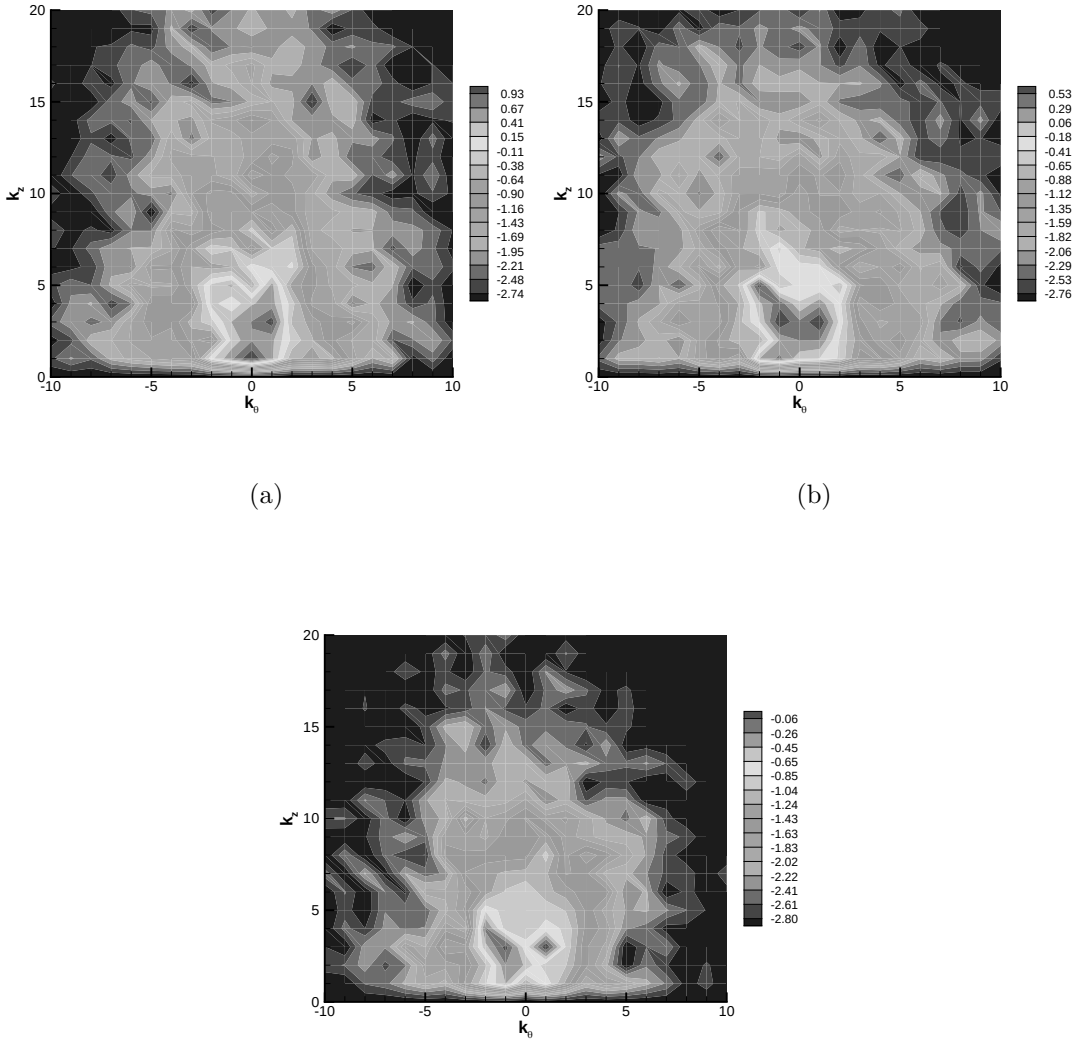


(a) (b)

(c)

Figure 3.23 2-D Energy spectra for STRN4 at $t/T = 56.83$; Contours of $log_{10}(E_{2D})$; (a), (b) and (c) correspond to $r/r_0 = 0.5$, 1.0 and 2.0 respectively

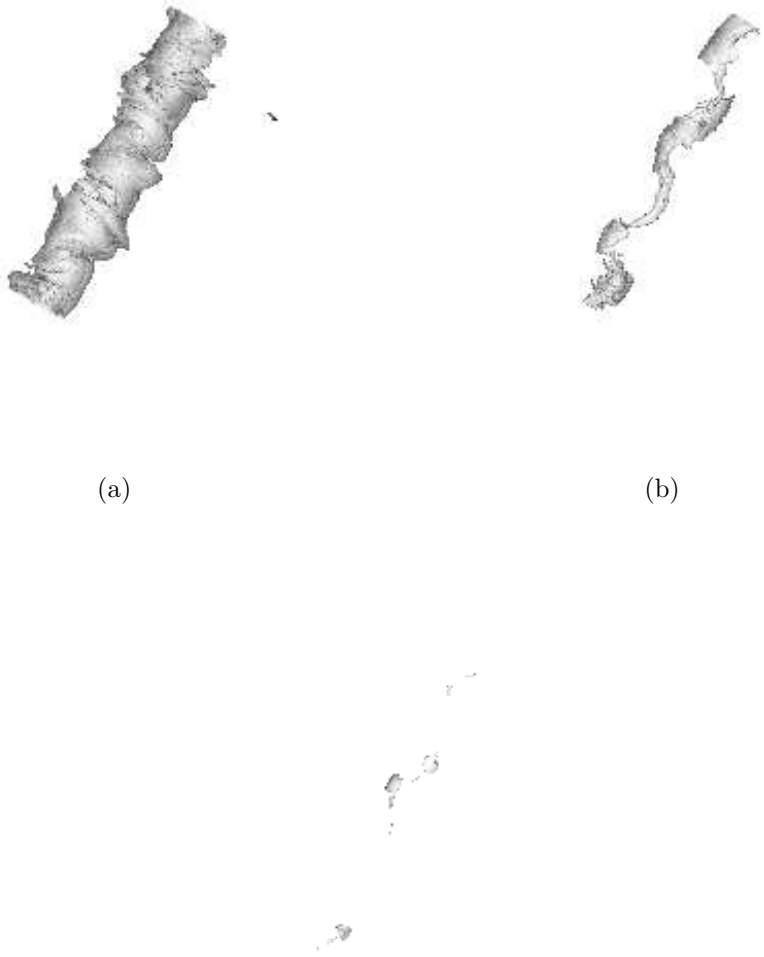

(a) (b)

(c)

Figure 3.24 Vorticity magnitude isosurfaces for STRN4 at t/T = 67.56; (a), (b), and (c) correspond to 0.1, 0.25, and 0.5 times the peak vorticity magnitude respectively

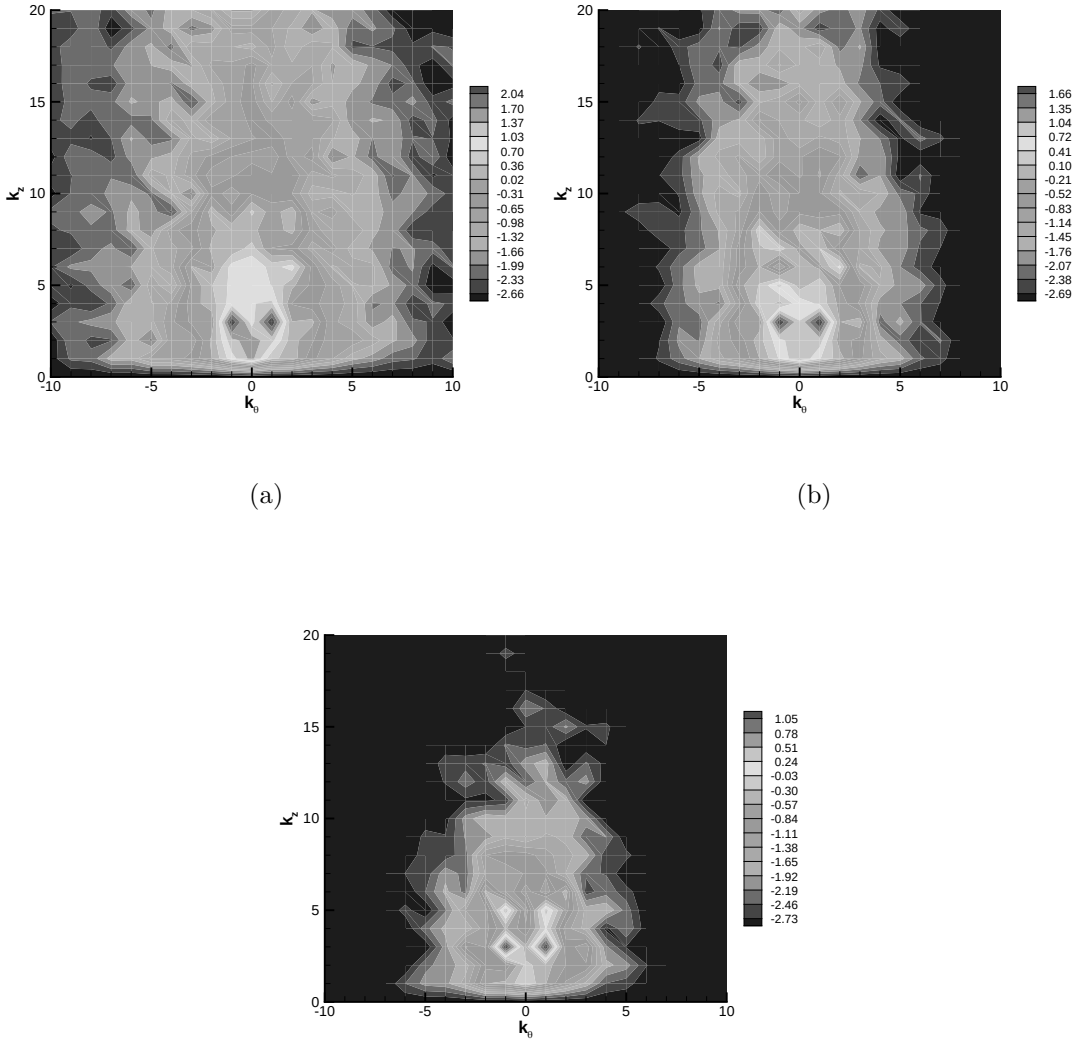


(a) (b)

(c)

Figure 3.25 2-D Energy spectra for STRN4 at $t/T = 67.56$; Contours of $log_{10}(E_{2D})$; (a), (b) and (c) correspond to $r/r_0 = 0.5$, 1.0 and 2.0 respectively

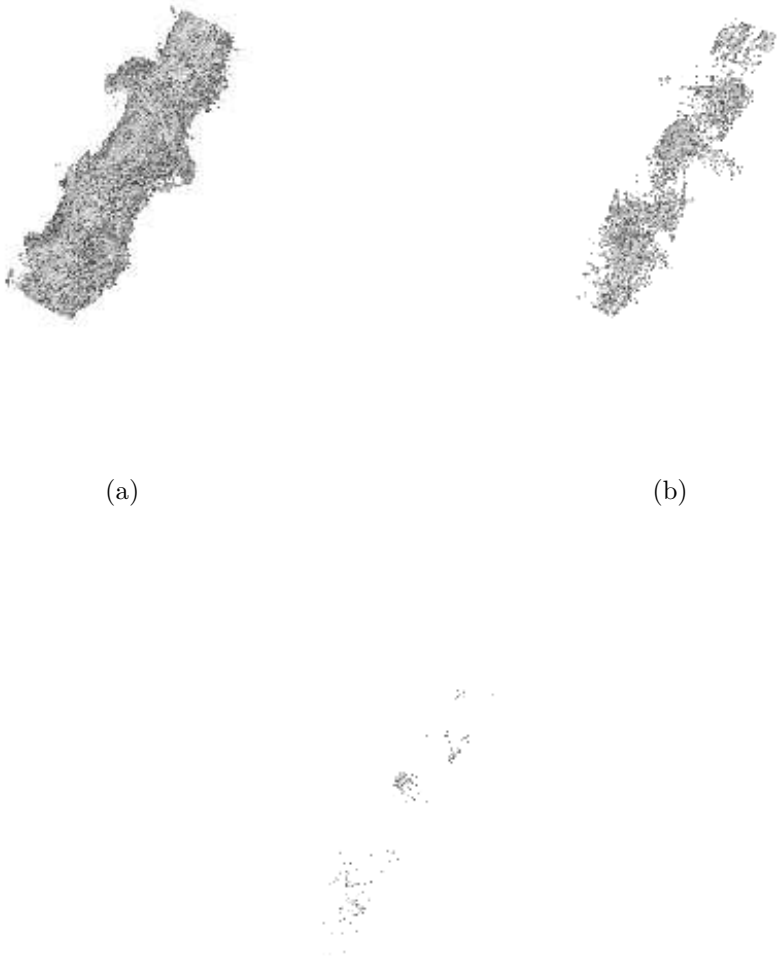

(a) (b)

(c)

Figure 3.26 Vorticity magnitude isosurfaces for STRN4 at t/T = 72.01; (a), (b), and (c) correspond to 0.1, 0.25, and 0.5 times the peak vorticity magnitude respectively

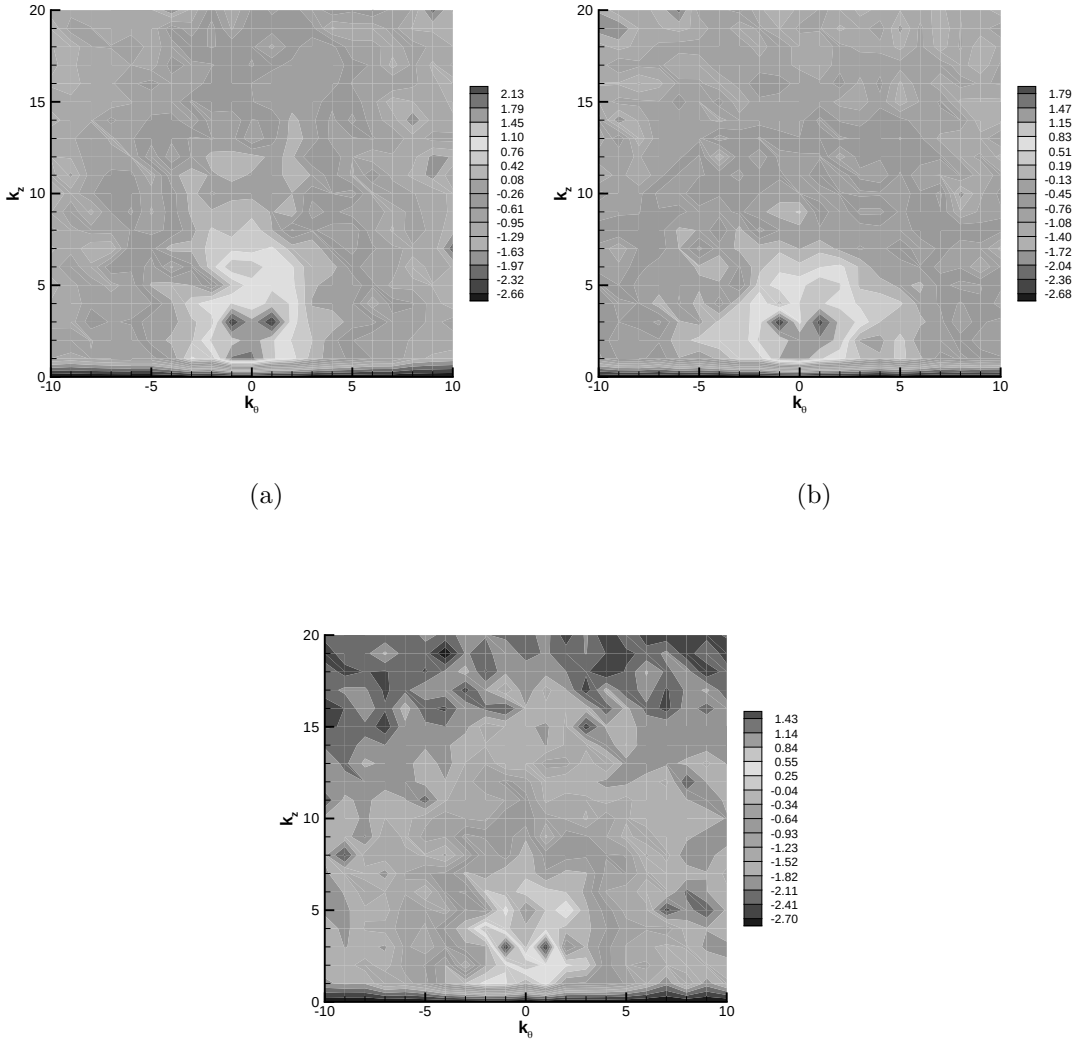


(a) (b)

(c)

Figure 3.27 2-D Energy spectra for STRN4 at $t/T = 72.01$; Contours of $log_{10}(E_{2D})$; (a), (b) and (c) correspond to $r/r_0 = 0.5$, 1.0 and 2.0 respectively

(a) (b)

(c)

Figure 3.28 Vorticity magnitude isosurfaces for STRN4 at t/T = 78.51; (a), (b), and (c) correspond to 0.1, 0.25, and 0.5 times the peak vorticity magnitude respectively

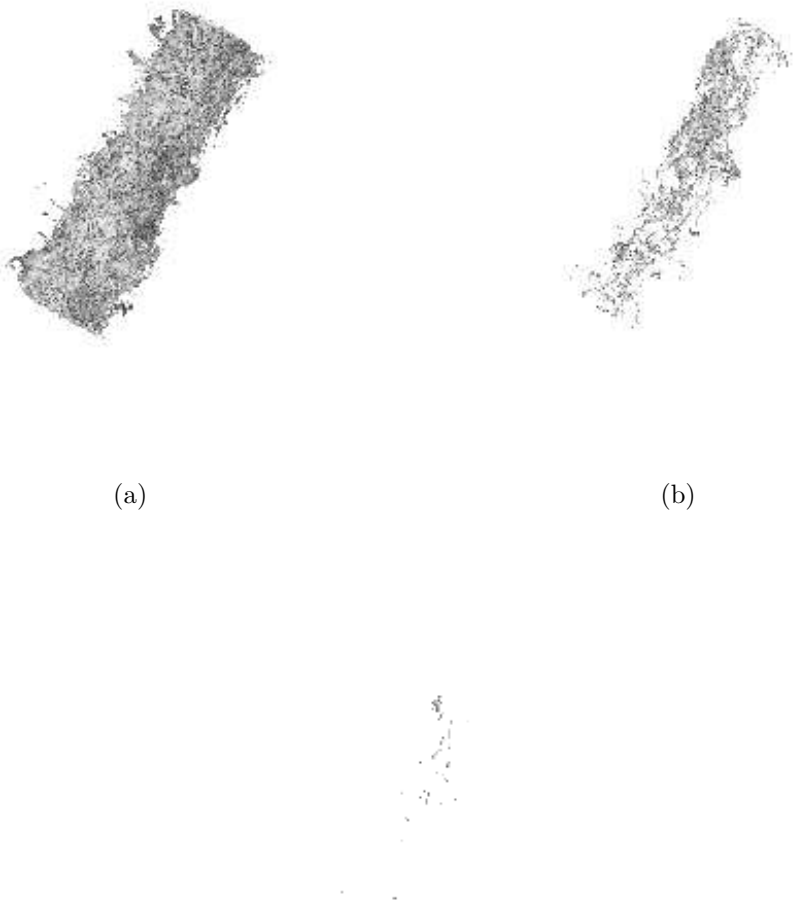

(a) (b)

(c)

Figure 3.29 Vorticity magnitude isosurfaces for STRN4 at t/T = 90.14; (a), (b), and (c) correspond to 0.1, 0.25, and 0.5 times the peak vorticity magnitude respectively

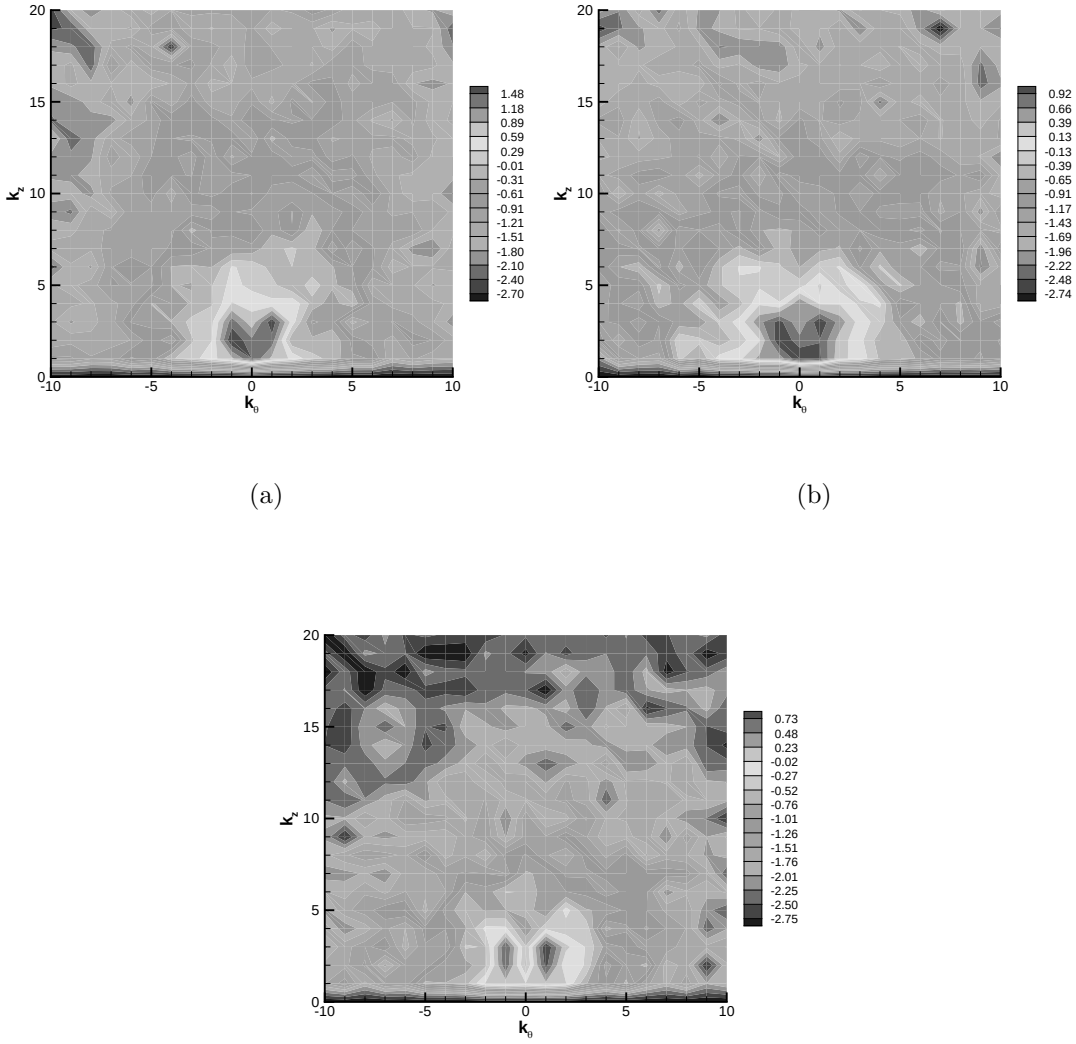


(a) (b)

(c)

Figure 3.30 2-D Energy spectra for STRN4 at $t/T = 90.14$; Contours of $log_{10}(E_{2D})$; (a), (b) and (c) correspond to $r/r_0 = 0.5$, 1.0 and 2.0 respectively

(a) (b)

(c)

Figure 3.31 Vorticity magnitude isosurfaces for STRN4 at t/T = 100.78; (a), (b), and (c) correspond to 0.1, 0.25, and 0.5 times the peak vorticity magnitude respectively

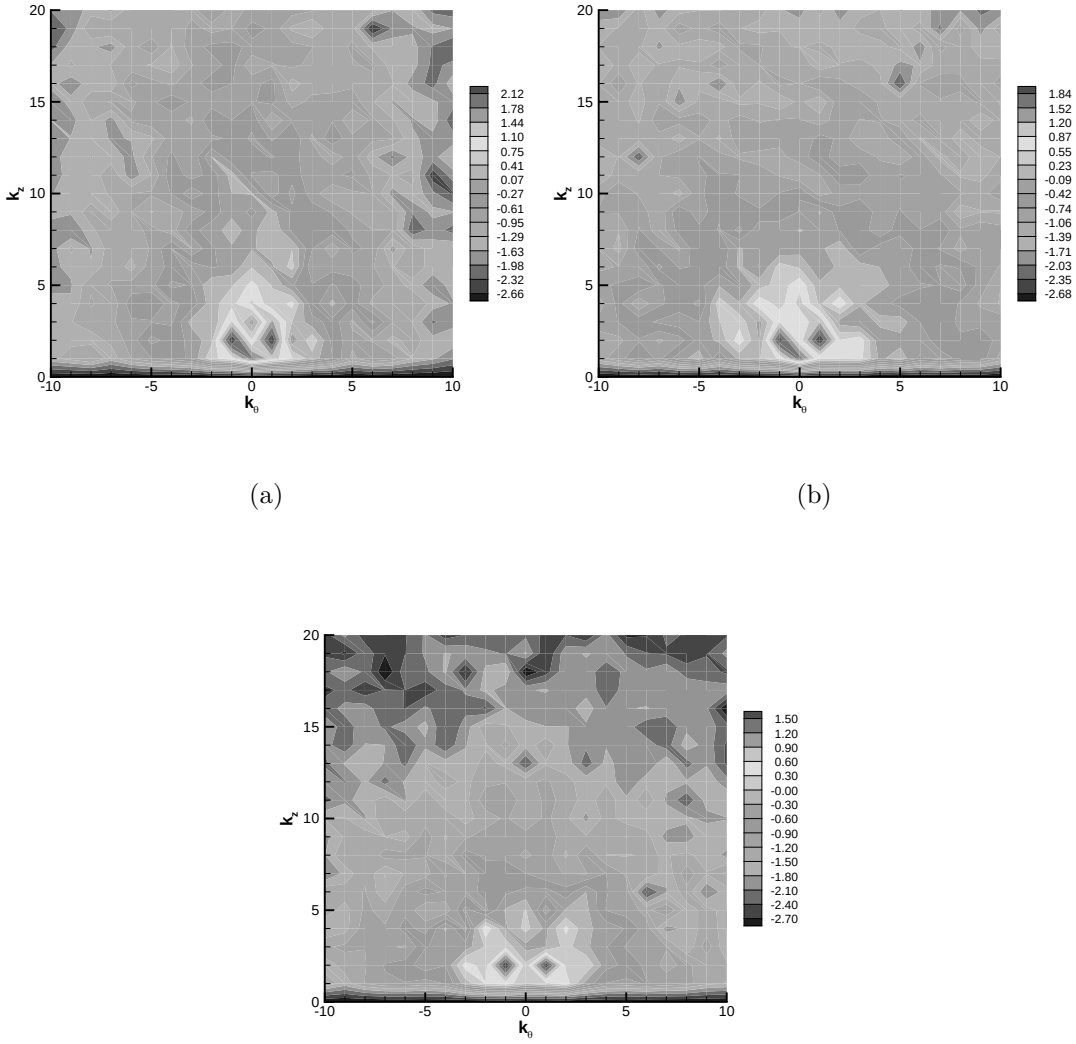


(a) (b)

(c)

Figure 3.32 2-D Energy spectra for STRN4 at $t/T = 100.78$; Contours of $log_{10}(E_{2D})$; (a), (b) and (c) correspond to $r/r_0 = 0.5$, 1.0 and 2.0 respectively

(a) (b)

(c)

Figure 3.33 Vorticity magnitude isosurfaces for STRN4 at t/T = 104.37; (a), (b), and (c) correspond to 0.1, 0.25, and 0.5 times the peak vorticity magnitude respectively

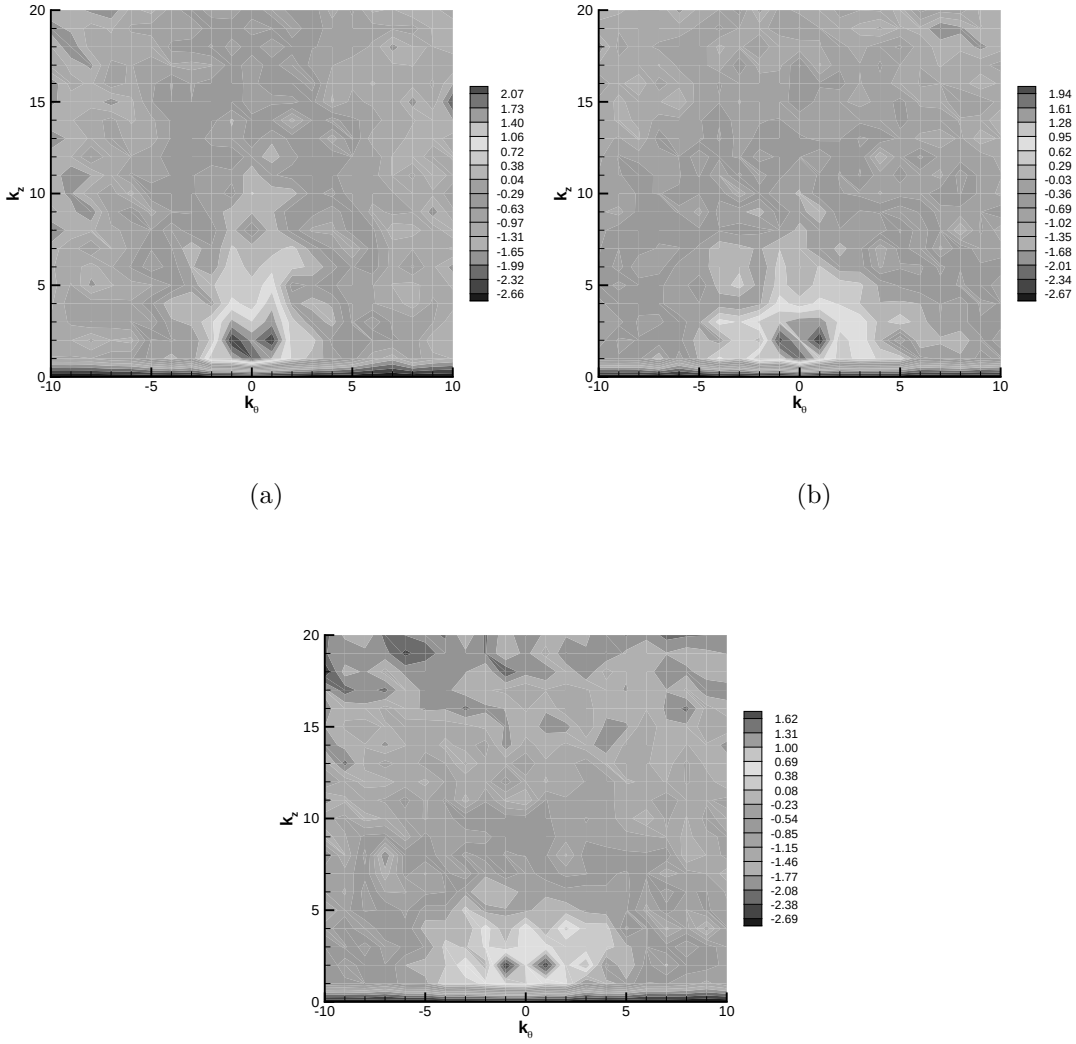


(a) (b)

(c)

Figure 3.34 2-D Energy spectra for STRN4 at $t/T = 104.37$; Contours of $log_{10}(E_{2D})$; (a), (b) and (c) correspond to $r/r_0 = 0.5$, 1.0 and 2.0 respectively

(a) (b)

(c)

Figure 3.35 Vorticity magnitude isosurfaces for STRN4 at t/T = 107.57; (a), (b), and (c) correspond to 0.1, 0.25, and 0.5 times the peak vorticity magnitude respectively

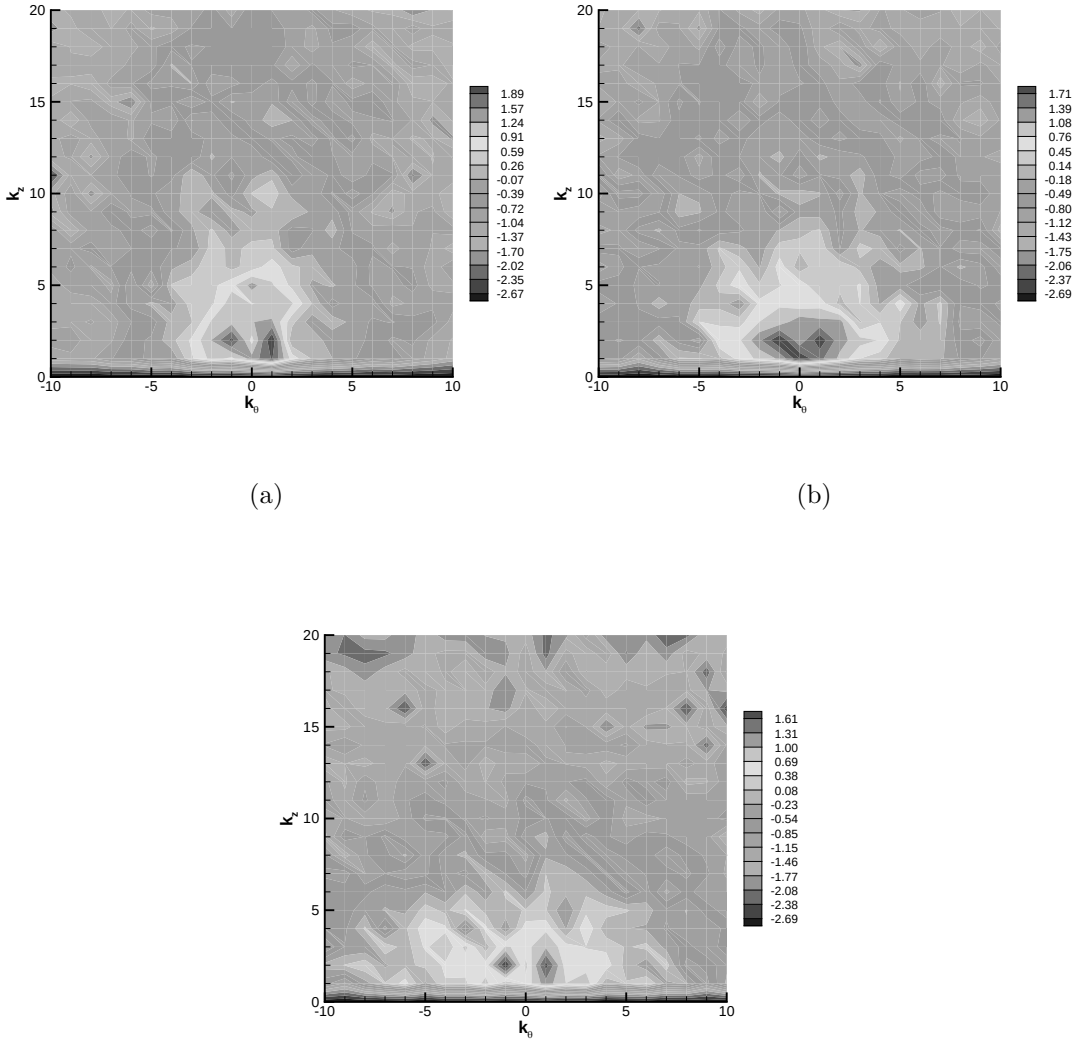


(a) (b)

(c)

Figure 3.36 2-D Energy spectra for STRN4 at $t/T = 107.57$; Contours of $log_{10}(E_{2D})$; (a), (b) and (c) correspond to $r/r_0 = 0.5$, 1.0 and 2.0 respectively

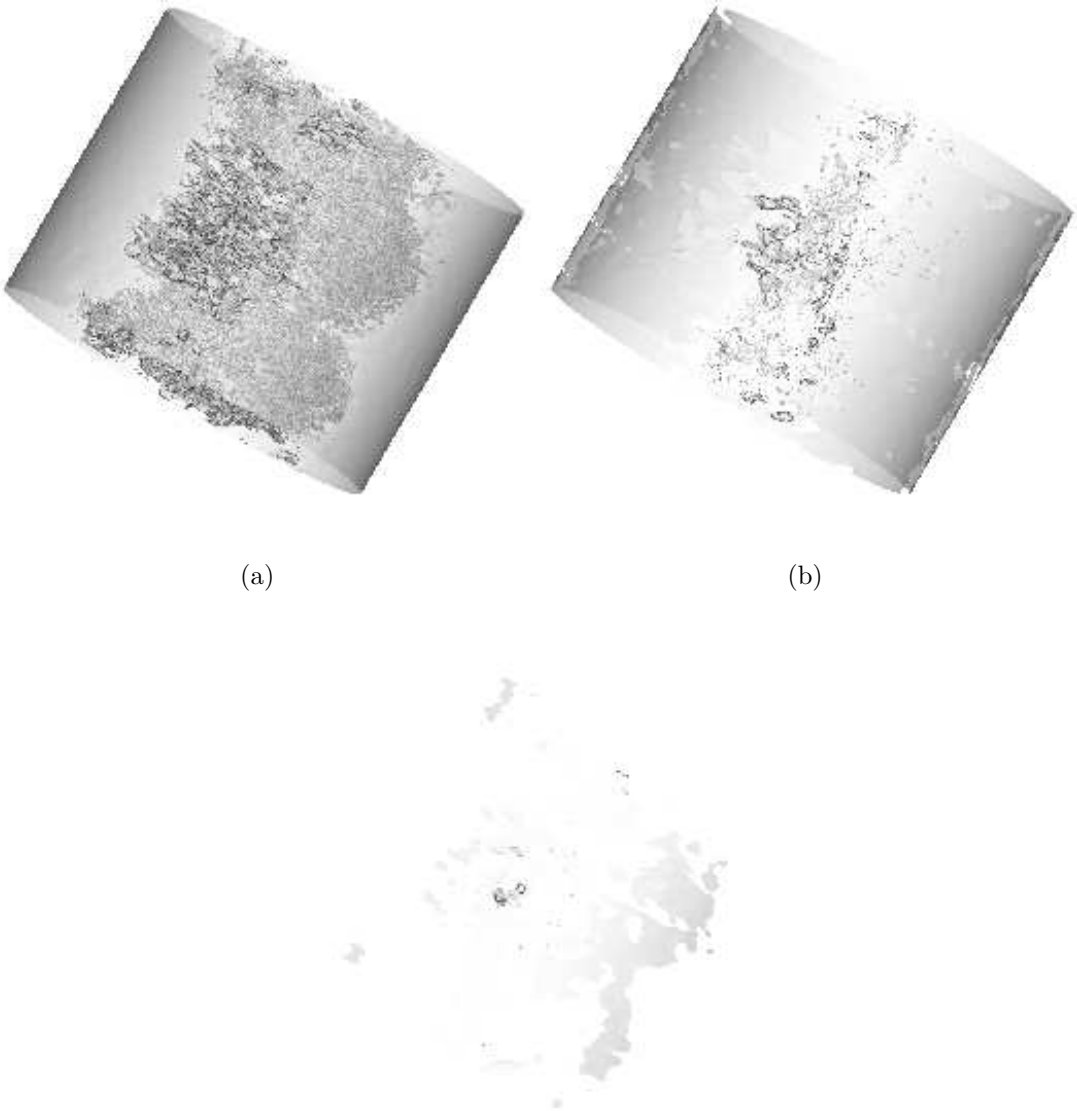

(a) (b)

(c)

Figure 3.37 Vorticity magnitude isosurfaces for STRN4 at t/T = 127.08; (a), (b), and (c) correspond to 0.1, 0.25, and 0.5 times the peak vorticity magnitude respectively

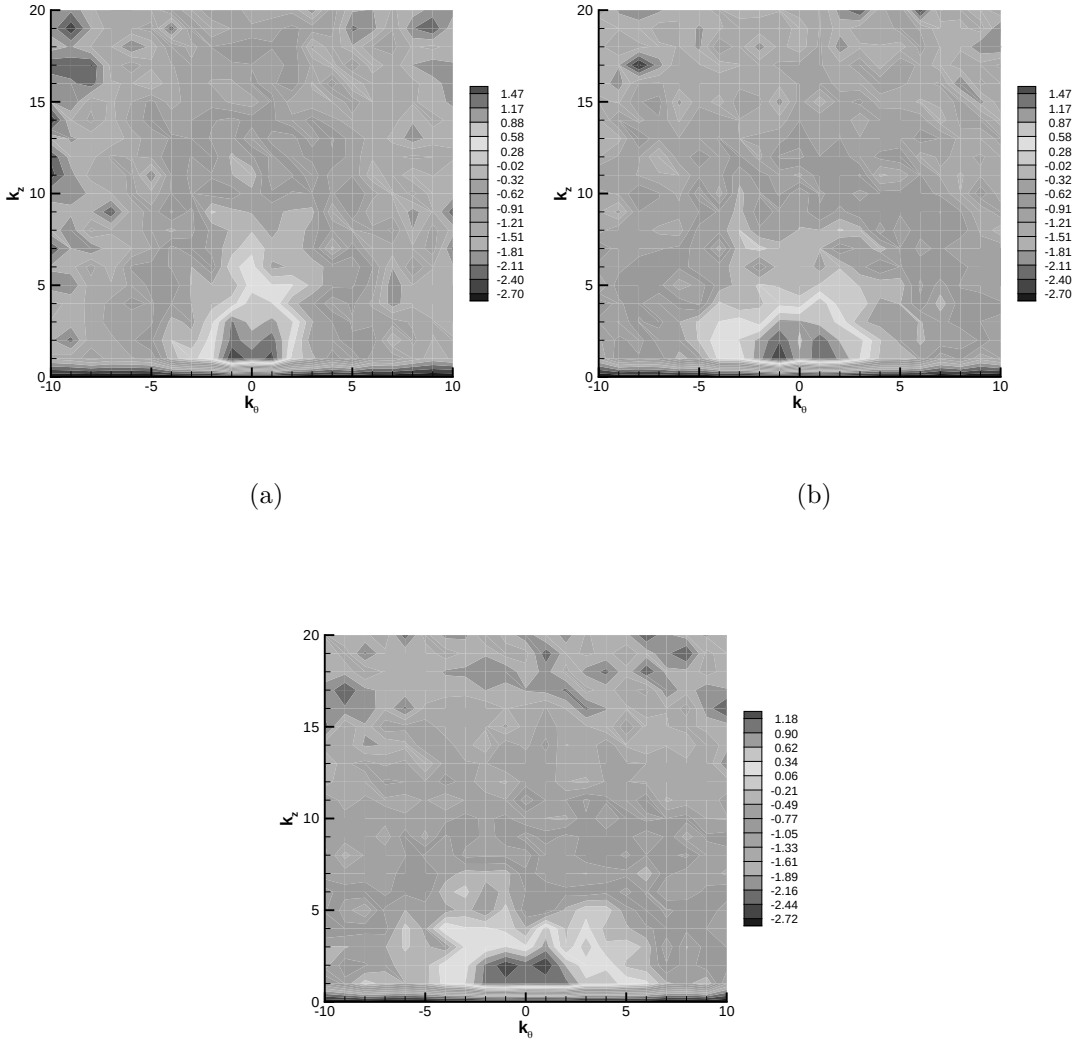


Figure 3.38 2-D Energy spectra for STRN4 at $t/T = 127.08$; Contours of $log_{10}(E_{2D})$; (a), (b) and (c) correspond to $r/r_0 = 0.5$, 1.0 and 2.0 respectively

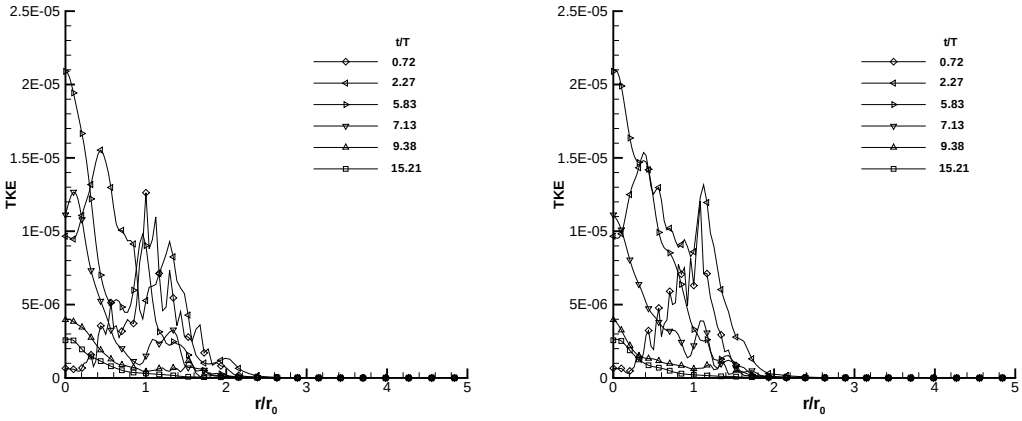


(a) (b)

Figure 3.39 Variation of turbulent kinetic energy for STRN4 in the first period at (a) $\theta = 45^o$ and (b) $\theta = 135^o$

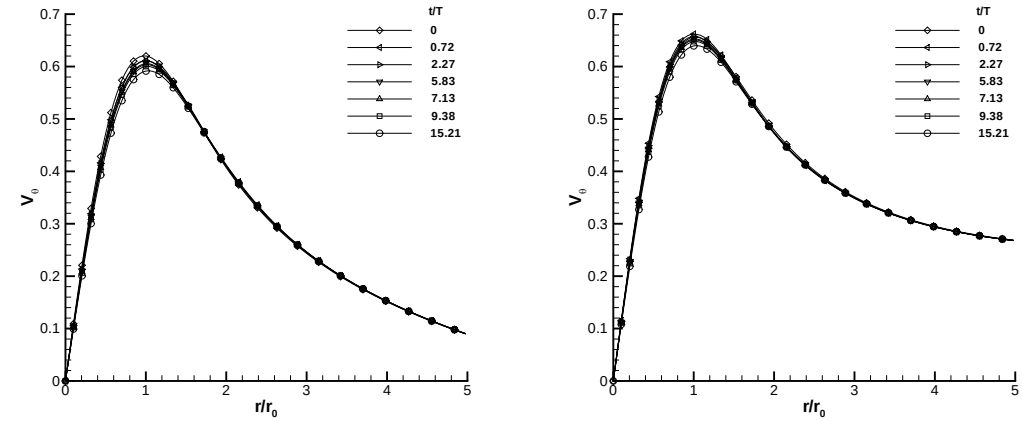


(a) (b)

Figure 3.40 Variation of mean tangential velocity for STRN4 in the first period at (a) $\theta = 45^o$ and (b) $\theta = 135^o$

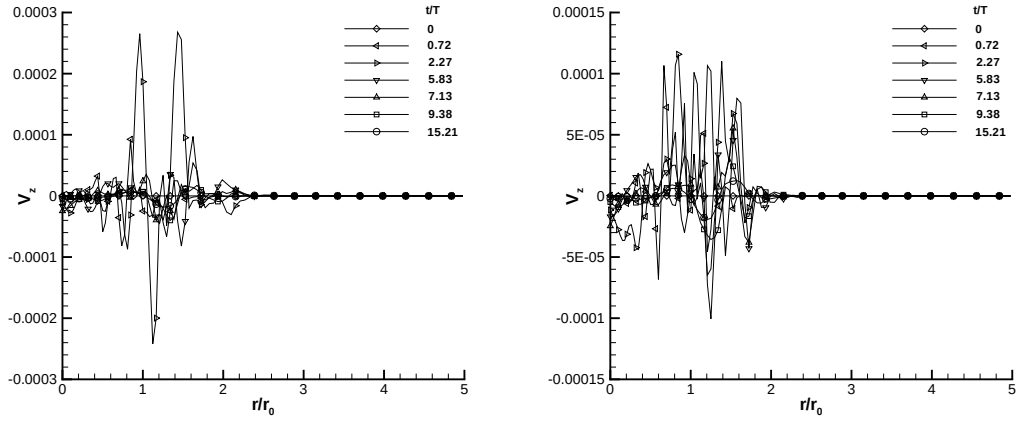


(a) (b)

Figure 3.41 Variation of mean axial velocity for STRN4 in the first period at (a) $\theta = 45^o$ and (b) $\theta = 135^o$

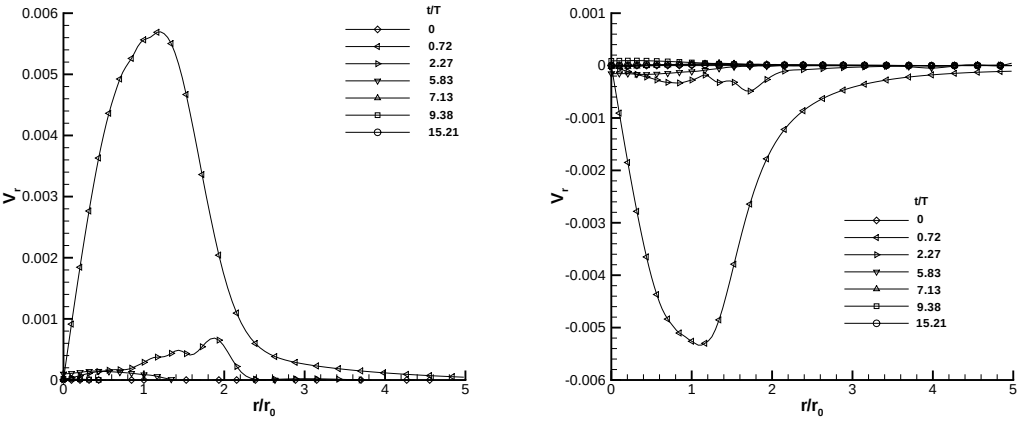


(a) (b)

Figure 3.42 Variation of mean radial velocity for STRN4 in the first period at (a) $\theta = 45^o$ and (b) $\theta = 135^o$

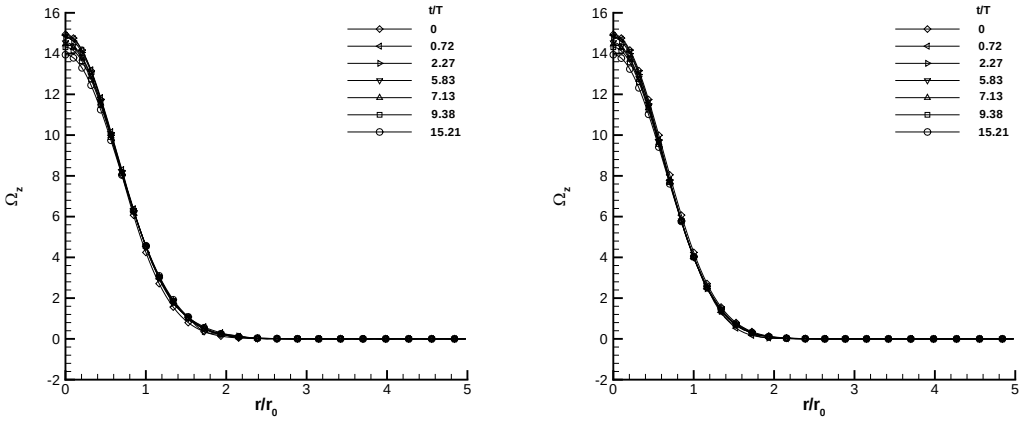


(a) (b)

Figure 3.43 Variation of mean axial vorticity for STRN4 in the first period at (a) $\theta = 45^o$ and (b) $\theta = 135^o$

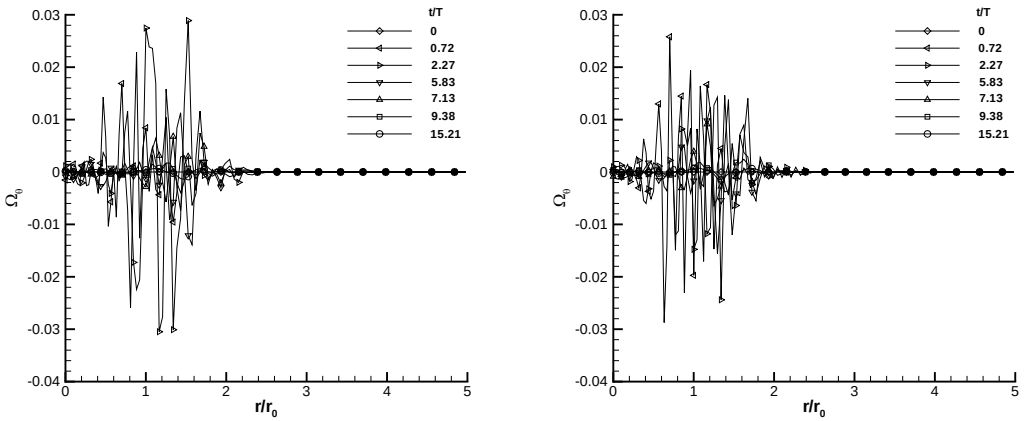


(a) (b)

Figure 3.44 Variation of mean tangential vorticity for STRN4 in the first period at (a) $\theta = 45^o$ and (b) $\theta = 135^o$

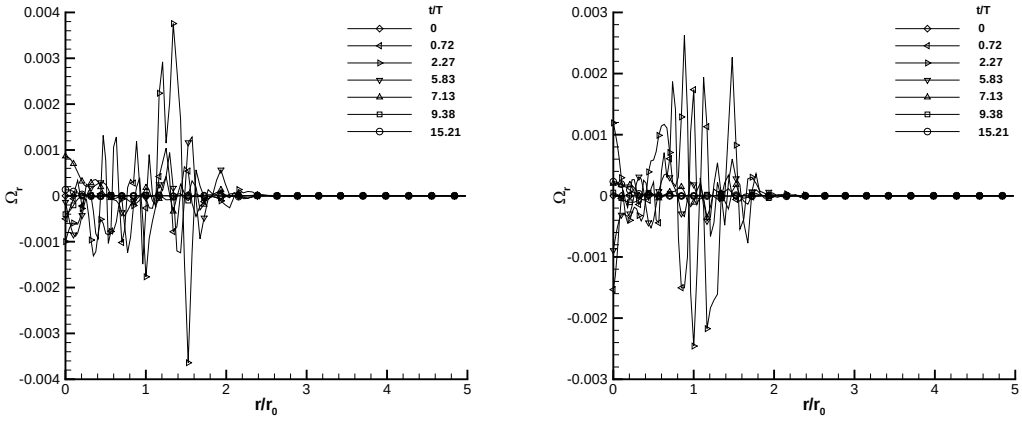


(a) (b)

Figure 3.45 Variation of mean radial vorticity for STRN4 in the first period at (a) $\theta = 45^o$ and (b) $\theta = 135^o$

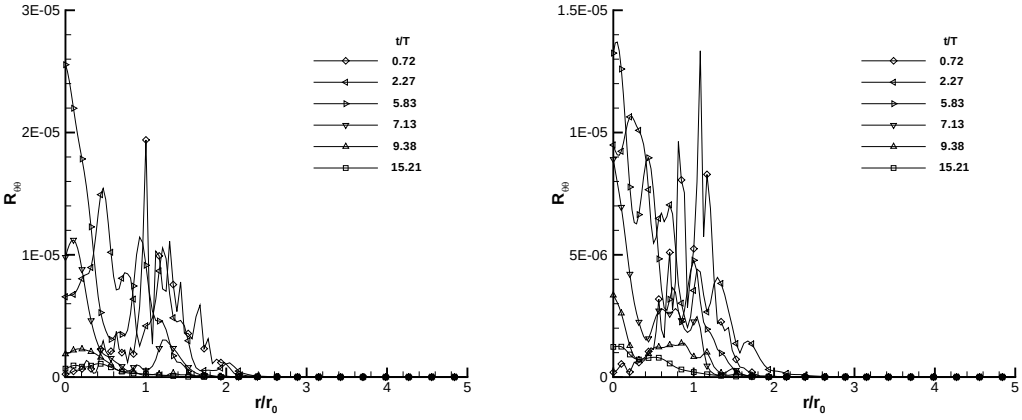


(a) (b)

Figure 3.46 Variation of $R_{\theta\theta}$ for STRN4 in the first period at (a) $\theta = 45^o$ and (b) $\theta = 135^o$

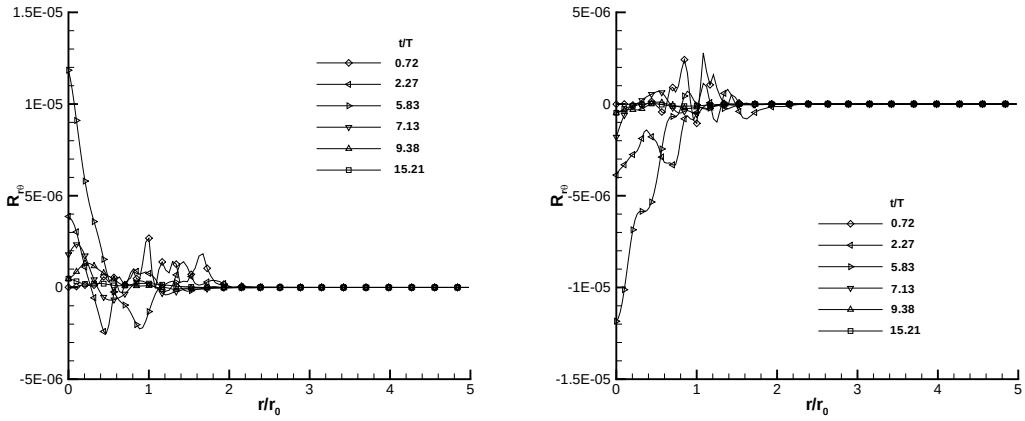


(a) (b)

Figure 3.47 Variation of $R_{r\theta}$ for STRN4 in the first period at (a) $\theta = 45^o$ and (b) $\theta = 135^o$

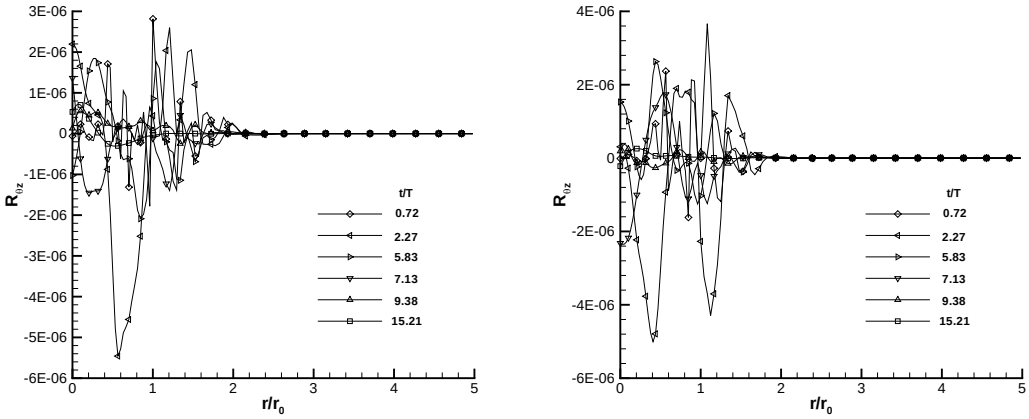


(a) (b)

Figure 3.48 Variation of $R_{\theta z}$ for STRN4 in the first period at (a) $\theta = 45^o$ and (b) $\theta = 135^o$

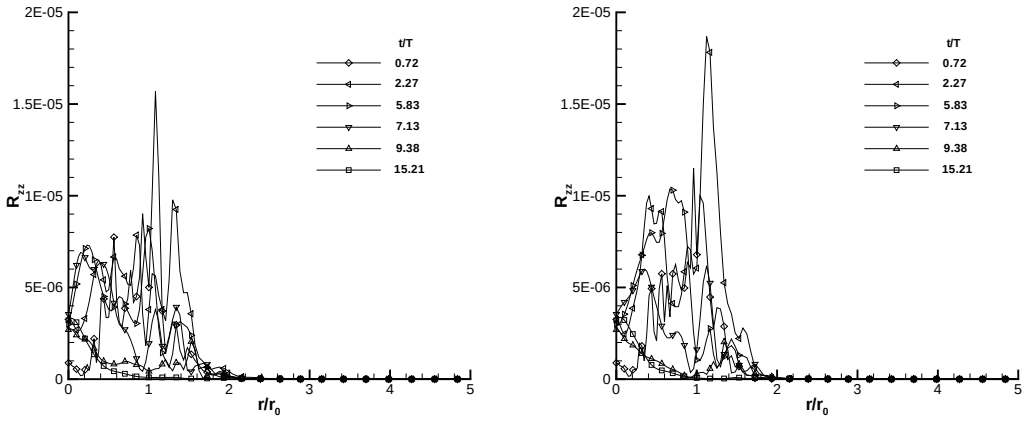


(a) (b)

Figure 3.49 Variation of $R_{zz}$ for STRN4 in the first period at (a) $\theta = 45^o$ and (b) $\theta = 135^o$

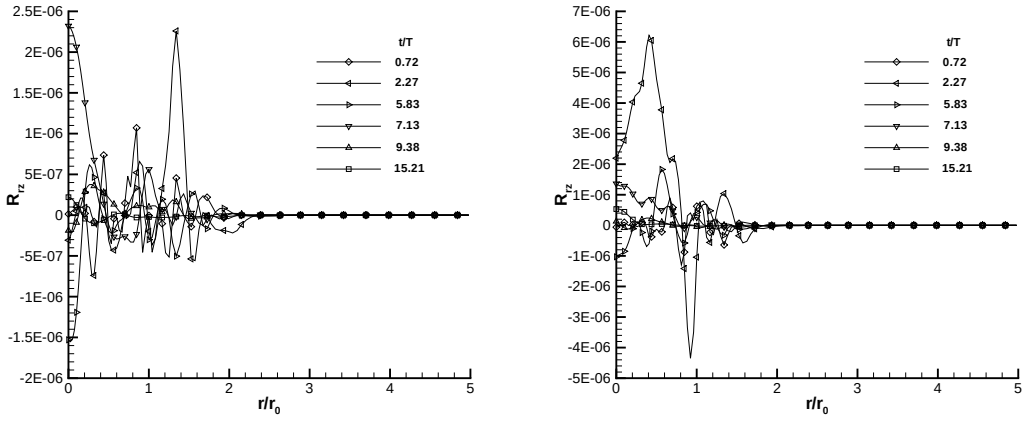


(a) (b)

Figure 3.50 Variation of $R_{rz}$ for STRN4 in the first period at (a) $\theta = 45^o$ and (b) $\theta = 135^o$

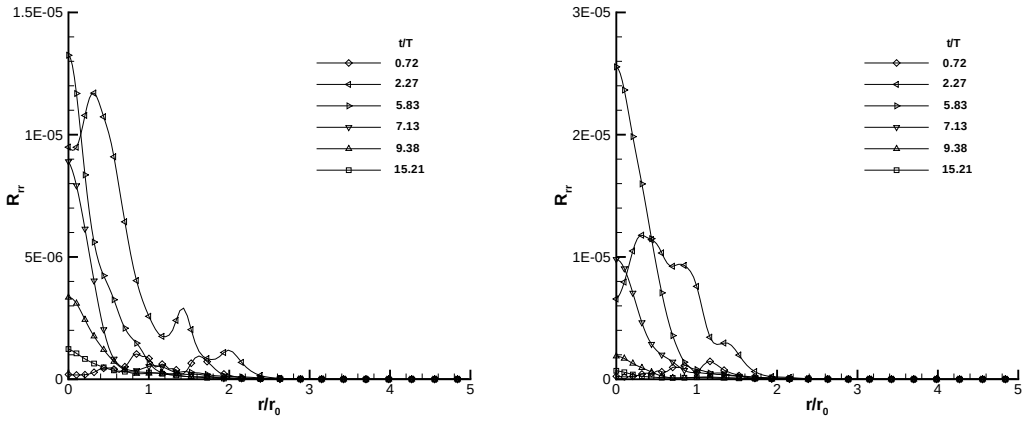


(a) (b)

Figure 3.51 Variation of $R_{rr}$ for STRN4 in the first period at (a) $\theta = 45^o$ and (b) $\theta = 135^o$

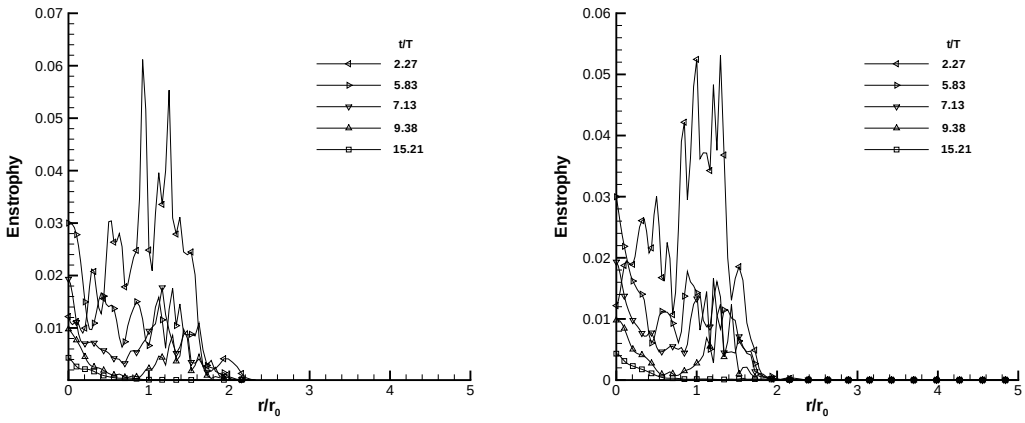


(a) (b)

Figure 3.52 Variation of enstrophy for STRN4 in the first period at (a) $\theta = 45^o$ and (b) $\theta = 135^o$

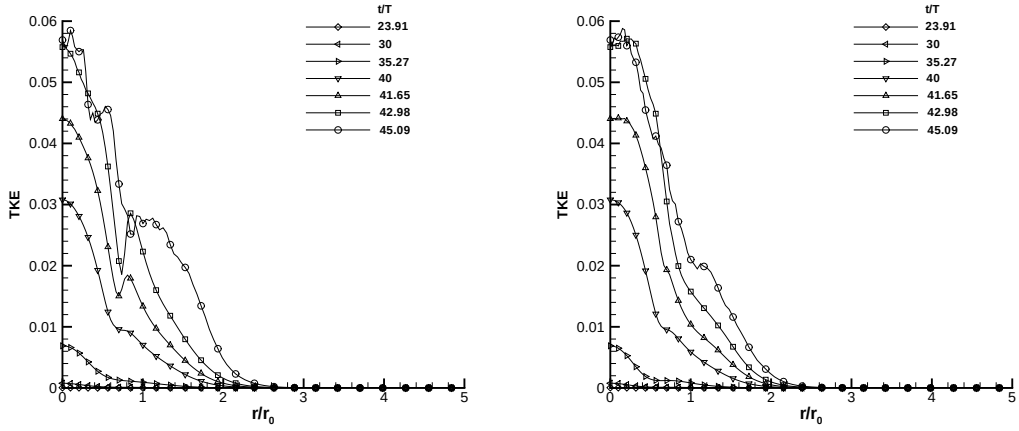


(a) (b)

Figure 3.53 Variation of turbulent kinetic energy for STRN4 in the second period at (a) $\theta = 45^o$ and (b) $\theta = 135^o$

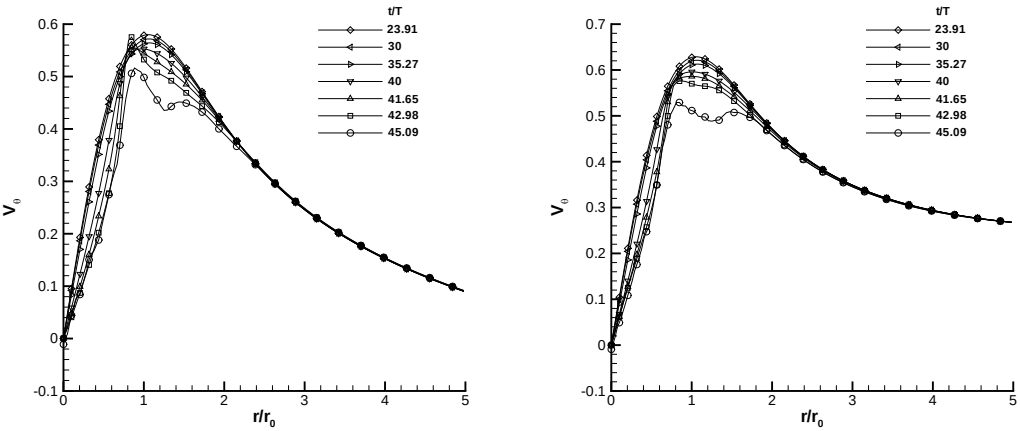


(a) (b)

Figure 3.54 Variation of mean tangential velocity for STRN4 in the second period at (a) $\theta = 45^o$ and (b) $\theta = 135^o$

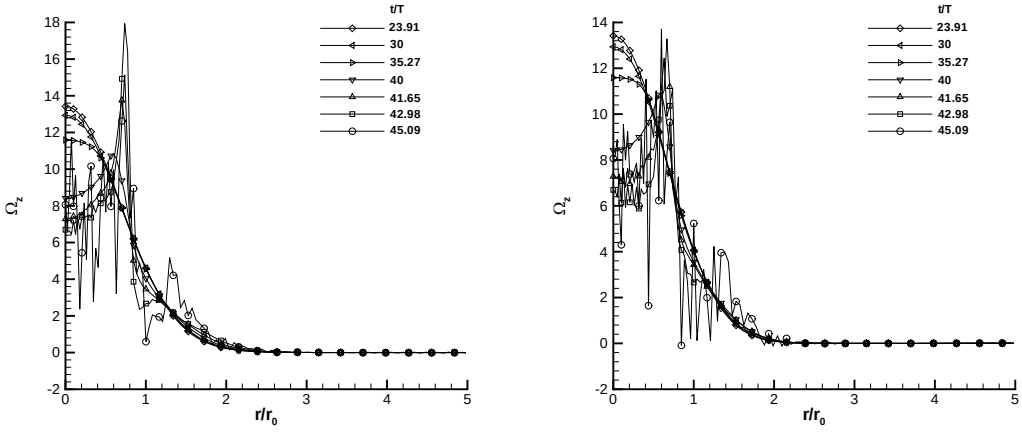


(a) (b)

Figure 3.55 Variation of mean axial vorticity for STRN4 in the second period at (a) $\theta = 45^o$ and (b) $\theta = 135^o$

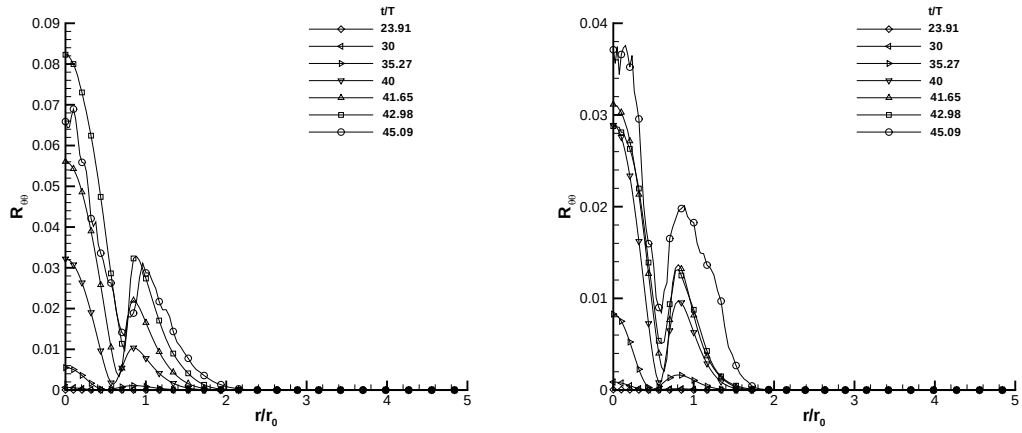


(a) (b)

Figure 3.56 Variation of $R_{\theta\theta}$ for STRN4 in the second period at (a) $\theta = 45^o$ and (b) $\theta = 135^o$

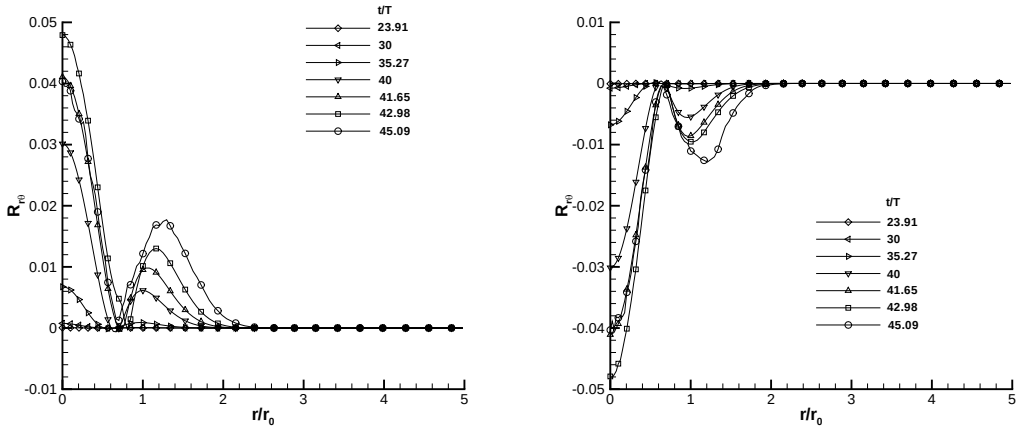


(a) (b)

Figure 3.57 Variation of $R_{r\theta}$ for STRN4 in the second period at (a) $\theta = 45^o$ and (b) $\theta = 135^o$

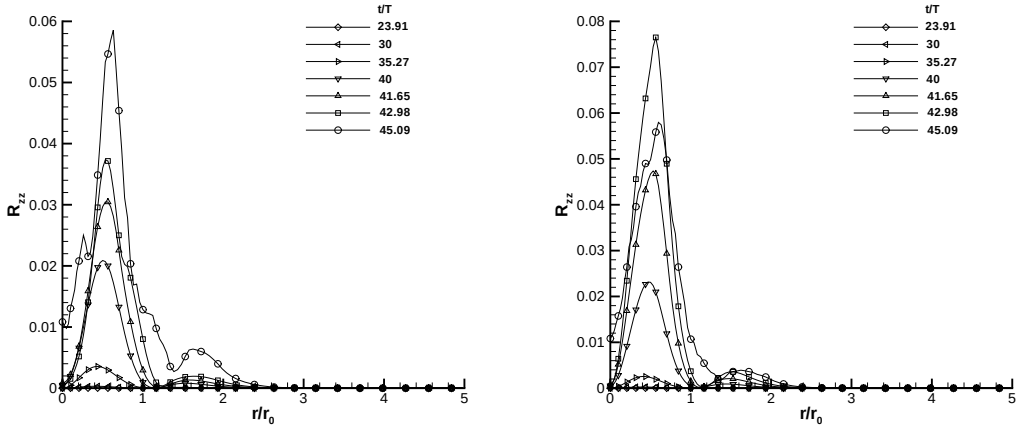


(a) (b)

Figure 3.58 Variation of $R_{zz}$ for STRN4 in the second period at (a) $\theta = 45^o$ and (b) $\theta = 135^o$

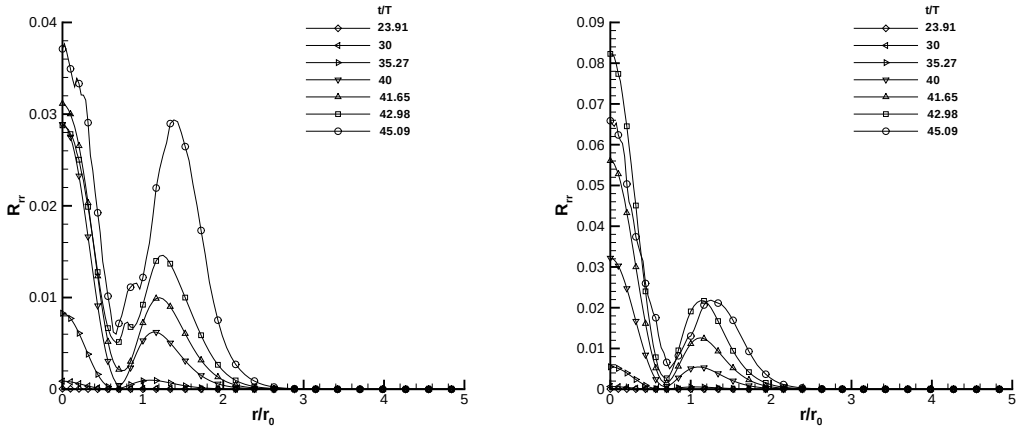


(a) (b)

Figure 3.59 Variation of $R_{rr}$ for STRN4 in the second period at (a) $\theta = 45^o$ and (b) $\theta = 135^o$

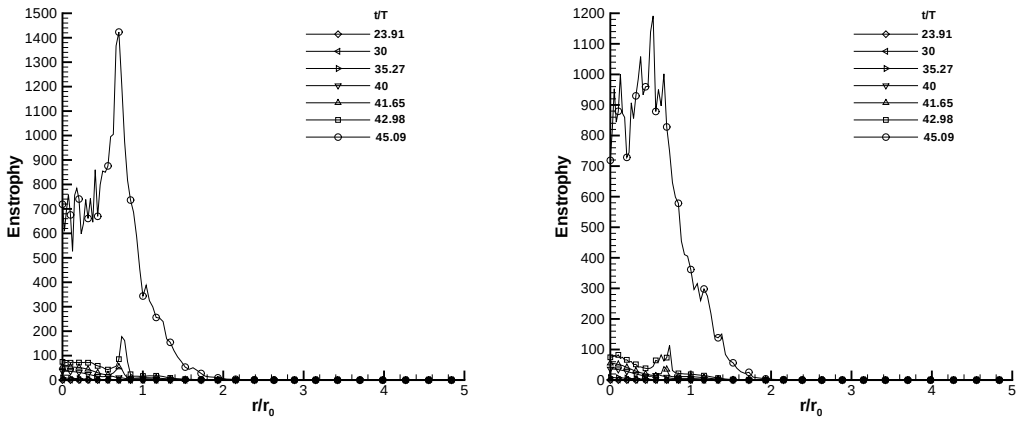


(a) (b)

Figure 3.60 Variation of enstrophy for STRN4 in the second period at (a) $\theta = 45^o$ and (b) $\theta = 135^o$

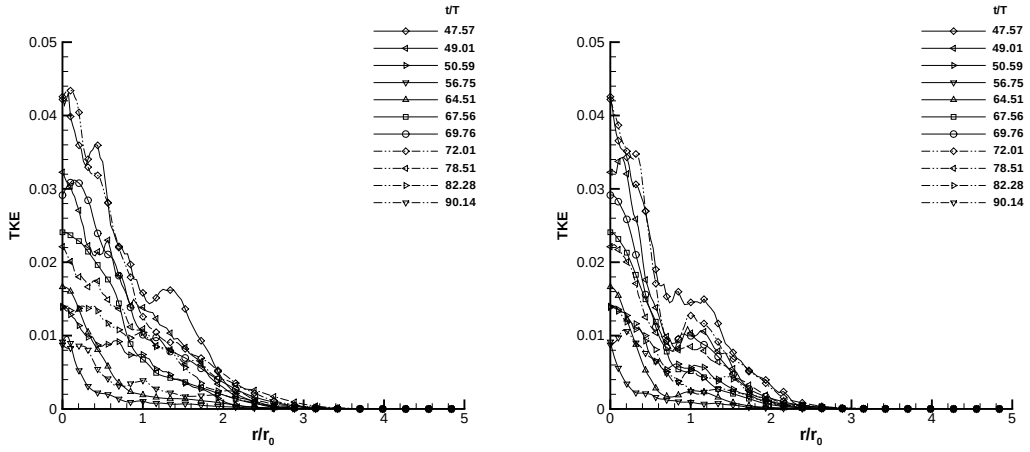


(a) (b)

Figure 3.61 Variation of turbulent kinetic energy for STRN4 in the third period at (a) $\theta = 45^o$ and (b) $\theta = 135^o$

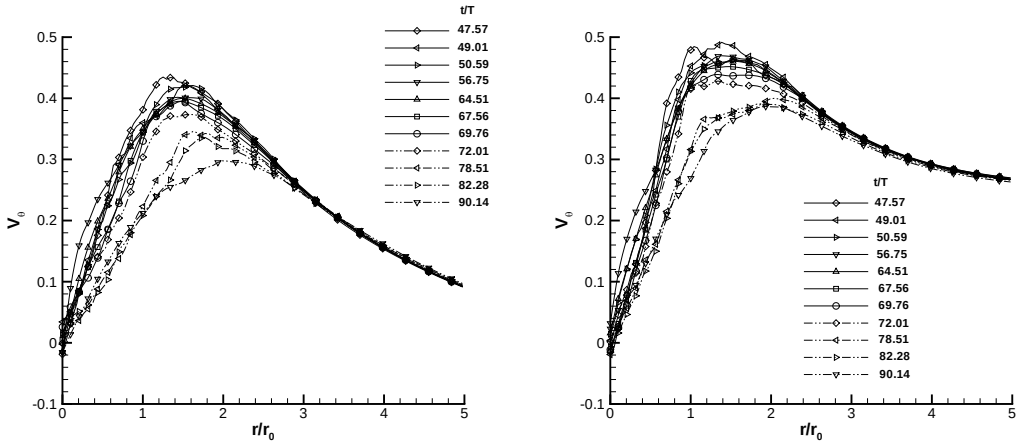


(a) (b)

Figure 3.62 Variation of mean tangential velocity for STRN4 in the third period at (a) $\theta = 45^o$ and (b) $\theta = 135^o$

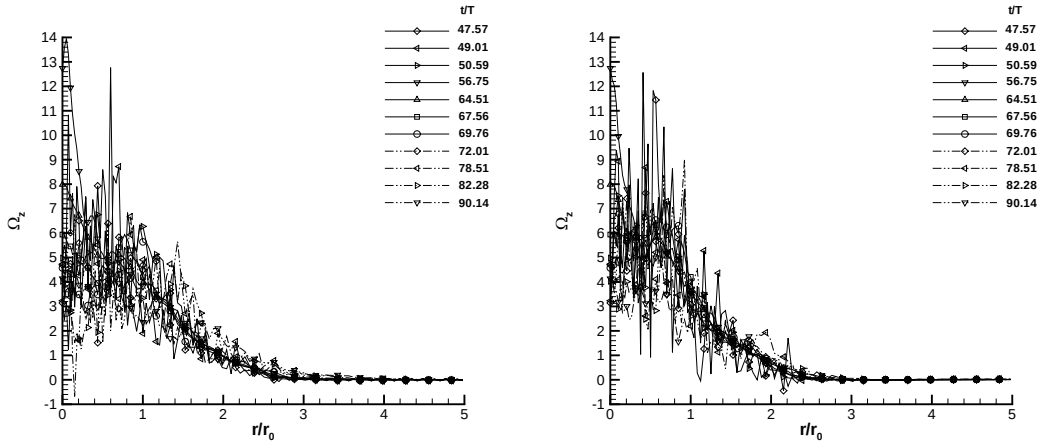


(a) (b)

Figure 3.63 Variation of mean axial vorticity for STRN4 in the third period at (a) $\theta = 45^o$ and (b) $\theta = 135^o$

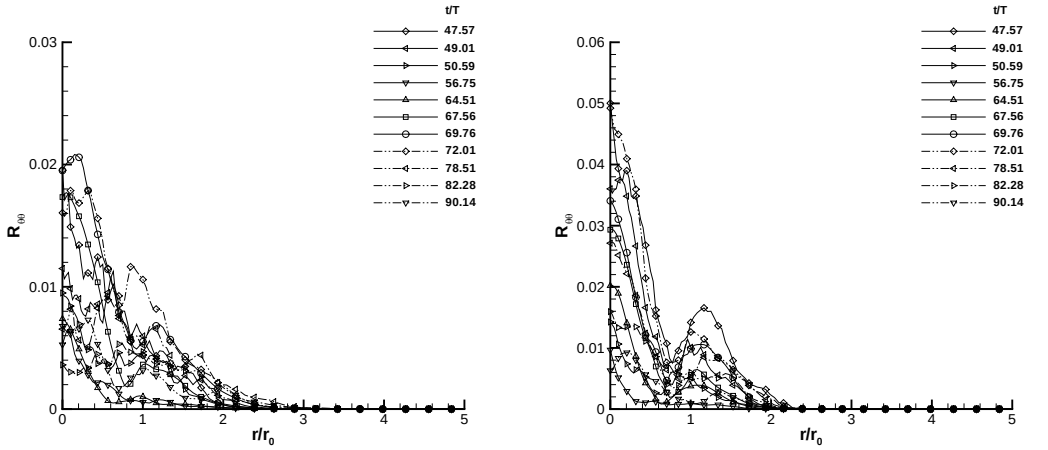


(a) (b)

Figure 3.64 Variation of $R_{\theta\theta}$ for STRN4 in the third period at (a) $\theta = 45^o$ and (b) $\theta = 135^o$

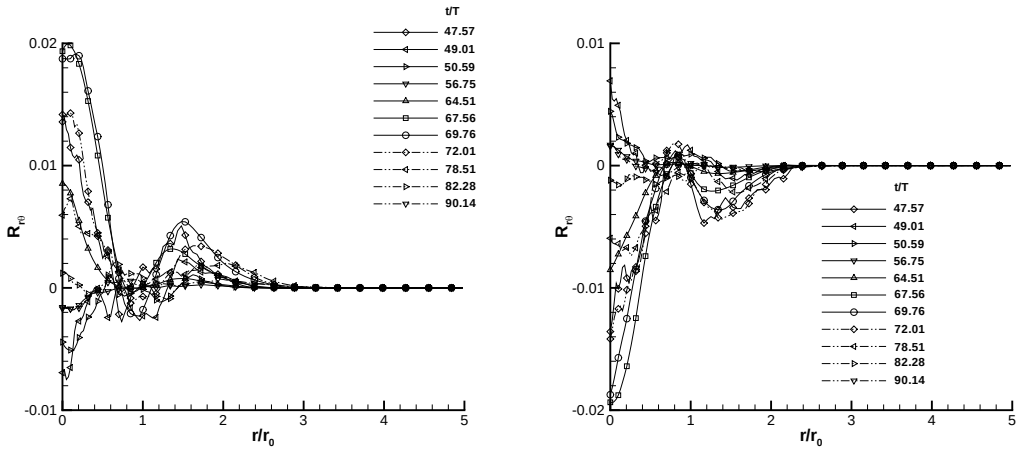


(a) (b)

Figure 3.65 Variation of $R_{r\theta}$ for STRN4 in the third period at (a) $\theta = 45^o$ and (b) $\theta = 135^o$

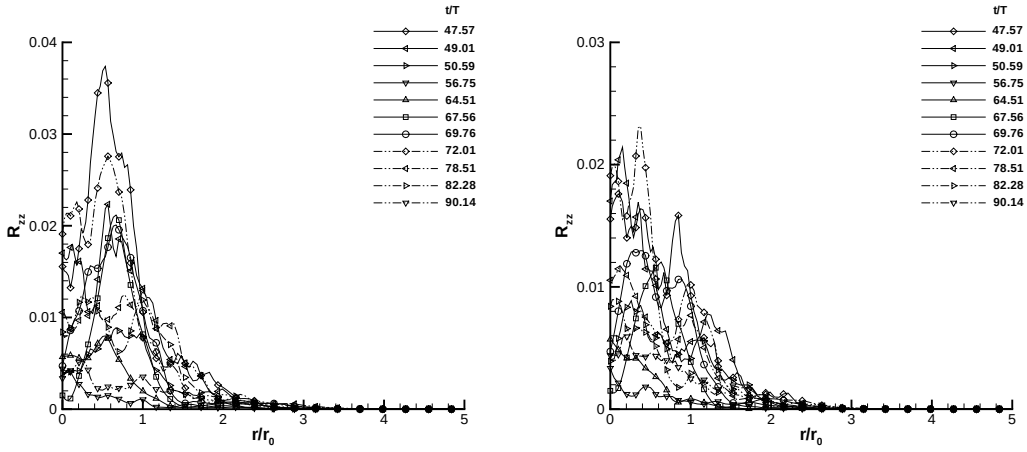


(a) (b)

Figure 3.66 Variation of $R_{zz}$ for STRN4 in the third period at (a) $\theta = 45^o$ and (b) $\theta = 135^o$

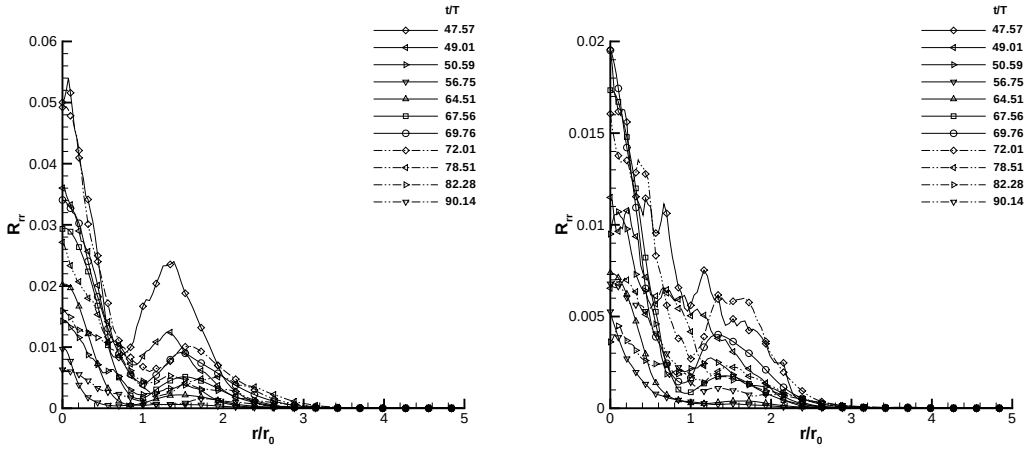


(a) (b)

Figure 3.67 Variation of $R_{rr}$ for STRN4 in the third period at (a) $\theta = 45^o$ and (b) $\theta = 135^o$

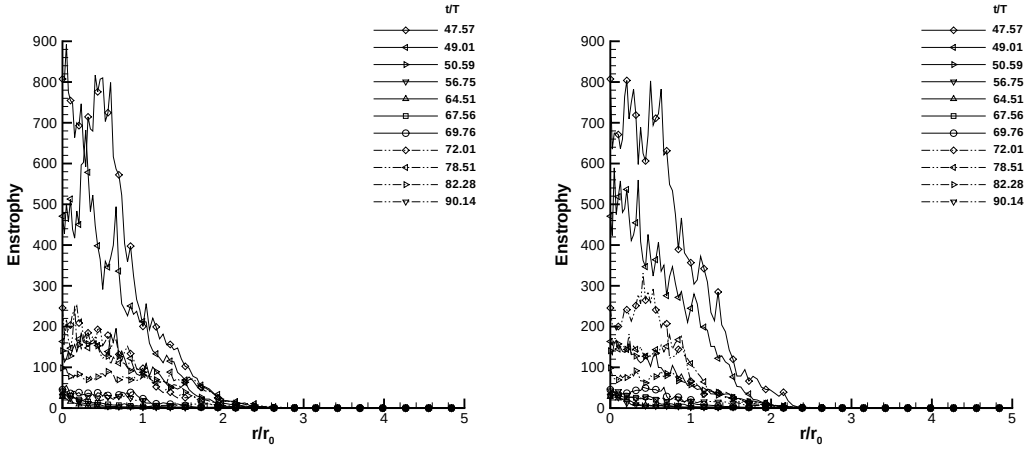


(a) (b)

Figure 3.68 Variation of enstrophy for STRN4 in the third period at (a) $\theta = 45^o$ and (b) $\theta = 135^o$

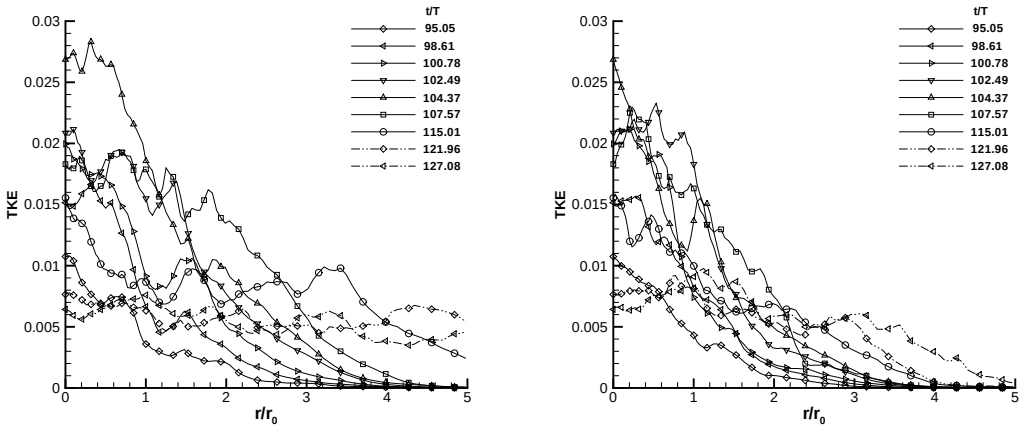


(a) (b)

Figure 3.69 Variation of turbulent kinetic energy for STRN4 in the fourth period at (a) $\theta = 45^o$ and (b) $\theta = 135^o$

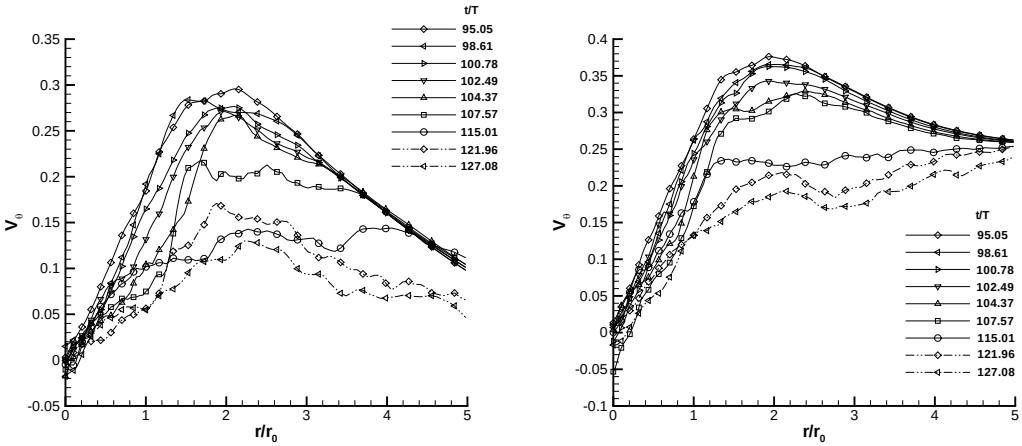


(a) (b)

Figure 3.70 Variation of mean tangential velocity for STRN4 in the fourth period at (a) $\theta = 45^o$ and (b) $\theta = 135^o$

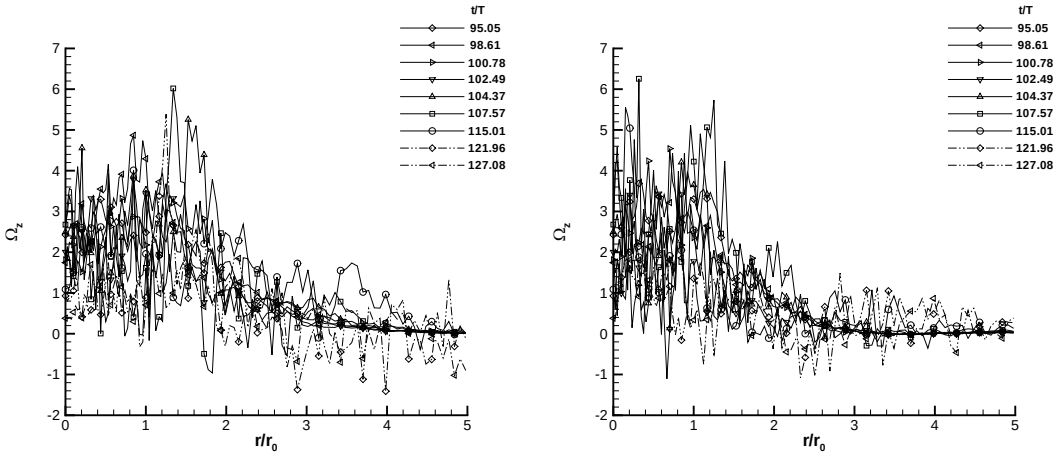


(a) (b)

Figure 3.71 Variation of mean axial vorticity for STRN4 in the fourth period at (a) $\theta = 45^o$ and (b) $\theta = 135^o$

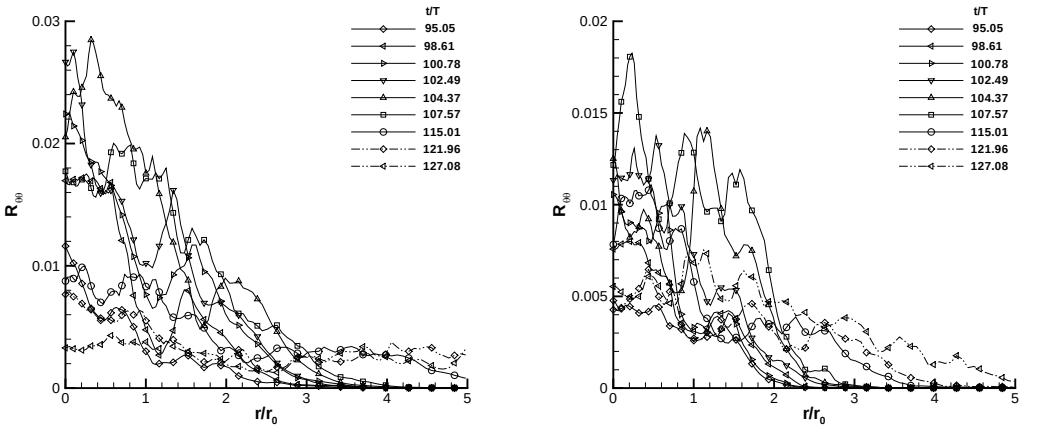


(a) (b)

Figure 3.72 Variation of $R_{\theta\theta}$ for STRN4 in the fourth period at (a) $\theta = 45^o$ and (b) $\theta = 135^o$

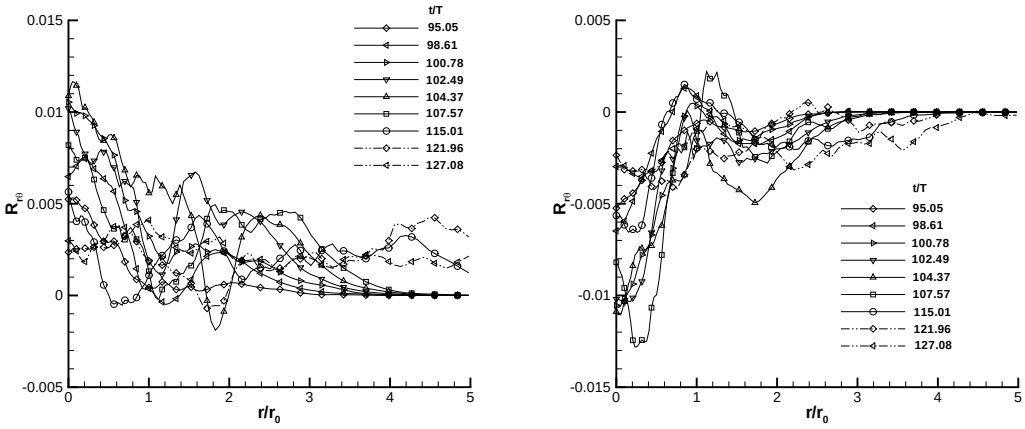


(a) (b)

Figure 3.73 Variation of $R_{r\theta}$ for STRN4 in the fourth period at (a) $\theta = 45^o$ and (b) $\theta = 135^o$

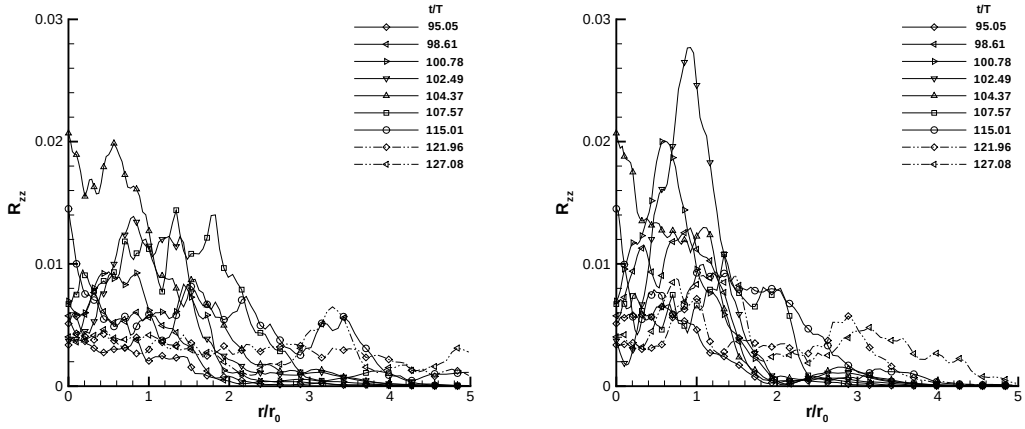


(a) (b)

Figure 3.74 Variation of $R_{zz}$ for STRN4 in the fourth period at (a) $\theta = 45^o$ and (b) $\theta = 135^o$

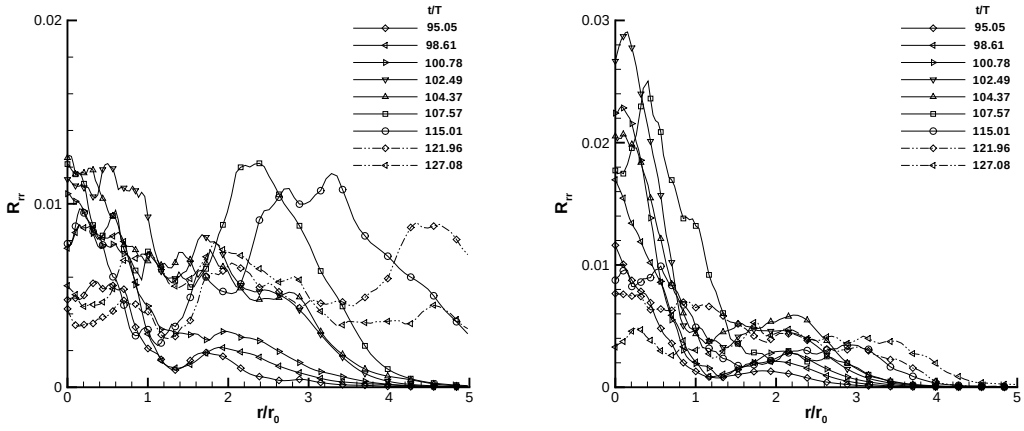


(a) (b)

Figure 3.75 Variation of $R_{rr}$ for STRN4 in the fourth period at (a) $\theta = 45^o$ and (b) $\theta = 135^o$

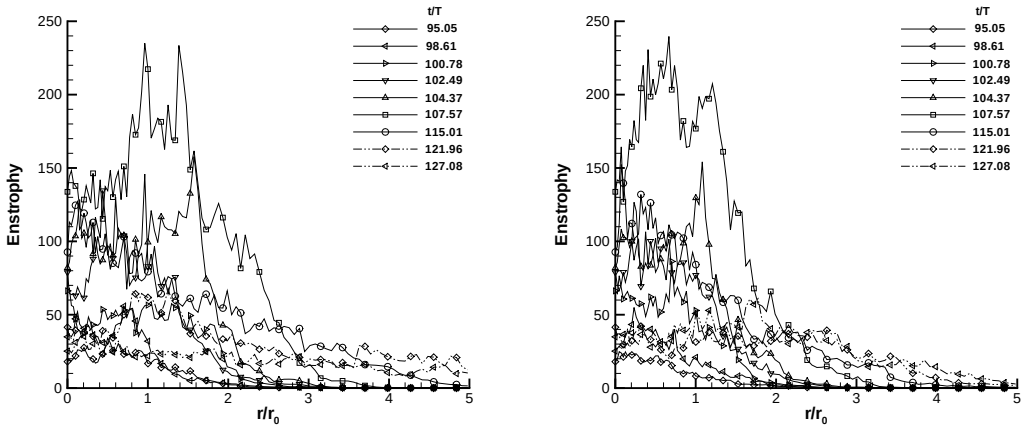


(a) (b)

Figure 3.76 Variation of enstrophy for STRN4 in the fourth period at (a) $\theta = 45^o$ and (b) $\theta = 135^o$

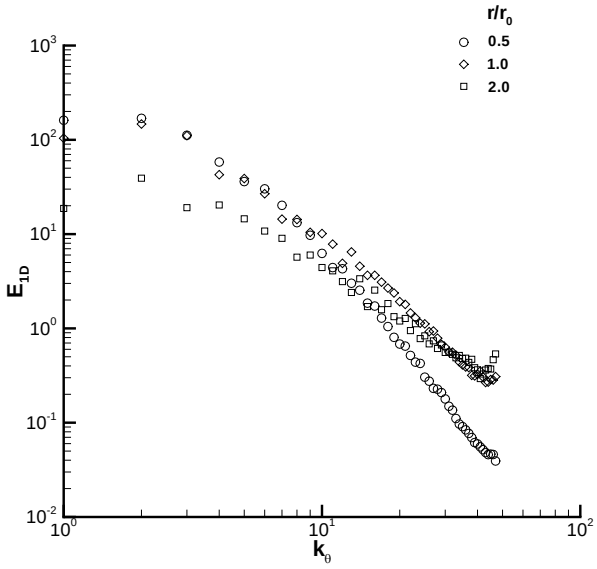


Figure 3.77 1-D energy spectra for STRN2 at t/T = 4.79

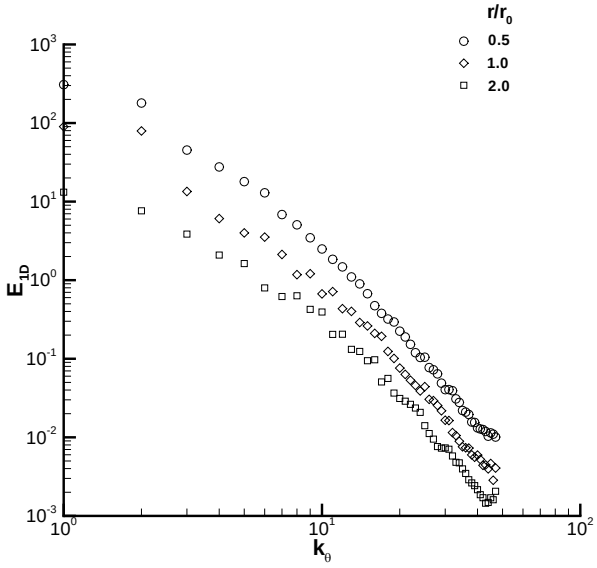


Figure 3.78 1-D energy spectra for STRN2 at t/T = 25.61

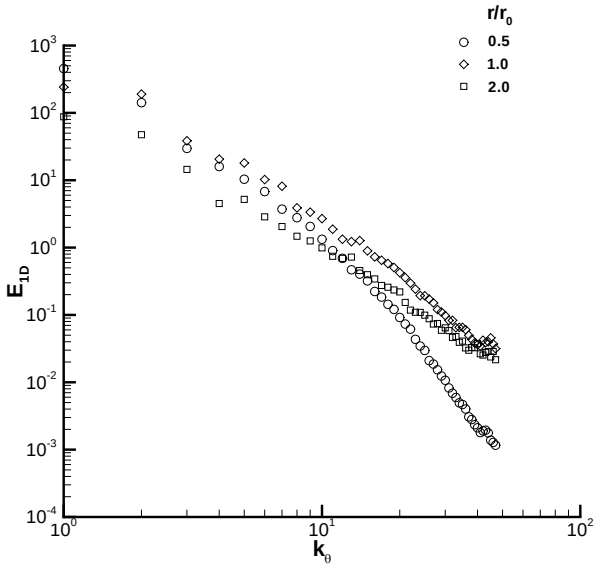


Figure 3.79 1-D energy spectra for STRN2 at t/T = 104.3

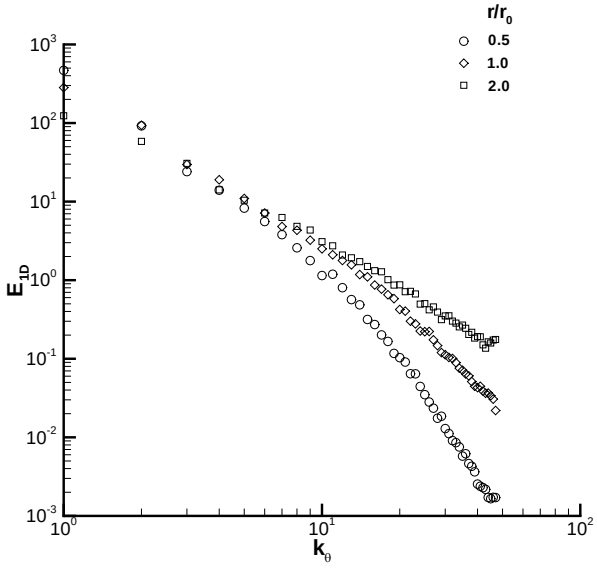


Figure 3.80 1-D energy spectra for STRN2 at t/T = 111.27

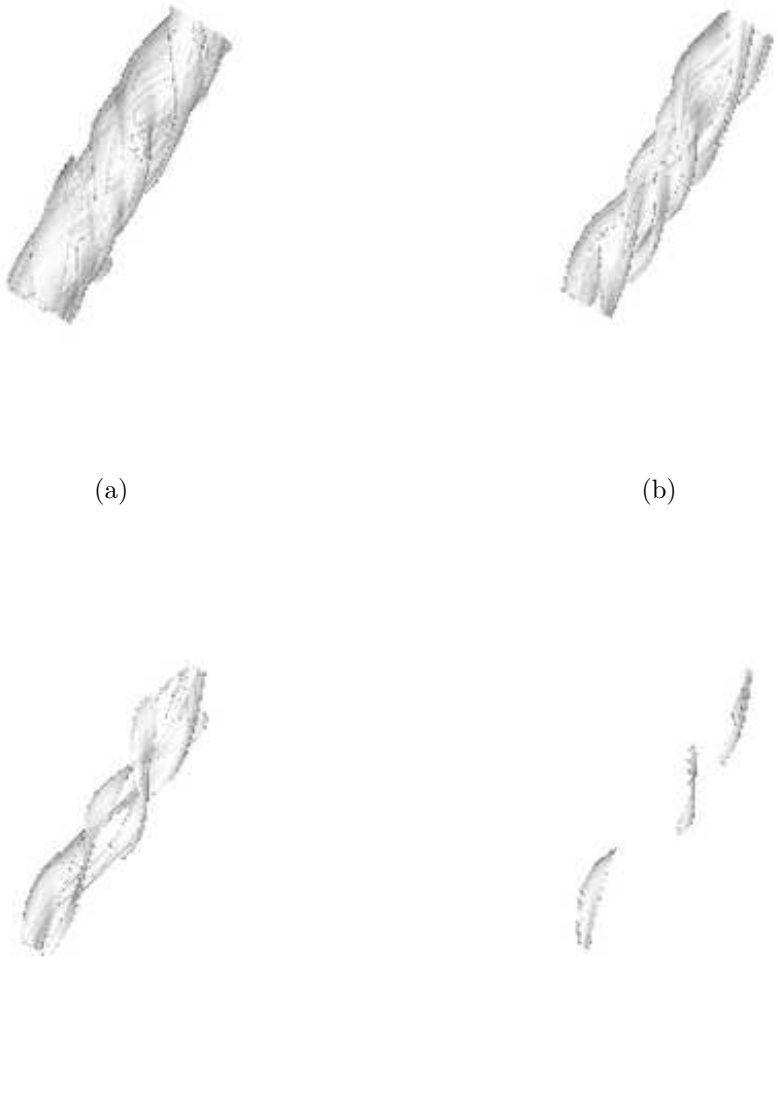

(a) (b)

(c) (d)

Figure 3.81 Vorticity magnitude isosurfaces for STRN2 at t/T = 2.53; (a), (b), (c) and (d) correspond to 0.1, 0.25, 0.5 and 0.75 times the peak vorticity magnitude respectively

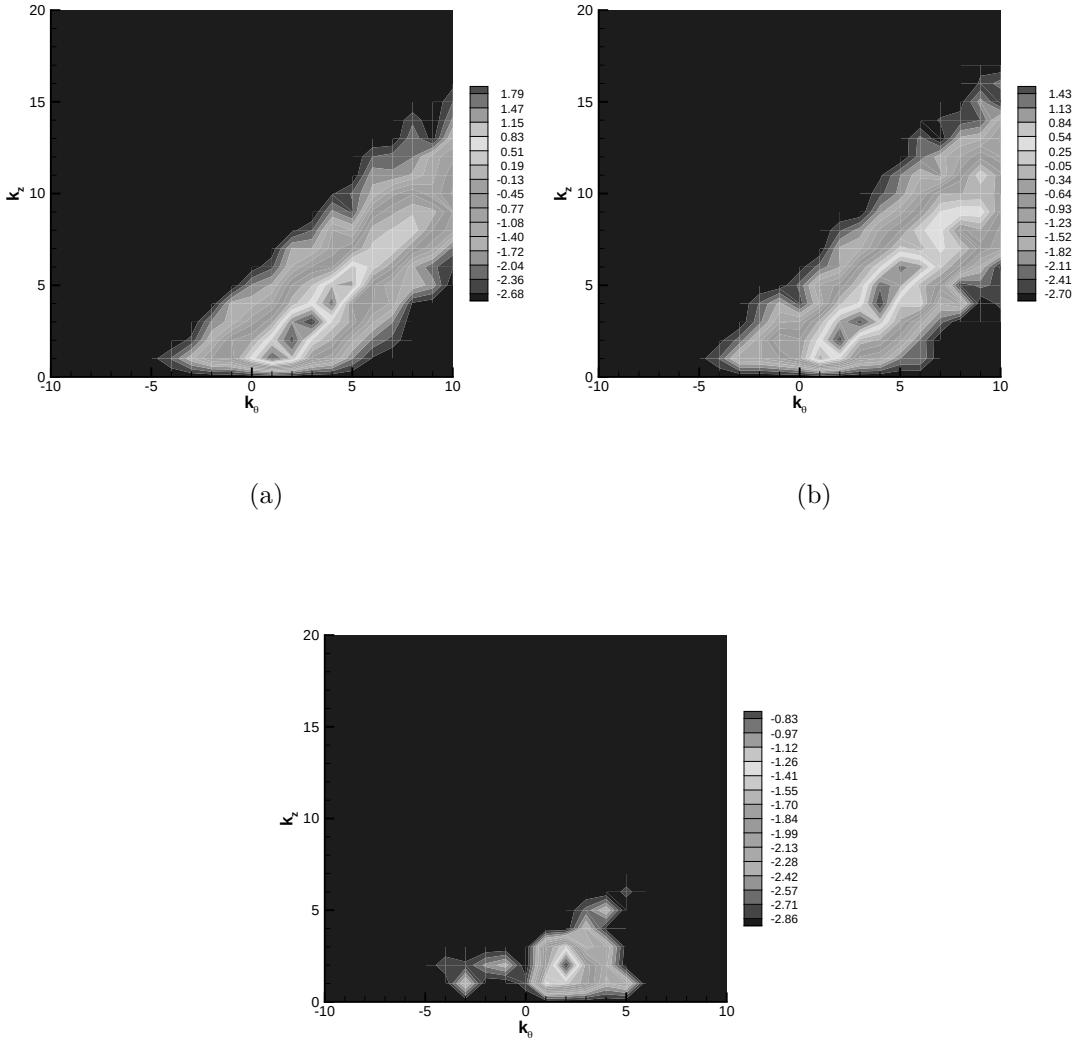


(a) (b)

(c)

Figure 3.82 2-D Energy spectra for STRN2 at $t/T = 2.53$; Contours of $log_{10}(E_{2D})$; (a), (b) and (c) correspond to $r/r_0 = 0.5$, 1.0 and 2.0 respectively

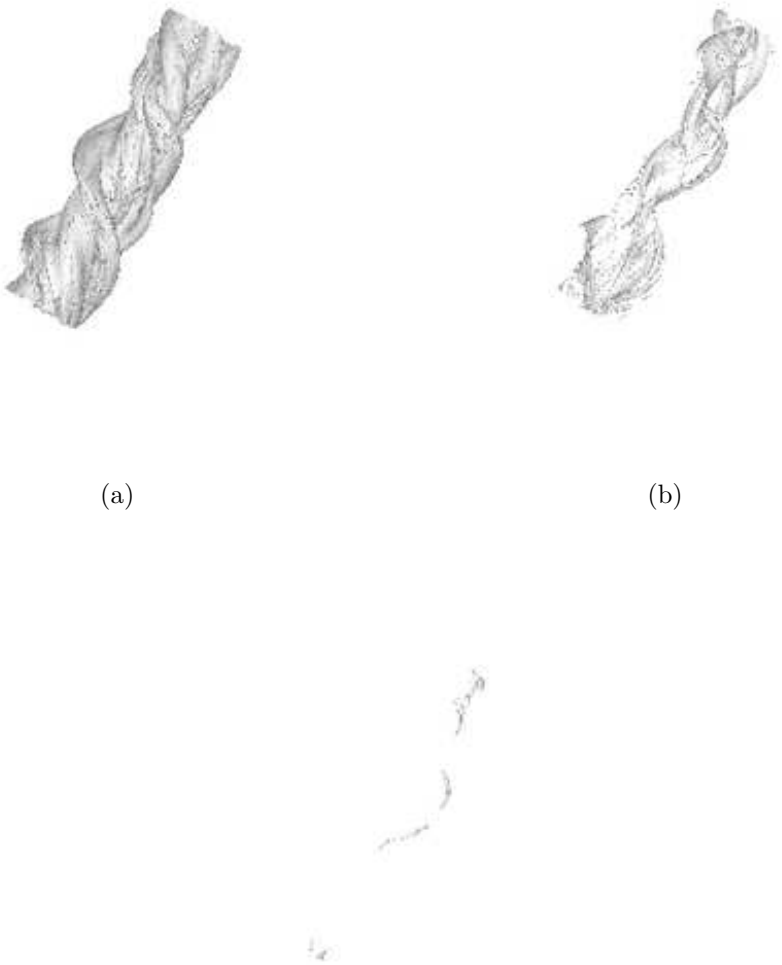

(a) (b)

(c)

Figure 3.83 Vorticity magnitude isosurfaces for STRN2 at t/T = 3.07; (a), (b) and (c) correspond to 0.1, 0.25 and 0.5 times the peak vorticity magnitude respectively

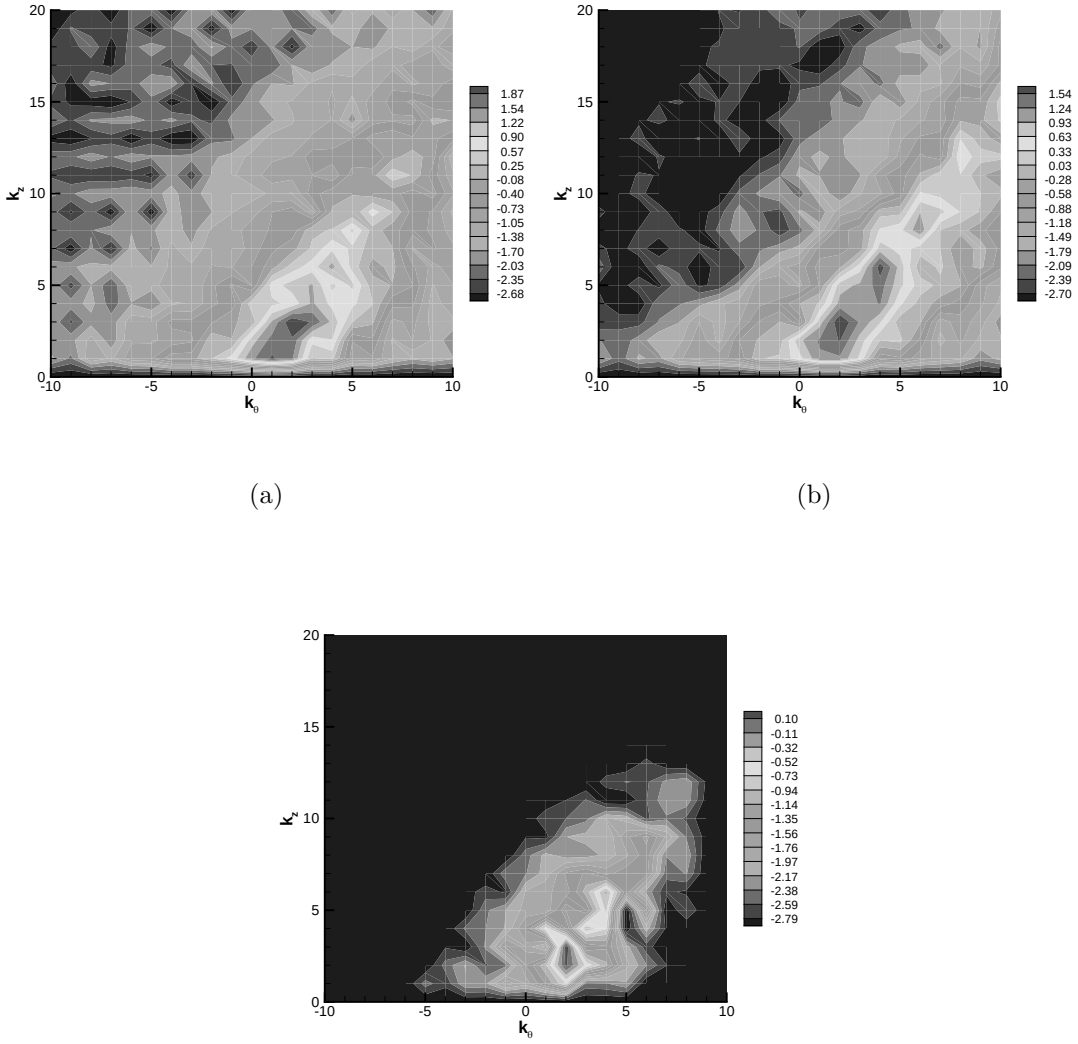


(a) (b)

(c)

Figure 3.84 2-D Energy spectra for STRN2 at $t/T = 3.07$; Contours of $log_{10}(E_{2D})$; (a), (b) and (c) correspond to $r/r_0 = 0.5$, 1.0 and 2.0 respectively

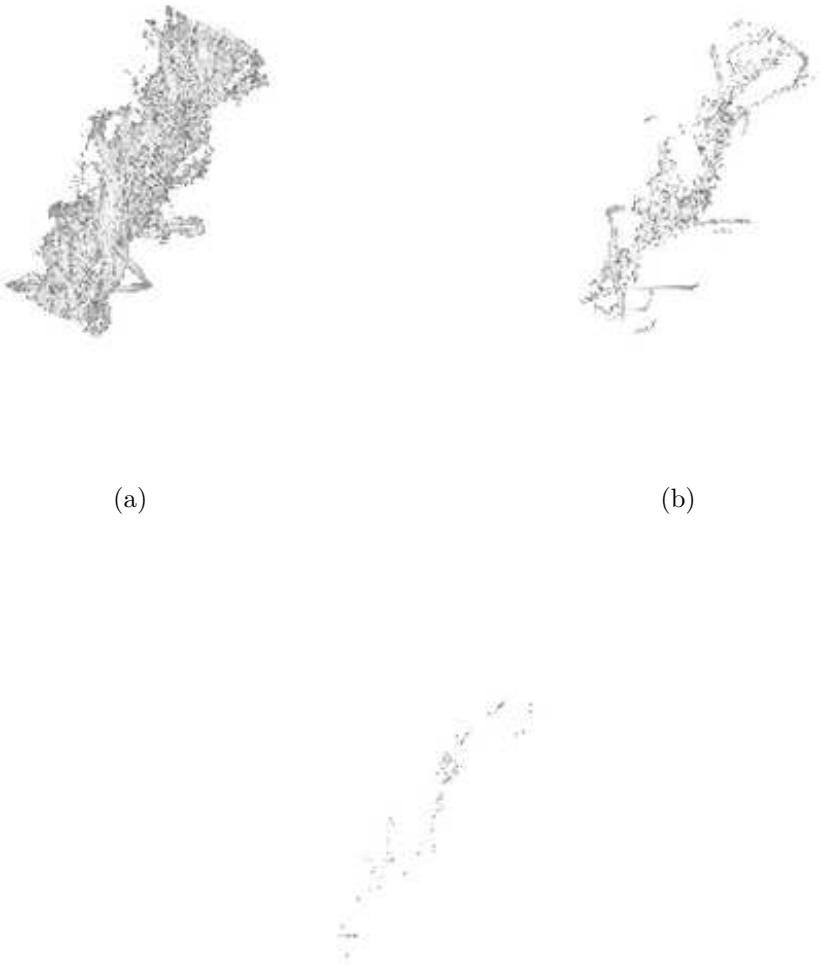

(a) (b)

(c)

Figure 3.85 Vorticity magnitude isosurfaces for STRN2 at t/T = 3.91; (a), (b) and (c) correspond to 0.1, 0.25 and 0.5 times the peak vorticity magnitude respectively

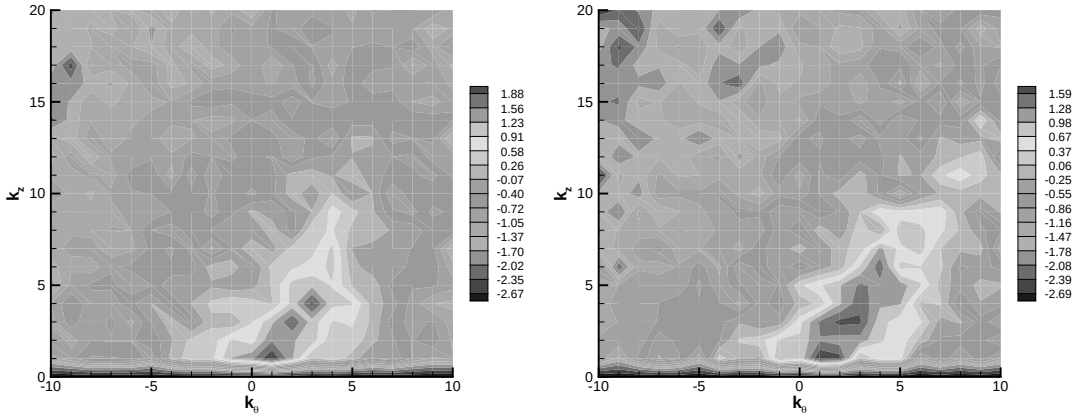


(a) (b)

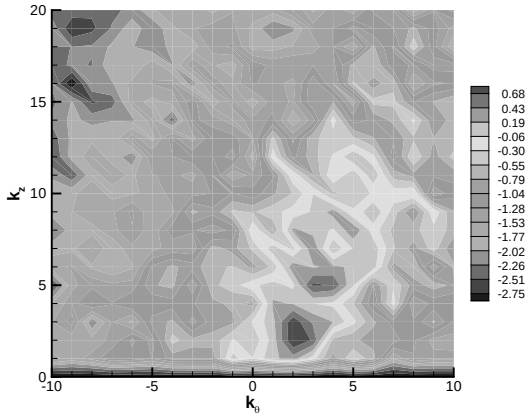


(c)

Figure 3.86 2-D Energy spectra for STRN2 at $t/T = 3.91$; Contours of $log_{10}(E_{2D})$; (a), (b) and (c) correspond to $r/r_0 = 0.5$, 1.0 and 2.0 respectively

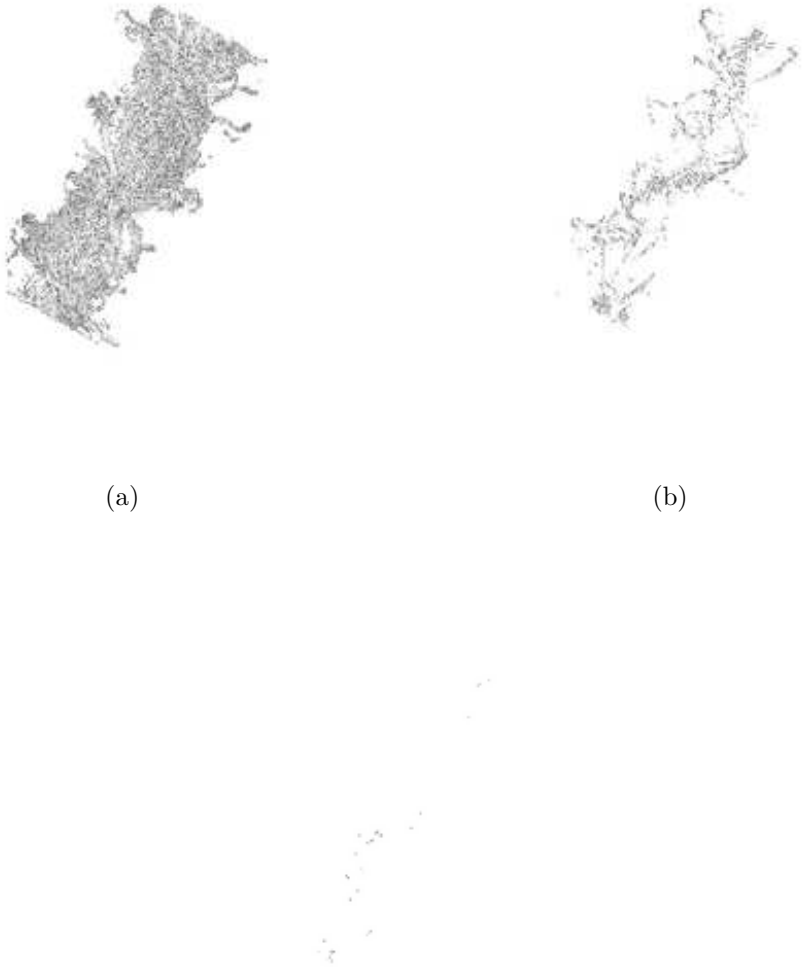

(a) (b)

(c)

Figure 3.87 Vorticity magnitude isosurfaces for STRN2 at t/T = 4.79; (a), (b) and (c) correspond to 0.1, 0.25 and 0.5 times the peak vorticity magnitude respectively

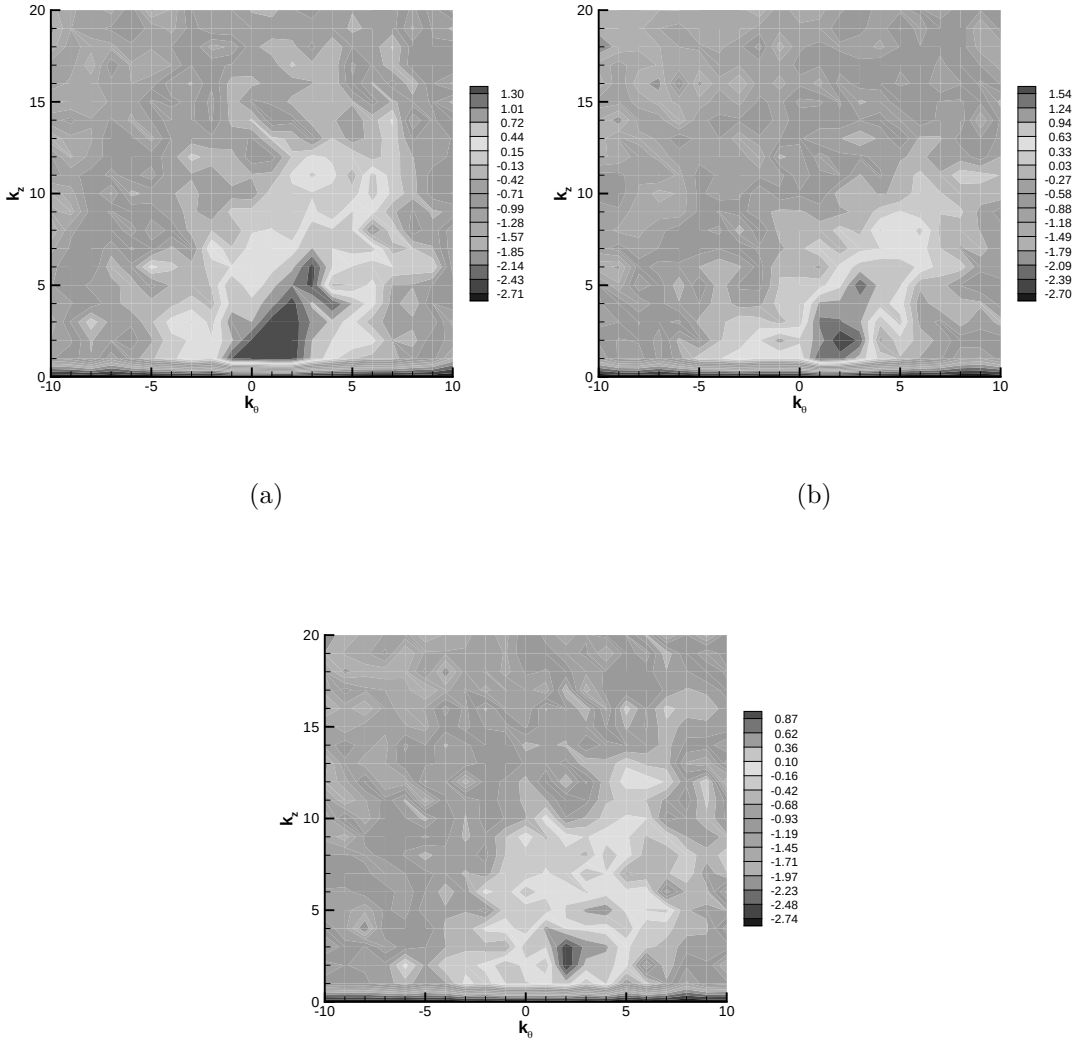


(a) (b)

(c)

Figure 3.88 2-D Energy spectra for STRN2 at $t/T = 4.79$; Contours of $log_{10}(E_{2D})$; (a), (b) and (c) correspond to $r/r_0 = 0.5$, 1.0 and 2.0 respectively

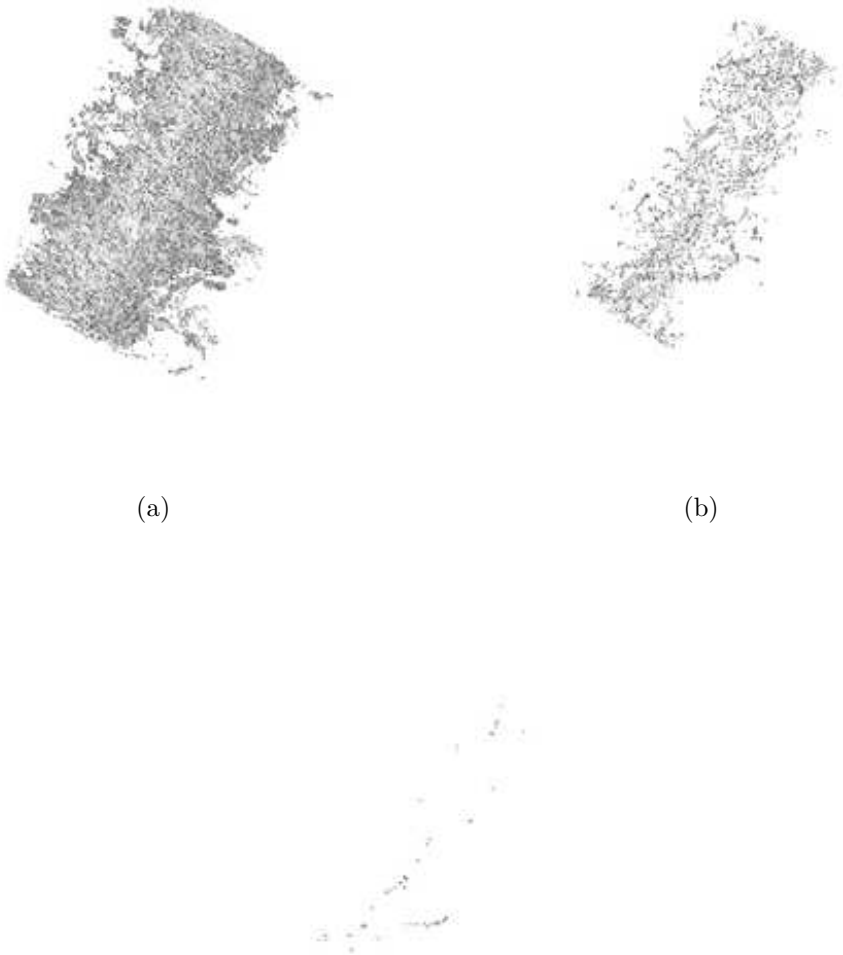

(a) (b)

(c)

Figure 3.89 Vorticity magnitude isosurfaces for STRN2 at t/T = 7.61; (a), (b) and (c) correspond to 0.1, 0.25 and 0.5 times the peak vorticity magnitude respectively

(a) (b)

(c)

Figure 3.90 Vorticity magnitude isosurfaces for STRN2 at t/T = 11.43; (a), (b) and (c) correspond to 0.1, 0.25 and 0.5 times the peak vorticity magnitude respectively

(a) (b)

(c)

Figure 3.91 Vorticity magnitude isosurfaces for STRN2 at t/T = 16.22; (a), (b) and (c) correspond to 0.1, 0.25 and 0.5 times the peak vorticity magnitude respectively

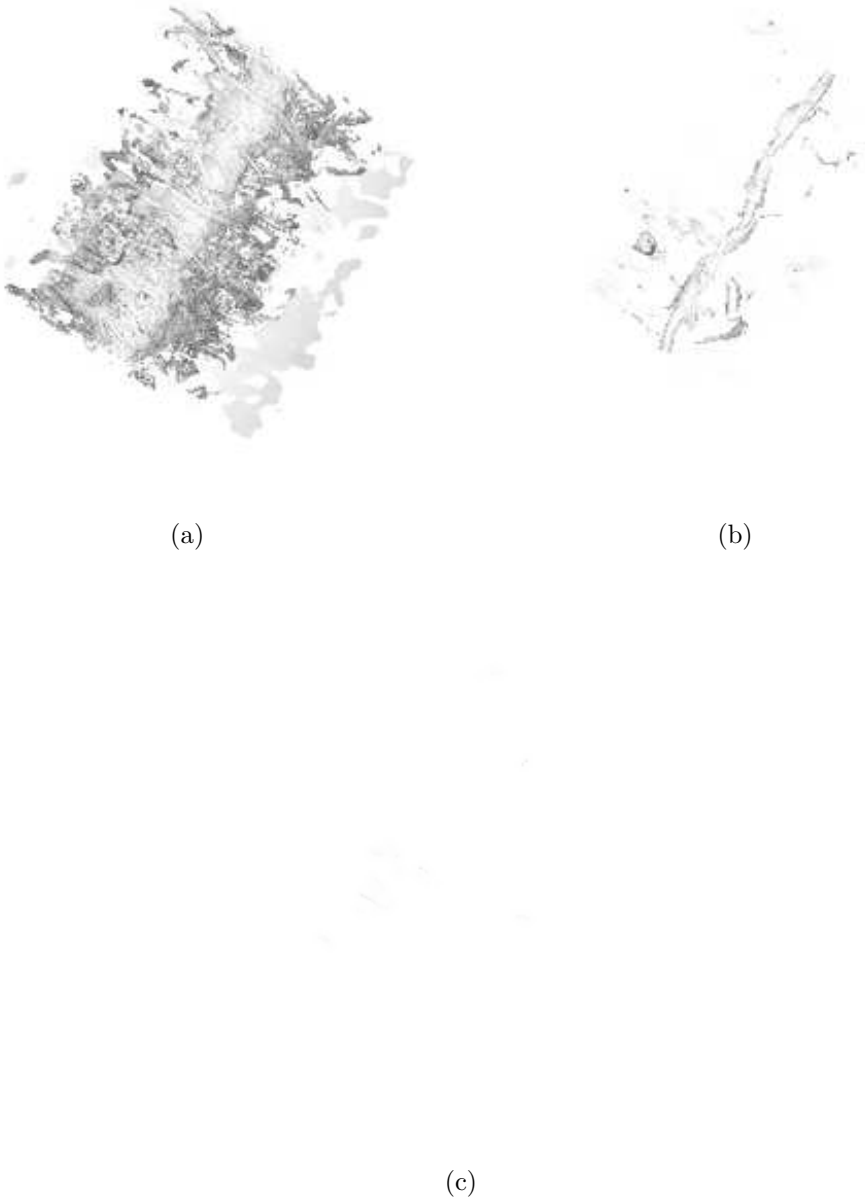

(a) (b)

(c)

Figure 3.92 Vorticity magnitude isosurfaces for STRN2 at t/T = 18.46; (a), (b) and (c) correspond to 0.1, 0.25 and 0.5 times the peak vorticity magnitude respectively

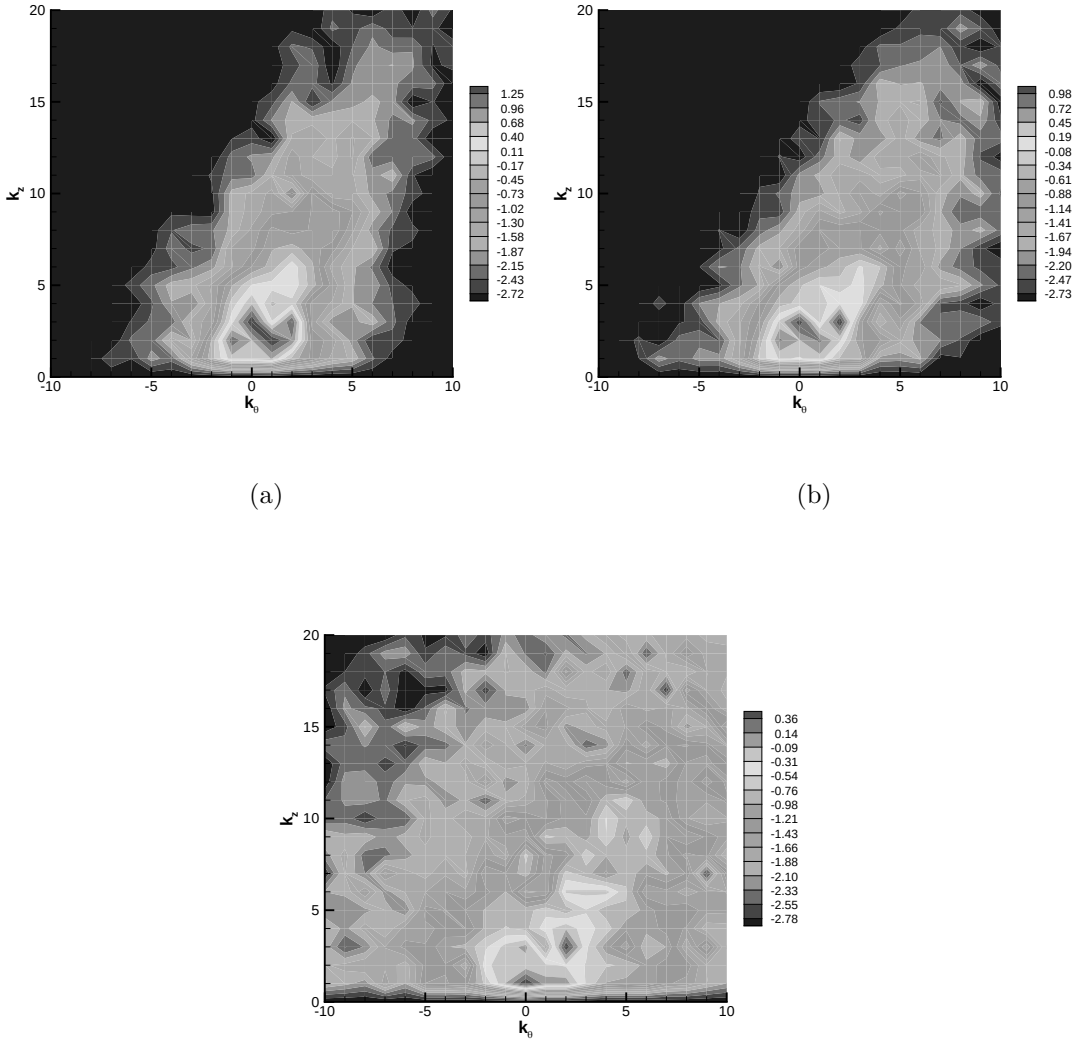


(a) (b)

(c)

Figure 3.93 2-D Energy spectra for STRN2 at $t/T = 18.46$; Contours of $log_{10}(E_{2D})$; (a), (b) and (c) correspond to $r/r_0 = 0.5$, 1.0 and 2.0 respectively

(a) (b)

(c)

Figure 3.94 Vorticity magnitude isosurfaces for STRN2 at t/T = 22.07; (a), (b) and (c) correspond to 0.1, 0.25 and 0.5 times the peak vorticity magnitude respectively

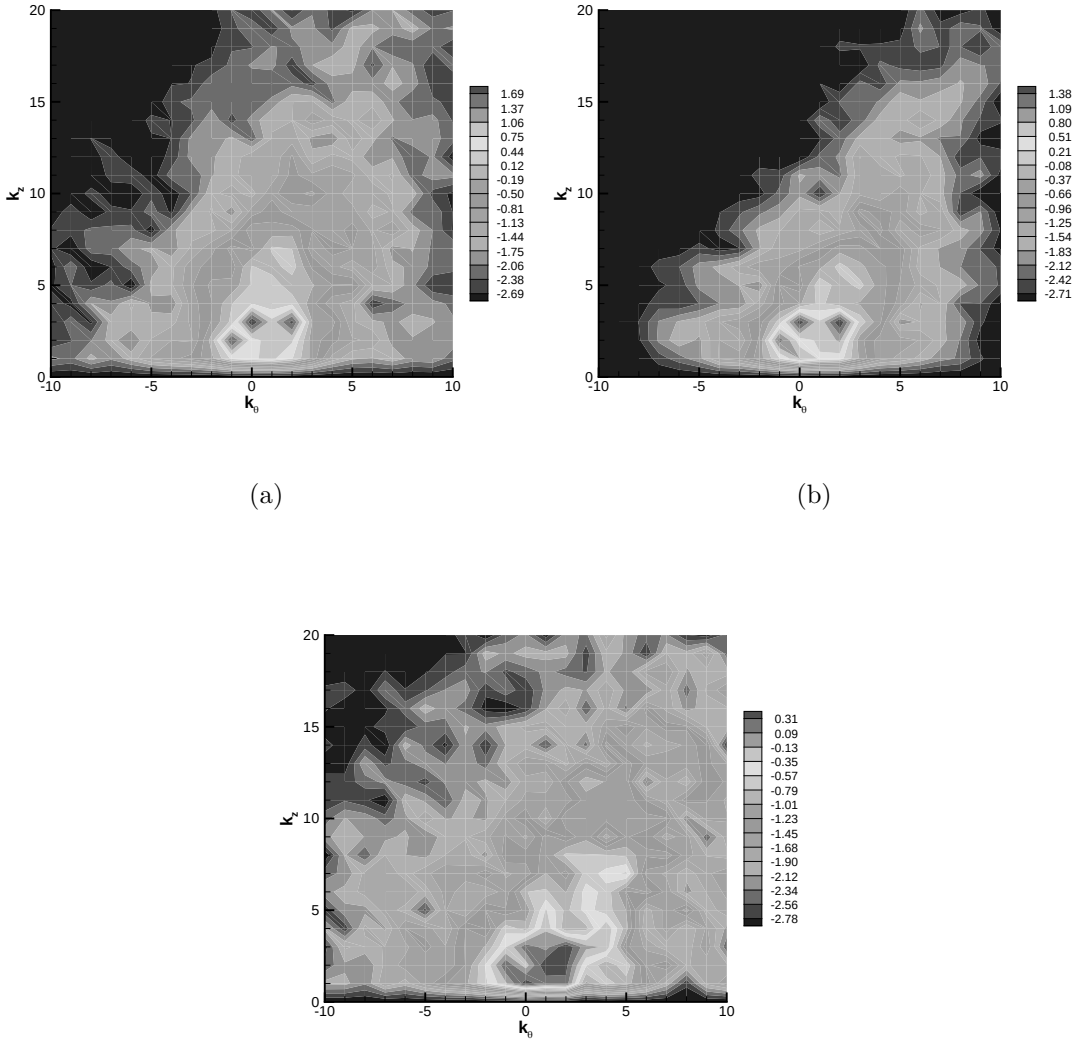


(a) (b)

(c)

Figure 3.95 2-D Energy spectra for STRN2 at $t/T = 22.07$; Contours of $log_{10}(E_{2D})$; (a), (b) and (c) correspond to $r/r_0 = 0.5$, 1.0 and 2.0 respectively

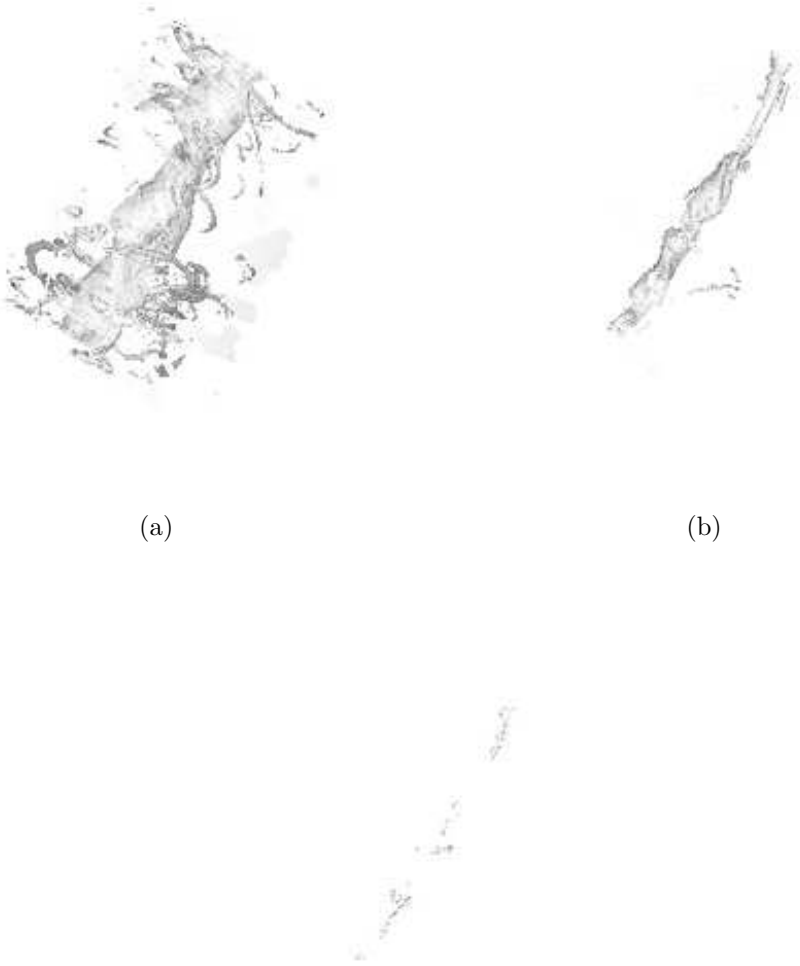

(a) (b)

(c)

Figure 3.96 Vorticity magnitude isosurfaces for STRN2 at t/T = 23.58; (a), (b) and (c) correspond to 0.1, 0.25 and 0.5 times the peak vorticity magnitude respectively

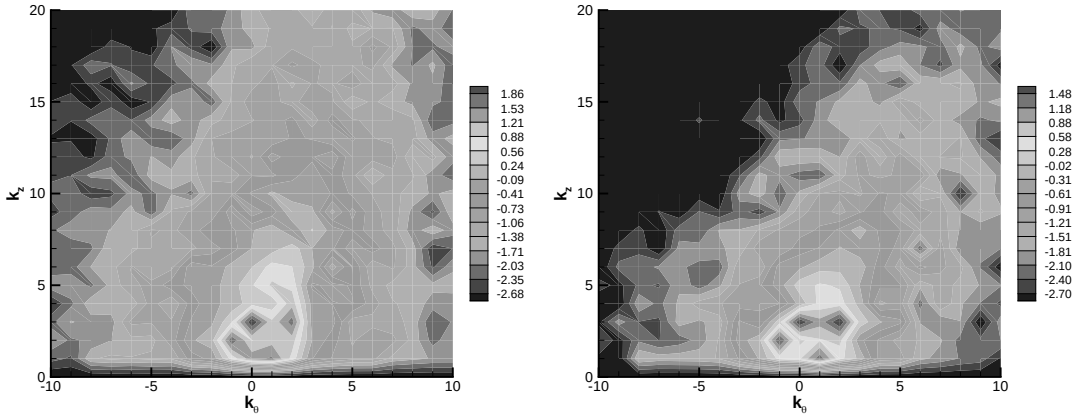


(a) (b)

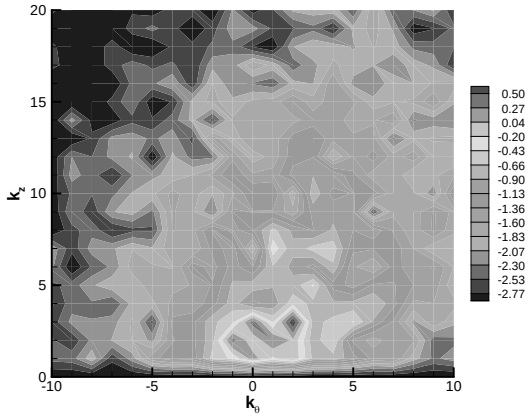


(c)

Figure 3.97 2-D Energy spectra for STRN2 at $t/T = 23.58$; Contours of $log_{10}(E_{2D})$; (a), (b) and (c) correspond to $r/r_0 = 0.5$, 1.0 and 2.0 respectively

(a) (b)

(c)

Figure 3.98 Vorticity magnitude isosurfaces for STRN2 at t/T = 25.61; (a), (b) and (c) correspond to 0.1, 0.25 and 0.5 times the peak vorticity magnitude respectively

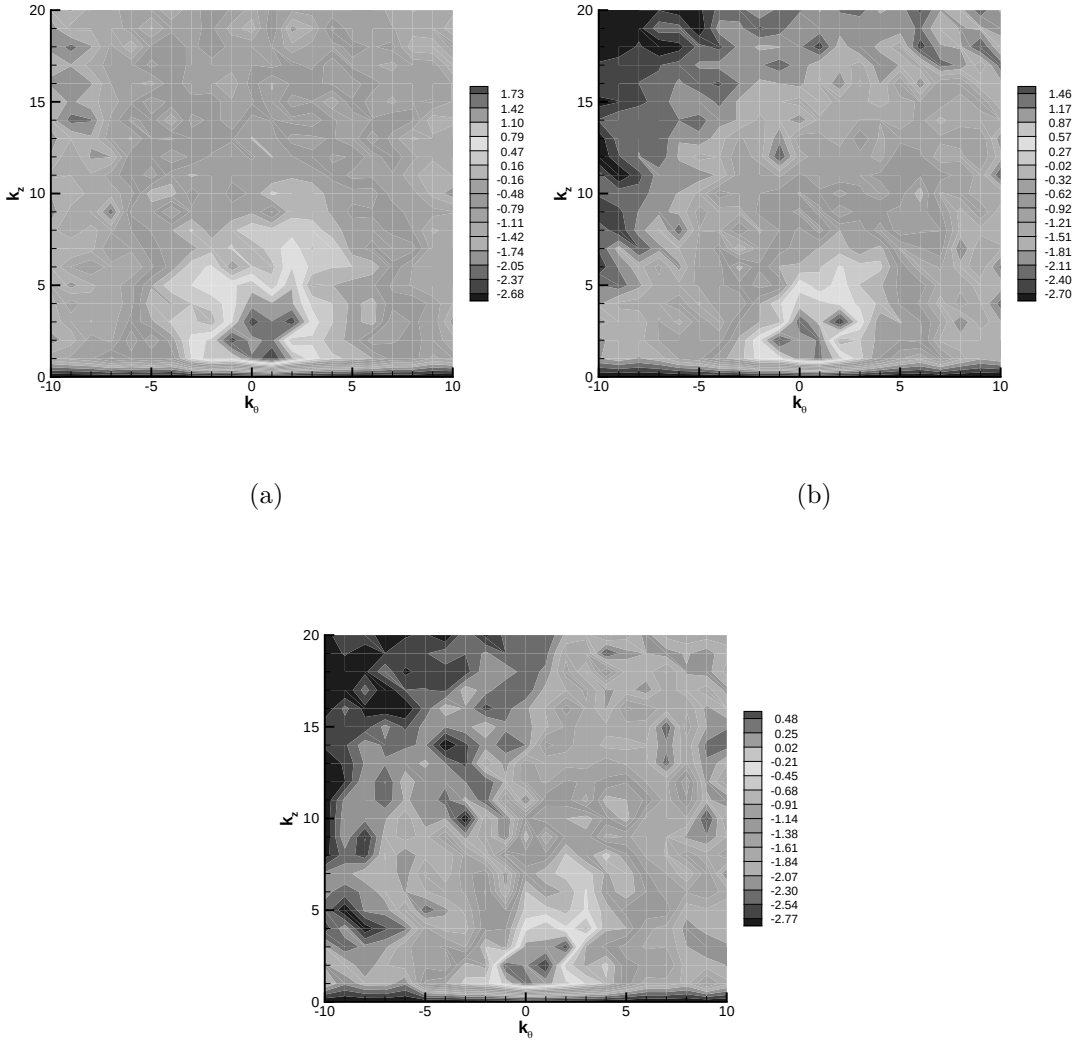


(a) (b)

(c)

Figure 3.99 2-D Energy spectra for STRN2 at $t/T = 25.61$; Contours of $log_{10}(E_{2D})$; (a), (b) and (c) correspond to $r/r_0 = 0.5$, 1.0 and 2.0 respectively

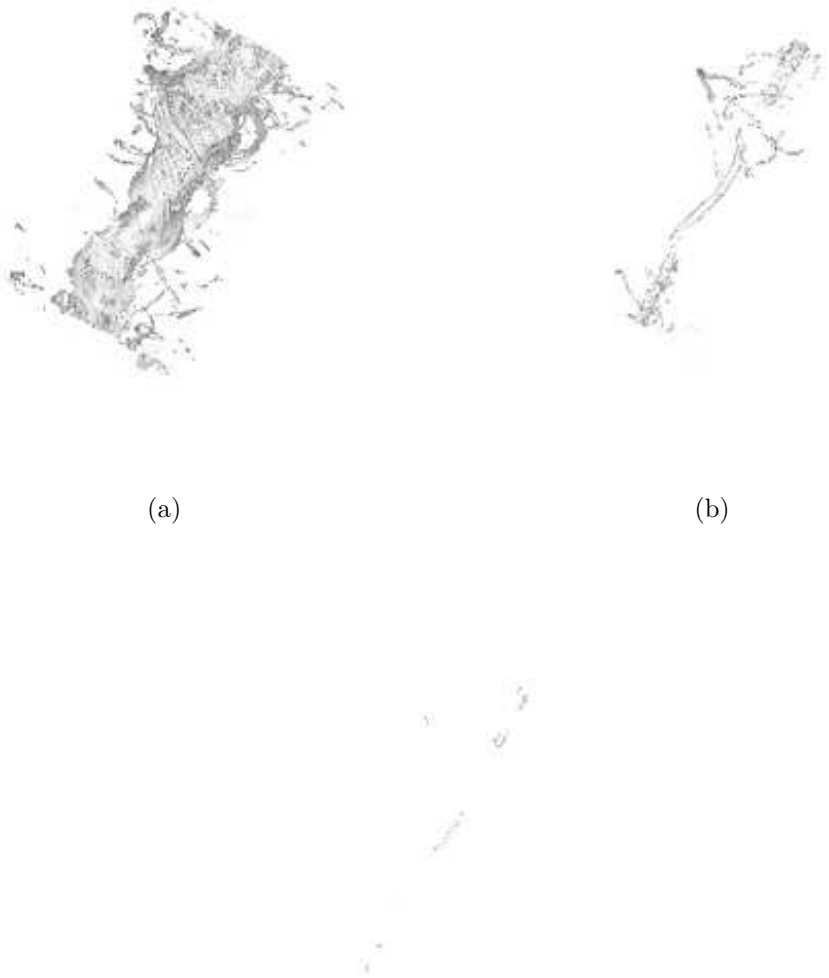

(a) (b)

(c)

Figure 3.100 Vorticity magnitude isosurfaces for STRN2 at t/T = 32.01; (a), (b) and (c) correspond to 0.1, 0.25 and 0.5 times the peak vorticity magnitude respectively

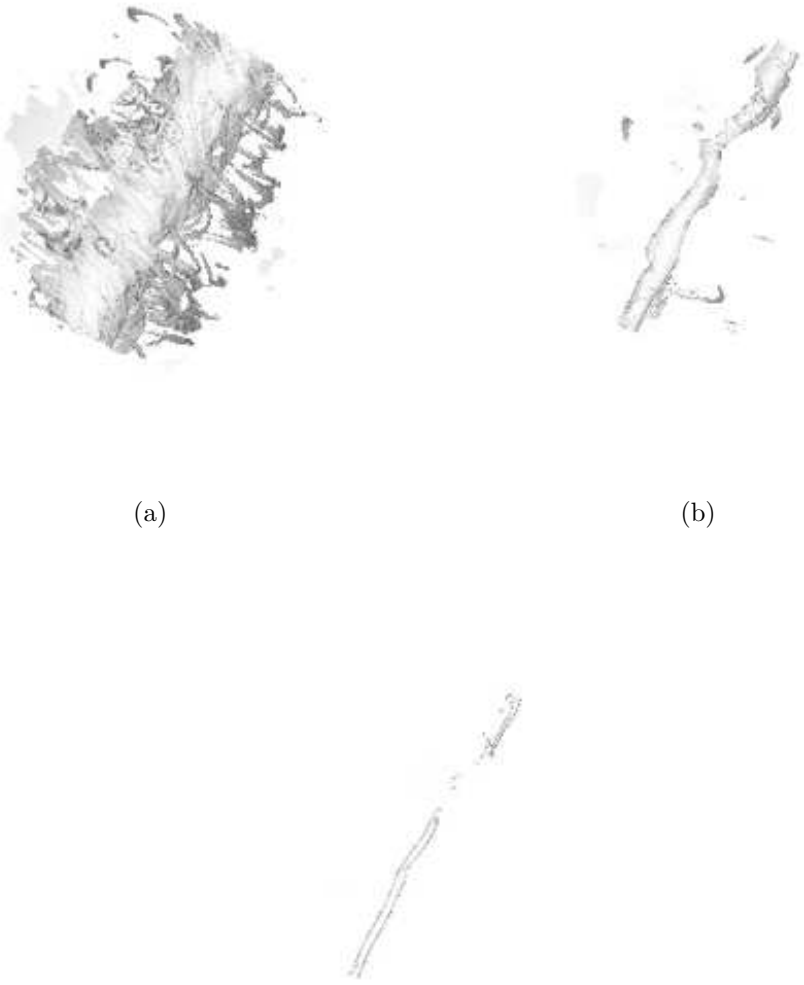

(a) (b)

(c)

Figure 3.101 Vorticity magnitude isosurfaces for STRN2 at t/T = 40.01; (a), (b) and (c) correspond to 0.1, 0.25 and 0.5 times the peak vorticity magnitude respectively

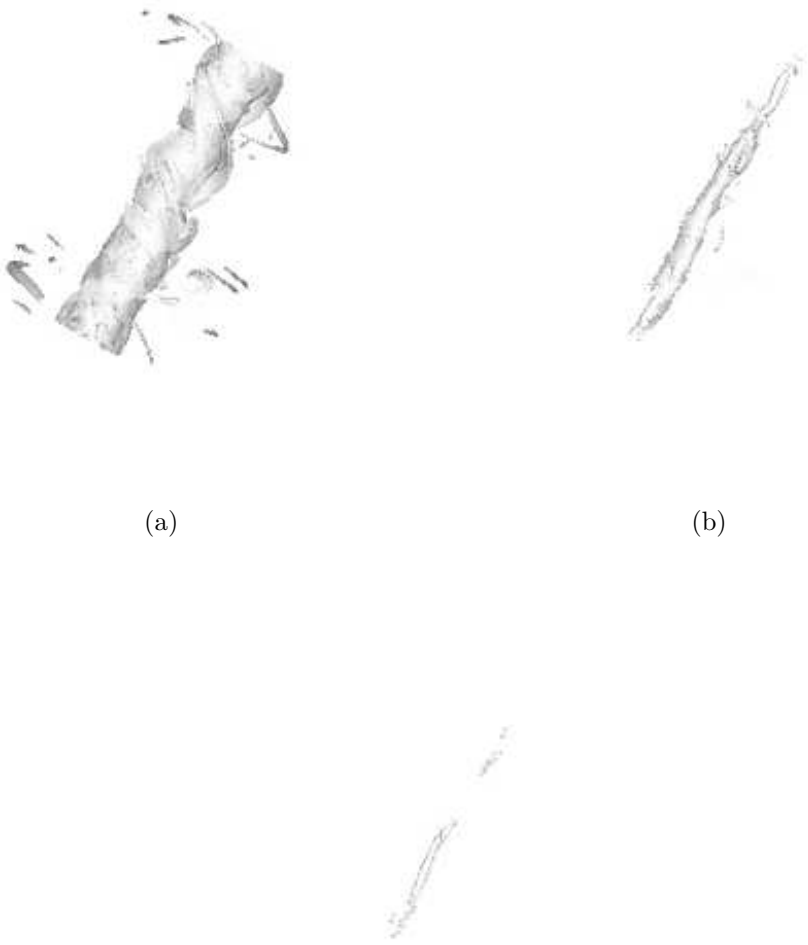

(a) (b)

(c)

Figure 3.102 Vorticity magnitude isosurfaces for STRN2 at t/T = 51.53; (a), (b) and (c) correspond to 0.1, 0.25 and 0.5 times the peak vorticity magnitude respectively

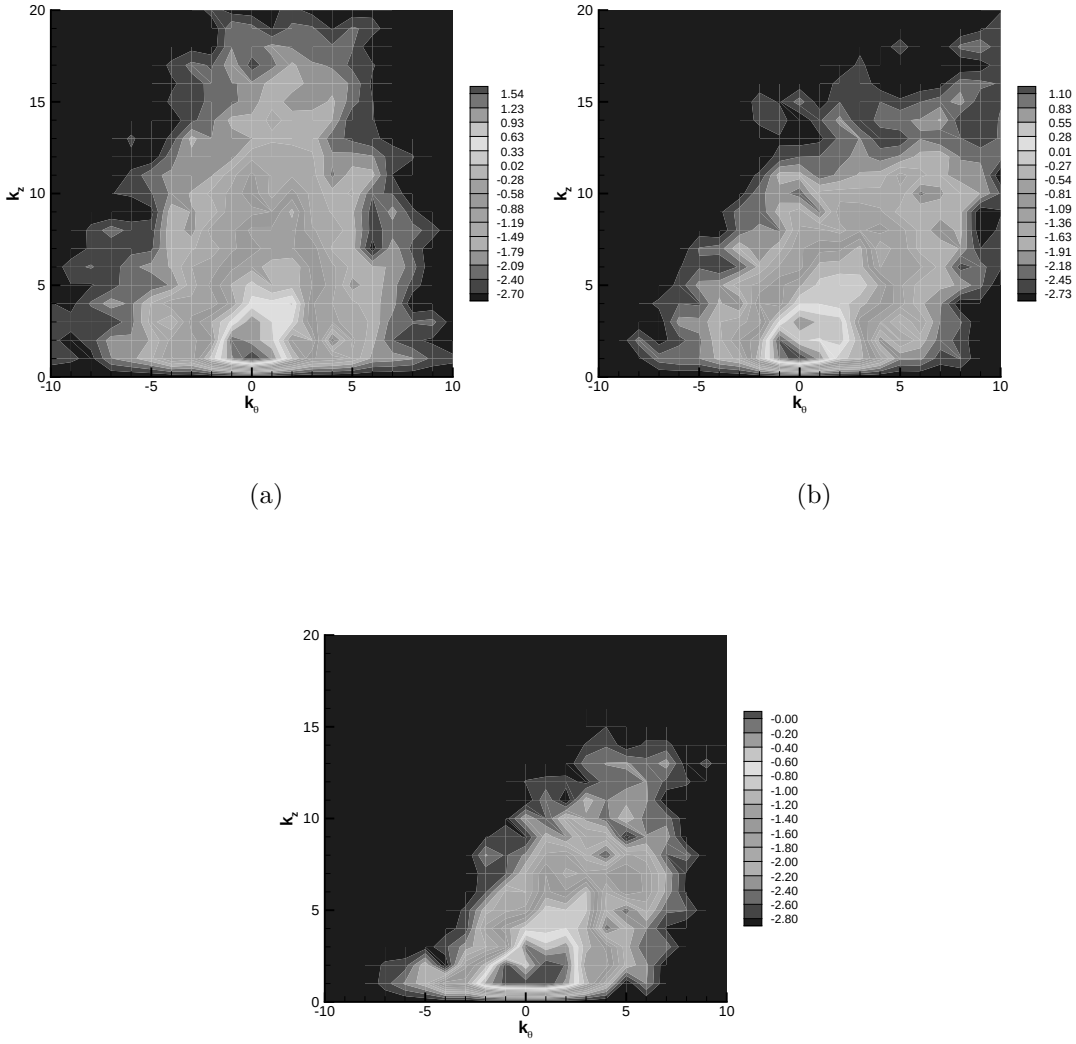


(a) (b)

(c)

Figure 3.103 2-D Energy spectra for STRN2 at $t/T = 51.53$; Contours of $log_{10}(E_{2D})$; (a), (b) and (c) correspond to $r/r_0 = 0.5$, 1.0 and 2.0 respectively

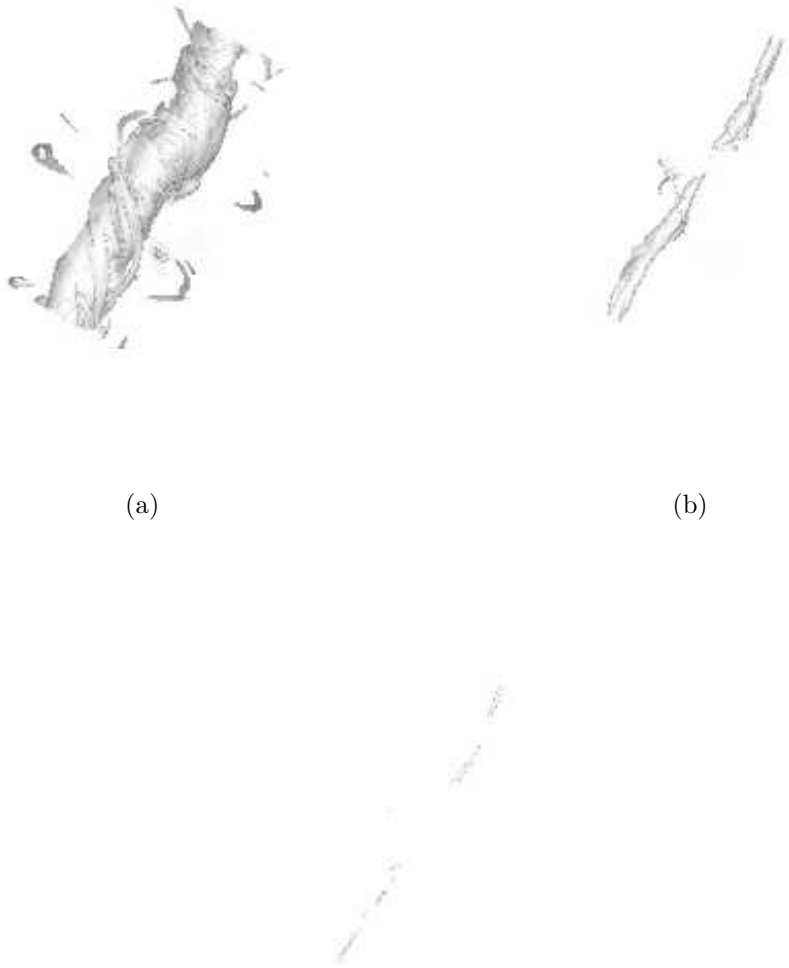

(a) (b)

(c)

Figure 3.104 Vorticity magnitude isosurfaces for STRN2 at t/T = 56.01; (a), (b) and (c) correspond to 0.1, 0.25 and 0.5 times the peak vorticity magnitude respectively

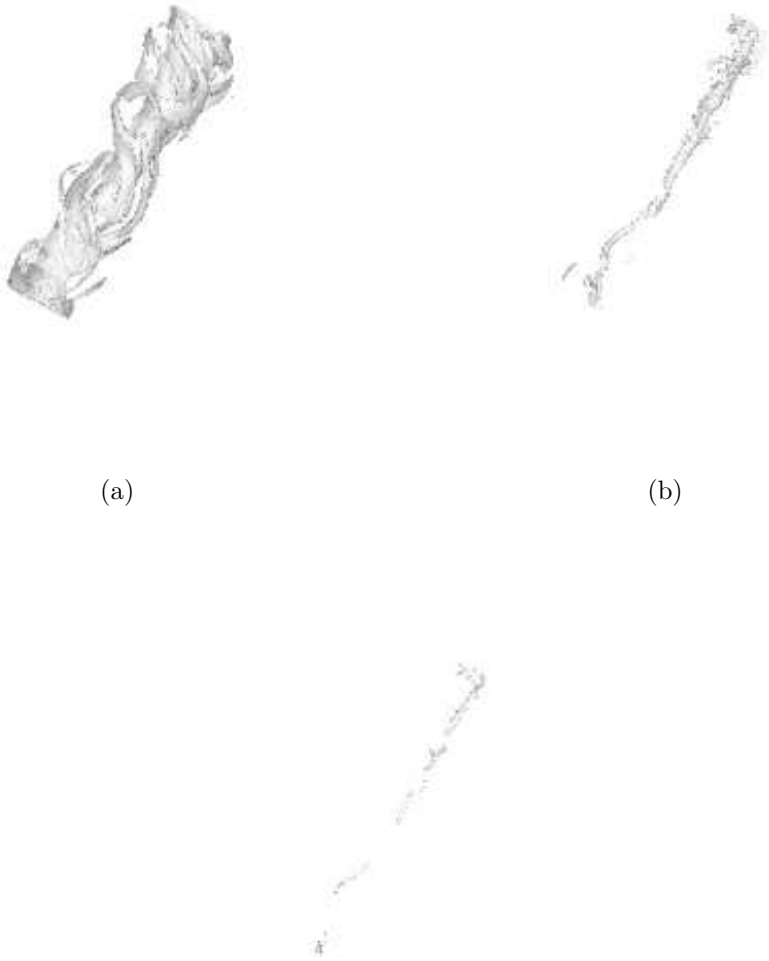

(a) (b)

(c)

Figure 3.105 Vorticity magnitude isosurfaces for STRN2 at t/T = 62; (a), (b) and (c) correspond to 0.1, 0.25 and 0.5 times the peak vorticity magnitude respectively

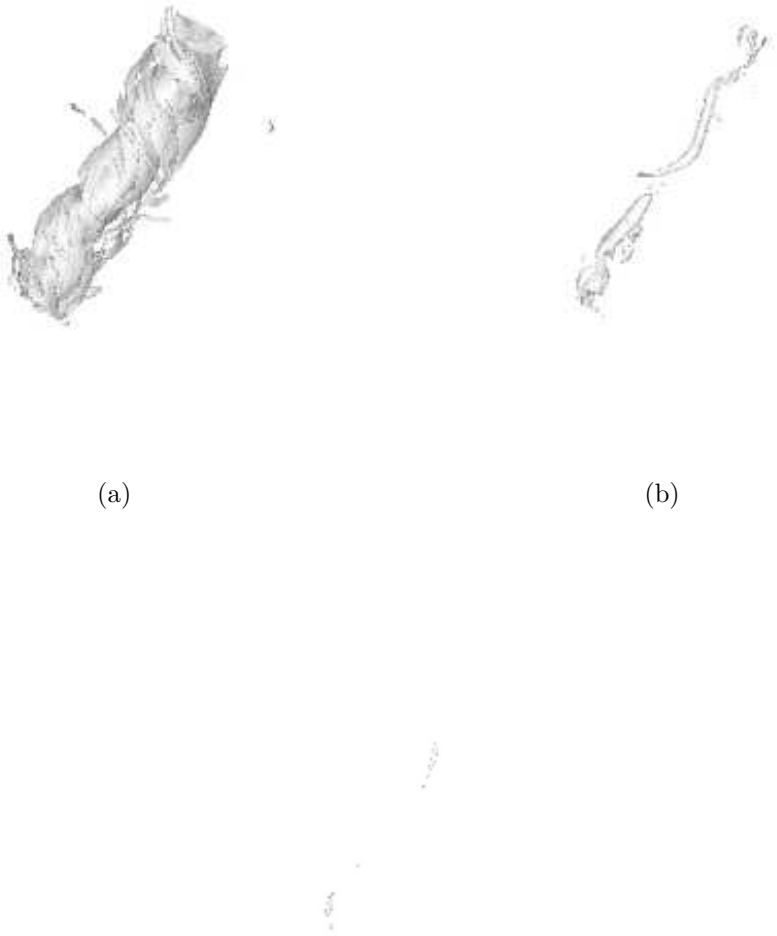

(a) (b)

(c)

Figure 3.106 Vorticity magnitude isosurfaces for STRN2 at t/T = 68.08; (a), (b) and (c) correspond to 0.1, 0.25 and 0.5 times the peak vorticity magnitude respectively

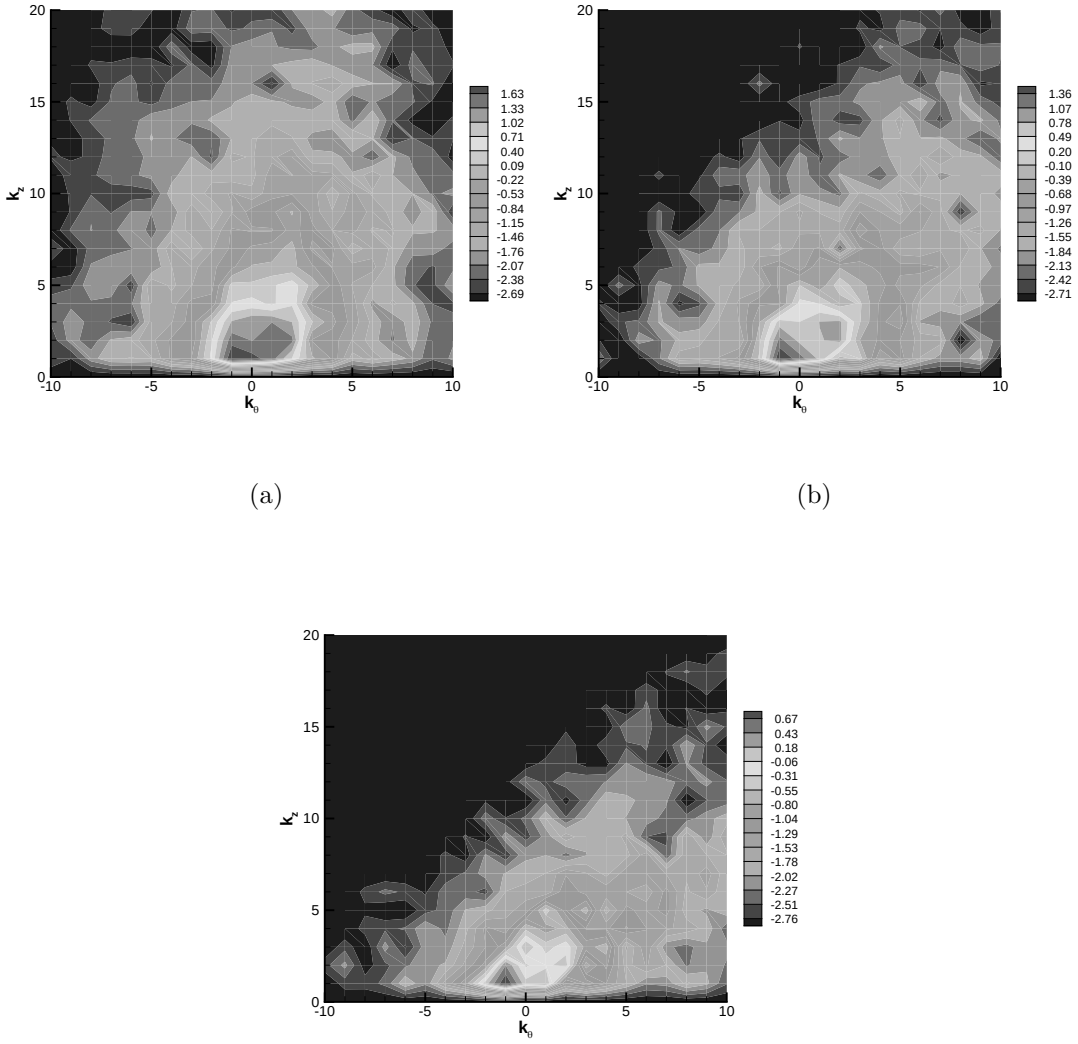


(a) (b)

(c)

Figure 3.107 2-D Energy spectra for STRN2 at $t/T = 68.08$; Contours of $log_{10}(E_{2D})$; (a), (b) and (c) correspond to $r/r_0 = 0.5$, 1.0 and 2.0 respectively

(a) (b)

(c)

Figure 3.108 Vorticity magnitude isosurfaces for STRN2 at t/T = 74.04; (a), (b) and (c) correspond to 0.1, 0.25 and 0.5 times the peak vorticity magnitude respectively

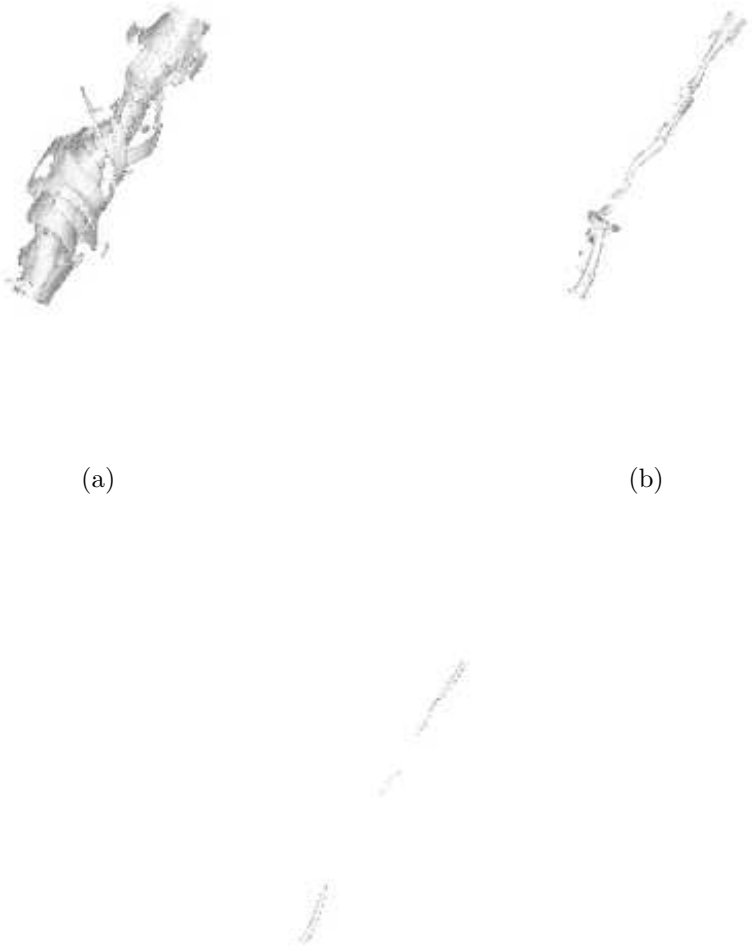

(a) (b)

(c)

Figure 3.109 Vorticity magnitude isosurfaces for STRN2 at t/T = 80.52; (a), (b) and (c) correspond to 0.1, 0.25 and 0.5 times the peak vorticity magnitude respectively

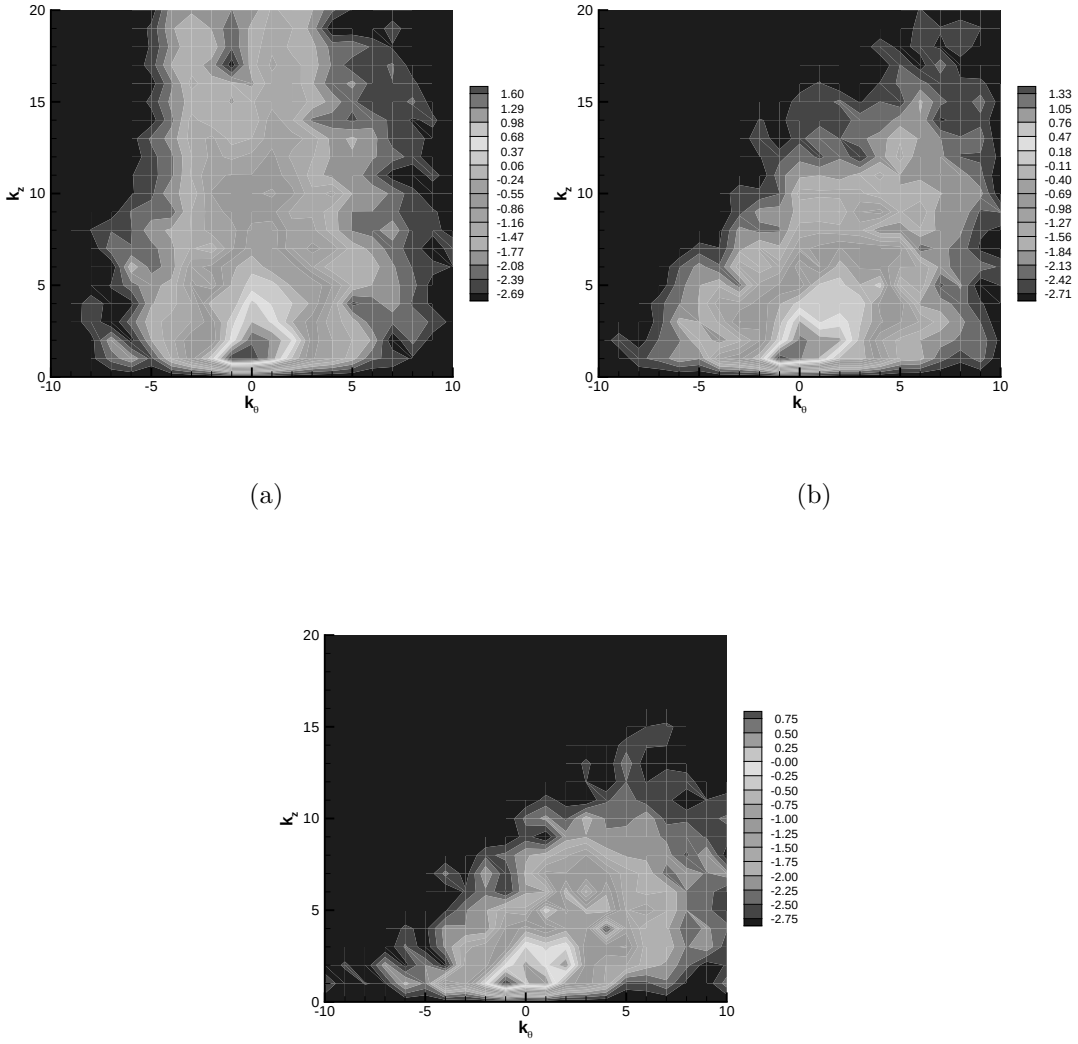


(a) (b)

(c)

Figure 3.110 2-D Energy spectra for STRN2 at $t/T = 80.52$; Contours of $log_{10}(E_{2D})$; (a), (b) and (c) correspond to $r/r_0 = 0.5$, 1.0 and 2.0 respectively

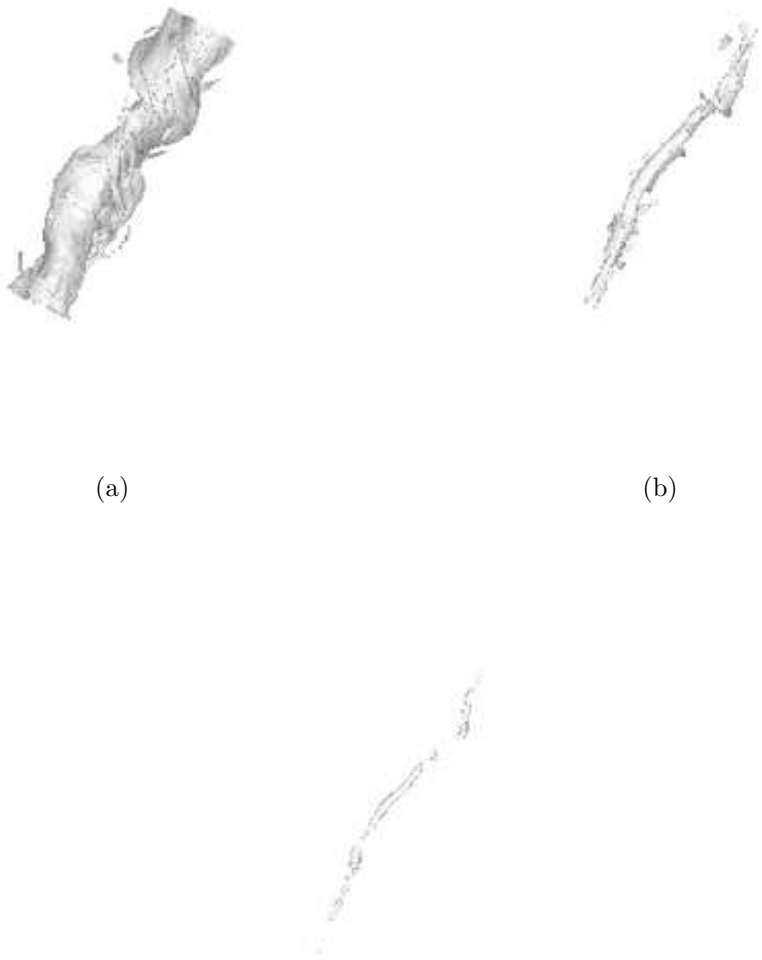

(a) (b)

(c)

Figure 3.111 Vorticity magnitude isosurfaces for STRN2 at t/T = 83.51; (a), (b) and (c) correspond to 0.1, 0.25 and 0.5 times the peak vorticity magnitude respectively

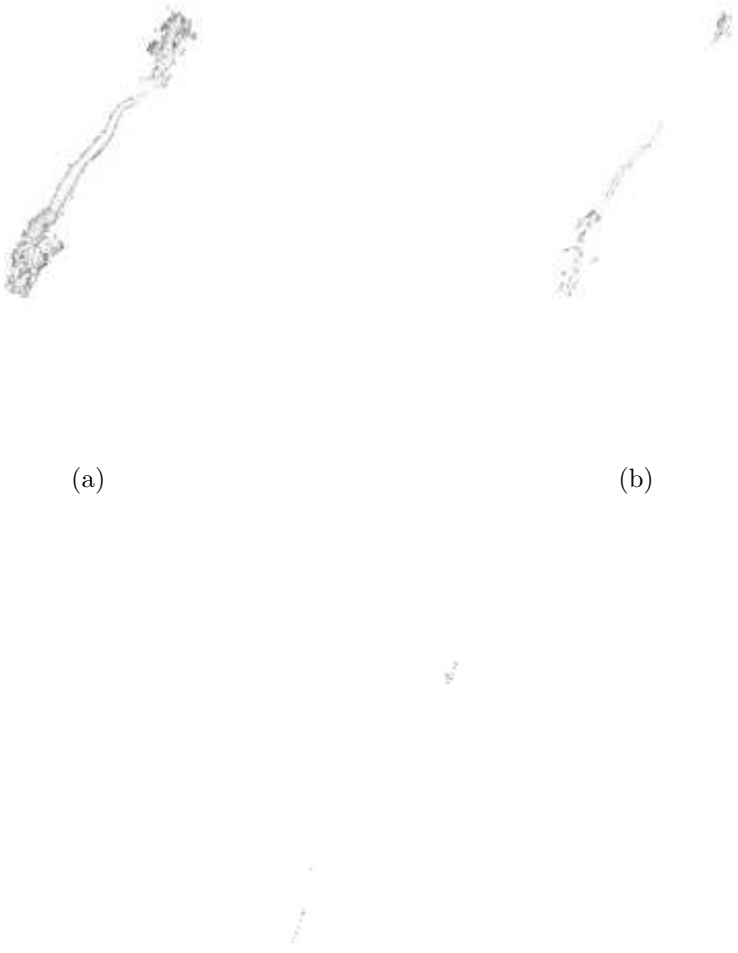

(a) (b)

(c)

Figure 3.112 Vorticity magnitude isosurfaces for STRN2 at t/T = 85.45; (a), (b) and (c) correspond to 0.1, 0.25 and 0.5 times the peak vorticity magnitude respectively

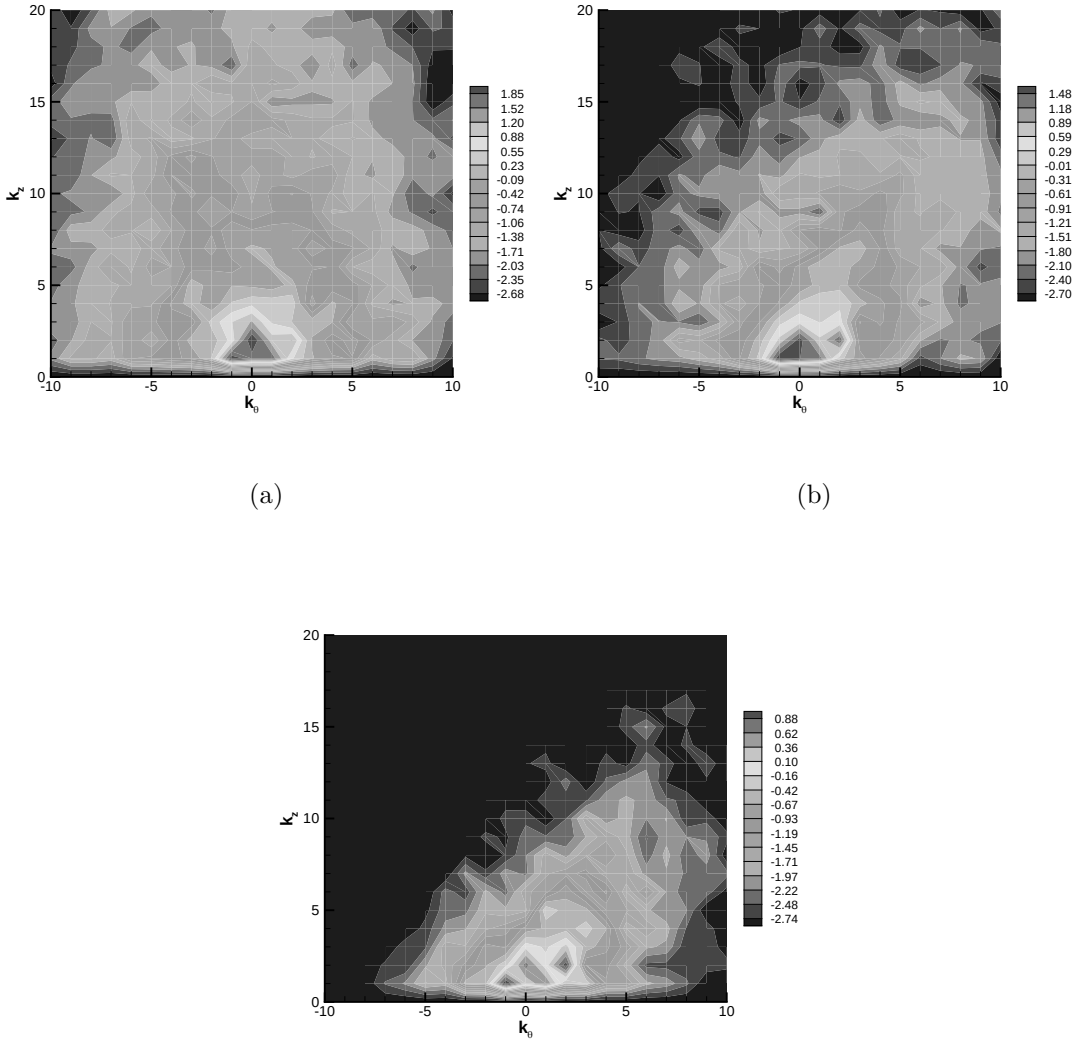


(a) (b)

(c)

Figure 3.113 2-D Energy spectra for STRN2 at $t/T = 85.45$; Contours of $log_{10}(E_{2D})$; (a), (b) and (c) correspond to $r/r_0 = 0.5$, 1.0 and 2.0 respectively

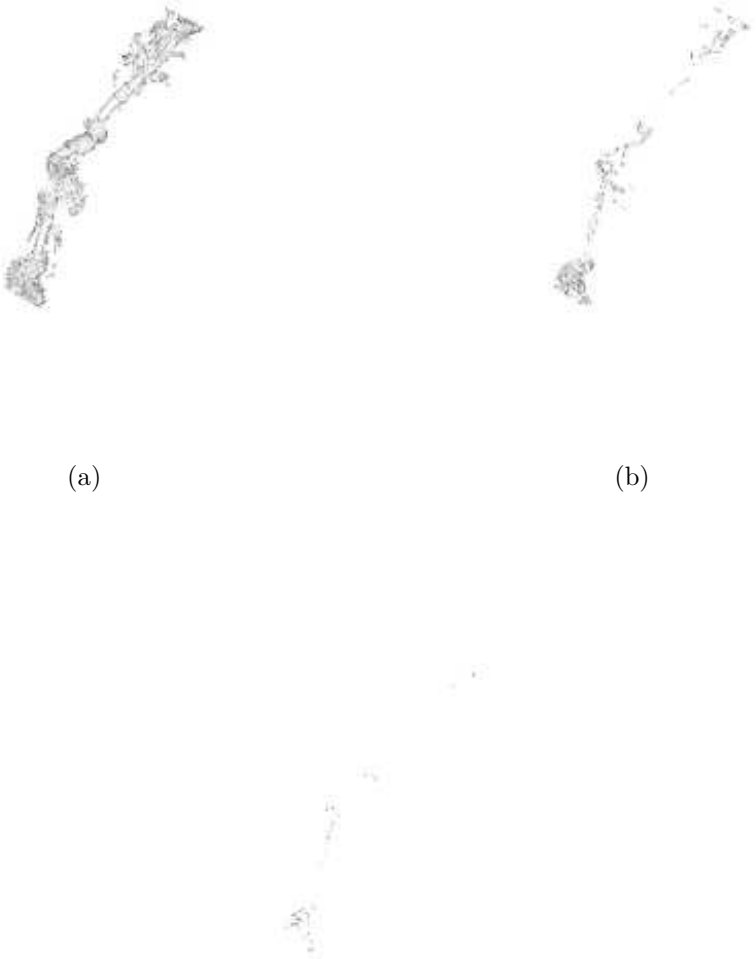

(a) (b)

(c)

Figure 3.114 Vorticity magnitude isosurfaces for STRN2 at t/T = 87.66; (a), (b) and (c) correspond to 0.1, 0.25 and 0.5 times the peak vorticity magnitude respectively

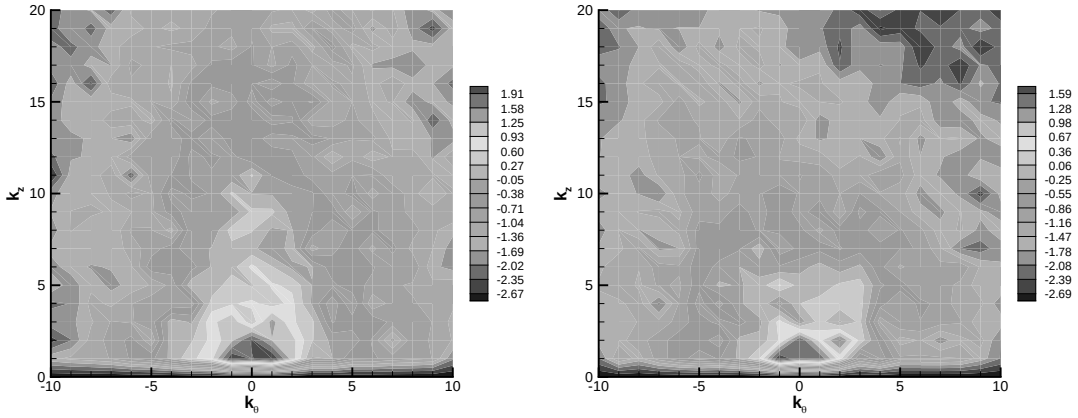


(a) (b)

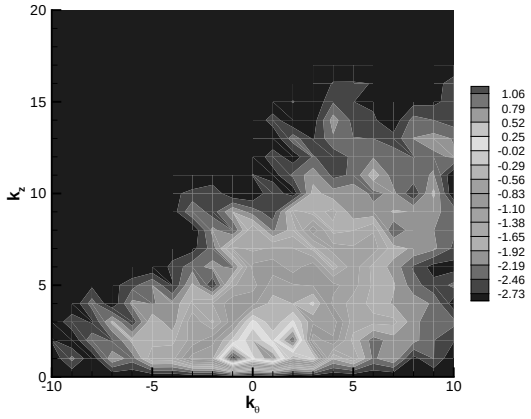


(c)

Figure 3.115 2-D Energy spectra for STRN2 at $t/T = 87.66$; Contours of $log_{10}(E_{2D})$; (a), (b) and (c) correspond to $r/r_0 = 0.5$, 1.0 and 2.0 respectively

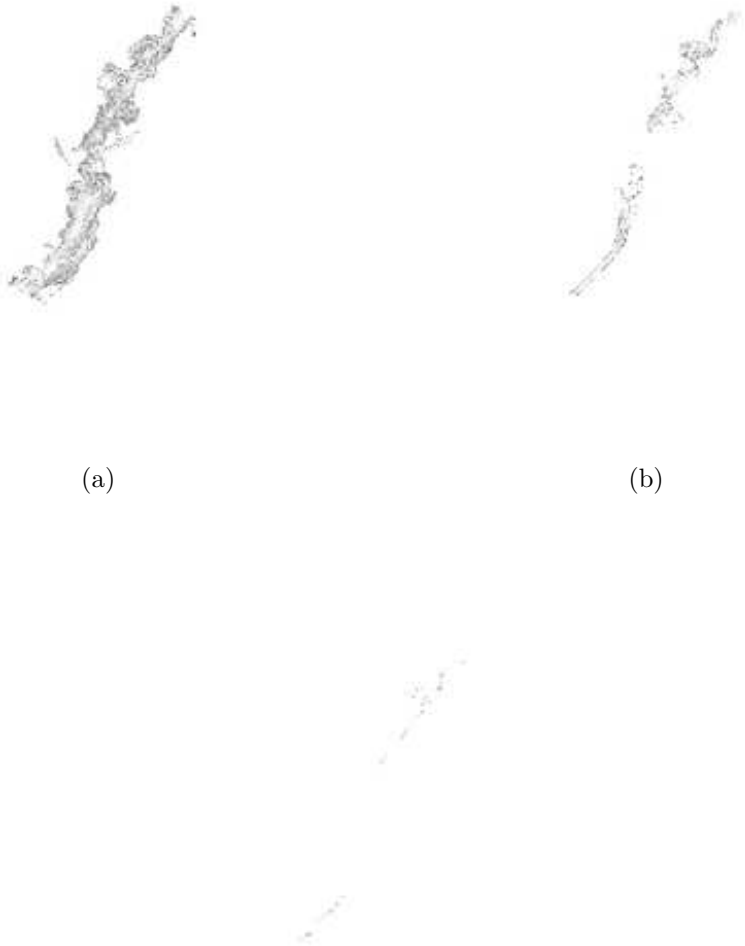

(a) (b)

(c)

Figure 3.116 Vorticity magnitude isosurfaces for STRN2 at t/T = 90.92; (a), (b) and (c) correspond to 0.1, 0.25 and 0.5 times the peak vorticity magnitude respectively

(a) (b)

(c)

Figure 3.117 Vorticity magnitude isosurfaces for STRN2 at t/T = 94.12; (a), (b) and (c) correspond to 0.1, 0.25 and 0.5 times the peak vorticity magnitude respectively

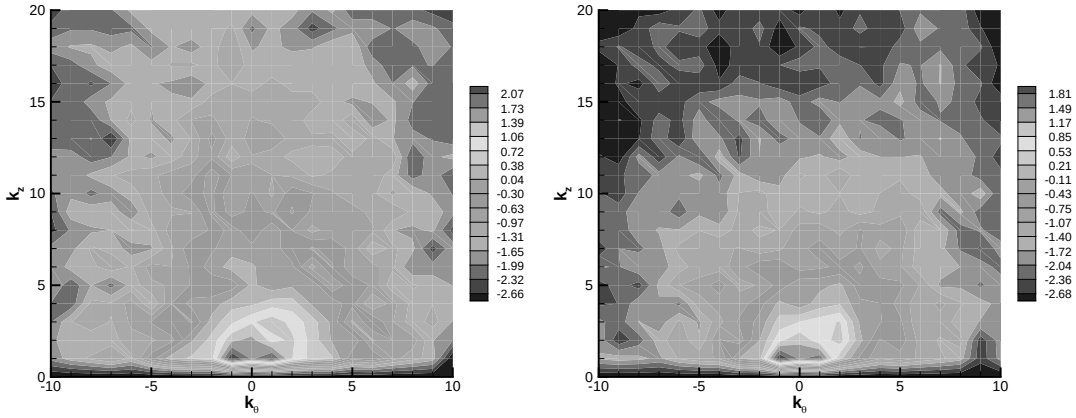


(a) (b)

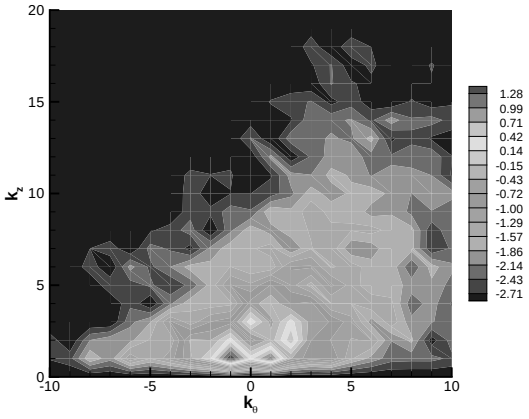


(c)

Figure 3.118 2-D Energy spectra for STRN2 at $t/T = 94.12$; Contours of $log_{10}(E_{2D})$; (a), (b) and (c) correspond to $r/r_0 = 0.5$, 1.0 and 2.0 respectively

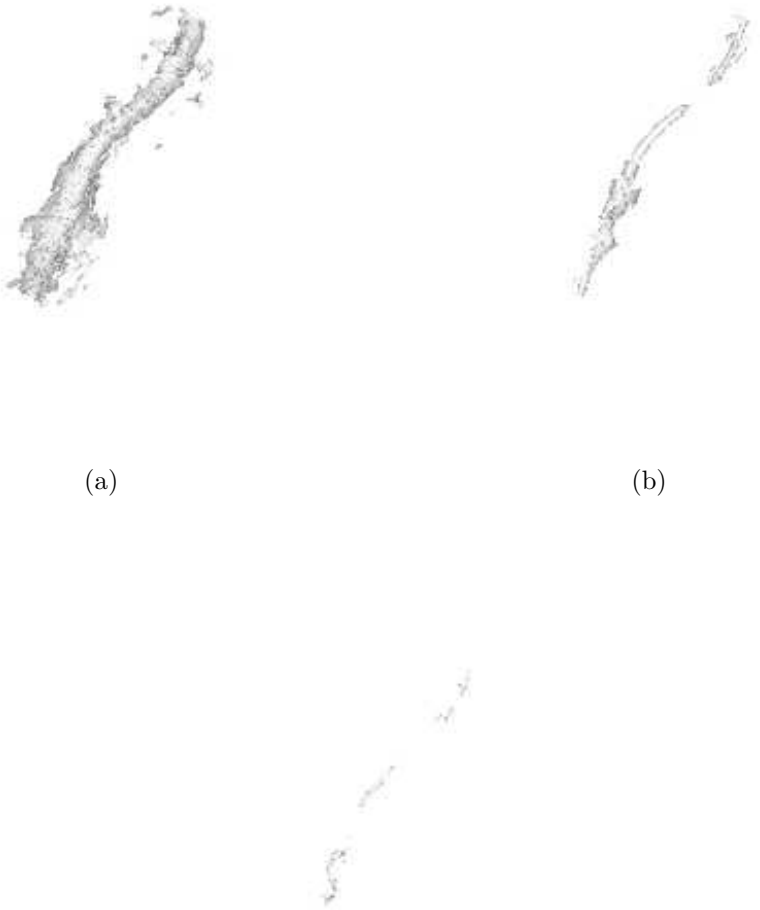

(a) (b)

(c)

Figure 3.119 Vorticity magnitude isosurfaces for STRN2 at t/T = 96.77; (a), (b) and (c) correspond to 0.1, 0.25 and 0.5 times the peak vorticity magnitude respectively

(a) (b)

(c)

Figure 3.120 Vorticity magnitude isosurfaces for STRN2 at t/T = 98.45; (a), (b) and (c) correspond to 0.1, 0.25 and 0.5 times the peak vorticity magnitude respectively

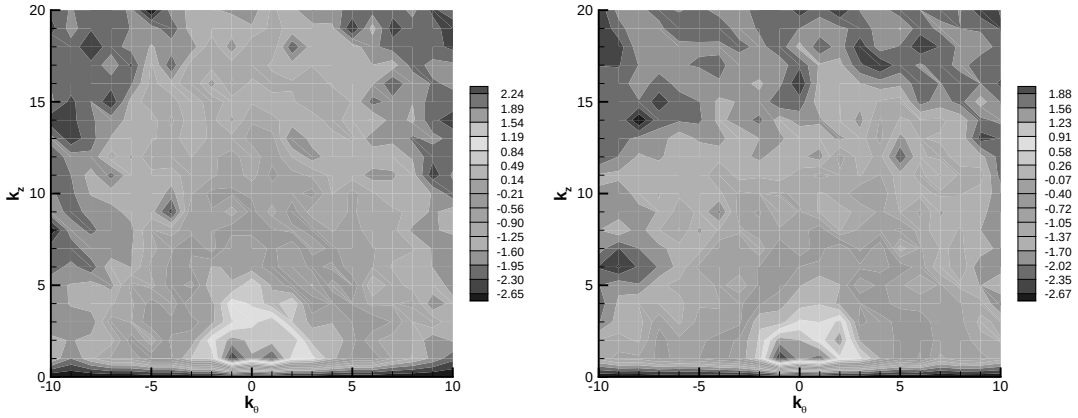


(a) (b)

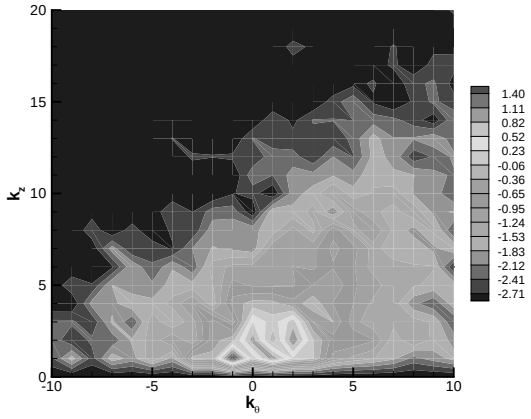


(c)

Figure 3.121 2-D Energy spectra for STRN2 at $t/T = 98.45$; Contours of $log_{10}(E_{2D})$; (a), (b) and (c) correspond to $r/r_0 = 0.5$, 1.0 and 2.0 respectively

(a) (b)

(c)

Figure 3.122 Vorticity magnitude isosurfaces for STRN2 at t/T = 100.29; (a), (b) and (c) correspond to 0.1, 0.25 and 0.5 times the peak vorticity magnitude respectively

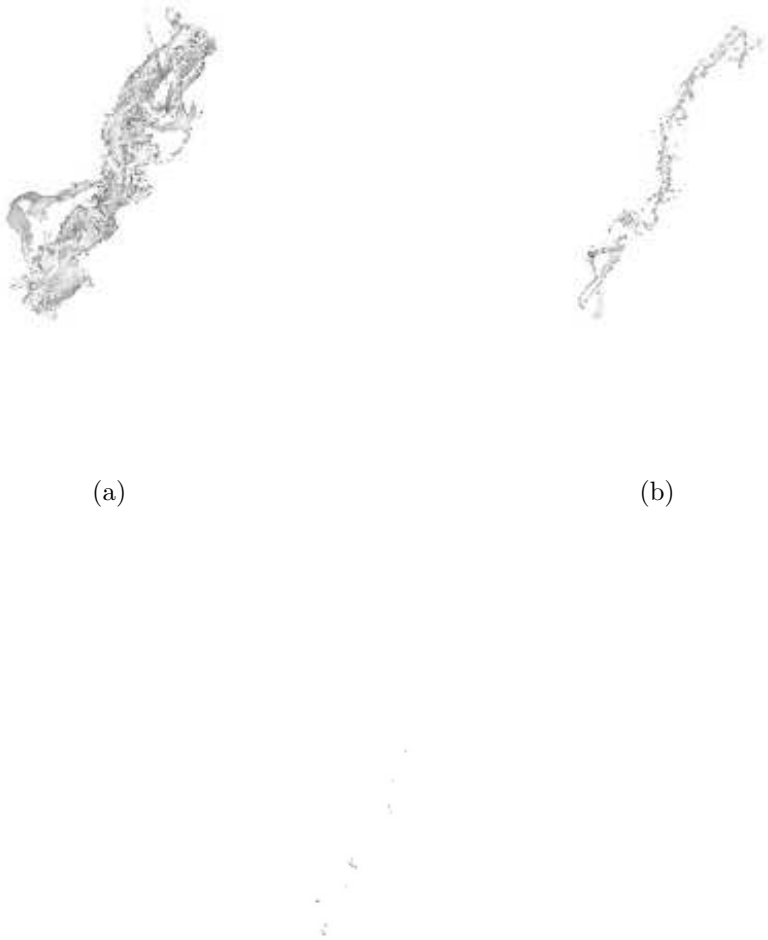

(a) (b)

(c)

Figure 3.123 Vorticity magnitude isosurfaces for STRN2 at t/T = 101.34; (a), (b) and (c) correspond to 0.1, 0.25 and 0.5 times the peak vorticity magnitude respectively

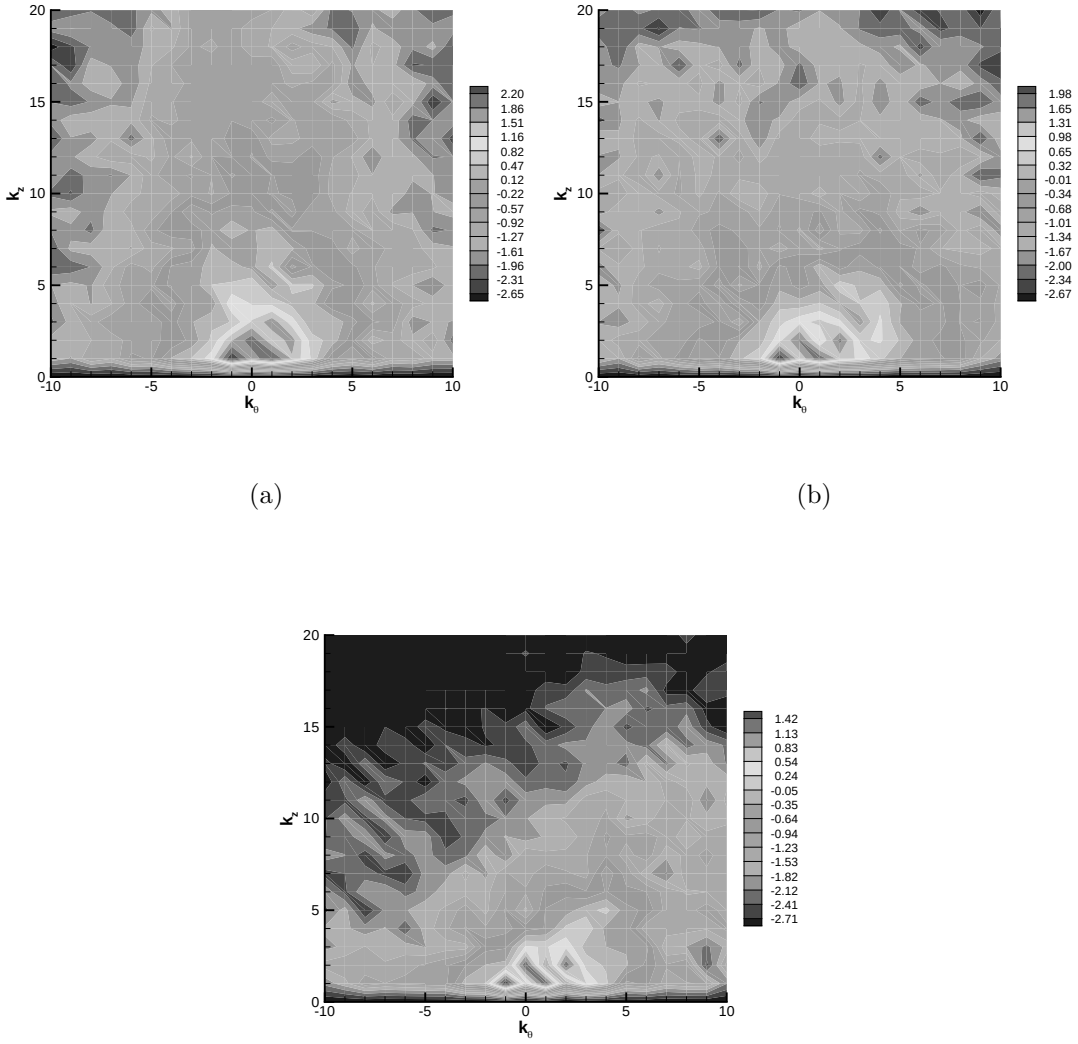


(a) (b)

(c)

Figure 3.124 2-D Energy spectra for STRN2 at $t/T = 101.34$; Contours of $log_{10}(E_{2D})$; (a), (b) and (c) correspond to $r/r_0 = 0.5$, 1.0 and 2.0 respectively

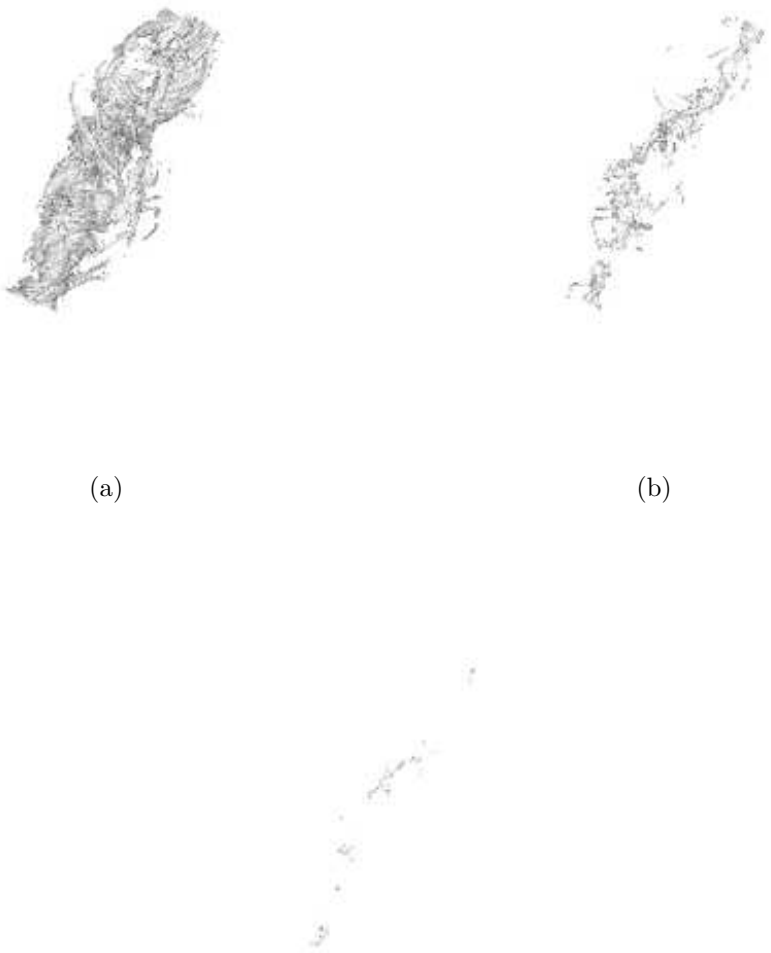

(a) (b)

(c)

Figure 3.125 Vorticity magnitude isosurfaces for STRN2 at t/T = 103.05; (a), (b) and (c) correspond to 0.1, 0.25 and 0.5 times the peak vorticity magnitude respectively

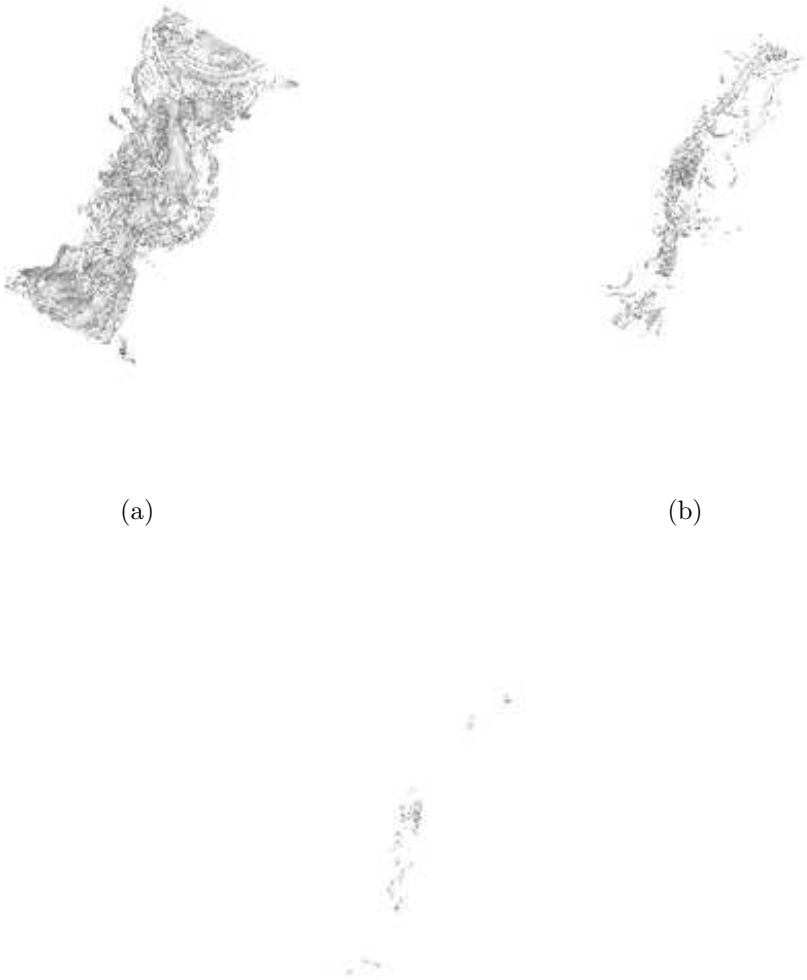

(a) (b)

(c)

Figure 3.126 Vorticity magnitude isosurfaces for STRN2 at t/T = 104.3; (a), (b) and (c) correspond to 0.1, 0.25 and 0.5 times the peak vorticity magnitude respectively

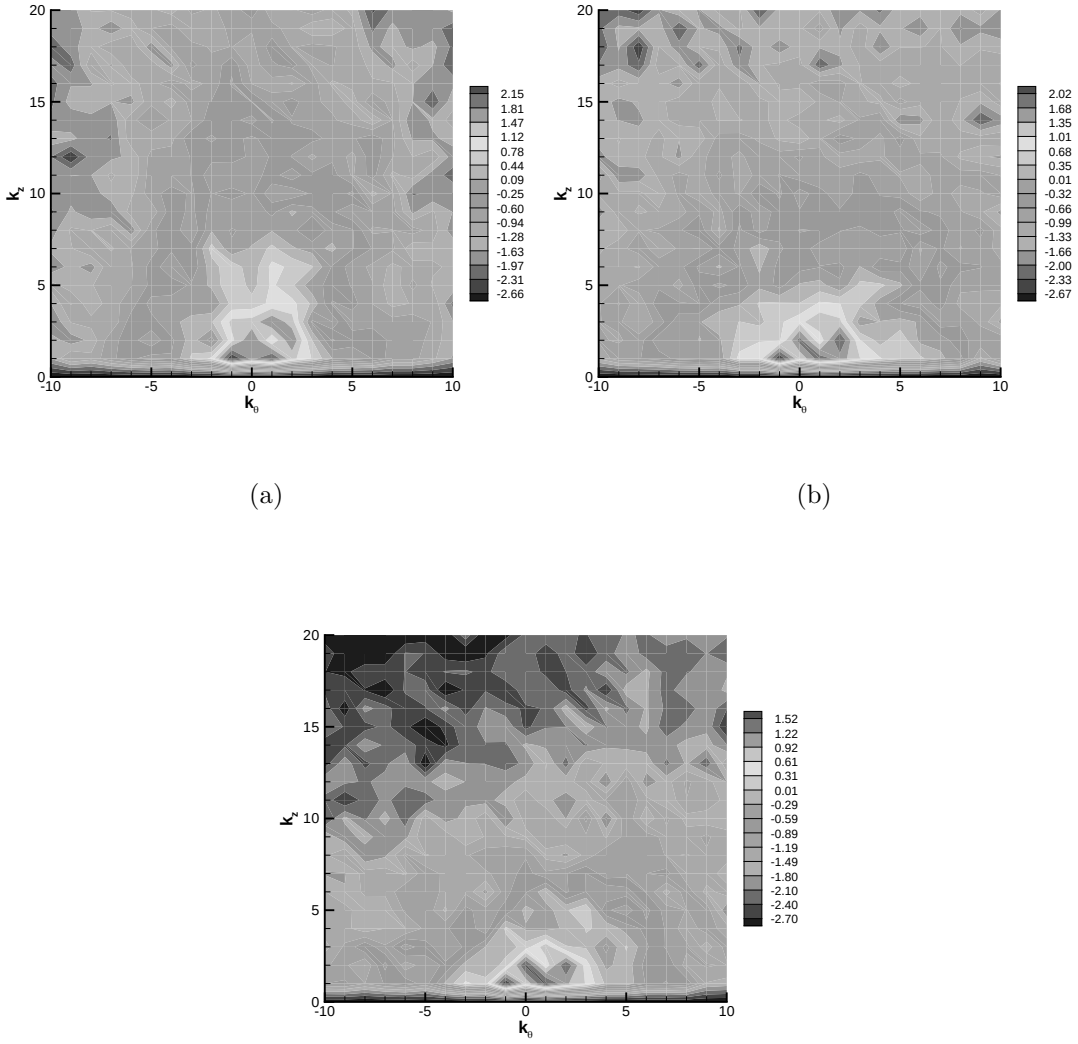


(a) (b)

(c)

Figure 3.127 2-D Energy spectra for STRN2 at $t/T = 104.3$; Contours of $log_{10}(E_{2D})$; (a), (b) and (c) correspond to $r/r_0 = 0.5$, 1.0 and 2.0 respectively

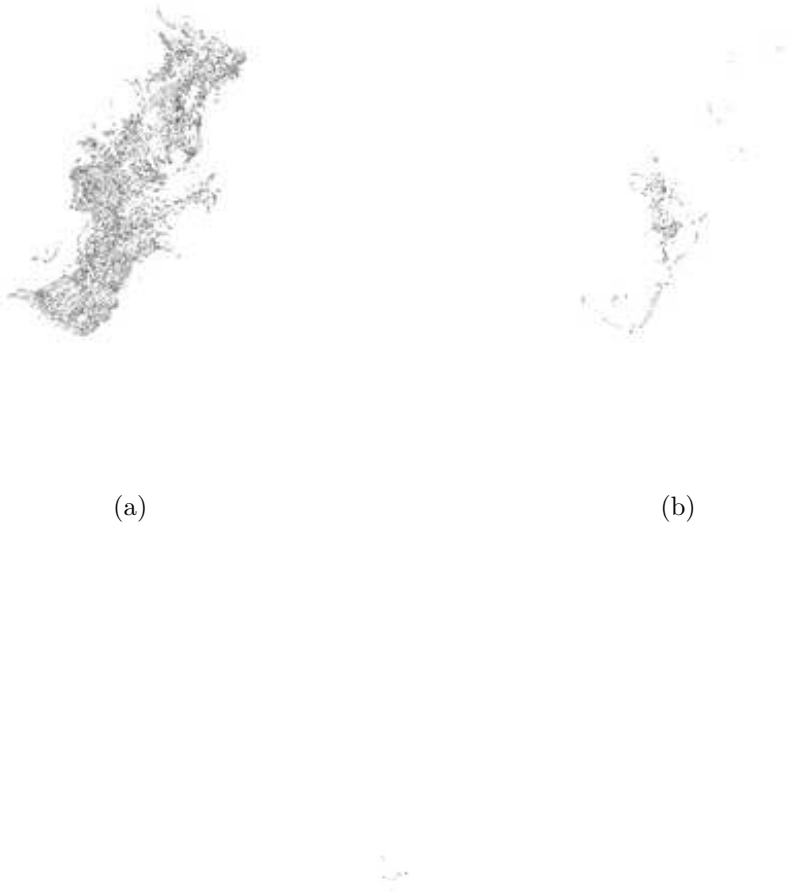

(a) (b)

(c)

Figure 3.128 Vorticity magnitude isosurfaces for STRN2 at t/T = 106.41; (a), (b) and (c) correspond to 0.1, 0.25 and 0.5 times the peak vorticity magnitude respectively

(a) (b)

(c)

Figure 3.129 Vorticity magnitude isosurfaces for STRN2 at t/T = 108.55; (a), (b) and (c) correspond to 0.1, 0.25 and 0.5 times the peak vorticity magnitude respectively

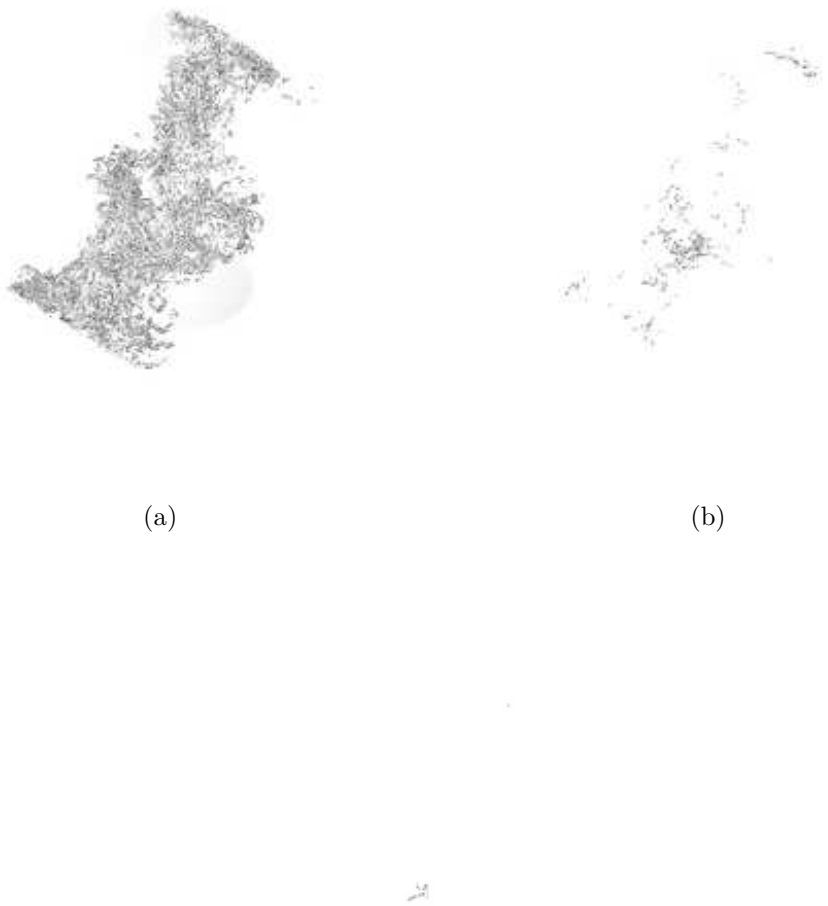

(a) (b)

(c)

Figure 3.130 Vorticity magnitude isosurfaces for STRN2 at t/T = 109.52; (a), (b) and (c) correspond to 0.1, 0.25 and 0.5 times the peak vorticity magnitude respectively

(a) (b)

(c)

Figure 3.131 Vorticity magnitude isosurfaces for STRN2 at t/T = 111.27; (a), (b) and (c) correspond to 0.1, 0.25 and 0.5 times the peak vorticity magnitude respectively

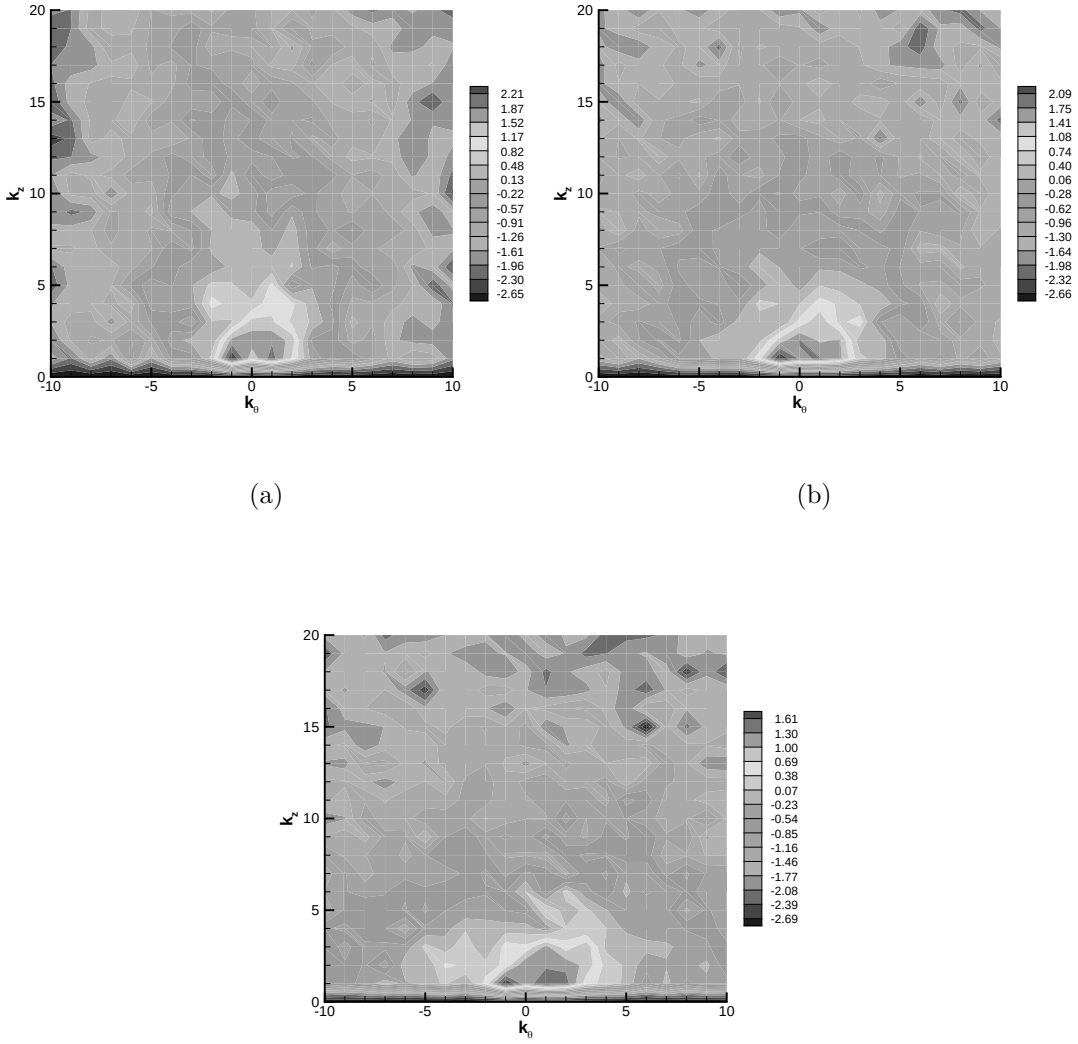


(a) (b)

(c)

Figure 3.132 2-D Energy spectra for STRN2 at $t/T = 111.27$; Contours of $log_{10}(E_{2D})$; (a), (b) and (c) correspond to $r/r_0 = 0.5$, 1.0 and 2.0 respectively

(a) (b)

(c)

Figure 3.133 Vorticity magnitude isosurfaces for STRN2 at t/T = 112.53; (a), (b) and (c) correspond to 0.1, 0.25 and 0.5 times the peak vorticity magnitude respectively

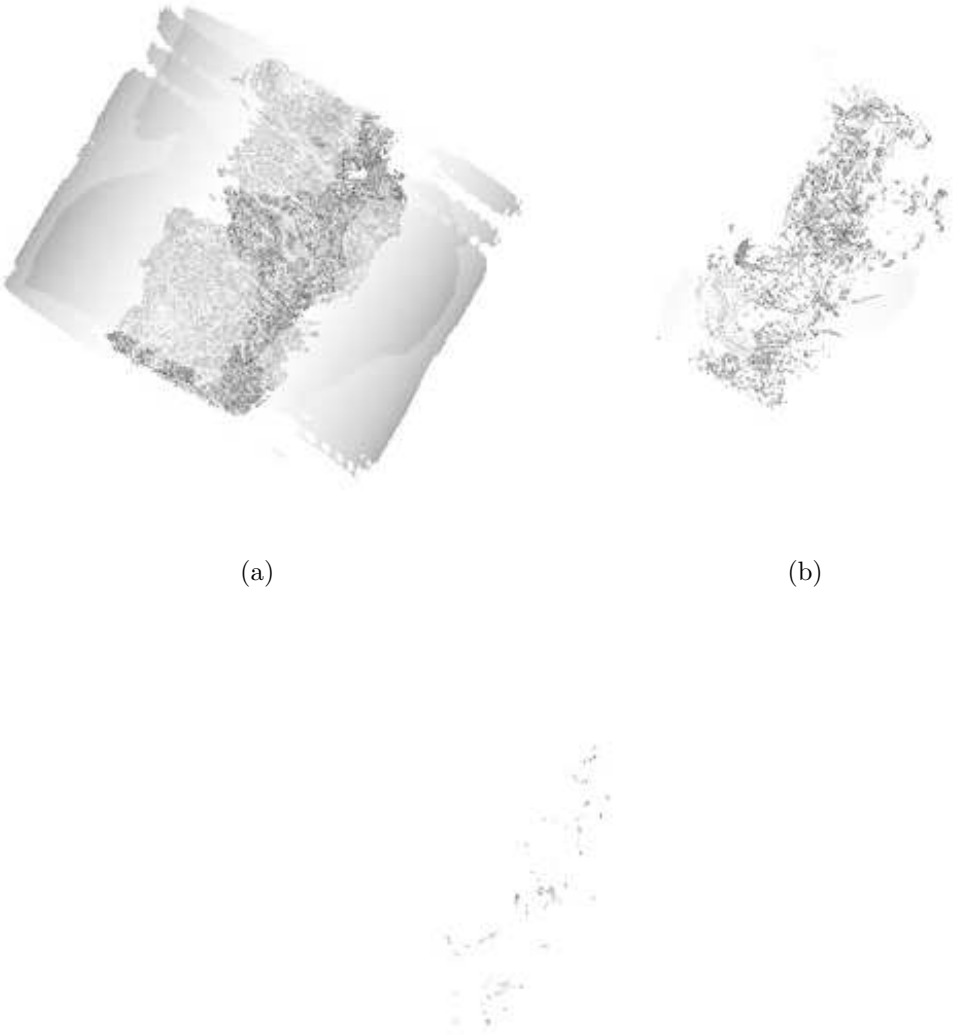

(a) (b)

(c)

Figure 3.134 Vorticity magnitude isosurfaces for STRN2 at t/T = 113.93; (a), (b) and (c) correspond to 0.1, 0.25 and 0.5 times the peak vorticity magnitude respectively

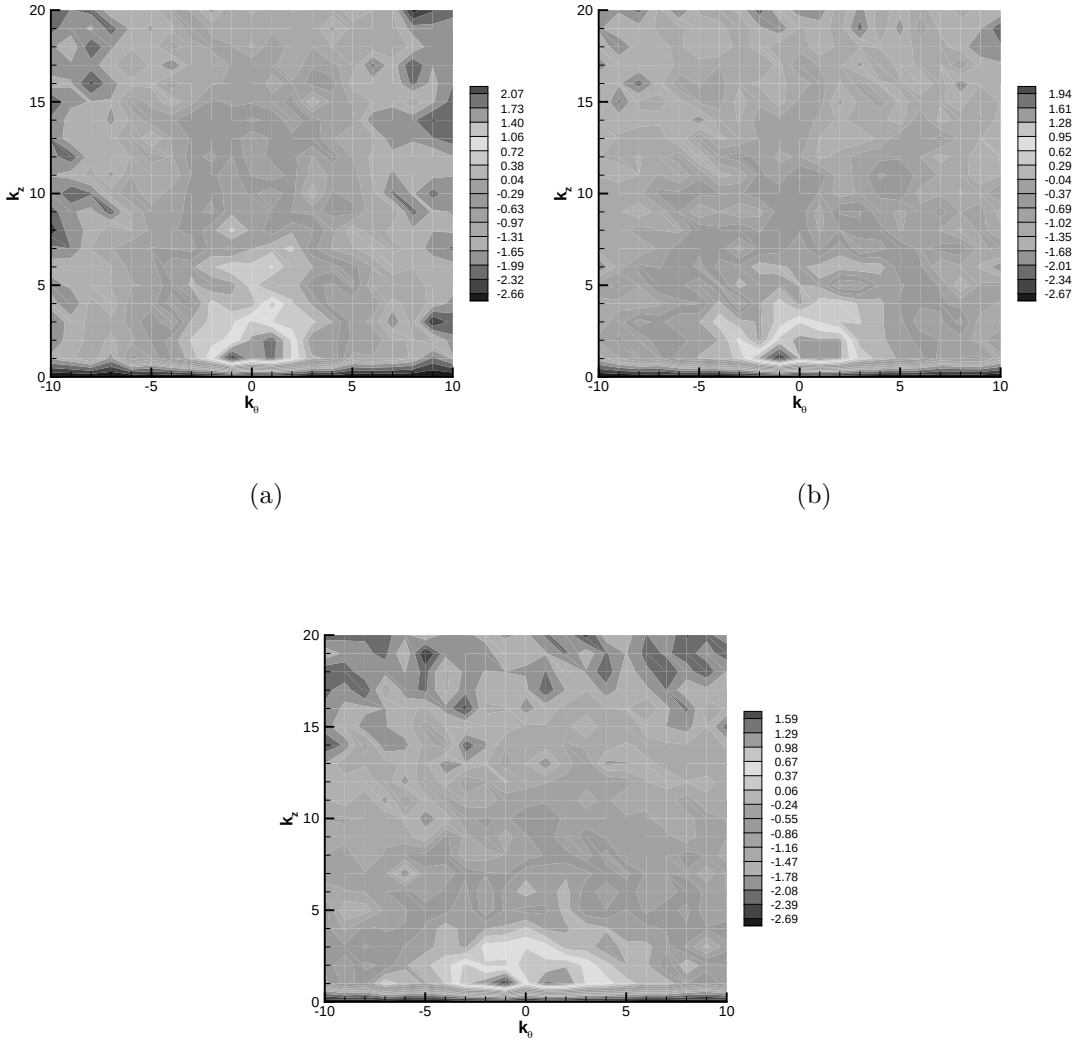


(a) (b)

(c)

Figure 3.135 2-D Energy spectra for STRN2 at $t/T = 113.93$; Contours of $log_{10}(E_{2D})$; (a), (b) and (c) correspond to $r/r_0 = 0.5$, 1.0 and 2.0 respectively

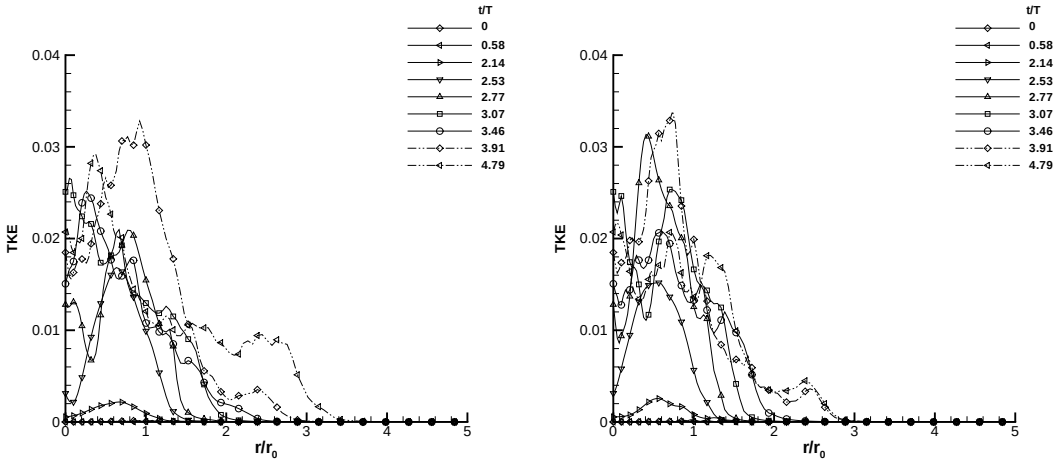


(a) (b)

Figure 3.136 Variation of turbulent kinetic energy for STRN2 in the first period at (a) $\theta = 45^o$ and (b) $\theta = 135^o$

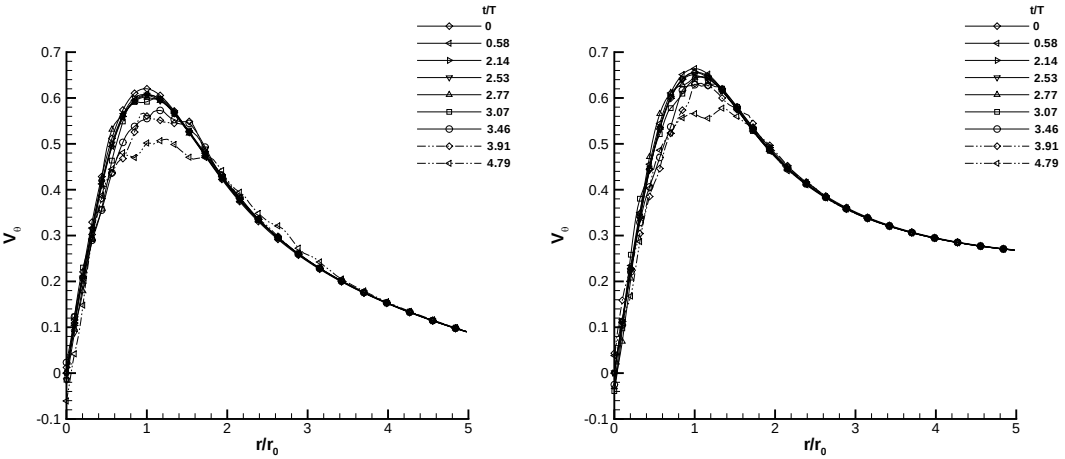


(a) (b)

Figure 3.137 Variation of mean tangential velocity for STRN2 in the first period at (a) $\theta = 45^o$ and (b) $\theta = 135^o$

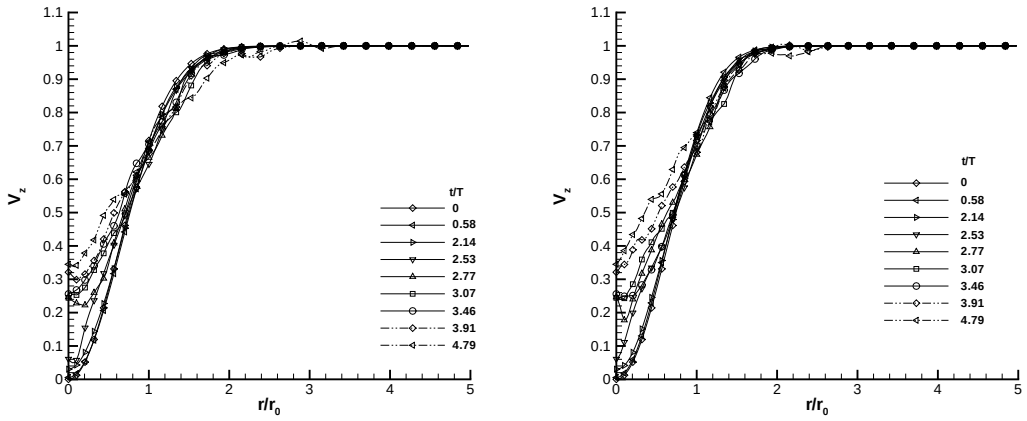


(a) (b)

Figure 3.138 Variation of mean axial velocity for STRN2 in the first period at (a) $\theta = 45^o$ and (b) $\theta = 135^o$

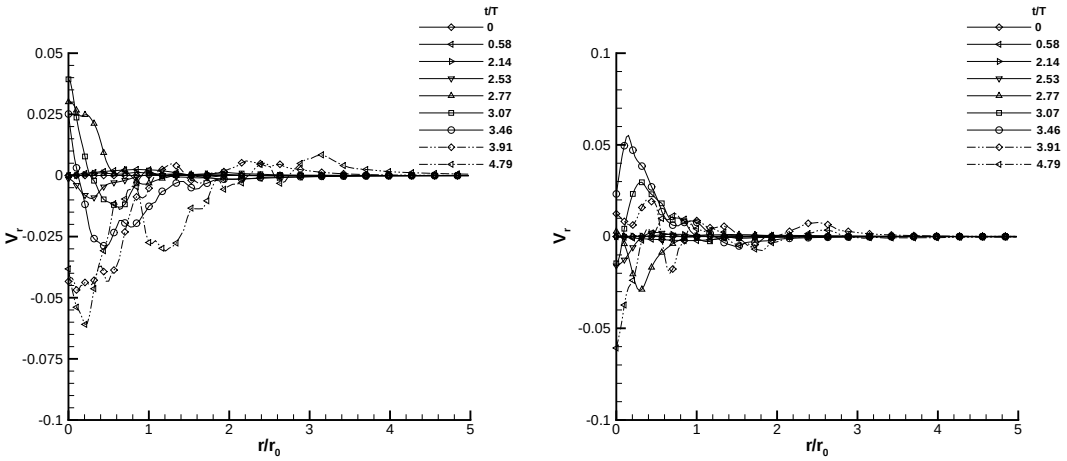


(a) (b)

Figure 3.139 Variation of mean radial velocity for STRN2 in the first period at (a) $\theta = 45^o$ and (b) $\theta = 135^o$

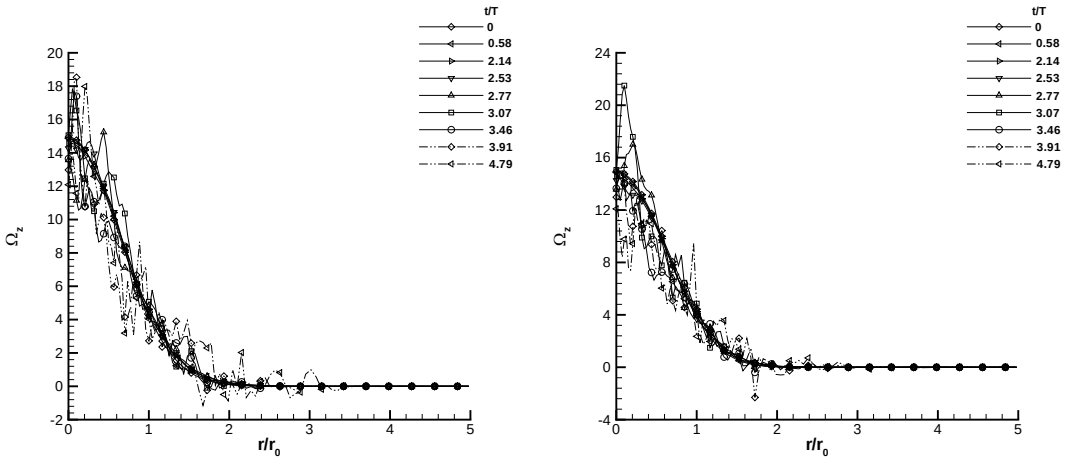


(a) (b)

Figure 3.140 Variation of mean axial vorticity for STRN2 in the first period at (a) $\theta = 45^o$ and (b) $\theta = 135^o$

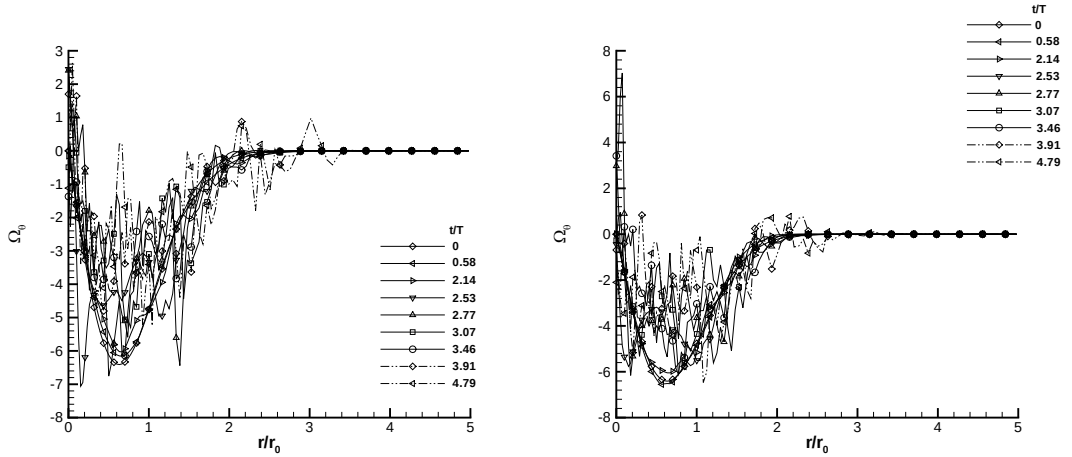


(a) (b)

Figure 3.141 Variation of mean tangential vorticity for STRN2 in the first period at (a) $\theta = 45^o$ and (b) $\theta = 135^o$

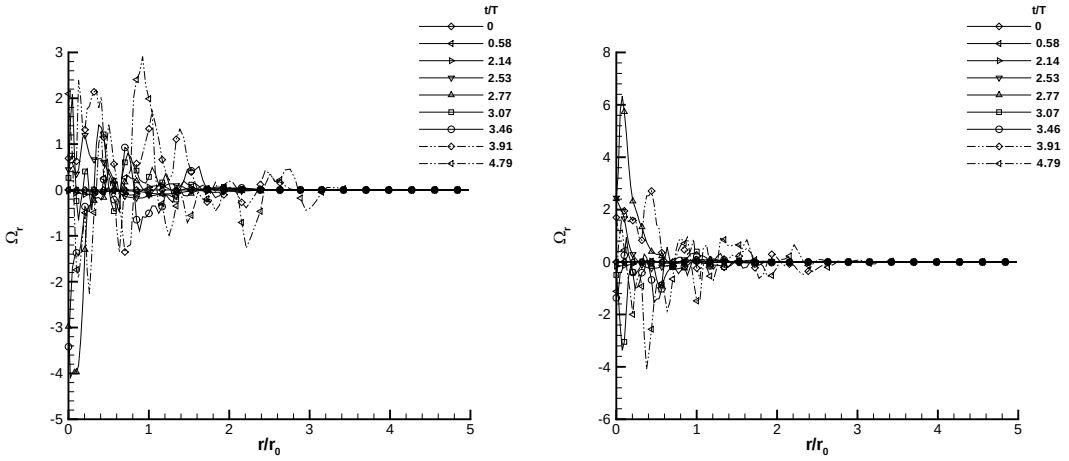


(a) (b)

Figure 3.142 Variation of mean radial vorticity for STRN2 in the first period at (a) $\theta = 45^o$ and (b) $\theta = 135^o$

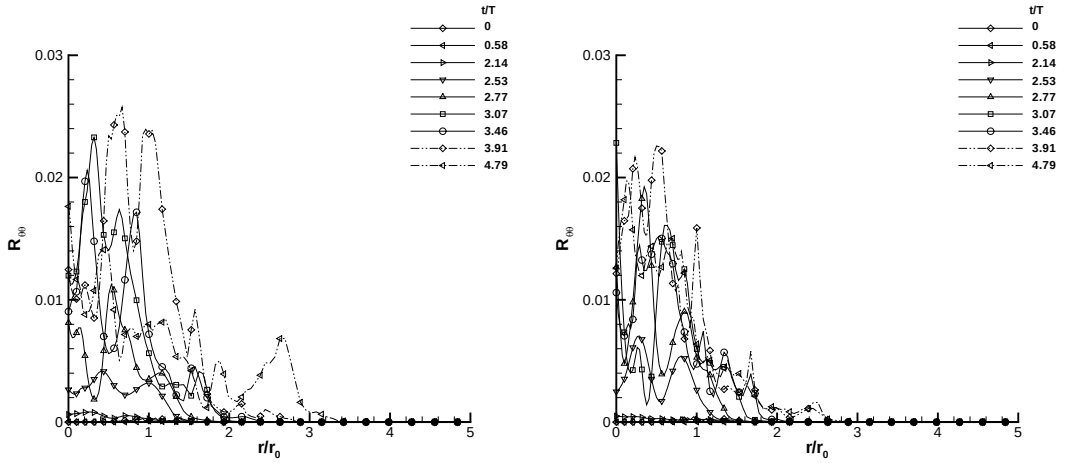


(a) (b)

Figure 3.143 Variation of $R_{\theta\theta}$ for STRN2 in the first period at (a) $\theta = 45^o$ and (b) $\theta = 135^o$

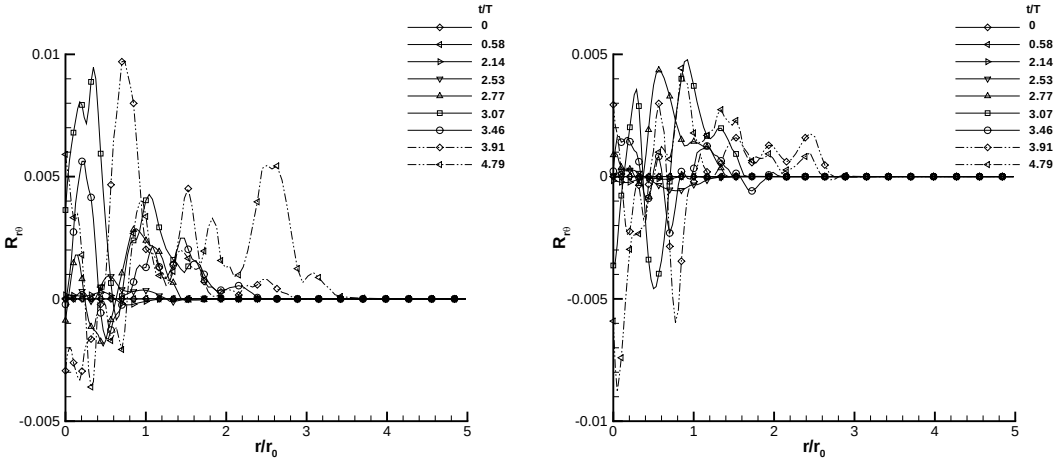


(a) (b)

Figure 3.144 Variation of $R_{r\theta}$ for STRN2 in the first period at (a) $\theta = 45^o$ and (b) $\theta = 135^o$

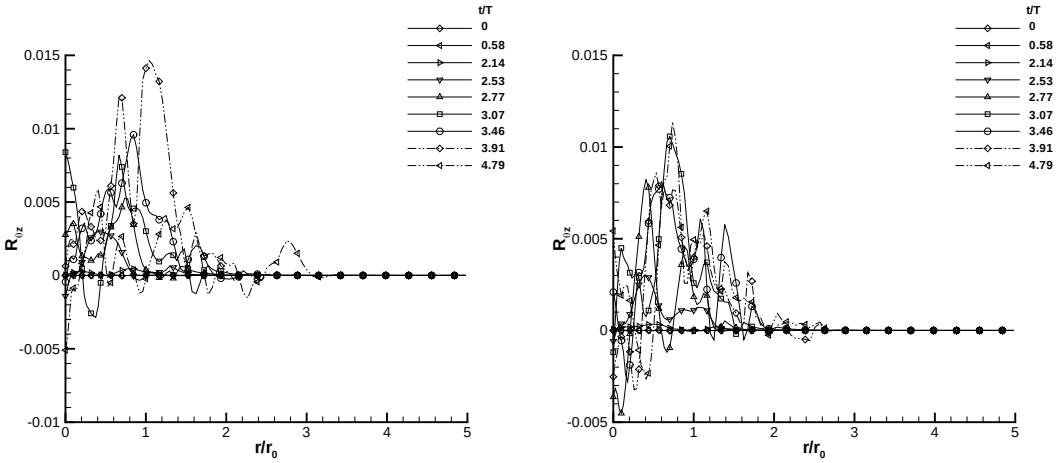


(a) (b)

Figure 3.145 Variation of $R_{\theta z}$ for STRN2 in the first period at (a) $\theta = 45^o$ and (b) $\theta = 135^o$

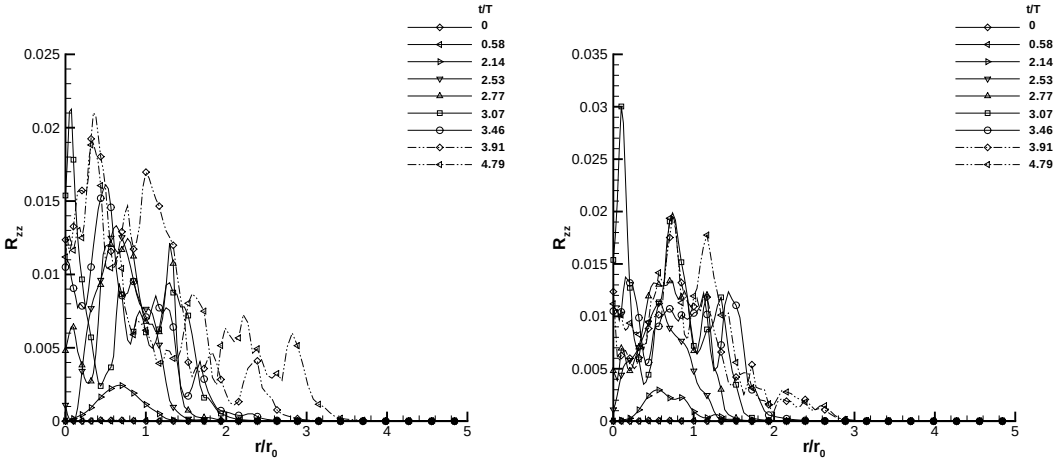


(a) (b)

Figure 3.146 Variation of $R_{zz}$ for STRN2 in the first period at (a) $\theta = 45^o$ and (b) $\theta = 135^o$

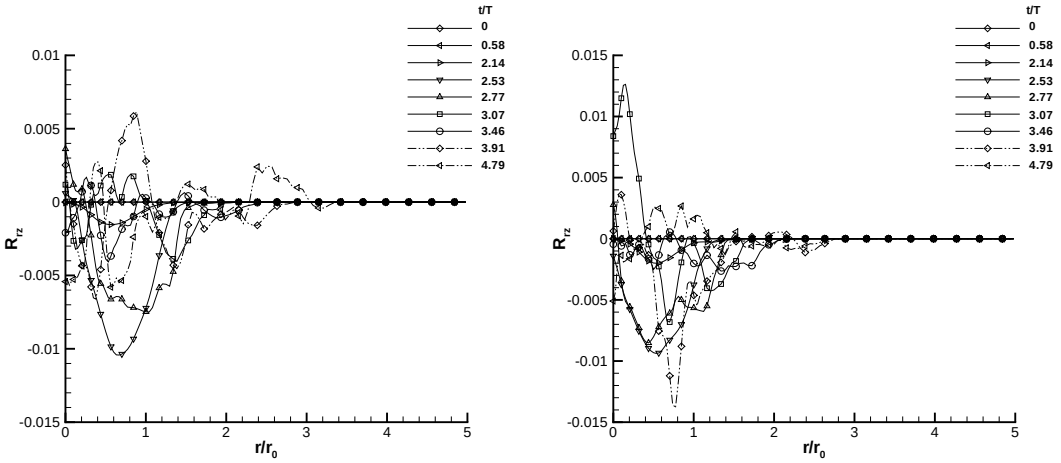


(a) (b)

Figure 3.147 Variation of $R_{rz}$ for STRN2 in the first period at (a) $\theta = 45^o$ and (b) $\theta = 135^o$

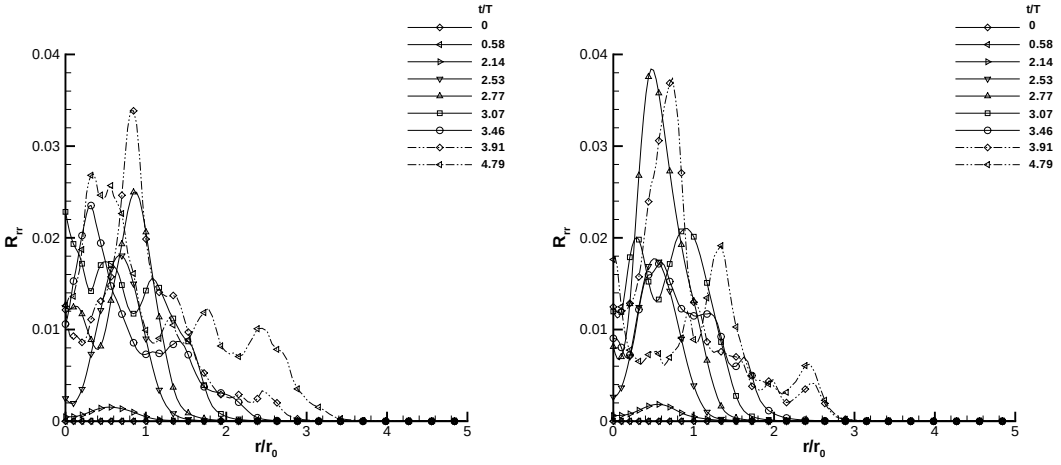


(a) (b)

Figure 3.148 Variation of $R_{rr}$ for STRN2 in the first period at (a) $\theta = 45^o$ and (b) $\theta = 135^o$

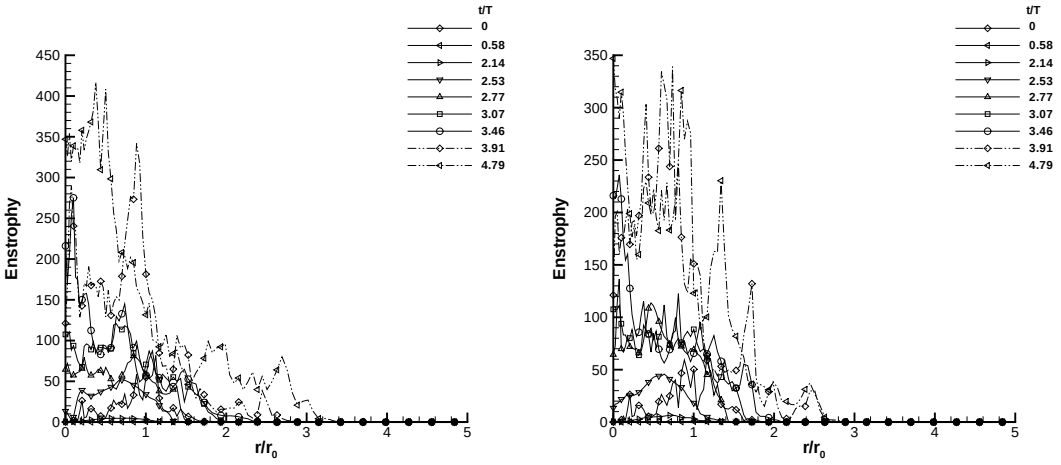


(a) (b)

Figure 3.149 Variation of enstrophy for STRN2 in the first period at (a) $\theta = 45^o$ and (b) $\theta = 135^o$

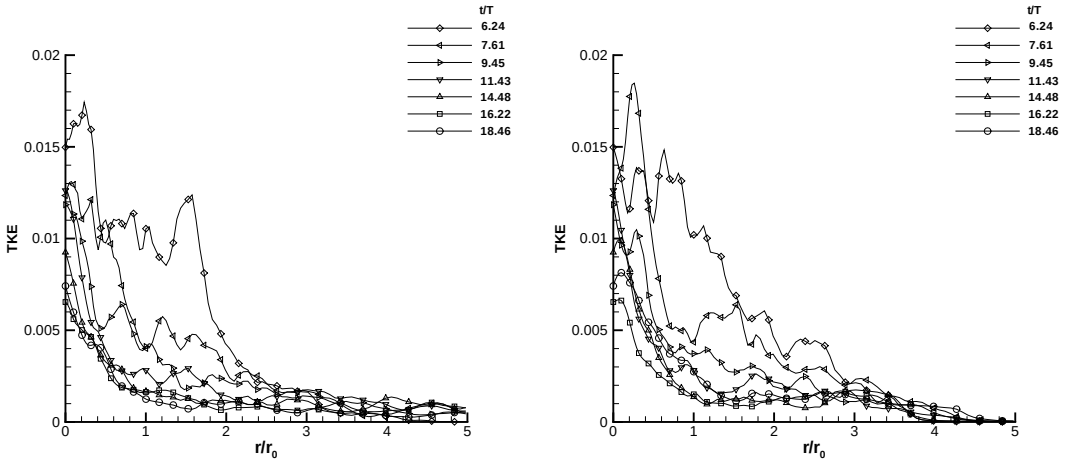


(a) (b)

Figure 3.150 Variation of turbulent kinetic energy for STRN2 in the second period at (a) $\theta = 45^o$ and (b) $\theta = 135^o$

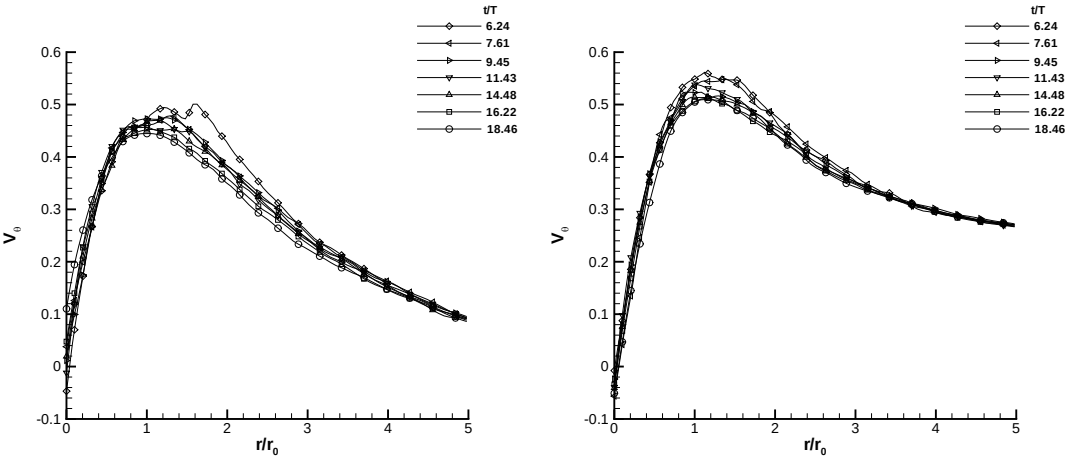


(a) (b)

Figure 3.151 Variation of mean tangential velocity for STRN2 in the second period at (a) $\theta = 45^o$ and (b) $\theta = 135^o$

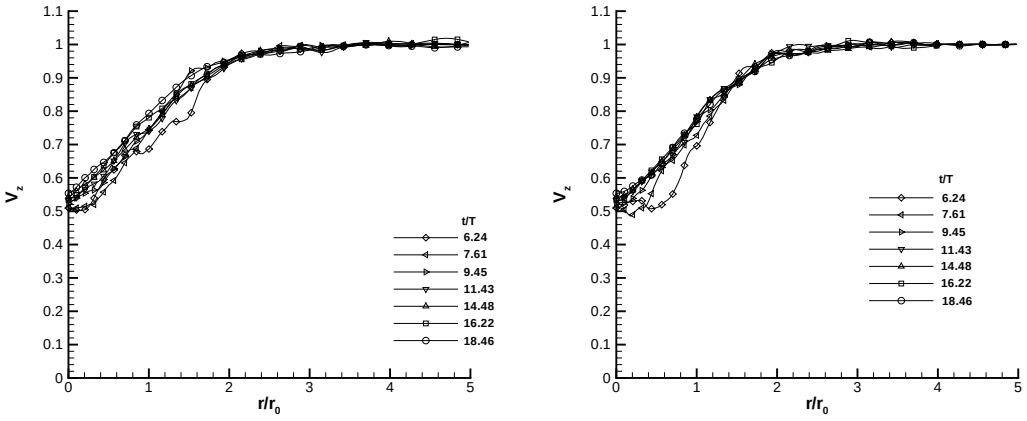


(a) (b)

Figure 3.152 Variation of mean axial velocity for STRN2 in the second period at (a) $\theta = 45^o$ and (b) $\theta = 135^o$

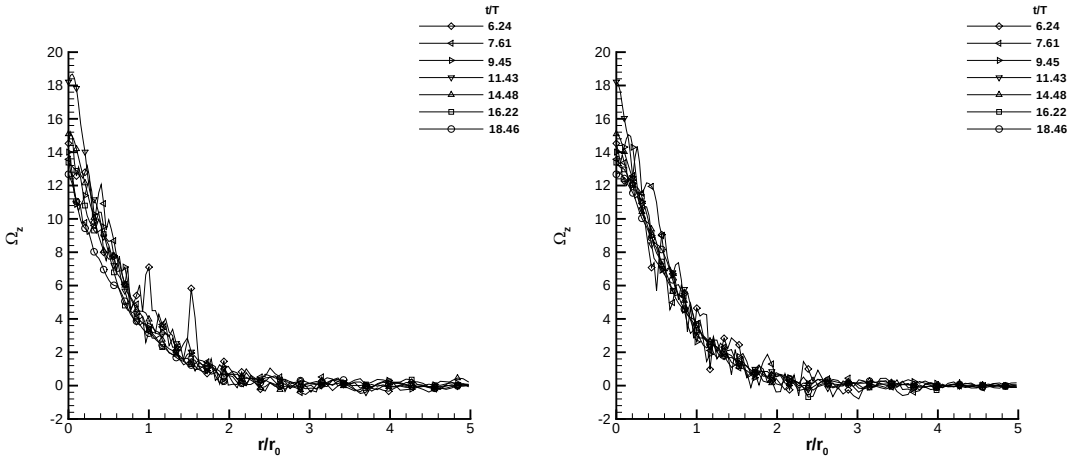


(a) (b)

Figure 3.153 Variation of mean axial vorticity for STRN2 in the second period at (a) $\theta = 45^o$ and (b) $\theta = 135^o$

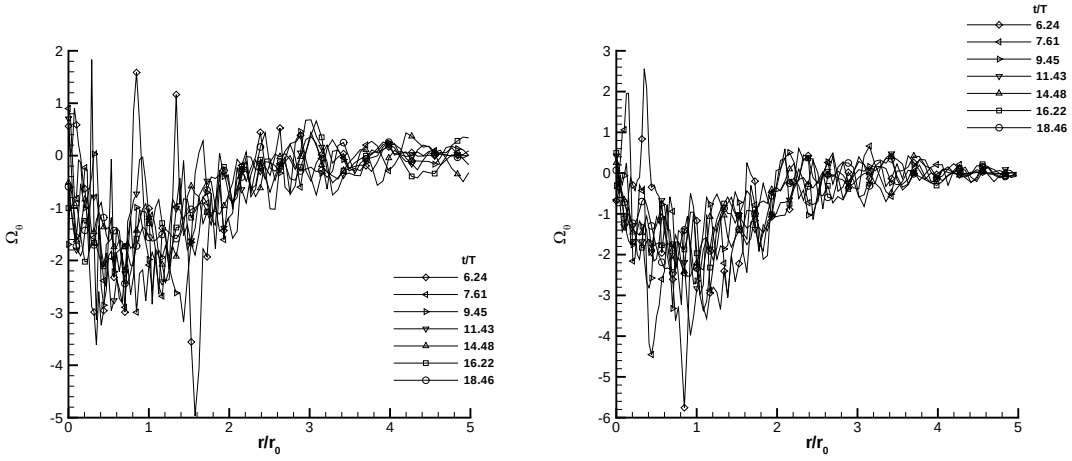


(a) (b)

Figure 3.154 Variation of mean tangential vorticity for STRN2 in the second period at (a) $\theta = 45^o$ and (b) $\theta = 135^o$

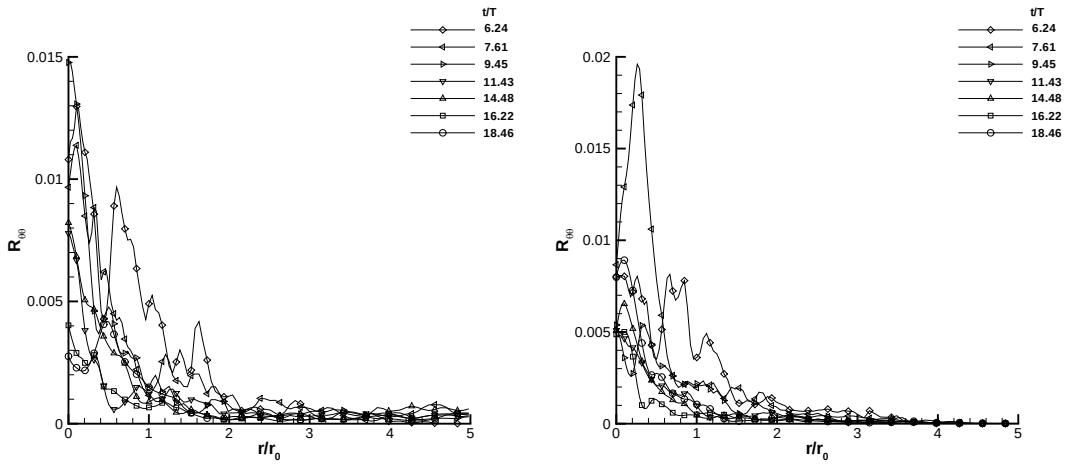


(a) (b)

Figure 3.155 Variation of $R_{\theta\theta}$ for STRN2 in the second period at (a) $\theta = 45^o$ and (b) $\theta = 135^o$

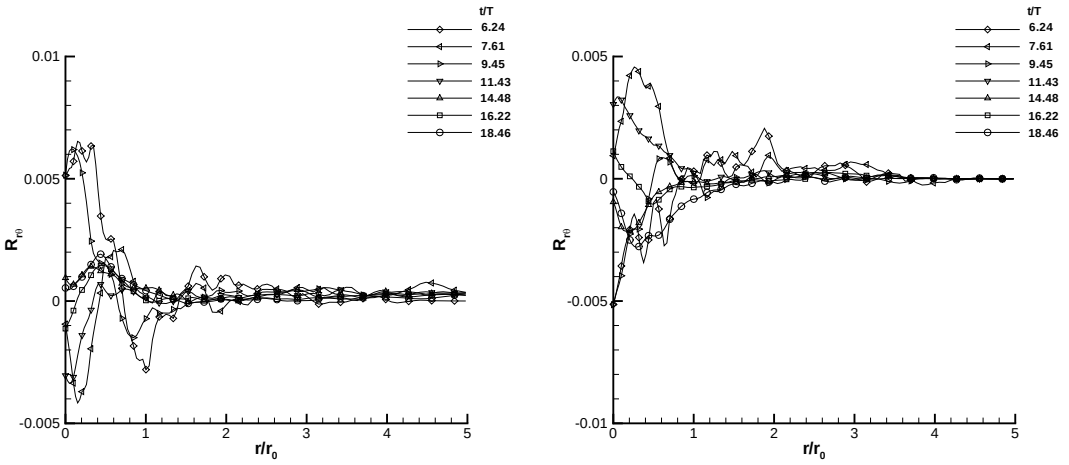


(a) (b)

Figure 3.156 Variation of $R_{r\theta}$ for STRN2 in the second period at (a) $\theta = 45^o$ and (b) $\theta = 135^o$

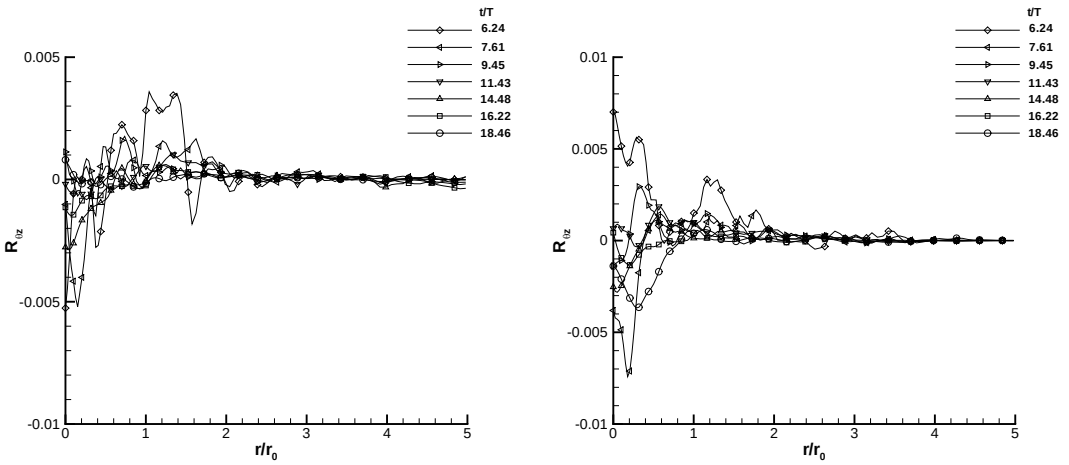


(a) (b)

Figure 3.157 Variation of $R_{\theta z}$ for STRN2 in the second period at (a) $\theta = 45^o$ and (b) $\theta = 135^o$

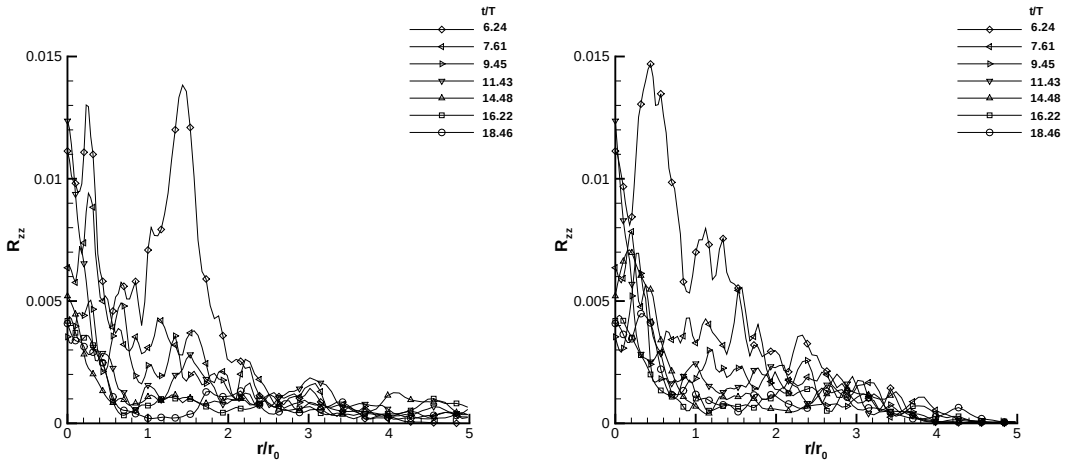


(a) (b)

Figure 3.158 Variation of $R_{zz}$ for STRN2 in the second period at (a) $\theta = 45^o$ and (b) $\theta = 135^o$

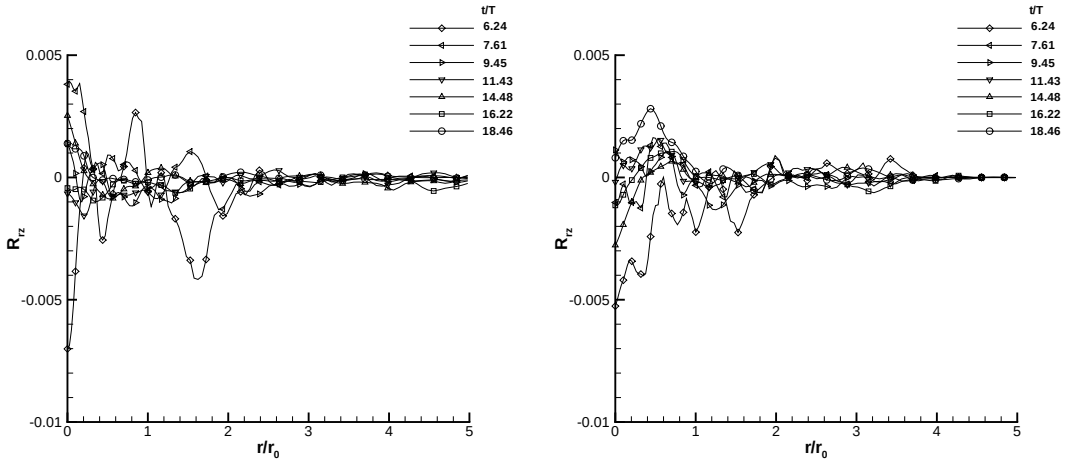


(a) (b)

Figure 3.159 Variation of $R_{rz}$ for STRN2 in the second period at (a) $\theta = 45^o$ and (b) $\theta = 135^o$

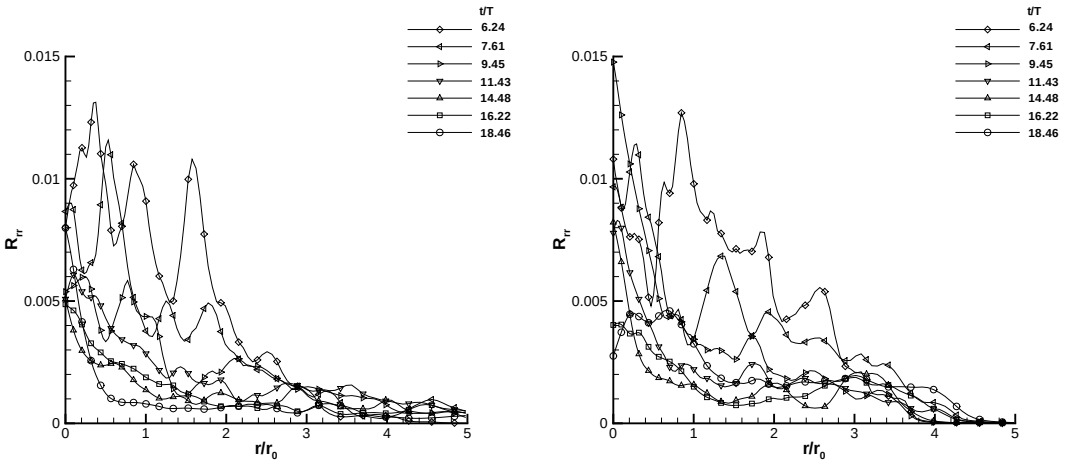


(a) (b)

Figure 3.160 Variation of $R_{rr}$ for STRN2 in the second period at (a) $\theta = 45^o$ and (b) $\theta = 135^o$

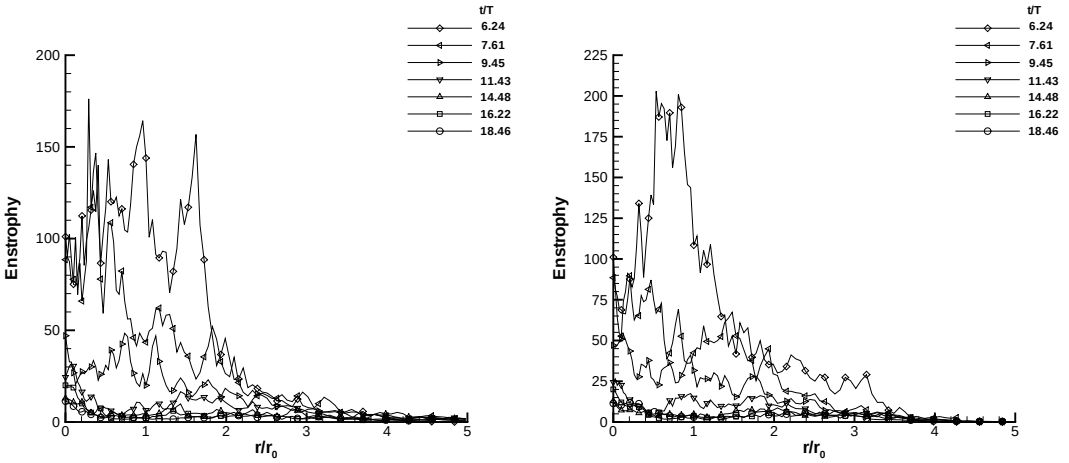


(a) (b)

Figure 3.161 Variation of enstrophy for STRN2 in the second period at (a) $\theta = 45^o$ and (b) $\theta = 135^o$

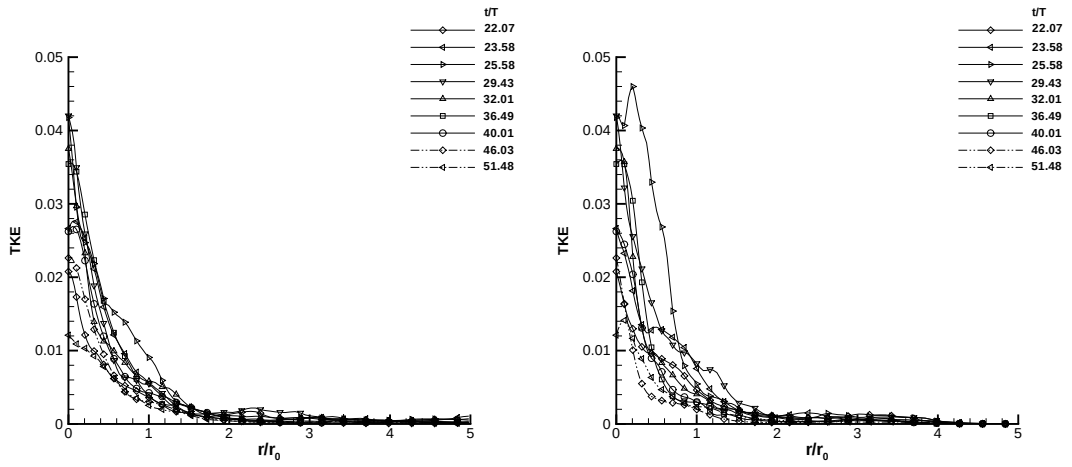


(a) (b)

Figure 3.162 Variation of turbulent kinetic energy for STRN2 in the third period at (a) $\theta = 45^o$ and (b) $\theta = 135^o$

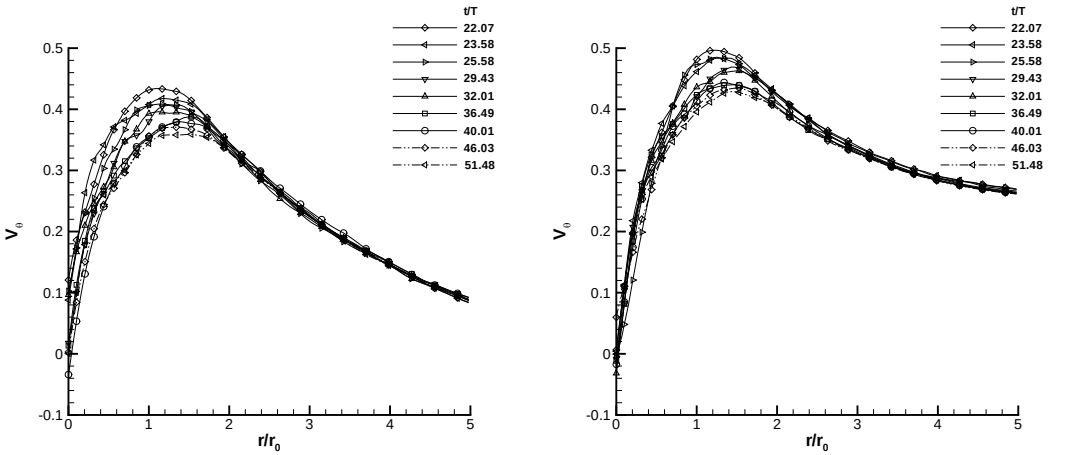


(a) (b)

Figure 3.163 Variation of mean tangential velocity for STRN2 in the third period at (a) $\theta = 45^o$ and (b) $\theta = 135^o$

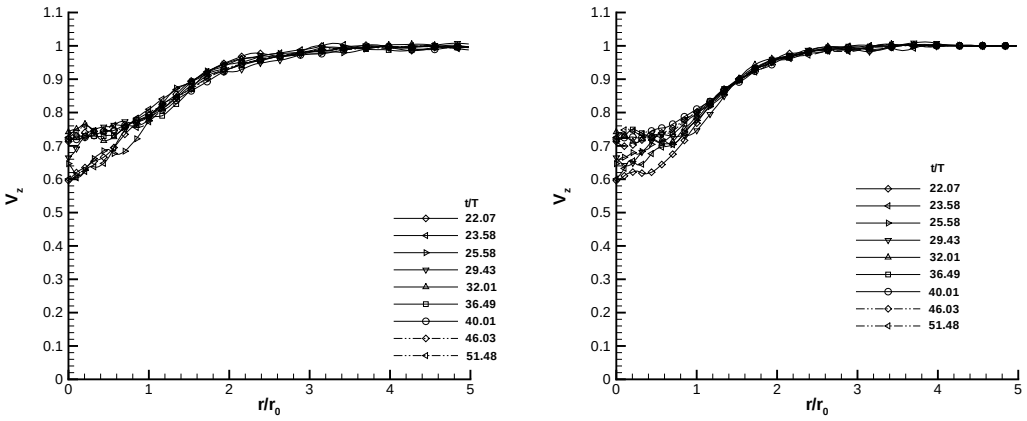


(a) (b)

Figure 3.164 Variation of mean axial velocity for STRN2 in the third period at (a) $\theta = 45^o$ and (b) $\theta = 135^o$

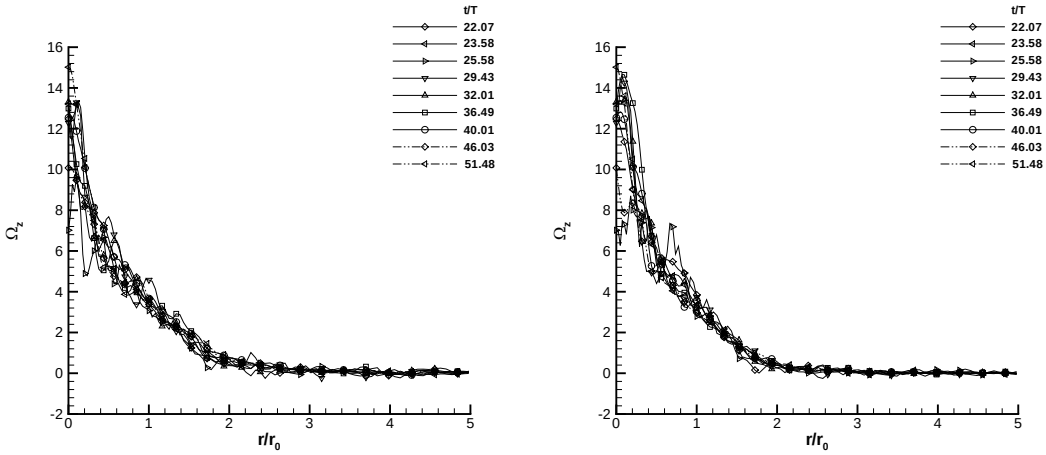


(a) (b)

Figure 3.165 Variation of mean axial vorticity for STRN2 in the third period at (a) $\theta = 45^o$ and (b) $\theta = 135^o$

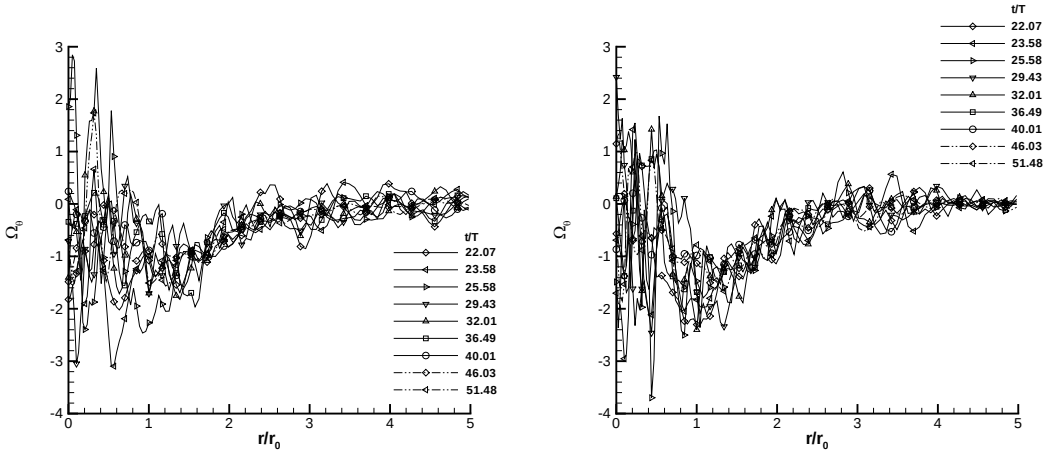


(a) (b)

Figure 3.166 Variation of mean tangential vorticity for STRN2 in the third period at (a) $\theta = 45^o$ and (b) $\theta = 135^o$

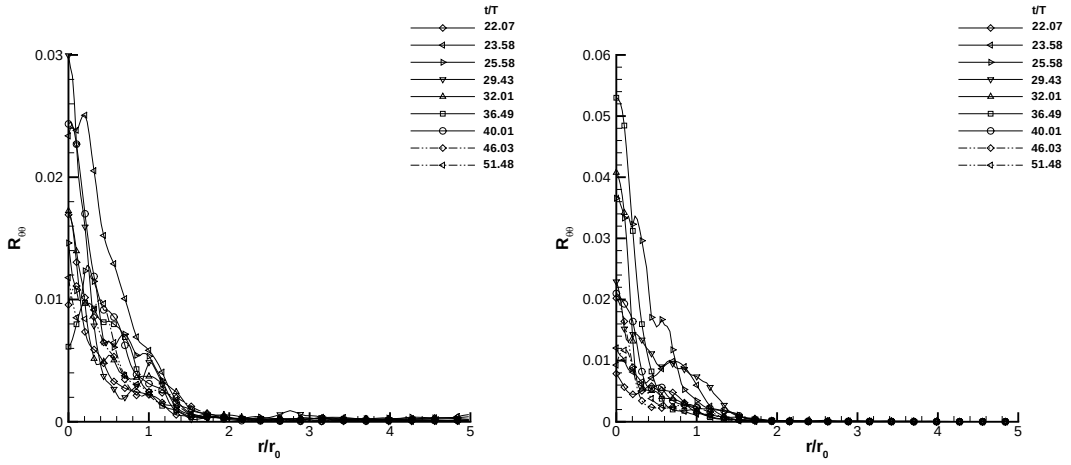


(a) (b)

Figure 3.167 Variation of $R_{\theta\theta}$ for STRN2 in the third period at (a) $\theta = 45^o$ and (b) $\theta = 135^o$

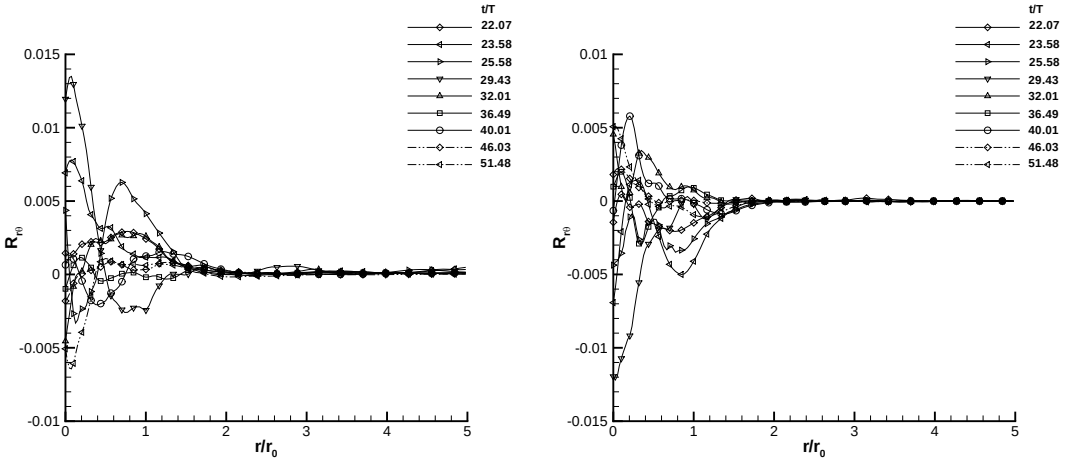


(a) (b)

Figure 3.168 Variation of $R_{r\theta}$ for STRN2 in the third period at (a) $\theta = 45^o$ and (b) $\theta = 135^o$

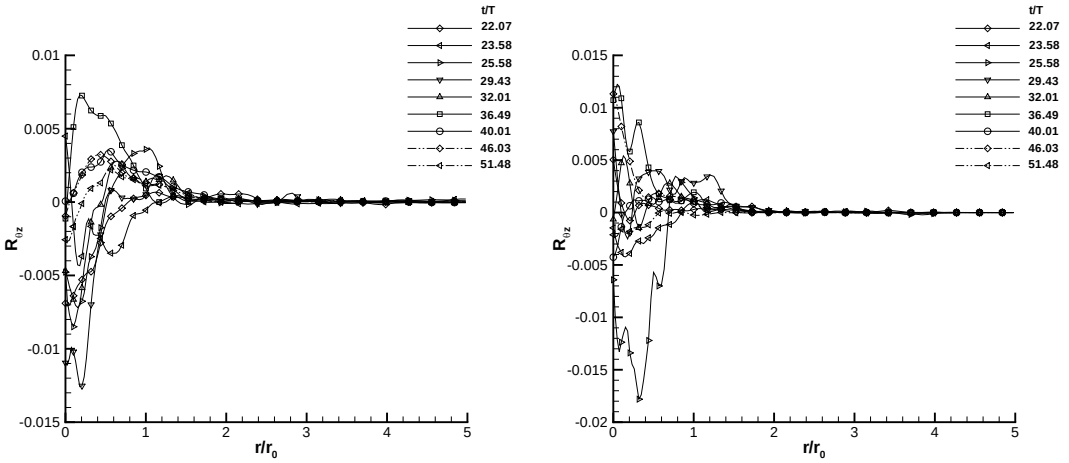


(a) (b)

Figure 3.169 Variation of $R_{\theta z}$ for STRN2 in the third period at (a) $\theta = 45^o$ and (b) $\theta = 135^o$

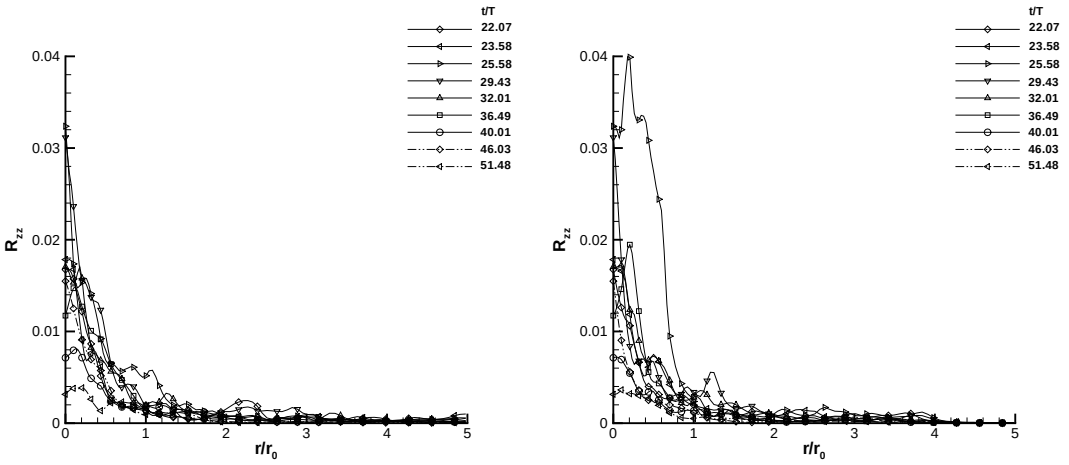


(a) (b)

Figure 3.170 Variation of $R_{zz}$ for STRN2 in the third period at (a) $\theta = 45^o$ and (b) $\theta = 135^o$

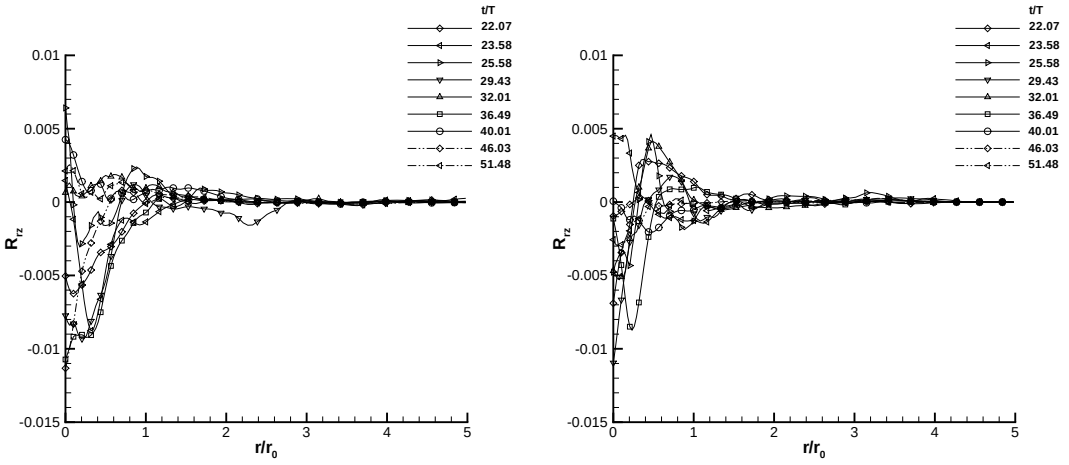


(a) (b)

Figure 3.171 Variation of $R_{rz}$ for STRN2 in the third period at (a) $\theta = 45^o$ and (b) $\theta = 135^o$

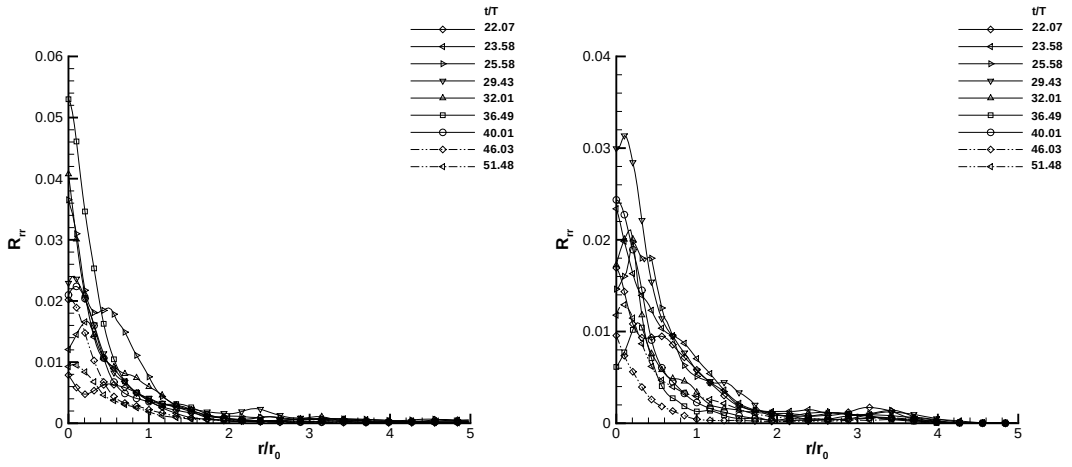


(a) (b)

Figure 3.172 Variation of $R_{rr}$ for STRN2 in the third period at (a) $\theta = 45^o$ and (b) $\theta = 135^o$

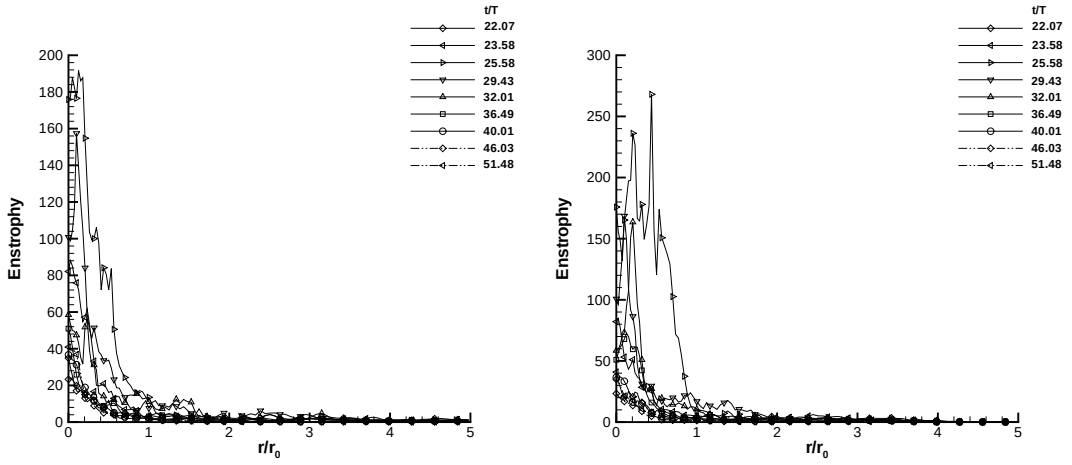


(a) (b)

Figure 3.173 Variation of enstrophy for STRN2 in the third period at (a) $\theta = 45^o$ and (b) $\theta = 135^o$

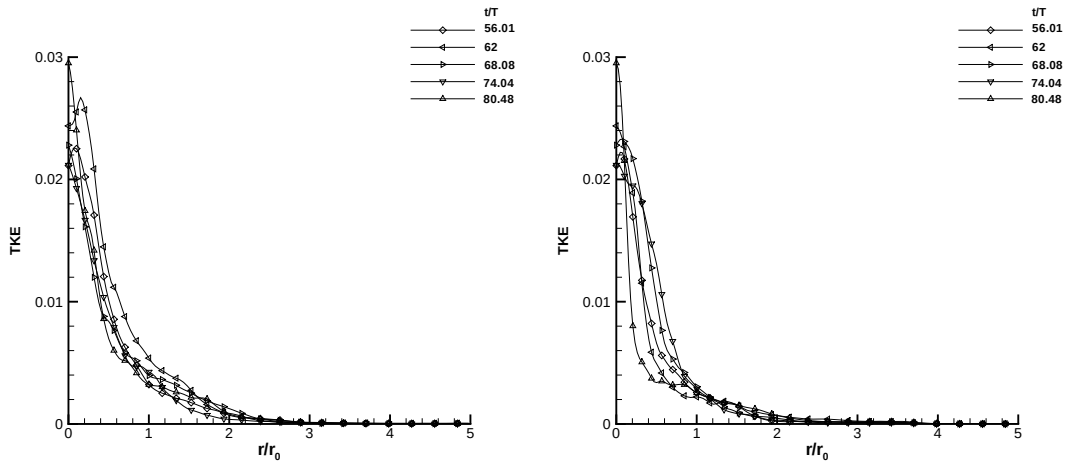


(a) (b)

Figure 3.174 Variation of turbulent kinetic energy for STRN2 in the fourth period at (a) $\theta = 45^o$ and (b) $\theta = 135^o$

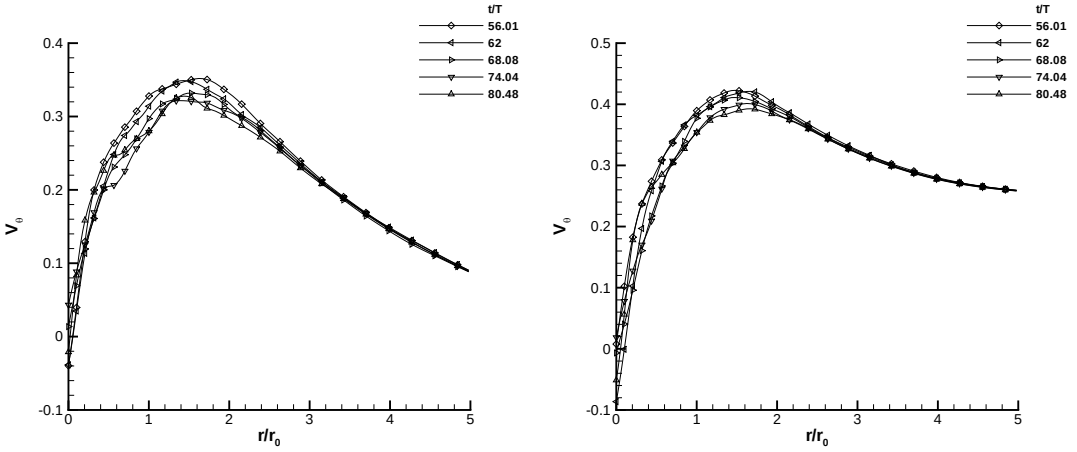


(a) (b)

Figure 3.175 Variation of mean tangential velocity for STRN2 in the fourth period at (a) $\theta = 45^o$ and (b) $\theta = 135^o$

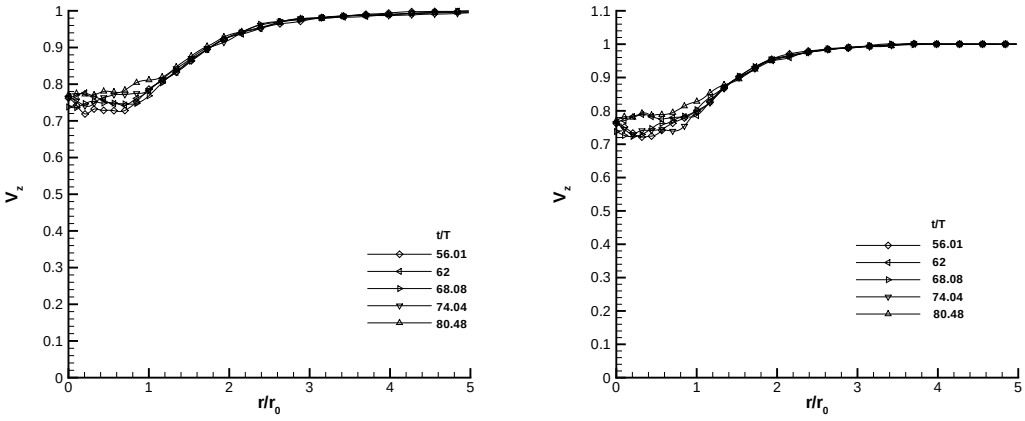


(a) (b)

Figure 3.176 Variation of mean axial velocity for STRN2 in the fourth period at (a) $\theta = 45^o$ and (b) $\theta = 135^o$

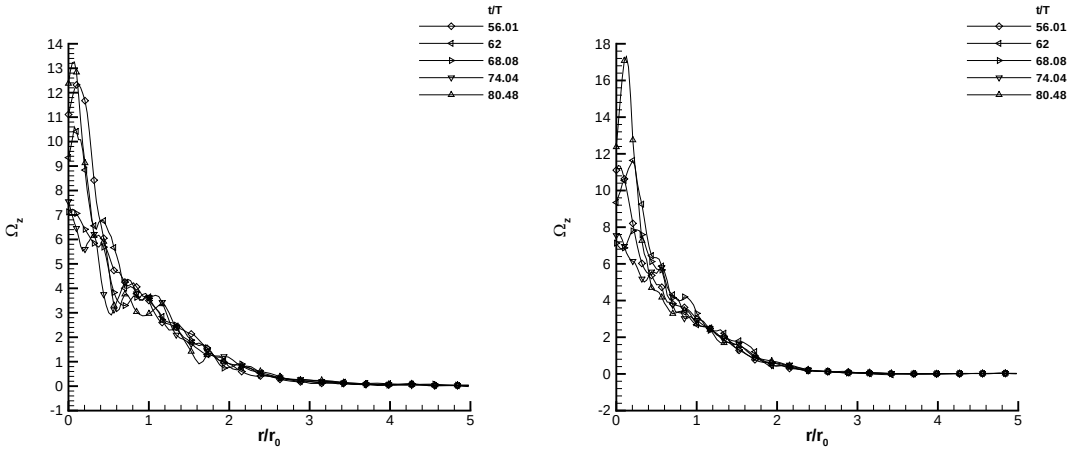


(a) (b)

Figure 3.177 Variation of mean axial vorticity for STRN2 in the fourth period at (a) $\theta = 45^o$ and (b) $\theta = 135^o$

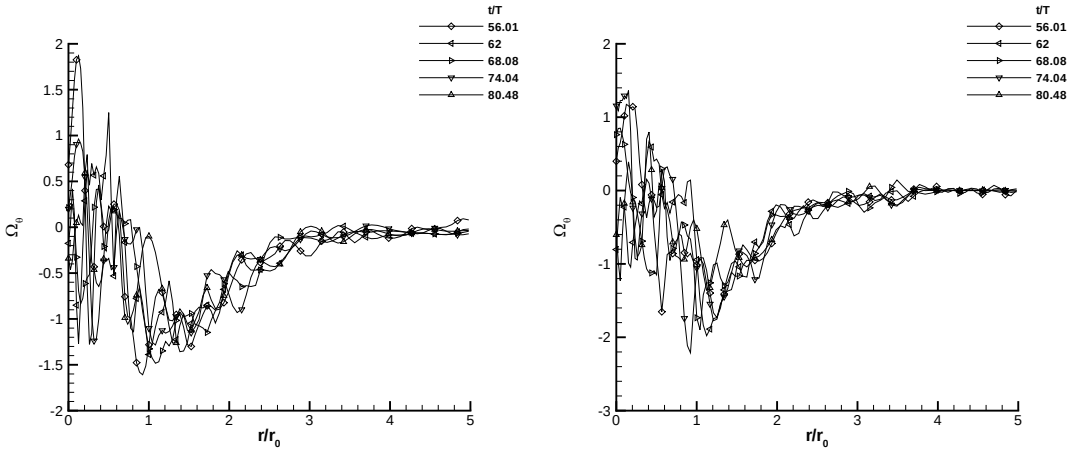


(a) (b)

Figure 3.178 Variation of mean tangential vorticity for STRN2 in the fourth period at (a) $\theta = 45^o$ and (b) $\theta = 135^o$

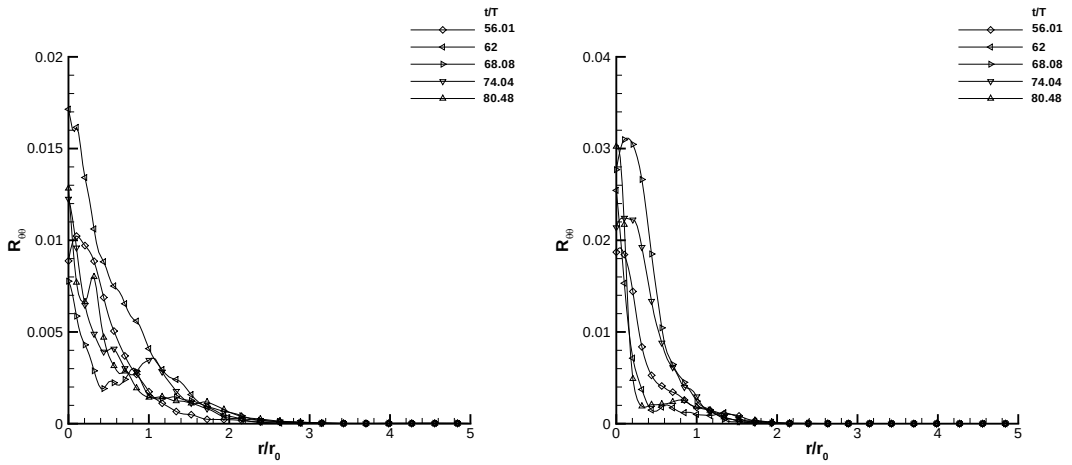


(a) (b)

Figure 3.179 Variation of $R_{\theta\theta}$ for STRN2 in the fourth period at (a) $\theta = 45^o$ and (b) $\theta = 135^o$

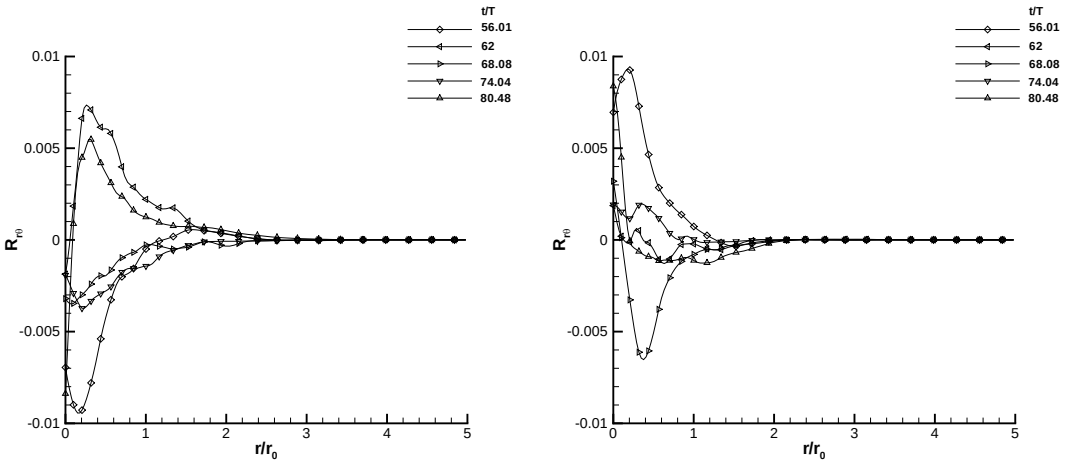


(a) (b)

Figure 3.180 Variation of $R_{r\theta}$ for STRN2 in the fourth period at (a) $\theta = 45^o$ and (b) $\theta = 135^o$

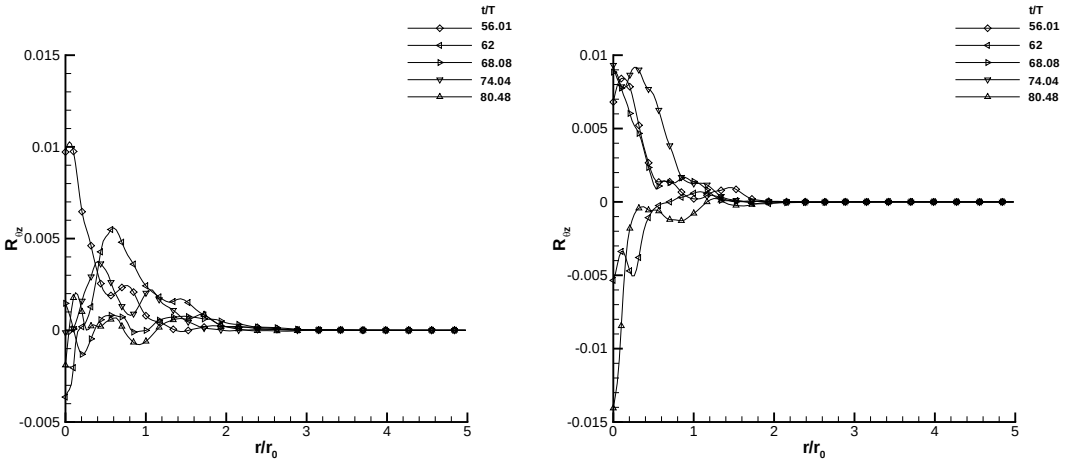


(a) (b)

Figure 3.181 Variation of $R_{\theta z}$ for STRN2 in the fourth period at (a) $\theta = 45^o$ and (b) $\theta = 135^o$

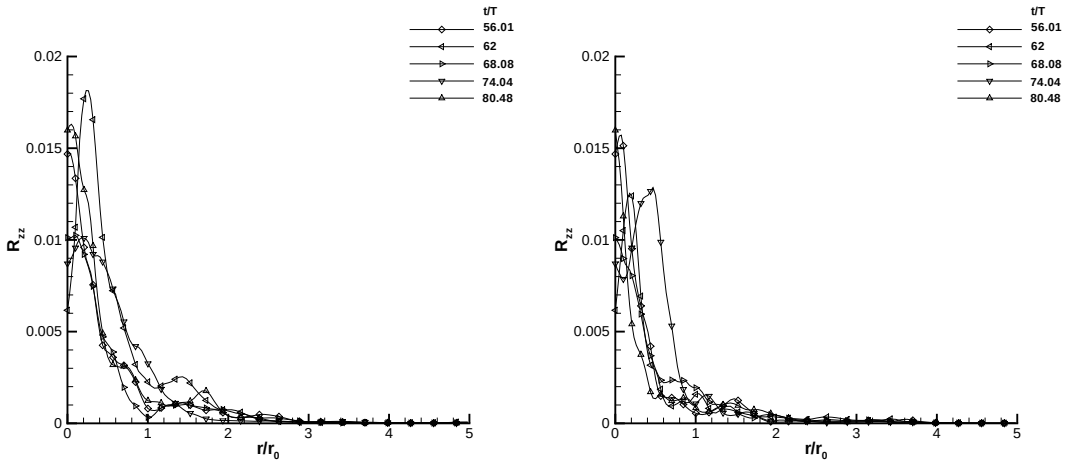


(a) (b)

Figure 3.182 Variation of $R_{zz}$ for STRN2 in the fourth period at (a) $\theta = 45^o$ and (b) $\theta = 135^o$

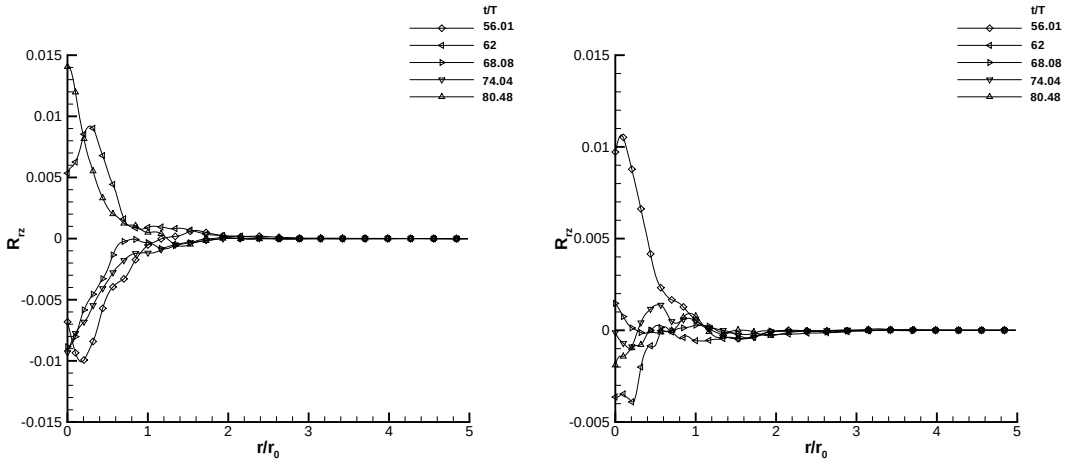


(a) (b)

Figure 3.183 Variation of $R_{rz}$ for STRN2 in the fourth period at (a) $\theta = 45^o$ and (b) $\theta = 135^o$

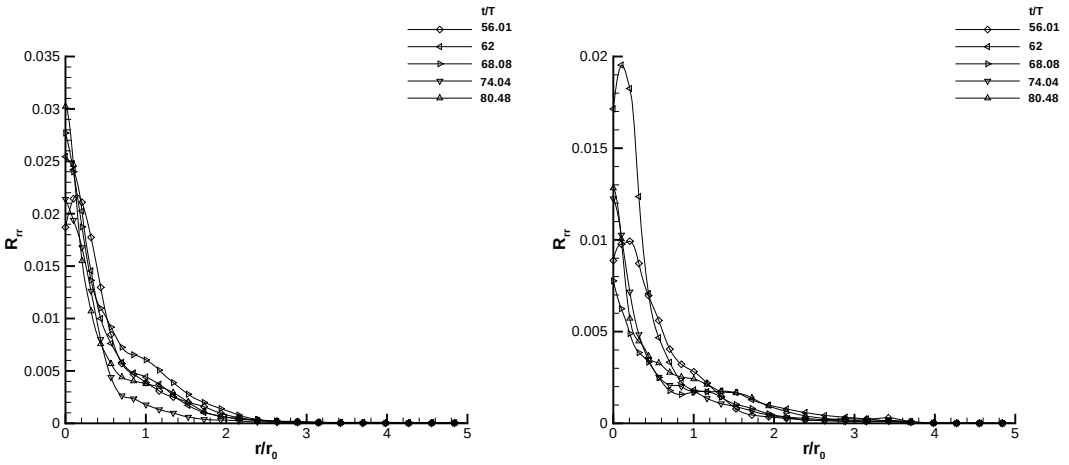


(a) (b)

Figure 3.184 Variation of $R_{rr}$ for STRN2 in the fourth period at (a) $\theta = 45^o$ and (b) $\theta = 135^o$

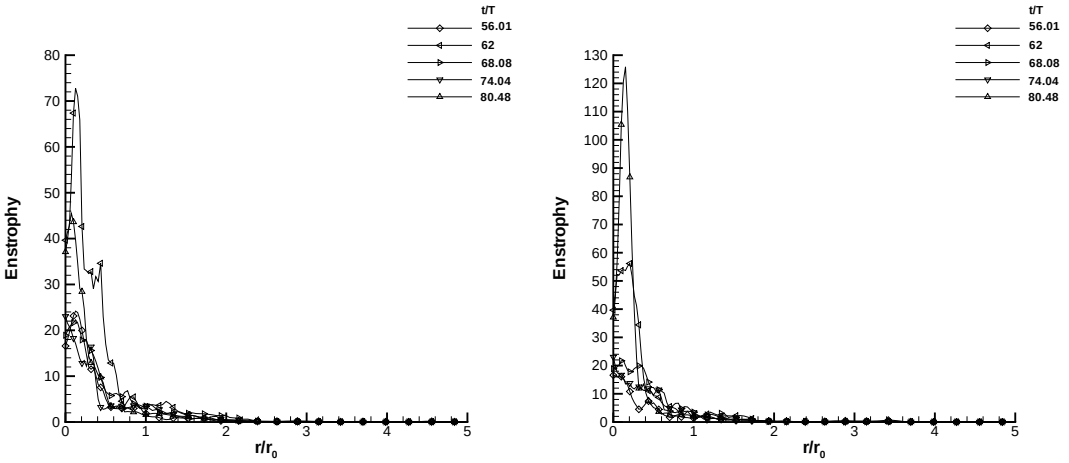


(a) (b)

Figure 3.185 Variation of enstrophy for STRN2 in the fourth period at (a) $\theta = 45^o$ and (b) $\theta = 135^o$

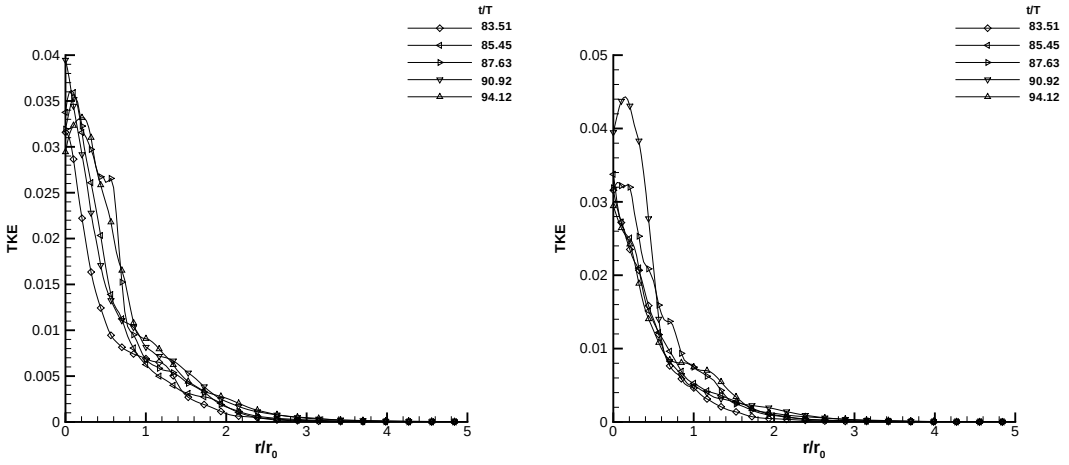


Figure 3.186 Variation of turbulent kinetic energy for STRN2 in the fifth period at (a) $\theta = 45^o$ and (b) $\theta = 135^o$

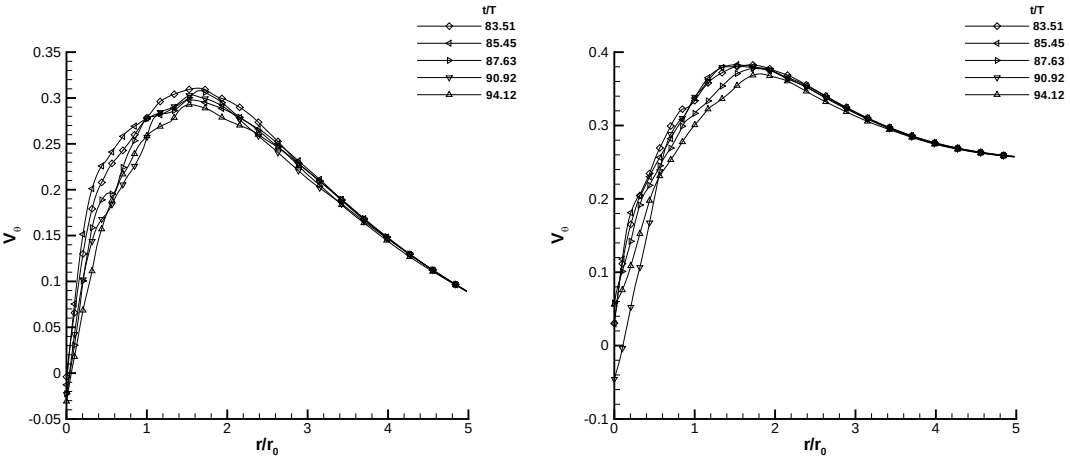


Figure 3.187 Variation of mean tangential velocity for STRN2 in the fifth period at (a) $\theta = 45^o$ and (b) $\theta = 135^o$

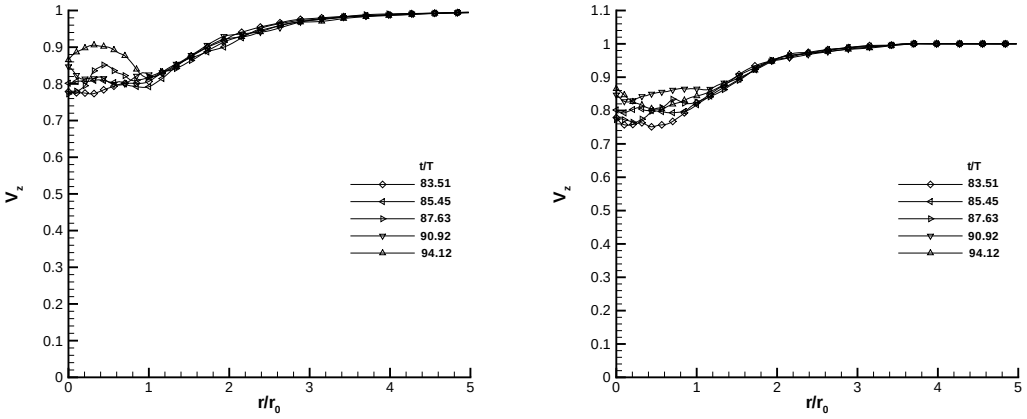


(a) (b)

Figure 3.188 Variation of mean axial velocity for STRN2 in the fifth period at (a) $\theta = 45^o$ and (b) $\theta = 135^o$

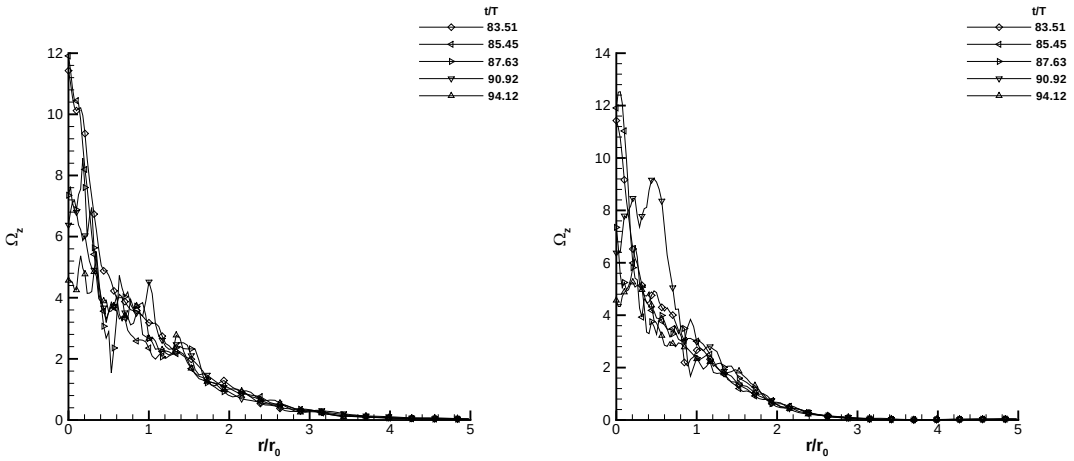


(a) (b)

Figure 3.189 Variation of mean axial vorticity for STRN2 in the fifth period at (a) $\theta = 45^o$ and (b) $\theta = 135^o$

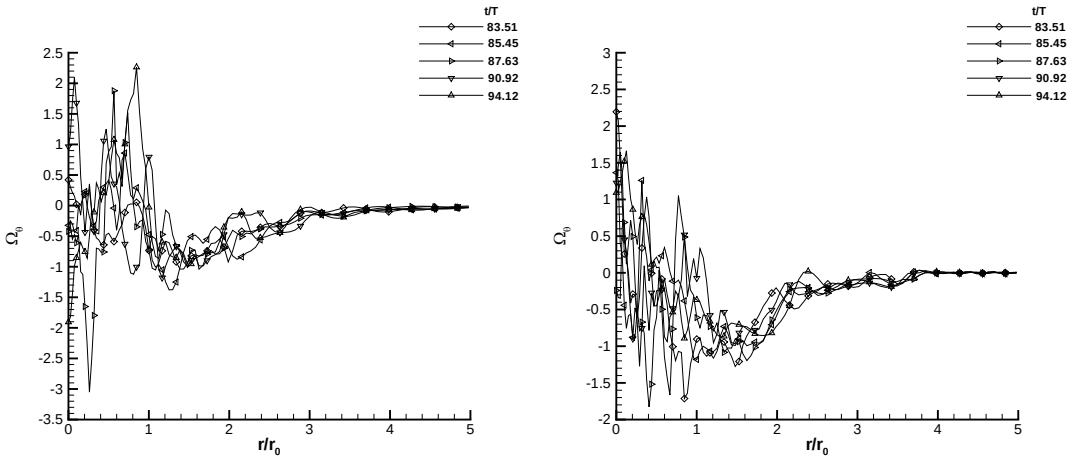


Figure 3.190 Variation of mean tangential vorticity for STRN2 in the fifth period at (a) $\theta = 45^o$ and (b) $\theta = 135^o$

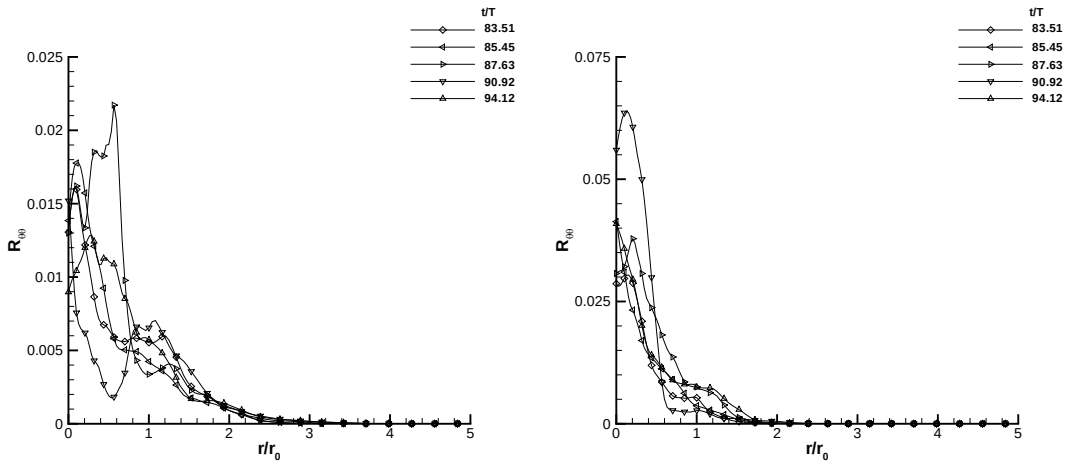


Figure 3.191 Variation of $R_{\theta\theta}$ for STRN2 in the fifth period at (a) $\theta = 45^o$ and (b) $\theta = 135^o$

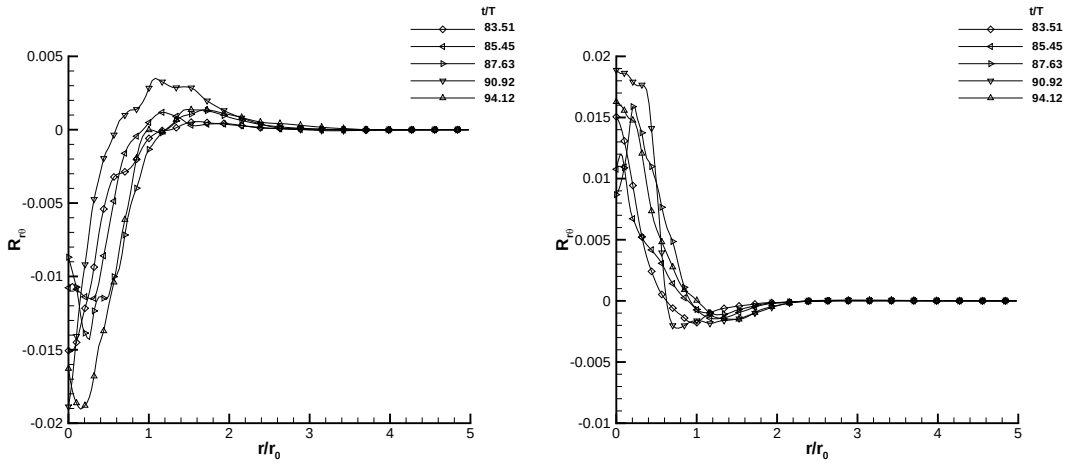


(a) (b)

Figure 3.192 Variation of $R_{r\theta}$ for STRN2 in the fifth period at (a) $\theta = 45^o$ and (b) $\theta = 135^o$

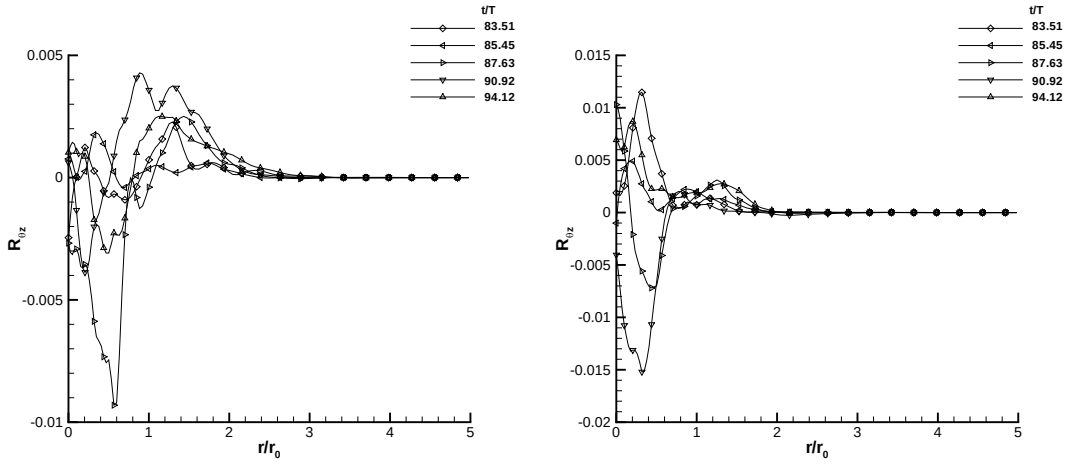


(a) (b)

Figure 3.193 Variation of $R_{\theta z}$ for STRN2 in the fifth period at (a) $\theta = 45^o$ and (b) $\theta = 135^o$

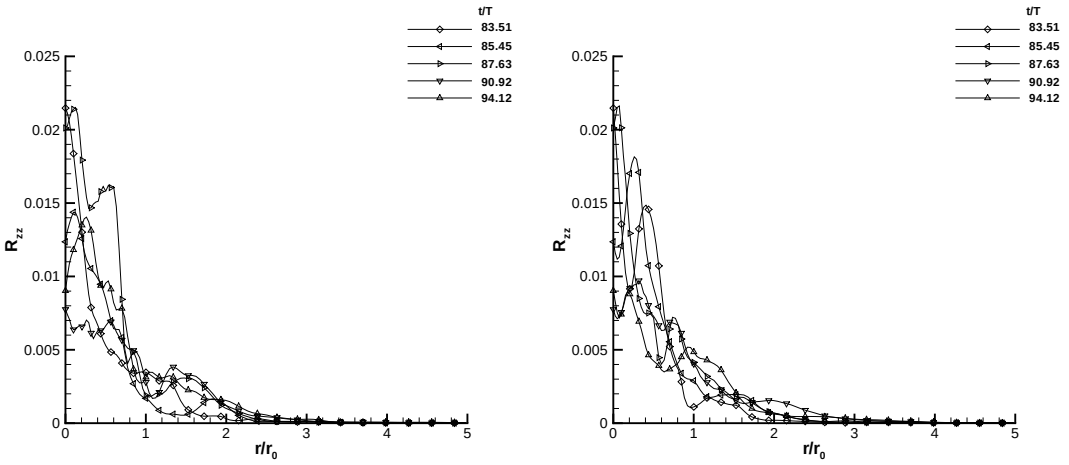


(a) (b)

Figure 3.194 Variation of $R_{zz}$ for STRN2 in the fifth period at (a) $\theta = 45^o$ and (b) $\theta = 135^o$

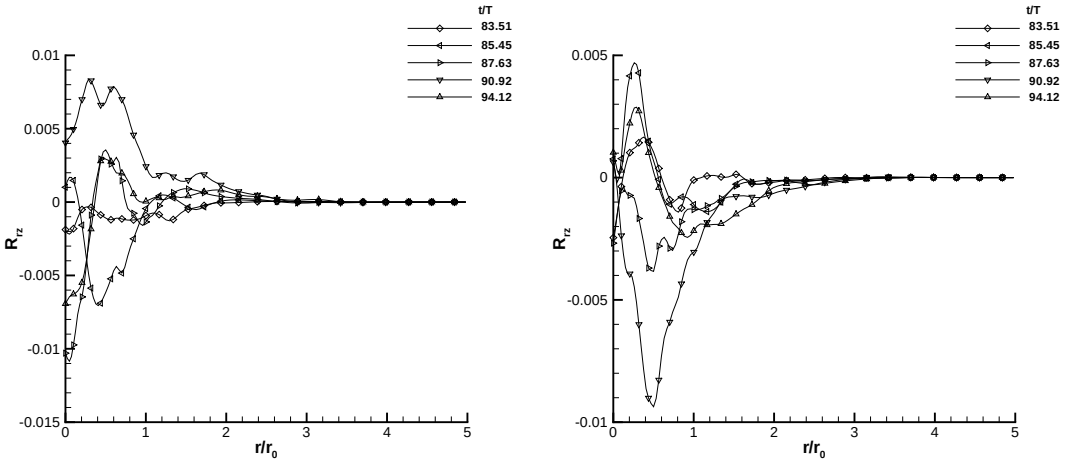


(a) (b)

Figure 3.195 Variation of $R_{rz}$ for STRN2 in the fifth period at (a) $\theta = 45^o$ and (b) $\theta = 135^o$

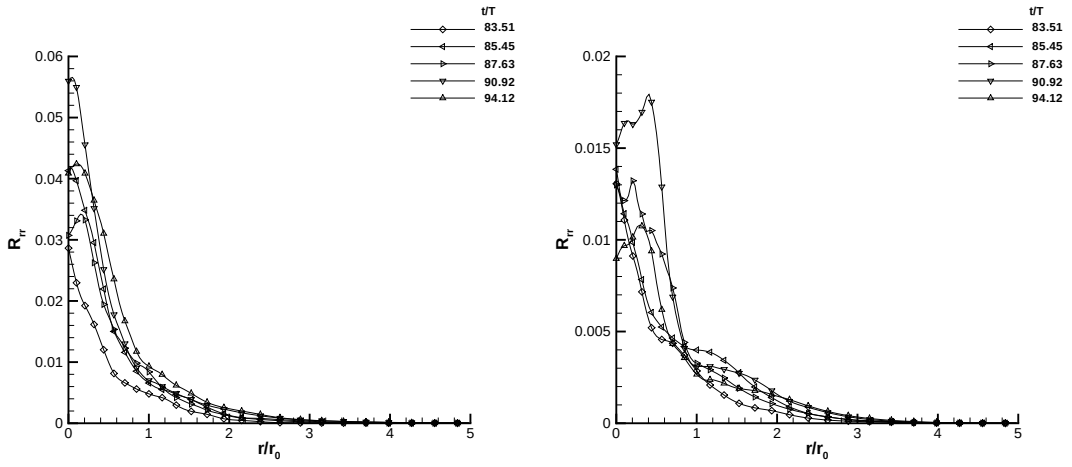


(a) (b)

Figure 3.196 Variation of $R_{rr}$ for STRN2 in the fifth period at (a) $\theta = 45^o$ and (b) $\theta = 135^o$

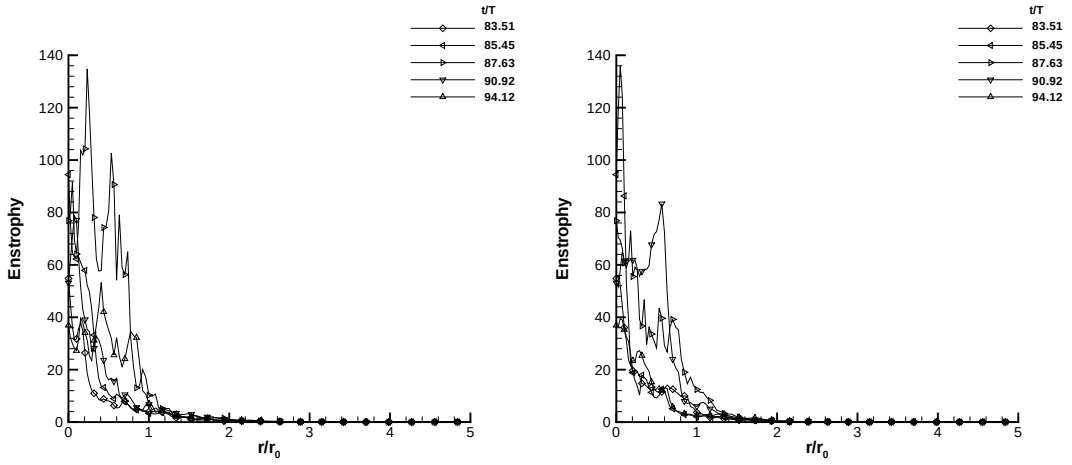


(a) (b)

Figure 3.197 Variation of enstrophy for STRN2 in the fifth period at (a) $\theta = 45^o$ and (b) $\theta = 135^o$

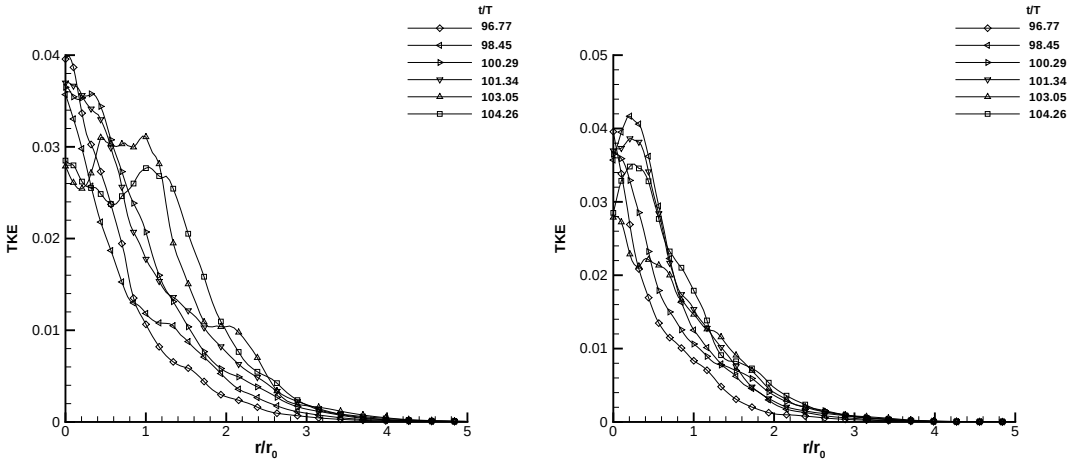


Figure 3.198 Variation of turbulent kinetic energy for STRN2 in the sixth period at (a) $\theta = 45^o$ and (b) $\theta = 135^o$

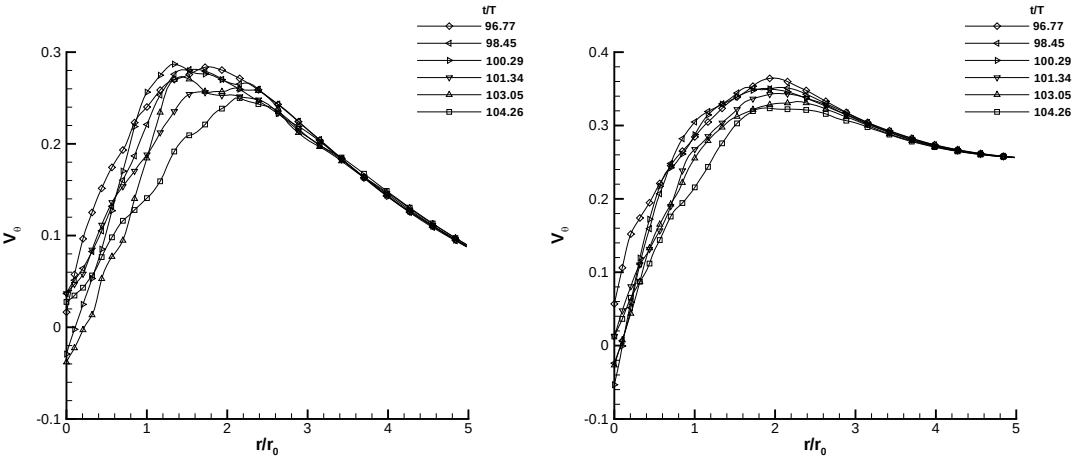


Figure 3.199 Variation of mean tangential velocity for STRN2 in the sixth period at (a) $\theta = 45^o$ and (b) $\theta = 135^o$

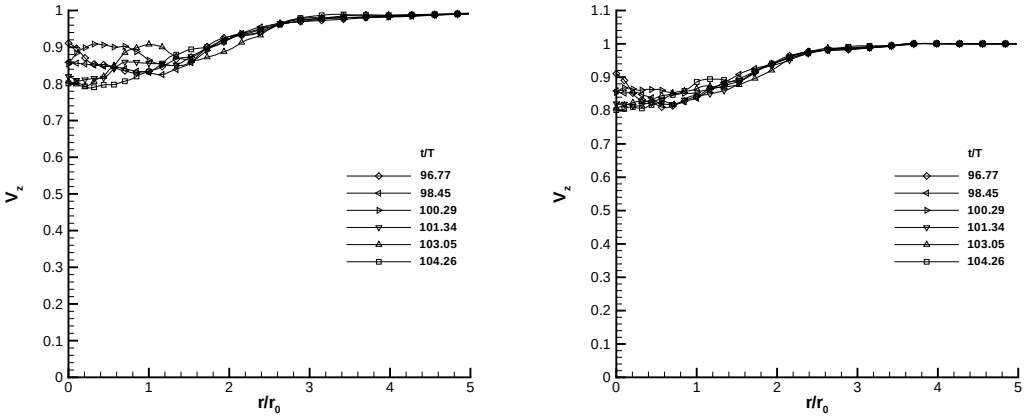


(a) (b)

Figure 3.200 Variation of mean axial velocity for STRN2 in the sixth period at (a) $\theta = 45^o$ and (b) $\theta = 135^o$

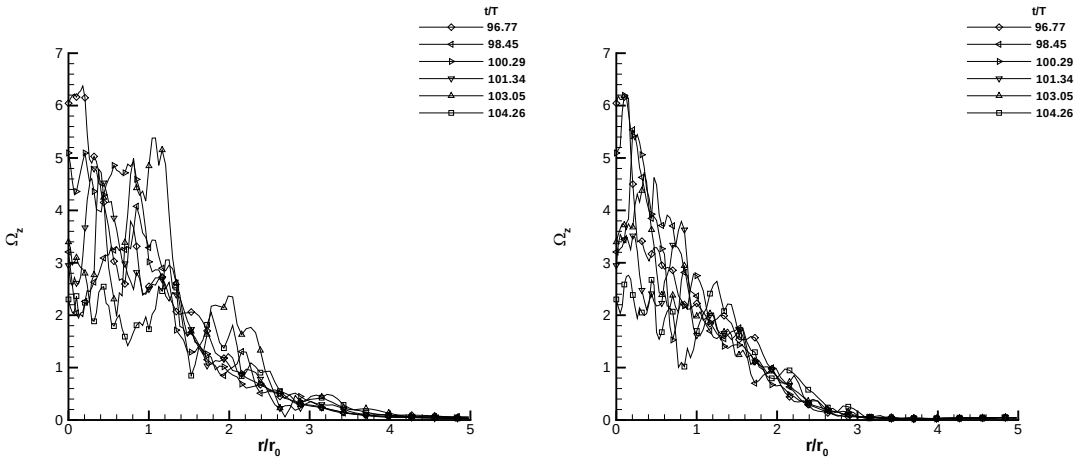


(a) (b)

Figure 3.201 Variation of mean axial vorticity for STRN2 in the sixth period at (a) $\theta = 45^o$ and (b) $\theta = 135^o$

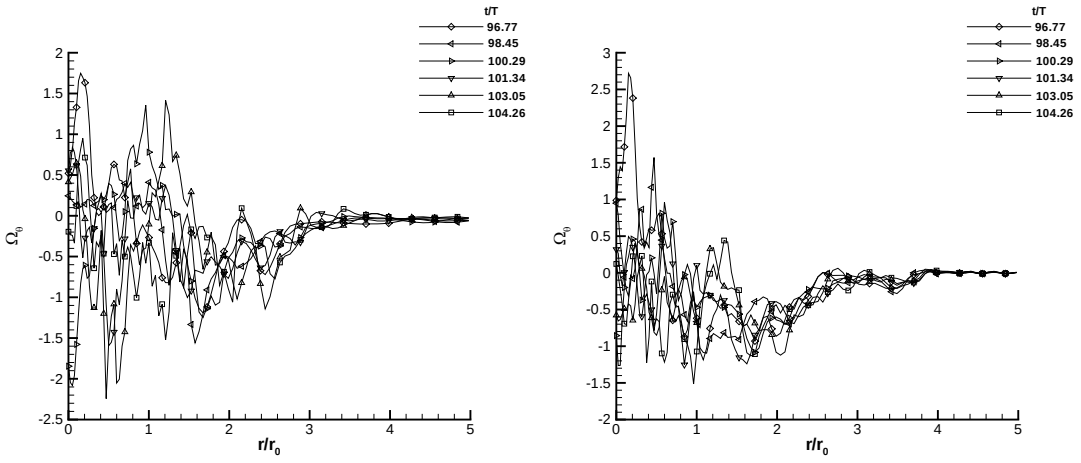


(a) (b)

Figure 3.202 Variation of mean tangential vorticity for STRN2 in the sixth period at (a) $\theta = 45^o$ and (b) $\theta = 135^o$

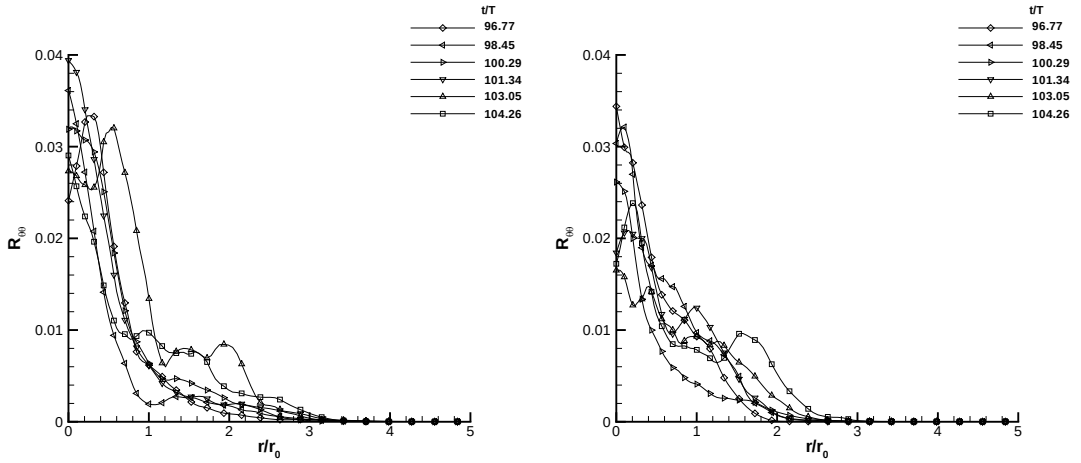


(a) (b)

Figure 3.203 Variation of $R_{\theta\theta}$ for STRN2 in the sixth period at (a) $\theta = 45^o$ and (b) $\theta = 135^o$

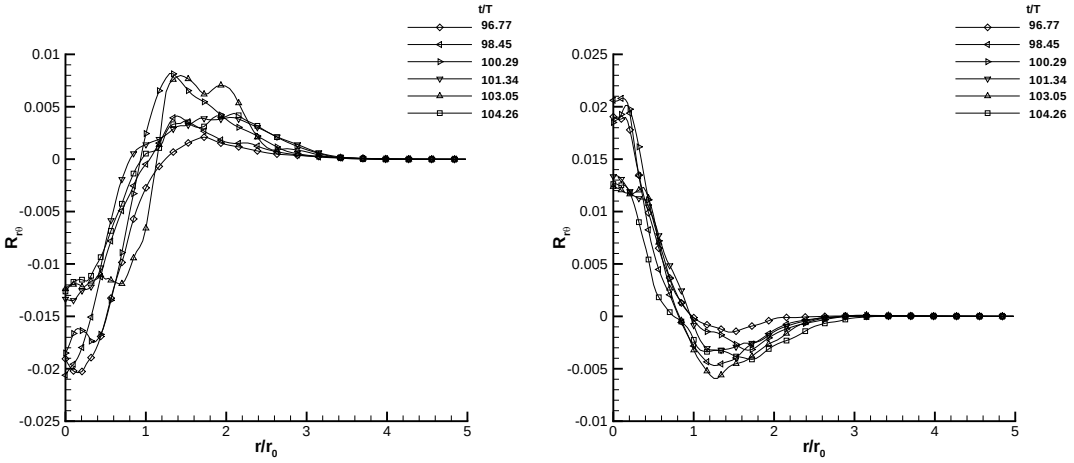


(a) (b)

Figure 3.204 Variation of $R_{r\theta}$ for STRN2 in the sixth period at (a) $\theta = 45^o$ and (b) $\theta = 135^o$

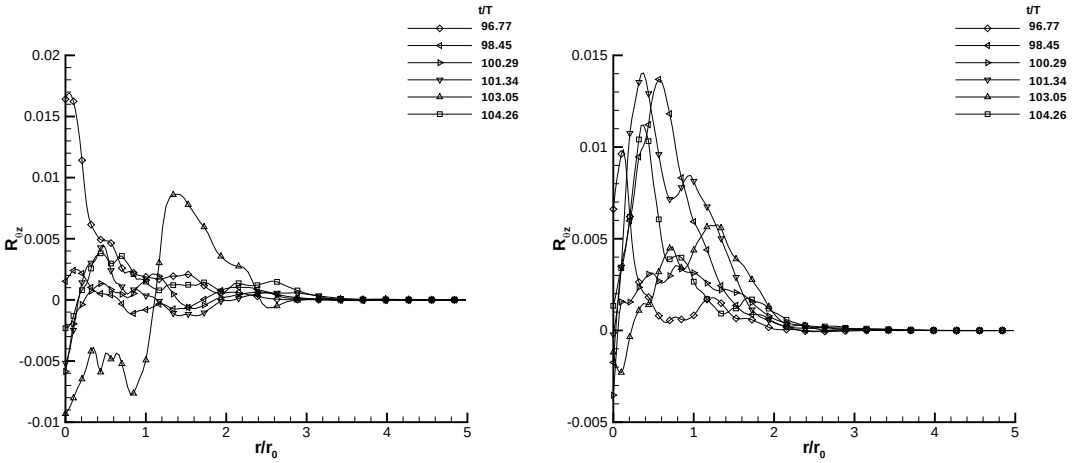


(a) (b)

Figure 3.205 Variation of $R_{\theta z}$ for STRN2 in the sixth period at (a) $\theta = 45^o$ and (b) $\theta = 135^o$

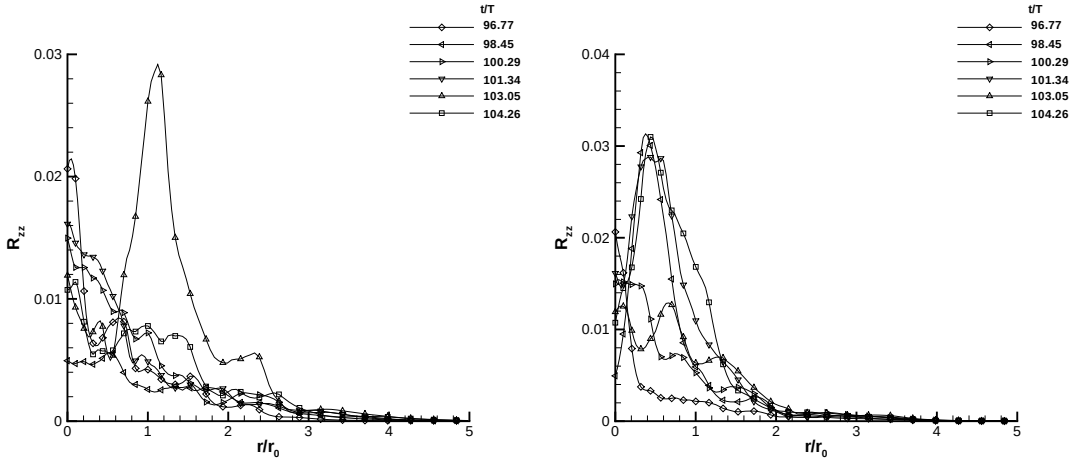


(a) (b)

Figure 3.206 Variation of $R_{zz}$ for STRN2 in the sixth period at (a) $\theta = 45^o$ and (b) $\theta = 135^o$

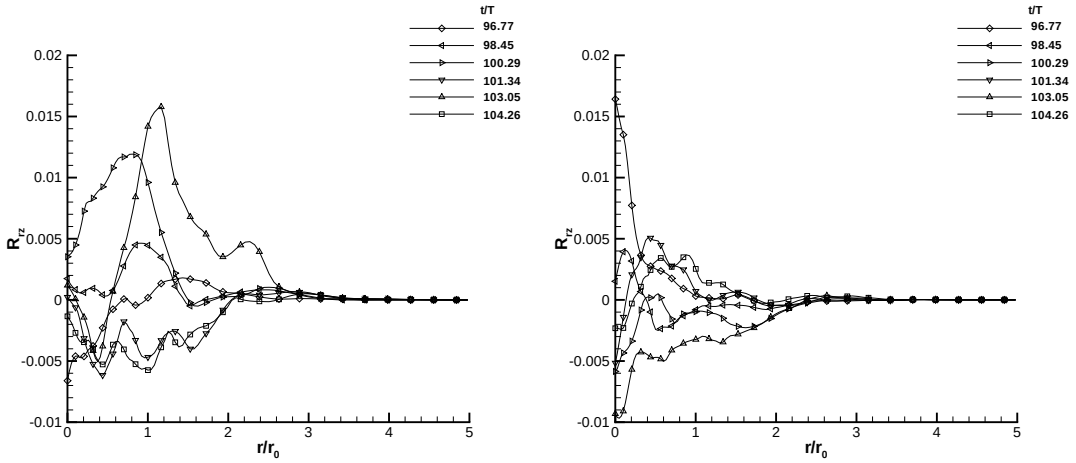


(a) (b)

Figure 3.207 Variation of $R_{rz}$ for STRN2 in the sixth period at (a) $\theta = 45^o$ and (b) $\theta = 135^o$

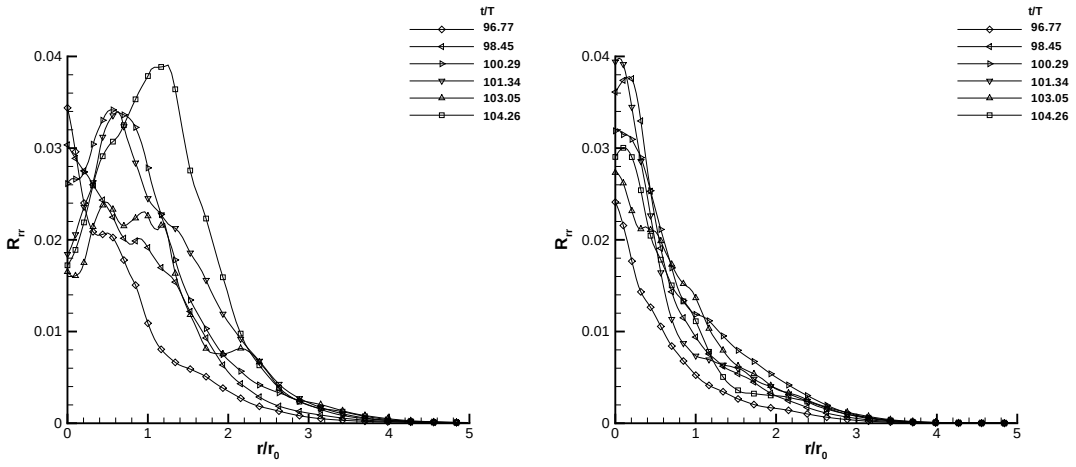


(a) (b)

Figure 3.208 Variation of $R_{rr}$ for STRN2 in the sixth period at (a) $\theta = 45^o$ and (b) $\theta = 135^o$

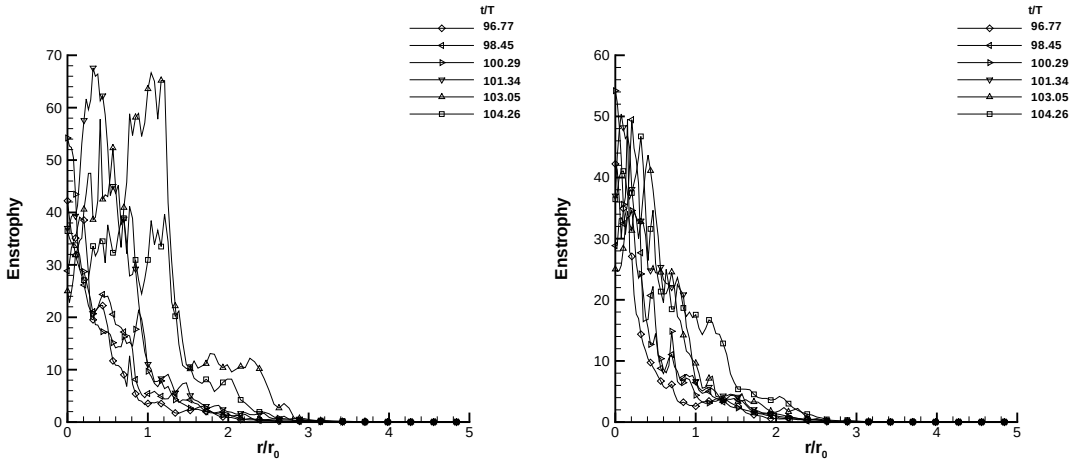


(a) (b)

Figure 3.209 Variation of enstrophy for STRN2 in the sixth period at (a) $\theta = 45^o$ and (b) $\theta = 135^o$

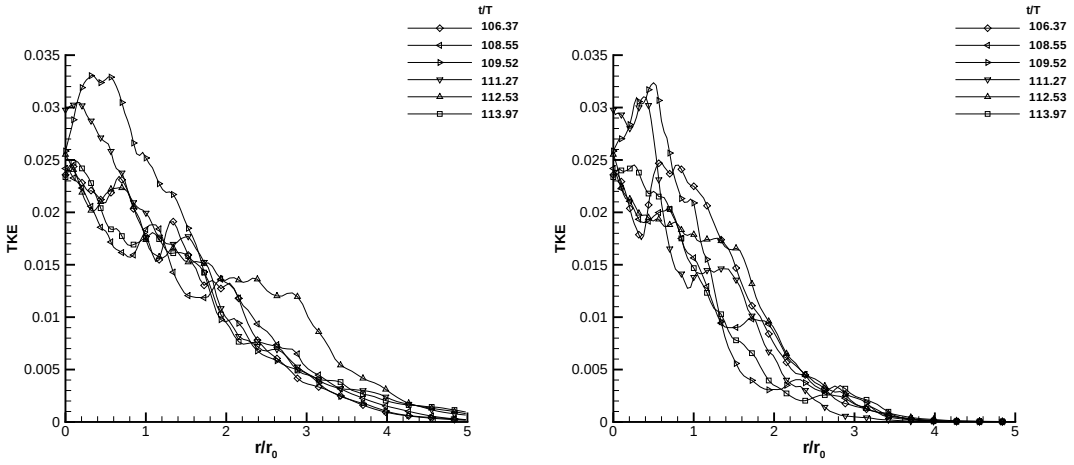


(a) (b)

Figure 3.210 Variation of turbulent kinetic energy for STRN2 in the seventh period at (a) $\theta = 45^o$ and (b) $\theta = 135^o$

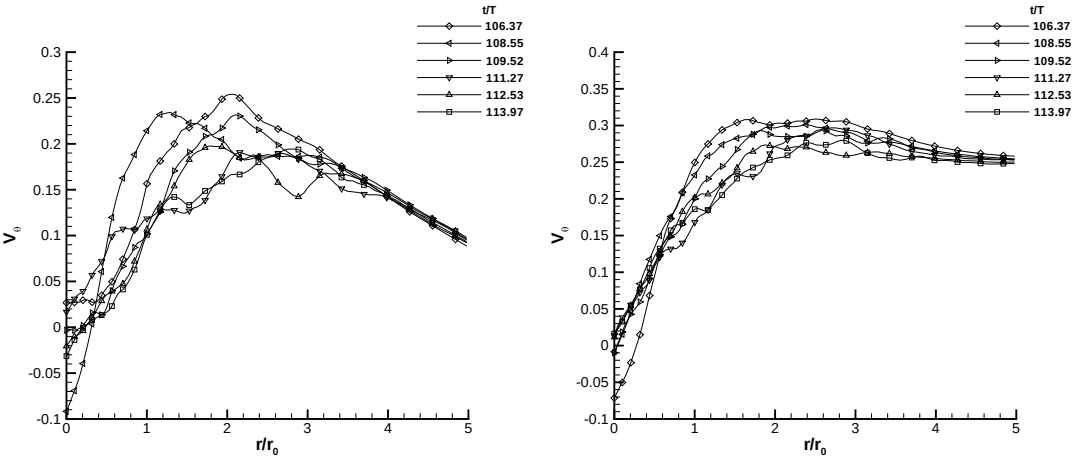


(a) (b)

Figure 3.211 Variation of mean tangential velocity for STRN2 in the seventh period at (a) $\theta = 45^o$ and (b) $\theta = 135^o$

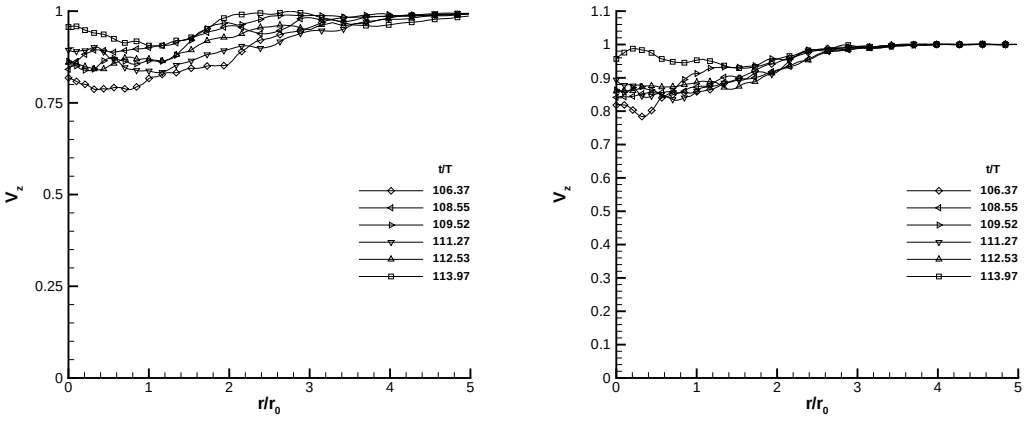


(a) (b)

Figure 3.212 Variation of mean axial velocity for STRN2 in the seventh period at (a) $\theta = 45^o$ and (b) $\theta = 135^o$

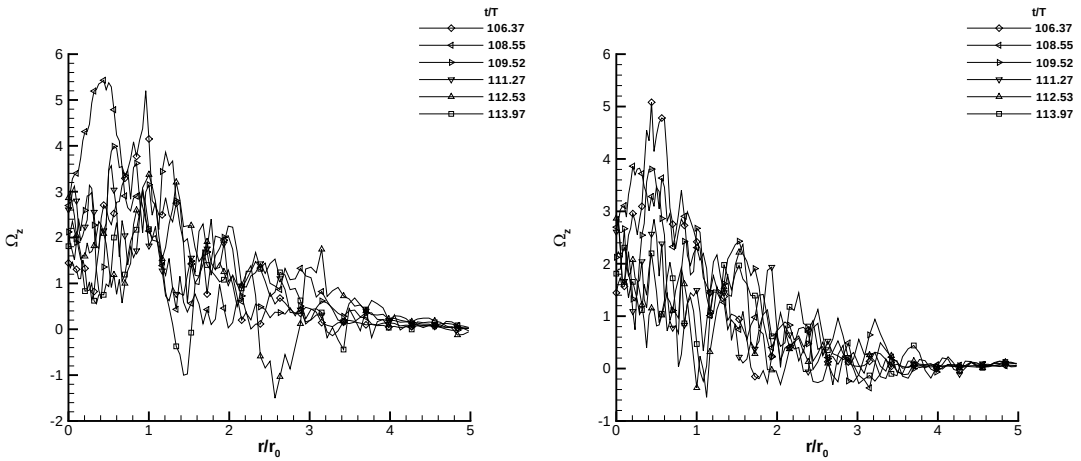


(a) (b)

Figure 3.213 Variation of mean axial vorticity for STRN2 in the seventh period at (a) $\theta = 45^o$ and (b) $\theta = 135^o$

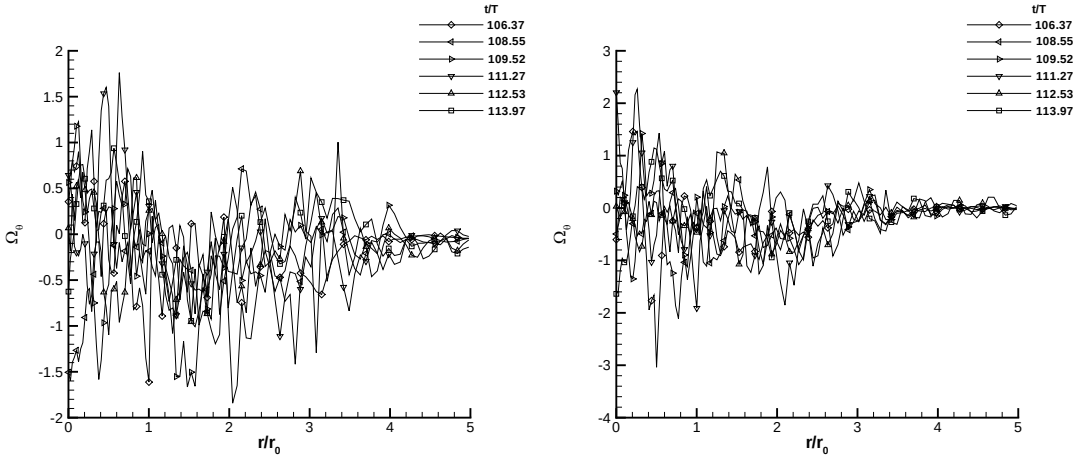


(a) (b)

Figure 3.214 Variation of mean tangential vorticity for STRN2 in the seventh period at (a) $\theta = 45^o$ and (b) $\theta = 135^o$

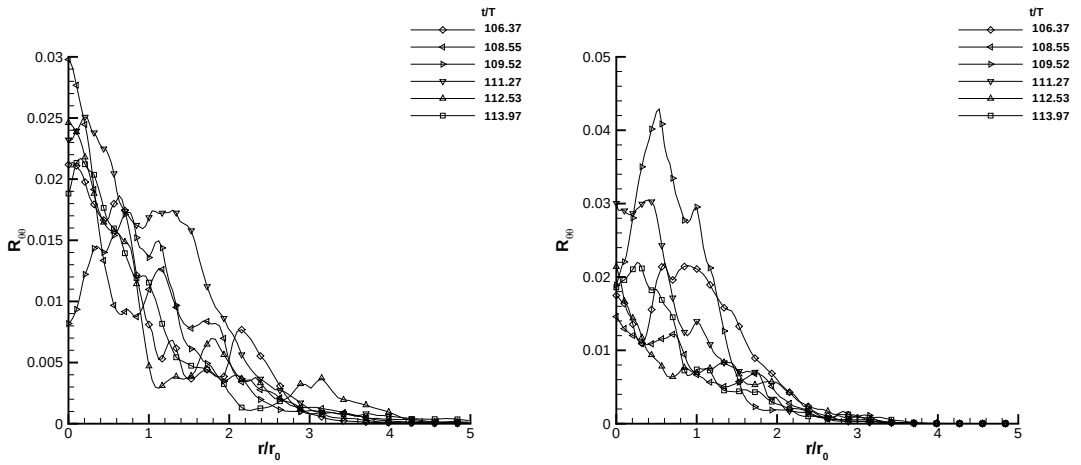


(a) (b)

Figure 3.215 Variation of $R_{\theta\theta}$ for STRN2 in the seventh period at (a) $\theta = 45^o$ and (b) $\theta = 135^o$

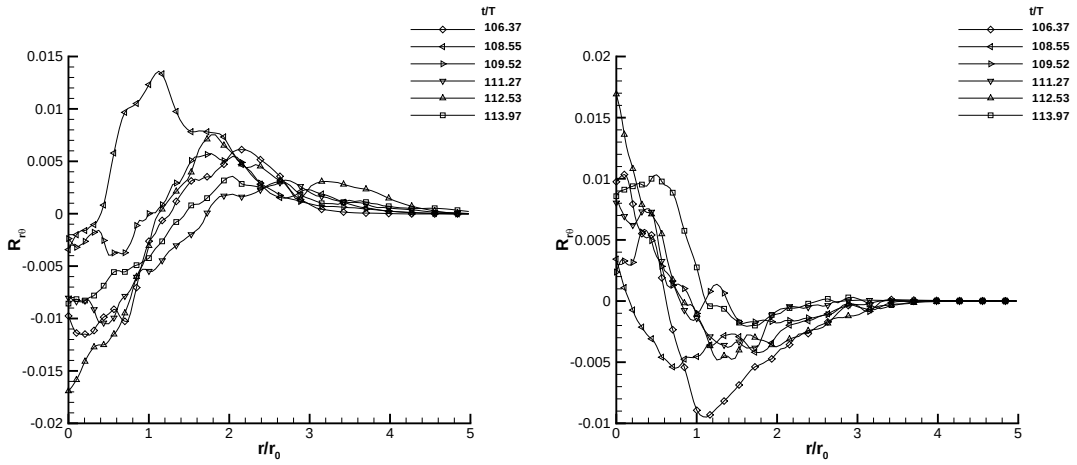


(a) (b)

Figure 3.216 Variation of $R_{r\theta}$ for STRN2 in the seventh period at (a) $\theta = 45^o$ and (b) $\theta = 135^o$

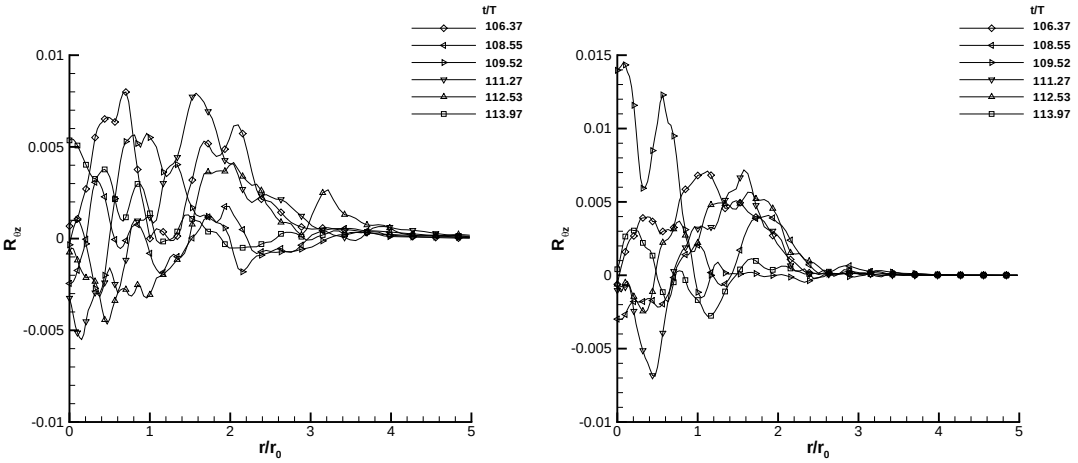


(a) (b)

Figure 3.217 Variation of $R_{\theta z}$ for STRN2 in the seventh period at (a) $\theta = 45^o$ and (b) $\theta = 135^o$

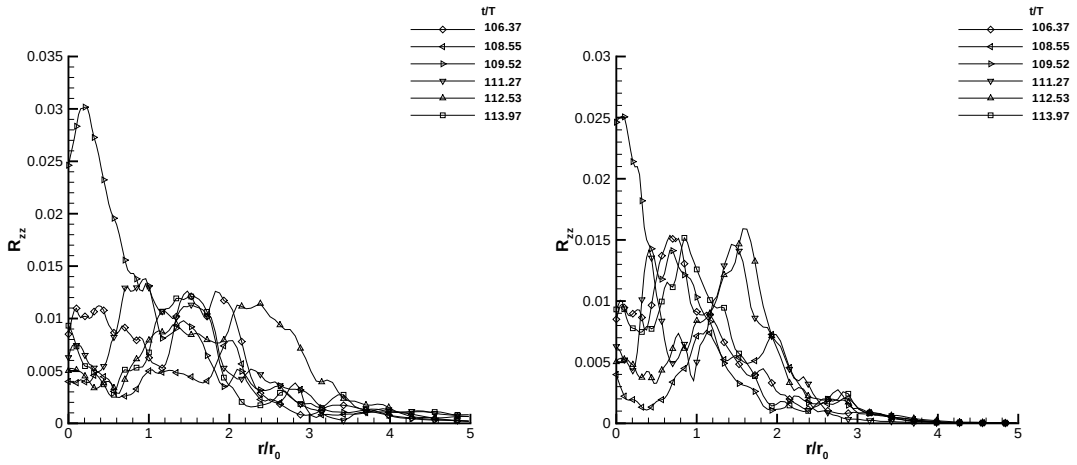


(a) (b)

Figure 3.218 Variation of $R_{zz}$ for STRN2 in the seventh period at (a) $\theta = 45^o$ and (b) $\theta = 135^o$

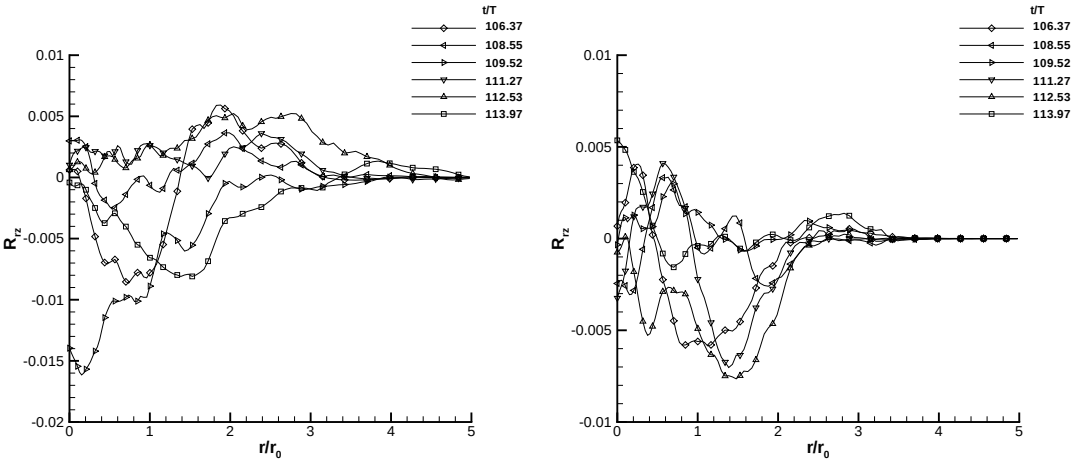


(a) (b)

Figure 3.219 Variation of $R_{rz}$ for STRN2 in the seventh period at (a) $\theta = 45^o$ and (b) $\theta = 135^o$

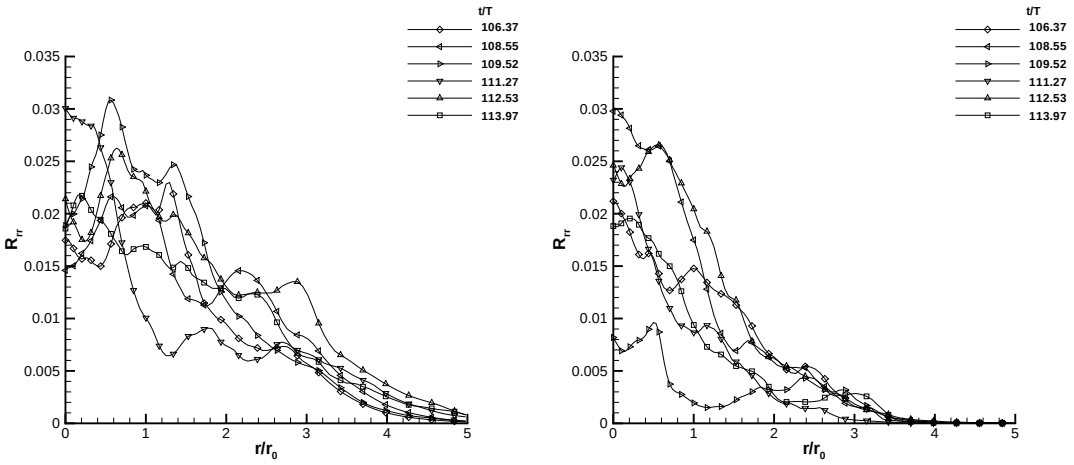


(a) (b)

Figure 3.220 Variation of $R_{rr}$ for STRN2 in the seventh period at (a) $\theta = 45^o$ and (b) $\theta = 135^o$

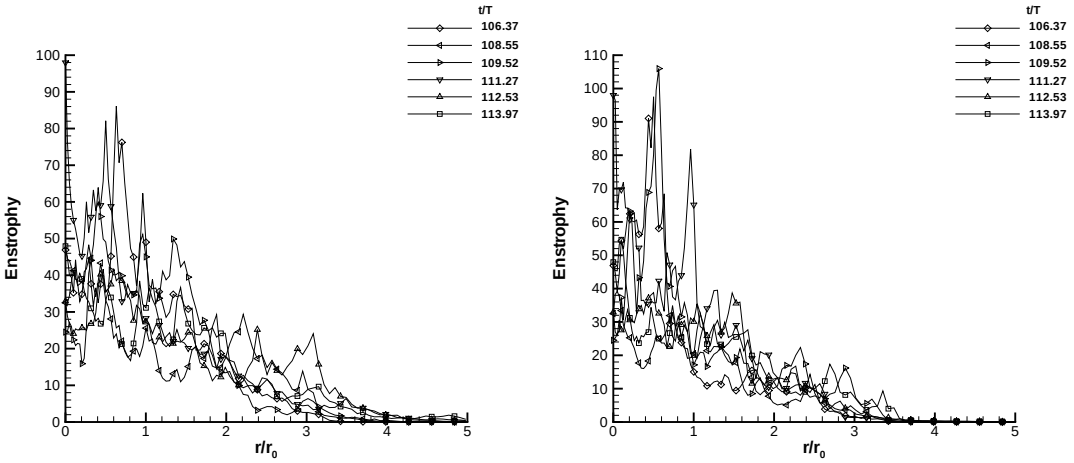


(a) (b)

Figure 3.221 Variation of enstrophy for STRN2 in the seventh period at (a) $\theta = 45^o$ and (b) $\theta = 135^o$

# 4. CONCLUSIONS AND FUTURE WORK

## 4.1 Conclusions

The overall aim of the research work presented in this thesis has been to enhance our understanding of strained turbulent axial vortices. The approach taken is that of direct numerical simulations (DNS). Two specific cases have been considered:

- An initially laminar vortex with no axial flow. This simulation is referred to as STRN4.
- An initially laminar vortex with a wake like axial velocity profile. This simulation is referred to as STRN2.

Both these simulations start with a random perturbation of the initially laminar vortices. The evolution of the overall level of turbulence is studied by computing the global turbulent kinetic energy (GTKE). One dimensional energy spectra are computed at times when the vortex is highly turbulent. This gives us an idea of how well the smaller length scales are being resolved in our simulations. Flow visualization is performed by plotting isosurfaces of vorticity magnitude. In this manner we have been able to study the evolution of the vortices in terms of their structure. Two dimensional energy spectra are computed to study the distribution of turbulent kinetic energy over different wavenumbers. This gives us information about the range of length scales present (higher wavenumbers correspond to smaller length scales). Also, we can pick out modes that are dominant and correlate this information with features observed in the vortex structure. In addition to gaining a broad understanding of the flow in this manner, the evolution of some mean and statistical quantities of interest

(mean velocity and vorticity components, turbulent kinetic energy, Reynolds stresses and enstrophy) has been looked at.

STRN4, the simulation without an axial flow, is studied in detail first so that we may focus on the effect of the strain field exclusively. We observe an initial decay of turbulence. This is followed by a period during which the turbulence grows exponentially. During this period we can identify $(k_\theta, k_z) = (\pm 1, 4)$ to be be the most energetic modes. This corresponds to a sinusoidal bending along the vortex axis with a wavenumber of 4 and the presence of left and right running helical waves. These features can indeed be observed in the vortex structure. We also observe that the instability is initiated inside the vortex core. These observations assure us that we are indeed capturing the elliptical instability. As the level of turbulence grows, we observe an increased presence of small scale structure. This can be seen in the flow visualization pictures as well as in the 2-D energy spectra, where turbulent kinetic energy is seen to be spread over a larger range of wavenumbers.

The turbulence then saturates and begins to decay. During this period the vortex is seen to re-consolidate (meaning it has less fine scale structure). At the end of this period of decay the dominant modes are observed to be shifting to $(k_\theta, k_z) = (\pm 1, 3)$. This shift is confirmed when $(\pm 1, 3)$ are observed to be the dominant modes as the GTKE again grows exponentially, albeit with a lower growth rate than before. The increase in wavelength of the sinusoidal bending of the vortex axis is reflected in the flow visualization pictures. As the GTKE peaks again, we observe an increased presence of small scale structure. As before this is reflected in the flow visualization pictures and the 2-D energy spectra.

Once again the turbulence decays. This time as the GTKE approaches an ebb, we do not observe a significant decrease in the presence of fine scale structure. However, the level of turbulent kinetic energy in these small length scales (higher wavenumbers) is seen to have decreased. This is as expected since the overall level of turbulence is decreasing. The dominant modes are again observed to be shifting, now to $(\pm 1, 2)$. This is confirmed as the GTKE begins its final ascent of the simulation. Turbulence

again grows exponentially, with a still lower growth rate. In the inner regions of the vortex the mode (0,1) is also seen to have a substantial level of energy. As the turbulence keeps growing, the outer regions of the vortex start showing an increased presence of fine scale structure. In the outer regions we also observe an increase in the energy carried by the dominant modes $(\pm 1, 2)$. This corresponds well with the helical waves being more pronounced in the vortex structure. In the inner regions however, the energy contained by the dominant modes starts reducing. This trend of the dominant modes carrying lower levels of energy is carried out into the outer regions as the turbulence grows. The range of wavenumbers carrying a significant amount of turbulent kinetic energy increases though. Eventually we see that a substantial level of vorticity reaches out near the boundary. This is in conflict with our use of potential flow boundary conditions. The simulation thus has to be stopped. Although we cannot make a definite statement of what the vortex would do next, it seems that we now have an unbounded growth of turbulence. This is reflected in the dominant modes further moving to $(\pm 1, 1)$.

In addition to gaining the above broad vision of the flow physics, a close look has also been taken at evolution of some mean and statistical quantities of interest (mean velocity and vorticity components, turbulent kinetic energy, Reynolds stresses and enstrophy). Some of the principal observations can be listed as follows:

- The turbulent kinetic energy (TKE) peak moves to the center early on in the simulation. This is consistent with the fact that the elliptic instability gets initiated inside the vortex core. The TKE peak stays established at the center and increases and decreases in value as the overall level of turbulence rises and falls during the simulation.

- The peak of the mean axial vorticity moves away from the centerline during the first exponential growth of turbulence.

- The enstrophy peak also moves away from the centerline to the location established by the mean axial vorticity above.

- $R_{r\theta}$ values along the major and minor axes of the elliptical flow are of similar magnitudes but opposite sign.

- During the first and third ascents of GTKE, $R_{\theta\theta}$ values along the major axis are about twice as large as those along the minor axis. The opposite is observed during the time between these two GTKE ascents.

- During the first and third ascents of GTKE, $R_{rr}$ values along the minor axis are about twice as large as those along the major axis. The opposite is observed during the time between these two GTKE ascents.

STRN2, which included axial flow, was now looked at closely. In contrast to STRN4, where the turbulence turbulence went through a brief period of decay before growing exponentially, in STRN2 we observe an exponential growth of turbulence soon after the simulation starts. Initially the unstable modes are found to be $(k_\theta, k_z)$ = (1,1), (2,2), (3,3), (4,4) and (5,5). Helical waves are observed in the vortex structure. These observations tell us that the instability caused by the wake-like axial flow is dominating during this growth of turbulence. As the turbulence grows, we have an increased presence of fine scale structure. This gets reflected in the vorticity magnitude isosurfaces plots as well as in the 2-D spectra where turbulent kinetic energy is seen to be spread over a wide range of wavenumbers (higher wavenumbers correspond to smaller length scales). Also we see that the dominant modes are shifting in terms of the $k_z$ component. This is reflected in the number of times the helical waves are seen to twist around the vortex. The turbulence eventually saturates and begins to decay. At the peak of GTKE, we observe (-1,1) to be one of the dominant modes in the interior of the vortex. It is possible that we are now beginning to feel the presence of the elliptical instability. Also, the presence of this dominant mode only in the interior of the vortex could be a correspondence to the fact that the elliptical instability gets initiated inside the vortex core.

As the GTKE decays, the vortex consolidates (meaning we have a reduced presence of fine scale structure). We also identify the presence of both left and right running

helical waves in the vortex structure. As this descent of GTKE culminates in an ebb the dominant modes are observed to include the (0,1) mode. This corresponds to variations in core area as we move along the vortex axis. Thus we are observing the presence of dominant modes that correspond to different instability mechanisms. This corresponds well with the varied set of features observed in the vortex structure. We have sinusoidal bending of the vortex axis, variations in core area as we move along the vortex axis and left and right running helical waves.

As the GTKE rises again, this time with a much lower growth rate, we continue to see the presence of a varied set of features in the vortex structure. These correspond to dominant modes that indicate the presence of multiple instability mechanisms. As the GTKE peaks again we observe a tightening up of the vortex. Most of the vorticity is now contained in a small region around the vortex axis. The vortex loosens up as the GTKE decays again and approaches its next ebb. Upon reaching this ebb, we observe that the turbulence maintains its level for an extended period of time. Although the level of turbulence does not vary much during this period, we do observe a shift in the dominant modes. This could indicate that the eventual instability mechanisms are now getting selected. At the end of this period, which is marked by a lack of significant variation in how turbulent the vortex is, the dominant modes are found to be $(\pm 1, 1)$, (0,1) and (0,2).

The GTKE now begins its final ascent of this simulation with a still lower growth rate. The dominant modes are consistently observed to be $(\pm 1, 1)$, (0,2) and (2,2). The vortex is again found to be tightened up during this ascent. In the later phases of this ascent, the vortex loosens up again. Sinusoidal bending along the vortex axis and left and right running helical waves are prominent in the vortex structure. An increased presence of small scale structure is observed as the vortex becomes more and more turbulent. The GTKE peaks with $(\pm 1, 1)$ and (0,2) being the dominant modes. Finally the GTKE plunges and we see $(\pm 1, 1)$ to be the only dominant modes. These were also the eventual dominant modes in STRN4. The principal features of the vortex structure in STRN4 were a sinusoidal bending along the vortex axis and left

and right running helical waves. As noted above, these features are prominent in the final stages of STRN2 also. The growth rates during the final GTKE ascents in both the simulations are also comparable. It seems that the same instability mechanism eventually dominates in both the cases.

We now observe that a significant level of vorticity is now present near the boundary of the computational domain. As was the case in STRN4, this is in conflict with our choice of potential flow boundary conditions. With our current computational domain size, the simulation cannot be carried on meaningfully.

Following the trend set in STRN4, after obtaining the above broad understanding of the flow physics, the evolution of some mean and statistical quantities of interest was studied. Some of the principal observations are:

- In the early stages of the simulation, the turbulent kinetic energy (TKE) peak moves to a location just near the core edge. As the GTKE keeps growing the peak oscillates between moving inwards to the centerline and outwards to the core edge. As the GTKE peaks, the peak is found to be moving inwards. The peak moves to the centerline when the GTKE descends for the first time. It then stays at or near the centerline. Right towards the end of the final ascent of GTKE, the peak does move away from the centerline but then returns.

- Contrary to STRN4, the peak of the mean axial vorticity does not leave the centerline.

- During the period when GTKE maintains an almost uniform level, $R_{r\theta}$, $R_{\theta z}$ and $R_{rz}$ flip signs repeatedly. This is a strong indicator towards the presence of anti-diffusion.

- During the GTKE ascent after the "steady" state, $R_{r\theta}$ values along the major and minor axes of the elliptical flow are of similar magnitudes but opposite sign. This was observed throughout STRN4. This is an indication that in the final stages of STRN2, turbulence might be behaving in a manner similar to STRN4.

- During the final ascent of GTKE the mean axial velocity profile inside the core shows variations in shape. The classical "wake-like" shape is distorted. This gets reflected in the mean tangential vorticity attaining positive values inside the core. Towards the end, the initial wake like axial flow profile is observed to have almost completely decayed.

- Turbulent quantities show a general trend of extending further out (in terms of having a substantial level) along the major axis.

## 4.2 Suggestions for Future Work

Although we have looked at how the Reynolds stresses evolve in time, we still do not understand how they do so. This understanding can be obtained by performing a Reynolds stress budget analysis. For example, we will understand the relative importance of mechanisms of production, diffusion, dissipation, etc. However, on several occasions we have noted that the sampling space available to compute the mean and statistical quantities was not large enough. This might make it difficult to obtain meaningful results while computing the budgets. Also, as discussed in chapter two, the numerical formulation results in the pressure term dropping out from our governing equations. It is of interest to compute the pressure field to get a more complete understanding of the flow physics. This will involve writing a Poisson flow solver. Once we have the pressure field, we will able to compute statistical quantities like pressure strain.

As mentioned in chapter one, the Reynolds numbers for the DNS are about three orders of magnitude smaller than those found in the wake vortices of large commercial aircraft. While LES will not be able to reach full scale Reynolds numbers, it will allow us to study the effects of varying Reynolds numbers. The LES methodology is covered in detail in Appendix C, first in detail and then in the context of the current numerical method. The DNS code used for the current study has been modified to be able to

perform LES. This code needs to be validated and then used to study the vortex at higher Reynolds numbers.

With particular reference to the wake hazard problem, it would be of interest to simulate a pair of axial vortices (rather than accounting for the effect of one vortex on the other via a strain field). This will include effects such as a variable strain rate, cooperative instability, etc.

# REFERENCES

## REFERENCES


[1] Afanasyev, Ya.D., "Experiments on instability of columnar vortex pairs in rotating fluid", *Geophys. Astrophys. Fluid Dynamics*, Vol. 96(1) , pp. 31-48, 2002.

[2] Bayly, B.J., "Three-dimensional instability of elliptical flow", *Phys. Rev. Lett.*, Vol. 57, pp. 2160-2163, 1986.

[3] Blaisdell, G.A. and Shariff, K., "Homogeneous turbulence subjected to mean flow with elliptic streamlines", *Center for Turbulence Research, Proceedings of the Summer Program 1994*, pp. 355-371.

[4] Blaisdell, G.A. and Shariff, K., "Simulation and modeling of the elliptic streamline flow", *Center for Turbulence Research, Proceedings of the Summer Program 1996*, pp. 433-446.

[5] Blaisdell, G.A. and Qin, J.H., "Numerical simulation of a strained turbulent axial vortex", *Turbulence and Shear Flow Phenomenon - 1, First International Symposium, September 12-15, 1999, Santa Barbara, California*, pp. 1007-1012.

[6] Cadot, O., Douady, S. and Couder, Y., "Characterization of the low-pressure filaments in three-dimensional turbulent shear flow", *Phys. Fluids*, Vol. 7, pp. 630-646, 1995.

[7] Cambon, C., Benoit, J.P., Shao, L. and Jacquin, L., "Stability analysis and large-eddy simulation of rotating turbulence with organized eddies", *J. Fluid Mech.*, Vol. 278, pp. 175-200, 1994.

[8] Cambon, C., Teissedre, C. and Jeandel, D., "Etude d'effets couples de deformation et de rotation sur une turbulence homogene", *J. Mec Theo. Appl.*, Vol. 4, 1985.

[9] Coppens, F., "Simulations Numeriques Sur Le Developpement De La Turbulence Dans Un Tourbillon", *Ph.D. thesis, L'Institut Polytechnique De Toulouse, 3 June 1998.*

[10] Crow, S.C., "Stability theory for a pair of trailing vortices", *AIAA Journal*, Vol. 8, pp. 2172-2179, 1970.

[11] de Boor, C., *A practical guide to splines*, Vol. 27 of *Applied mathematical science*, Springer-Verlag, 1978.

[12] Duck, P.W. and Foster, M.R., "The inviscid stability of a trailing line vortex", *J. Appl. Math. Phys.*, Vol. 31, pp. 524-532, 1980.

[13] Le Dizes, S. and Laporte, F., "Theoretical predictions for the elliptical instability in a two-vortex flow", *J. Fluid Mech.*, Vol. 471, pp. 169-201, 2002.

[14] Eloy, C. and Le Dizes, S., "Three-dimensional instability of Burgers and Lamb-Oseen vortices in a strain field", *J. Fluid Mech.*, Vol. 378, 1999.

[15] Guckenheimer, J. and Mahalov, A., "Instability induced by symmetry reduction", *Phys. Rev. Lett.*, Vol. 68, 1992.

[16] Kerswell, R.R., "Elliptical instability", *Ann. Rev. Fluid Mech.*, Vol. 34, pp. 83-113, 2002.

[17] Khorrami, M.R., "On the viscous modes of instability of a trailing line vortex", *J. Fluid Mech.*, Vol. 225, pp. 197-212, 1991.

[18] , Knobloch, E., Mahalov, A. and Marsden, J., "Normal forms for three-dimensional parametric instabilities in ideal hydrodynamics", *Physica D*, Vol. 73, 1994.

[19] Kuchemann, D., "Report on the I.U.T.A.M. Symposium on concentrated vortex motions in fluids", *J. Fluid Mech.*, Vol. 21, pp. 1-20, 1965.

[20] Kida, S., "Tube-like structures in turbulence", *Lecture Notes Numer. Appl. Anal.*, Vol. 12, 1993.

[21] Landman, M.J. and Saffman, P.G., "The three-dimensional instability of strained vortices in a viscous fluid", *Phys. Fluids*, Vol. 30, pp. 2339-2342, 1987.

[22] Laporte, F. and Corjon, A., "Direct numerical simulations of the elliptical instability of a vortex pair", *Phys. Fluids*, Vol. 12, pp. 1016-1031, 2000.

[23] Lebovitz, N. and Saldanha, K., "On the weakly nonlinear development of the elliptic instability", *Phys. Fluids*, Vol. 11, pp. 3374-3379, 1999.

[24] Leibovich, S. and Stewartson, K., "A sufficient condition for the instability of columnar vortices", *J. Fluid Mech.*, Vol. 126, pp. 335-356, 1983.

[25] Lessen, M. and Paillet, F., "The stability of trailing line vortex. part2. viscous theory", *J. Fluid Mech.*, Vol. 65, pp. 769-779, 1974.

[26] Lessen, M., Singh, P.J. and Paillet, F., "The stability of trailing line vortex. part1. inviscid theory", *J. Fluid Mech.*, Vol. 63, pp. 753-763, 1974.

[27] Leweke, T. and Williamson, C.H.K., "Cooperative elliptic instability of a vortex pair", *J. Fluid Mech.*, Vol. 360, pp. 85-119, 1998.

[28] Lesieur, M. and Metais, O., "New trends in large-eddy simulations of turbulence", *Ann. Rev. Fluid Mech.*, Vol. 28, pp. 45-82, 1996.

[29] Lungren, T.S. and Mansour, N.M., "Transition to turbulence in an elliptical vortex", *J. Fluid Mech.*, Vol. 307, pp. 43-62, 1996.

[30] Lilly, D.K., "A proposed modification of the Germano subgrid-scale closure method", *Phys. Fluids A*, Vol. 4, pp. 633-635, 1992.

[31] Malkus, W.V.R., "An experimental study of the global instabilities due to the tidal (elliptical) distortion of a rotating elastic cylinder", *Geophys. Astrophys. Fluid Dynamics*, Vol. 48, pp. 123-134, 1989.

[32] Mason, D.M. and Kerswell, R.R., "Chaotic dynamics in a strained rotating flow: a precessing plane fluid layer", *J. Fluid Mech.*, Vol. 471, pp. 71-106, 2002.

[33] Mason, D.M. and Kerswell, R.R., "Nonlinear evolution of the elliptical instability: an example of inertial wave breakdown", *J. Fluid Mech.*, Vol. 396, pp. 73-108, 1999.

[34] Moore, D.W. and Saffman, P.G., "The instability of a straight vortex filament in a strain field", *Proc. R. Soc. Lond. A*, Vol. 346, pp. 413-425, 1975.

[35] Orlandi, P., Carnevale, G.F., Lele, S.K. and Shariff, K., "DNS study of stability of trailing vortices", *Center for Turbulence Research, Proceedings of the Summer Program 1998*, pp. 187-208.

[36] Pierrehumbert, R.T., "Universal short-wave instability of two-dimensional eddies in an inviscid fluid", *Phys. Rev. Lett.*, Vol. 57, pp. 2157-2159, 1986.

[37] Piomelli, U., Cabot, W.H., Moin, P. and Lee, S., "Subgrid-scale backscatter in turbulent and transitional flows", *Phys. Fluids A*, Vol. 3, pp. 1766-1771, 1991.

[38] Pradeep, D.S. and Hussain, F., "Core dynamics of a strained vortex: instability and transition", *J. Fluid Mech.*, Vol. 447, pp. 247-285, 2001.

[39] Qin, J.H., "Numerical Simulations of a Turbulent Axial Vortex", *Ph.D. thesis, Department of Aeronautics and Astronautics, Purdue University, December 1998.*

[40] Ragab, S. and Sreedhar, M., "Large-scale structures in a trailing vortex", *AIAA Paper*, 94-2316, 1994.

[41] Ragab, S. and Sreedhar, M., "Direct numerical simulation of instability waves in a trailing vortex", *AIAA Paper*, 95-0591, 1995a.

[42] Ragab, S. and Sreedhar, M., "Numerical simulation of vortices with axial velocity deficits", *Phys. Fluids A*, Vol. 7(3), pp. 549-558, 1995b.

[43] Robinson, A.C. and Saffman, P.G., "Three dimensional stability of an elliptical vortex in a straining field", *J. Fluid Mech.*, Vol. 142, pp. 451-466, 1984.

[44] Sarpkaya, T. and Daly, J.J., "Effect of ambient turbulence on trailing vortices", *Journal of Aircraft*, Vol. 24(6) , pp. 399-404, 1987.

[45] Singh, A.J. and Uberoi, M.S., "Experiments on vortex stability", *Phys. Fluids*, Vol. 19, pp. 1858-1863, 1976.

[46] Sipp, D., "Weakly nonlinear saturation of short-wave instabilities in a strained Lamb-Oseen vortex", *Phys. Fluids*, Vol. 12(7), pp. 1715-1729, 2000.

[47] Smagorinski, J.S., "General circulation experiments with the primitive equations. I. The basic experiment", *Monthly Weather Review*, Vol. 91, pp. 99-164, 1963.

[48] Spyropoulos, E.T., "On Dynamic Subgrid-Scale Modeling for Large-Eddy Simulation of Compressible Turbulent Flows", *Ph.D. thesis, Department of Aeronautics and Astronautics, Purdue University, December 1996.*

[49] Takahashi, R.K. and McAlister, K.W., "Preliminary study of a wing-tip vortex using laser velocimetry", Technical Report NASA TM 88343, 1987.

[50] Tsai, C., and Widnall, S.E., "The stability of short waves on a straight vortex filament in a weak externally imposed strain field", *J. Fluid Mech.*, Vol. 73, pp. 721-733, 1976.

[51] Vincent, A. and Meneguzzi, M., "The spatial structure and statistical properties of homogeneous turbulence", *J. Fluid Mech.*, Vol. 225, pp. 1-20, 1991.

[52] Waleffe, F., "The 3D instability of a strained vortex and its relation to turbulence", *Ph.D. thesis, Massachusetts Institute of Technology, 1989.*

[53] Waleffe, F., "On the three-dimensional instability of strained vortices", *Phys. Fluids A*, Vol. 2, pp. 76-80, 1990.

# APPENDICES

## Appendix A: B-splines : Construction and Properties

This appendix reviews briefly the construction and properties of B-splines. For an in-depth treatise the reader is directed to de Boor (1978).

### A.1 Construction

B-splines form a basis for the space of piecewise polynomial functions. de Boor (1978) developed the following recursive method to construct the $N$ splines of order $k$ for a given set of $N + k$ knot points $[\eta_1, \eta_1, \eta_2, \ldots, \eta_{N+k}]$:

$$g_l^k(r) = \frac{(r - \eta_l)}{(\eta_{l+k-1} - \eta_l)} g_l^{k-1}(r) + \frac{(\eta_{l+k} - r)}{(\eta_{l+k} - \eta_{l+1})} g_{l+1}^{k-1}(r) \tag{A.1}$$

where $g_l^k(r)$ is the $l^{th}$ B-spline of order $k$ and $\eta_l$ is the knot coordinate. The construction starts with the first order B-splines given by

$$g_l^1(r) = \begin{cases} 1, & \eta_l \leq r \leq \eta_{l+1} \\ 0, & \text{otherwise.} \end{cases} \tag{A.2}$$

B-splines at the boundaries are constructed using multiple knots. $k-1$ multiple knots are required at the boundaries for B-splines of order $k$. The first derivative of the B-splines can be constructed as follows:

$$\frac{d}{dr} g_l^k = \frac{(k-1) g_l^{k-1}}{(\eta_{l+k-1} - \eta_l)} - \frac{(k-1) g_{l+1}^{k-1}}{(\eta_{l+k} - \eta_{l+1})} \,. \tag{A.3}$$

Repeated application of the above equation gives the higher derivatives.

### A.2 Properties

1. B-splines have local support. In general, a B-spline of order $k$ has support on $k + 1$ intervals. Also, B-splines are positive.

$$\begin{aligned} g_l^k(r) &> 0 \,, \qquad \text{for} \quad \eta_l < r < \eta_{l+k} \,, \\ g_l^k(r) &= 0 \,, \qquad \text{for} \quad r < \eta_l \text{ or } r > \eta_{l+k} \,. \end{aligned}$$

2. The B-splines satisfy the following equation:

$$\sum_{l=1}^{N} g_l^k(r) = 1$$

3. At $r = 0$

$$g_l^q(0) = 0 \text{ for } l > q+1;\ q = 0, 1, 2, ...., k-1$$

and at the other boundary, $r = 1$

$$g_l^q(1) = 0 \text{ for } l < N-q;\ q = 0, 1, 2, ...., k-1$$

4. Properties 2 and 3 can be combined to deduce the following:

$$\begin{aligned} g_1^k(r)\Big|_{r=0} &= g_N^k(r)\Big|_{r=1} = 1\,, \\ \frac{d}{dr}\left[g_1^k(r)\right]\Big|_{r=0} &= -\frac{d}{dr}\left[g_2^k(r)\right]\Big|_{r=0}\,, \\ \frac{d}{dr}\left[g_N^k(r)\right]\Big|_{r=1} &= -\frac{d}{dr}\left[g_{N-1}^k(r)\right]\Big|_{r=1}\,. \end{aligned}$$

### A.3 Galerkin method

Consider the following model equation,

$$\frac{d^n}{dr^n}\phi(r) = f(r) \tag{A.4}$$

which is solved on the domain $r \in [r_i, r_f]$. If $n = 0$, equation A.4 is a representation problem. Let $\tilde{\phi}(r)$ be an approximation of $\phi$ in term of B-splines of order $k$ on the knot set that we have selected:

$$\tilde{\phi}(r) = \sum_l \alpha_l g_l(r) \tag{A.5}$$

The expansion coefficients in equation A.5 can be obtained by substituting the expansion equation A.5 into equation A.4 and applying the Galerkin projection

$$\int_{r_i}^{r_f} g_k(r) \sum_{l=1}^{N+k} \frac{d^n}{dr^n}\left[g_l(r)\right]\alpha_l r dr = \int_{r_i}^{r_f} g_k(r) f(r) r dr. \tag{A.6}$$

Evaluating the integrals in equation A.6, we obtain a system of linear equations for $\alpha$:

$$A\alpha = b \tag{A.7}$$

where

$$A = \{a_{kl}\} = \int_{r_i}^{r_f} g_k(r) \frac{d^n}{dr^n} g_l(r) r dr \,, \tag{A.8}$$

and

$$b = \{b_k\} = \int_{r_i}^{r_f} f(r) g_k(r) r dr \tag{A.9}$$

The matrix $A$ a multidiagonal matrix. The bandwidth of matrix $A$ in the Galerkin method is equal to $2k + 1$.

## Appendix B: B-spline Spectral Method

The formulation of the B-spline spectral method is presented in detail here. First the mass and viscous matrices are presented. This is followed by expressions for the velocity and vorticity components. And finally the details regarding the computation of the non-linear term are presented.

### B.1 Mass and Viscous Matrices

The following elemental matrices are used to assemble the mass and viscous matrices as defined in equations (3.8) to (3.11). The Guass quadrature technique is used to evaluate these elemental matrices at the beginning of the program. However, computer memory limitations necessitate the assembly of the complete mass and viscous matrices at every time step.

$$
\begin{aligned}
\mathbf{m}_1 &= \int_0^R \frac{1}{r} g_k(r) g_l(r) dr \,, \\
\mathbf{m}_2 &= \int_0^R g_k'(r) g_l'(r) r \, dr \,, \\
\mathbf{m}_3 &= \int_0^R g_k(r) g_l(r) r \, dr \,, \\
\mathbf{m}_4 &= \int_0^R g_k'(r) g_l'(r) r^3 \, dr + R^2 g_l(R) g_k(R) \,, \\
\mathbf{m}_5 &= \int_0^R g_k(r) g_l'(r) r^2 \, dr \,, \\
\mathbf{m}_6 &= \int_0^R g_k'(r) g_l(r) r^2 \, dr \,, \\
\mathbf{m}_7 &= \int_0^R \frac{1}{r^3} g_k(r) g_l(r) dr \; - g_k'(0) g_l'(0) \,, \\
\mathbf{m}_8 &= \int_0^R \frac{1}{r} g_k'(r) g_l'(r) \, dr \,, \\
\mathbf{m}_9 &= \int_0^R g_k''(r) g_l''(r) r \, dr - R g_k'(R) g_l''(R) \,,
\end{aligned}
$$

$$
\begin{aligned}
\mathbf{m}_{10} &= \int_0^R g_k''(r) g_l''(r) r^3 \, dr - R^3 g_k'(R) g_l''(R) - R^2 g_k(R) g_l''(R) \,, \\
\mathbf{m}_{11} &= \int_0^R g_k(r) g_l'(r) \, dr \,, \\
\mathbf{m}_{12} &= \int_0^R g_k'(r) g_l(r) \, dr \,, \\
\mathbf{m}_{13} &= \int_0^R g_k'(r) g_l''(r) r^2 \, dr - R^2 g_k(R) g_l''(R) \,, \\
\mathbf{m}_{14} &= \int_0^R g_k''(r) g_l'(r) r^2 \, dr - R^2 g_k'(R) g_l'(R) \,.
\end{aligned}
$$

In addition to the above elemental matrices, the following boundary terms are also necessary in assembling the mass and viscous matrices:

$$
\begin{aligned}
\mathbf{bt}_1 &= g_k(R) g_l(R), \\
\mathbf{bt}_2 &= R g_k(R) g_l'(R), \\
\mathbf{bt}_3 &= \frac{g_k(R) g_l(R)}{R^2}, \\
\mathbf{bt}_4 &= \frac{g_k(R) g_l'(R)}{R} + g_k(R) g_l''(R), \\
\mathbf{bt}_5 &= \frac{g_k(R) g_l'(R)}{R} + \frac{g_k(R) g_l(R)}{R^2}, \\
\mathbf{bt}_6 &= R^2 g_k(R) g_l''(R).
\end{aligned}
$$

### B.1.1 Mass matrices

The mass matrices for Fourier modes $(k_\theta, k_z)$ are:

- $k_z = 0$ and $k_\theta = 0$

  $\mathbf{A}^{++} = \mathbf{m}_3 \,,$

  $\mathbf{A}^{--} = \mathbf{m}_1 \,,$

  $\mathbf{A}^{+-} = 0 \,,$

  $\mathbf{A}^{-+} = 0 \,.$

- $k_z \neq 0$ and $k_\theta = 0$

  $\mathbf{A}^{++} = {k_z}^2 \mathbf{m}_3$ ,

  $\mathbf{A}^{--} = 2{k_z}^2 \mathbf{m}_3 + \mathbf{m}_1 + \mathbf{m}_2 + \mathbf{bt}_1$ ,

  $\mathbf{A}^{+-} = {k_z}^2 \mathbf{m}_3$ ,

  $\mathbf{A}^{-+} = {k_z}^2 \mathbf{m}_3$ .

- $k_z = 0$ and $k_\theta \neq 0$

  $\mathbf{A}^{++} = ({k_\theta}^2 - 1)\mathbf{m}_3 + \mathbf{m}_4 + R_2^2 \mathbf{bt}_1$ ,

  $\mathbf{A}^{--} = (k_\theta - 1)^2 \mathbf{m}_1 + \mathbf{m}_2 + (1 - k_\theta)\mathbf{bt}_1$ ,

  $\mathbf{A}^{+-} = 0$ ,

  $\mathbf{A}^{-+} = 0$

- $k_z \neq 0$ and $k_\theta \neq 0$

  $\mathbf{A}^{++} = {k_z}^2 \left[ ({k_\theta}^2 - 1)\mathbf{m}_3 + \mathbf{m}_4 + R_2^2 \mathbf{bt}_1 \right]$ ,

  $\mathbf{A}^{--} = 2{k_z}^2 \mathbf{m}_3 + (k_\theta - 1)^2 \mathbf{m}_1 + \mathbf{m}_2 + (1 - k_\theta)\mathbf{bt}_1$ ,

  $\mathbf{A}^{+-} = {k_z}^2 \left[ (k_\theta + 1)\mathbf{m}_3 + \mathbf{m}_5 \right]$ ,

  $\mathbf{A}^{-+} = {k_z}^2 \left[ (k_\theta + 1)\mathbf{m}_3 + \mathbf{m}_6 \right]$ .

### B.1.2 Viscous matrices

The mass matrices for Fourier modes $(k_\theta, k_z)$ are:

- $k_z = 0$ and $k_\theta = 0$

$$
\begin{aligned}
\mathbf{B}^{++} &= -\frac{1}{Re} \left( \mathbf{m}_1 + \mathbf{m}_2 - \mathbf{bt}_2 \right) , \\
\mathbf{B}^{--} &= -\frac{1}{Re} \left( \mathbf{m}_8 - \mathbf{m}_7 - \mathbf{bt}_5 - \mathbf{bt}_3 \right) , \\
\mathbf{B}^{+-} &= 0 , \\
\mathbf{B}^{-+} &= 0 .
\end{aligned}
$$

- $k_z \neq 0$ and $k_\theta = 0$

$$\begin{aligned}
\mathbf{B}^{++} &= -\frac{k_z^2}{Re}\left[k_z^2\mathbf{m}_3 + \mathbf{m}_1 + \mathbf{m}_2 - \mathbf{bt}_2\right] , \\
\mathbf{B}^{--} &= -\frac{1}{Re}\left[2k_z^4\mathbf{m}_3 - 3(\mathbf{m}_7 - \mathbf{m}_8) + 3k_z^2(\mathbf{m}_1 + \mathbf{m}_2) + \mathbf{m}_9 + \right. \\
&\qquad \left. k_z^2(\mathbf{bt}_1 - 2\mathbf{bt}_2) - 2\mathbf{bt}_3 - \mathbf{bt}_4 - \mathbf{bt}_5\right] , \\
\mathbf{B}^{+-} &= -\frac{k_z^2}{Re}\left[k_z^2\mathbf{m}_3 + \mathbf{m}_1 + \mathbf{m}_2 - \mathbf{bt}_2\right] , \\
\mathbf{B}^{-+} &= -\frac{k_z^2}{Re}\left[k_z^2\mathbf{m}_3 + \mathbf{m}_1 + \mathbf{m}_2 - \mathbf{bt}_2\right] .
\end{aligned}$$

- $k_z = 0$ and $k_\theta \neq 0$

$$\begin{aligned}
\mathbf{B}^{++} &= -\frac{1}{Re}\left[(k_\theta^2 - 1)^2\mathbf{m}_1 + (2k_\theta^2 + 1)\mathbf{m}_2 + \right. \\
&\qquad \left. \mathbf{m}_{10} + (1 - k_\theta^2)\mathbf{bt}_1 - (2 + k_\theta^2)\mathbf{bt}_2\right] , \\
\mathbf{B}^{--} &= -\frac{1}{Re}\left[(-3 + 4k_\theta + 2k_\theta^2 - 4k_\theta^3 + k_\theta^4)\mathbf{m}_7 + (3 - 4k_\theta + 2k_\theta^2)\mathbf{m}_8 + \mathbf{m}_9 + \right. \\
&\qquad \left. (-2 + 3k_\theta - k_\theta^3)\mathbf{bt}_3 + (k_\theta - 1)(\mathbf{bt}_4 - (k_\theta - 1)\mathbf{bt}_5)\right] , \\
\mathbf{B}^{+-} &= 0 , \\
\mathbf{B}^{-+} &= 0 .
\end{aligned}$$

- $k_z \neq 0$ and $k_\theta \neq 0$

$$\begin{aligned}
\mathbf{B}^{++} &= -\frac{k_z^2}{Re}\left[k_z^2((k_\theta^2 - 1)\mathbf{m}_3 + \mathbf{m}_4) + (k_\theta^2 - 1)^2\mathbf{m}_1 + (2k_\theta^2 + 1)\mathbf{m}_2 + \mathbf{m}_{10} + \right. \\
&\qquad \left. (1 - k_\theta^2)\mathbf{bt}_1 - (2 + k_\theta^2)\mathbf{bt}_2 + {k_z}^2 R_2^2\mathbf{bt}_1 - \mathbf{bt}_6\right] , \\
\mathbf{B}^{--} &= -\frac{1}{Re}\left[2k_z^4\mathbf{m}_3 + (-3 + 4k_\theta + 2k_\theta^2 - 4k_\theta^3 + k_\theta^4)\mathbf{m}_7 + \right. \\
&\qquad 3k_z^2((k_\theta - 1)^2\mathbf{m}_1 + \mathbf{m}_2) + (3 - 4k_\theta + 2k_\theta^2)\mathbf{m}_8 + \mathbf{m}_9 + \\
&\qquad k_z^2((1 - k_\theta)\mathbf{bt}_1 - 2\mathbf{bt}_2) + (-2 + 3k_\theta - k_\theta^3)\mathbf{bt}_3 + \\
&\qquad \left. (k_\theta - 1)(\mathbf{bt}_4 - (k_\theta - 1)\mathbf{bt}_5)\right] , \\
\mathbf{B}^{+-} &= -\frac{k_z^2}{Re}\left[k_z^2((k_\theta + 1)\mathbf{m}_3 + \mathbf{m}_5) + (k_\theta - 1)^2((k_\theta + 1)\mathbf{m}_1 + \mathbf{m}_{11}) + \right. \\
&\qquad \left. (k_\theta + 2)\mathbf{m}_2 + \mathbf{m}_{13} - (\mathbf{bt}_6 + (2 + k_\theta)\mathbf{bt}_2)\right] , \\
\mathbf{B}^{-+} &= -\frac{k_z^2}{Re}\left[k_z^2((k_\theta + 1)\mathbf{m}_3 + \mathbf{m}_6) + (k_\theta - 1)^2((k_\theta + 1)\mathbf{m}_1 + \mathbf{m}_{12}) + \right. \\
&\qquad \left. (k_\theta + 2)\mathbf{m}_2 + \mathbf{m}_{14} - (1 + k_\theta)\mathbf{bt}_2\right] .
\end{aligned}$$

## B.2 Computing the velocity and vorticity components

Upon using the chosen basis expansion vectors for the velocity function, the following expressions are obtained for the velocity and vorticity components:

$$v_r(r,\theta,z,t) = K_l g_l(r) \tag{B.1}$$

$$v_\theta(r,\theta,z,t) = J_l r g_l'(r) + I_l g_l(r) \tag{B.2}$$

$$v_z(r,\theta,z,t) = -G_l g_l'(r) - F_l \frac{g_l(r)}{r} \tag{B.3}$$

$$\omega_r(r,\theta,z,t) = A_l g_l(r) + B_l r g_l'(r) + C_l \frac{g_l(r)}{r^2} + D_l \frac{g_l'(r)}{r} \tag{B.4}$$

$$\omega_\theta(r,\theta,z,t) = E_l g_l(r) + F_l \left( \frac{g_l'(r)}{r} - \frac{g_l(r)}{r^2} \right) + G_l g_l''(r) \tag{B.5}$$

$$\omega_z(r,\theta,z,t) = H_l \frac{g_l(r)}{r} + (I_l + 2J_l) g_l'(r) + J_l r g_l''(r) \tag{B.6}$$

Here the summation convention, $a_l b_l = \sum_l^N a_l b_l$, is used for repeated indices. Also the following are defined:

$$A_l(r,\theta,z,t) = \sum_{k_\theta} \sum_{k_z} -i {k_z}^2 (\alpha_l^+ + \alpha_l^-) e^{i(k_\theta \theta + k_z z)} \tag{B.7}$$

$$B_l(r,\theta,z,t) = \begin{cases} \displaystyle\sum_{k_\theta} \sum_{k_z} -i {k_z}^2 \alpha_l^+ e^{i(k_\theta \theta + k_z z)} & , \quad k_\theta \neq 0 \\ 0 & , \quad k_\theta = 0 \end{cases} \tag{B.8}$$

$$C_l(r,\theta,z,t) = \sum_{k_\theta} \sum_{k_z} -i k_\theta (k_\theta - 1) \alpha_l^- e^{i(k_\theta \theta + k_z z)} \tag{B.9}$$

$$D_l(r,\theta,z,t) = \sum_{k_\theta} \sum_{k_z} i k_\theta \alpha_l^- e^{i(k_\theta \theta + k_z z)} \tag{B.10}$$

$$E_l(r,\theta,z,t) = \sum_{k_\theta} \sum_{k_z} {k_z}^2 (k_\theta \alpha_l^+ + \alpha_l^-) e^{i(k_\theta \theta + k_z z)} \tag{B.11}$$

$$F_l(r,\theta,z,t) = \sum_{k_\theta} \sum_{k_z} (k_\theta - 1) \alpha_l^- e^{i(k_\theta \theta + k_z z)} \tag{B.12}$$

$$G_l(r,\theta,z,t) = \begin{cases} \displaystyle\sum_{k_\theta} \sum_{k_z} -\alpha_l^- e^{i(k_\theta \theta + k_z z)} & , \quad k_\theta \neq 0 \text{ or } k_z \neq 0 \\ 0 & , \quad k_\theta = k_z = 0 \end{cases} \tag{B.13}$$

$$H_l(r,\theta,z,t) = \begin{cases} \sum_{k_\theta}\sum_{k_z} k_z(1-k_\theta)((1+k_\theta)\alpha_l^+ + \alpha_l^-)e^{i(k_\theta\theta+k_z z)} & , \ k_z \neq 0 \\ \sum_{k_\theta}\sum_{k_z} (1-{k_\theta}^2)\alpha_l^+ e^{i(k_\theta\theta+k_z z)} & , \ k_z = 0 \end{cases} \tag{B.14}$$

$$I_l(r,\theta,z,t) = \begin{cases} \sum_{k_\theta}\sum_{k_z} k_z(\alpha_l^+ + \alpha_l^-)e^{i(k_\theta\theta+k_z z)} & , \ k_z \neq 0 \\ \alpha_l^+ e^{i(k_\theta\theta+k_z z)} & , \ k_z = 0 \end{cases} \tag{B.15}$$

$$J_l(r,\theta,z,t) = \begin{cases} \sum_{k_\theta}\sum_{k_z} k_z\alpha_l^+ e^{i(k_\theta\theta+k_z z)} & , \ k_z \neq 0 \text{ and } k_\theta \neq 0 \\ \sum_{k_\theta}\sum_{k_z} \alpha_l^+ e^{i(k_\theta\theta+k_z z)} & , \ k_z = 0 \text{ and } k_\theta \neq 0 \\ 0 & , \ k_\theta = 0 \end{cases} \tag{B.16}$$

$$K_l(r,\theta,z,t) = \begin{cases} \sum_{k_\theta}\sum_{k_z} -k_z(k_\theta\alpha_l^+ + \alpha_l^-)e^{i(k_\theta\theta+k_z z)} & , \ k_z \neq 0 \text{ and } k_\theta \neq 0 \\ \sum_{k_\theta}\sum_{k_z} -ik_\theta\alpha_l^+ & , \ k_z = 0 \text{ and } k_\theta \neq 0 \\ 0 & , \ k_z = k_\theta = 0 \end{cases} \tag{B.17}$$

### B.3 Nonlinear Term

Now we can compute the product $\omega_{l'}^{\pm} \cdot (\mathbf{v} \times \omega)$ in physical space. As described in section 3.2.6, a pseudo-spectral approach is used. The following three-dimensional nonlinear matrices are defined:

$$\mathbf{f}_1 = \int_0^R g_k(r)g_l(r)g_m(r)dr\ , \qquad \mathbf{f}_2 = \int_0^R g_k(r)g_l'(r)g_m(r)dr$$
$$\mathbf{f}_3 = \int_0^R g_k'(r)g_l(r)g_m(r)dr\ , \qquad \mathbf{f}_4 = \int_0^R g_k'(r)g_l'(r)g_m(r)dr$$
$$\mathbf{f}_5 = \int_0^R g_k(r)g_l(r)g_m'(r)dr\ , \qquad \mathbf{f}_6 = \int_0^R g_k(r)g_l'(r)g_m'(r)dr$$
$$\mathbf{f}_7 = \int_0^R g_k'(r)g_l(r)g_m'(r)dr\ , \qquad \mathbf{f}_8 = \int_0^R g_k'(r)g_l'(r)g_m'(r)dr$$
$$\mathbf{f}_9 = \int_0^R g_k(r)g_l(r)g_m''(r)dr\ , \qquad \mathbf{f}_{10} = \int_0^R g_k(r)g_l'(r)g_m''(r)dr$$
$$\mathbf{f}_{11} = \int_0^R g_k'(r)g_l(r)g_m''(r)dr\ .$$

Now the following are defined in terms of these matrices and the expansion coefficients $A_l$ to $K_l$:

$$\begin{aligned}
\gamma_k^+ &= \sum_{m=1}^{N_r}\sum_{l=1}^{N_r} (E_mF_l + H_mI_l)\mathbf{f}_1 + (E_mG_l + H_mJ_l)r\mathbf{f}_2 + \\
&\quad (I_m + 2J_m)(I_l r\mathbf{f}_5 + J_l r^2\mathbf{f}_6) + F_m\left[F_l\left(\frac{\mathbf{f}_5}{r} - \frac{\mathbf{f}_1}{r^2}\right) + G_l\left(\mathbf{f}_6 - \frac{\mathbf{f}_2}{r}\right)\right] + \\
&\quad G_m(F_l\mathbf{f}_9 + G_l r\mathbf{f}_{10}) + J_m(I_l r^2\mathbf{f}_9 + J_l r^3\mathbf{f}_{10}) \\
\beta_k^- &= \sum_{m=1}^{N_r}\sum_{l=1}^{N_r} (A_mI_l - E_mK_l)\mathbf{f}_1 + (C_mI_l + F_mK_l)\frac{\mathbf{f}_1}{r^2} + J_l\left(A_m r\mathbf{f}_2 + C_m\frac{\mathbf{f}_2}{r}\right) + \\
&\quad D_mJ_l\mathbf{f}_6 - G_mK_l\mathbf{f}_9 + B_m(I_l r\mathbf{f}_5 + J_l r^2\mathbf{f}_6) + (D_mI_l - F_mK_l)\frac{\mathbf{f}_5}{r} \\
\Upsilon_k^- &= \sum_{m=1}^{N_r}\sum_{l=1}^{N_r} (A_mF_l + H_mK_l)\mathbf{f}_1 + A_mG_l r\mathbf{f}_2 + C_m\left(F_l\frac{\mathbf{f}_1}{r^2} + G_l\frac{\mathbf{f}_2}{r}\right) + B_mG_l r^2\mathbf{f}_6 + \\
&\quad (B_mF_l + I_mK_l + 2J_mK_l)r\mathbf{f}_5 + D_m\left(F_l\frac{\mathbf{f}_5}{r} + G_l\mathbf{f}_6\right) + J_mK_l r^2\mathbf{f}_9 \\
\tilde{\Upsilon}_k &= \sum_{m=1}^{N_r}\sum_{l=1}^{N_r} (A_mF_l + H_mK_l)r\mathbf{f}_3 + A_mG_l r^2\mathbf{f}_4 + C_m\left(F_l\frac{\mathbf{f}_3}{r} + G_l\mathbf{f}_4\right) + B_mG_l r^3\mathbf{f}_8 + \\
&\quad (B_mF_l + I_mK_l + 2J_mK_l)r^2\mathbf{f}_7 + D_m\left(K_l\mathbf{f}_7 + G_l r\mathbf{f}_8\right) + J_mK_l r^3\mathbf{f}_{11} \\
\tilde{\delta}_k &= \sum_{m=1}^{N_r}\sum_{l=1}^{N_r} (A_mI_l - E_mK_l)r\mathbf{f}_3 + (C_mI_l + F_mK_l)\frac{\mathbf{f}_3}{r} + J_l\mathbf{f}_4(C_m + r^2A_m) + \\
&\quad (D_mI_l - F_mK_l)\mathbf{f}_7 + B_m(I_l r^2\mathbf{f}_7 + J_l r^3\mathbf{f}_8) + D_mJ_l r\mathbf{f}_8 - G_mK_l r\mathbf{f}_{11}\ .
\end{aligned}$$

Here all products of the form $\mathbf{f}_i r^n$ are under the integral sign, and summation is carried out over the $m$ and $l$ indices, for example

$$B_mG_l r^2\mathbf{f}_6 = \sum_{m=1}^{N_r}\sum_{l=1}^{N_r} B_mG_l\int_0^R g_k(r)g_l'(r)g_m'(r)r^2dr \tag{B.18}$$

There are thus twenty four different integrals. These are computed at the beginning of the program. After evaluating $\gamma_k^+$, $\beta_k^-$, $\Upsilon_k^-$, $\tilde{\Upsilon}_k$, and $\tilde{\delta}_k$ in physical space, they are transformed to Fourier space. The final answer is obtained as:

$$\begin{aligned}
\mathbf{F}_k^+ &= \frac{1}{2\pi L_z}\int_0^{L_z}\int_0^{2\pi}\int_0^R \mathbf{w}_k^+\cdot(\mathbf{v}\times\omega)e^{-i(k_\theta\theta + k_z z)}\,rdrd\theta dz \\
&= \mathcal{I}^+(ik_\theta\gamma_k^+ - \Upsilon_k^-) - \mathcal{J}^+\tilde{\Upsilon}_k\ ,
\end{aligned} \tag{B.19}$$

$$\begin{aligned}\mathbf{F}_k^- &= \frac{1}{2\pi L_z}\int_0^{L_z}\int_0^{2\pi}\int_0^R \mathbf{w}_k^- \cdot (\mathbf{v}\times\omega)e^{-i(k_\theta\theta+k_z z)}\, r dr d\theta dz \\ &= \mathcal{I}^-(i\gamma_k^+ - \Upsilon_k^-) + \mathcal{F}^-\beta_k^- - \mathcal{G}^-\tilde{\delta}_k\,, \end{aligned} \tag{B.20}$$

where

$$\mathcal{I}^+ = \begin{cases} k_z, & k_z \neq 0 \\ 1, & k_z = 0 \end{cases}, \quad \mathcal{J}^+ = \begin{cases} k_z, & k_z \neq 0 \text{ and } k_\theta \neq 0 \\ 1, & k_z = 0 \text{ and } k_\theta \neq 0 \\ 0, & k_\theta = 0 \end{cases}, \tag{B.21}$$

$$\mathcal{I}^- = k_z, \quad \mathcal{F}^- = k_\theta - 1, \quad \mathcal{G}^- = \begin{cases} 1, & k_\theta \neq 0 \text{ or } k_\theta \neq 0 \\ 0, & \text{otherwise} \end{cases} \tag{B.22}$$

# Appendix C: Large Eddy Simulations The Philosophy and Methodology

## C.1 Some Basic Concepts

As explained in chapter 2, the turbulent flow simulation approach adopted in the current study relies on the assumption that the dynamics of turbulence is represented by a system of non-linear partial differential equations known as the Navier-Stokes equations. The inherent non-linearities of these equations give rise to a very broad range of spatial and temporal scales. The energy carrying large scale structures are responsible for the major part of turbulent diffusion as they carry most of the turbulent kinetic energy. These scales are directly affected by the boundary conditions and their structure and behavior can vary greatly from one flow to another. The small scales carry most of the vorticity and act as a sink of turbulent kinetic energy, thus accounting for the kinetic energy dissipation. For any numerical simulation to give physically meaningful results, it has to cover both diffusion and dissipation. The disparity between the energy carrying and dissipative eddy length scales is a rapidly growing function of the Reynolds number. This limits a direct numerical simulation to low and moderate Reynolds numbers, since the number of grid points required is proportional to the ratio of these scales.

Large eddy simulation bypasses the severe Reynolds number restriction of a direct numerical simulation by filtering the Navier-Stokes equations to directly simulate the large scales only, while using subgrid modeling to supply the effect of the missing scales. It retains the full three dimensionality and time dependence of the turbulent field. Large eddy simulation should resolve explicitly a range of turbulent scales comprised of structures that contribute significantly to the transport of mass and momentum and to the production of turbulent kinetic energy. However, although large eddy simulation is more affordable compared to a direct numerical simulation, it is a lot costlier than conventional turbulence modeling.

## C.2 The Basis for Large Eddy Simulations and its Consequences

Two fundamental presumptions form the basis for the large eddy simulation concept. These are:

1. Most global features of turbulent flow, e.g. averaged mixing rates, averaged losses, etc., are governed by the large scale dynamics and depend little on the small scale turbulence. This qualitative difference between the characteristics of large and small turbulent scales strongly supports the concept of large eddy simulation. Particular attention has to be given to clearly defining the resolved (grid scale) and unresolved (subgrid scale) motions, and then deriving the appropriate filtered governing equations.

2. The small scale turbulence (large wave number range), particularly at high Reynolds numbers, becomes independent of the strong inhomogeneities that are characteristic of the energy containing eddies (short wave number range), thus tending to local isotropy. A clear separation hence exists between the two bands and in between there forms the so called inertial subrange in which there is a non-linear transfer of energy to successively higher wave numbers at a rate prescribed by the largest scales. If it is ensured that the smallest resolved motions fall within this part of the spectrum by using a fine enough numerical discretization, the subgrid modeling problem is facilitated considerably, since the more universal nature of the small scales makes them easier to model.

Under these idealized conditions, some significant differences can be observed between grid scale and subgrid scale turbulence. The grid scale turbulence is produced by the mean flow and depends on the boundaries. It is ordered and requires a deterministic description. Diffusive in nature, it lives long, and being inhomogeneous and anisotropic it is difficult to model. Subgrid scale turbulence on the other hand is produced by the larger eddies. It is more universal, i.e. independent of the boundaries, and can be modeled statistically due to its chaotic nature. Dissipative in nature, it is short lived, and being nearly homogeneous and isotropic it is relatively easy to model.

## C.3 Scale Separation - The Filtering Concept

As mentioned before, dependent variables in large eddy simulations are broken down into grid and subgrid scale parts. This is achieved by filtering out the high wave number components of the variable (subgrid scale component). The numerical scheme employed then solves for the grid scale components of the dependent variables using a model for the effect of the subgrid scale (unresolved) components.

Consider the decomposition of a variable into its grid and subgrid scale components as follows:

$$f(x_1, x_2, x_3, t) = \overline{f}(x_1, x_2, x_3, t) + f'(x_1, x_2, x_3, t) \tag{C.1}$$

where

$$\begin{aligned} f(x_1, x_2, x_3, t) &= \text{is any dependent variable} \\ \overline{f}(x_1, x_2, x_3, t) &= \text{is the grid scale part} \\ f'(x_1, x_2, x_3, t) &= \text{is the sub grid scale part} \end{aligned}$$

Speaking in general, the part of the turbulent fluctuation which remains after some smoothing has been applied to the field is represented by the grid scale component $\overline{f}$. The design of this smoothing process has to be carried out in such a way that an accurate numerical treatment of the grid scale field is possible on the computational mesh employed in the simulation.

Developing an appropriate numerical method depends on the splitting, thus requiring a clear definition of the way in which the splitting is performed. Distinguishing the effects due to smoothing from those due to the application of a particular numerical scheme is very desirable from a theoretical standpoint. This introduces the concept of filtering. It is a concept which allows in principle, the subgrid scale turbulence to be examined without reference to a particular numerical method.

This approach defines the grid scale turbulence by applying a spatial filtering operation explicitly. The operation is based on a convolution integral extending over the whole domain.

$$\overline{f}(x_1, x_2, x_3, t) = \int_D \prod_{i=1}^{3} h_i(x_i - x'_i, \Delta_i) f(x'_1, x'_2, x'_3, t) dx'_1 dx'_2 dx'_3 \tag{C.2}$$

where

$$\begin{aligned} h_i &= \text{filter function in the } i^{th} \text{ direction} \\ \Delta_i &= \text{filter width in the } i^{th} \text{ direction} \end{aligned}$$

Here the filter width $\Delta_i$ defines the size of the smallest resolved eddies.

The normalization condition

$$\int_D \prod_{i=1}^{3} h_i(x_i) dx_1 dx_2 dx_3 = 1 \tag{C.3}$$

is imposed to ensure that the filtering operation will reproduce any spatially uniform and constant quantity.

The effect of the filtering operation is clearly seen if one takes the Fourier transform of the filtered grid scale part. By definition, the spatial Fourier transform of $f$, $\hat{f}^s$, is

$$\hat{f}^s(\vec{k}, t) = \iiint_{-\infty}^{\infty} f(\vec{x}, t) e^{-ik_i x_i} dx_1 dx_2 dx_3 \tag{C.4}$$

where the repeated index summation notation has been used and $\vec{k} = (k_1, k_2, k_3)$ represents the wave number vector. Then by the convolution theorem

$$\widehat{\overline{f}}^s(\vec{k}, t) = \prod_{i=1}^{3} \hat{h}_i^{x_i} \hat{f}^s \tag{C.5}$$

where

$$\hat{h}_i^{x_i} = \int_{-\infty}^{\infty} h_i(x_i) e^{-ik_i x_i} dx_i \tag{C.6}$$

is the spatial Fourier transform of the filter function in the $i^{th}$ direction. Please note that here $k_i x_i \neq \overrightarrow{k} . \overrightarrow{x}$, i.e., the repeated index summation notation is not used.

Now if $\hat{h}_i^{x_i} = 0$ for $|k_i| > k_c$, where $k_c$ is a "cut-off" wave number, all the high wave number components of $f$ are filtered out by convolving it with $h_i$. A filter with such characteristics is an "ideal low pass filter". A cut-off wave number can also be defined for all practical purposes if the filter function rapidly falls off in wave space. The cut-off filter of course arises naturally if one employs spectral methods for simulations.

An important difference between the filtering in large eddy simulation and Reynolds averaging is $\overline{\overline{f}g'} \neq 0$. Also in general, $\overline{\overline{f}} \neq \overline{f}$ and $\overline{f'} \neq 0$. However, for a sharp cut-off filter, these inequalities are replaced by equal signs since single filtered and double filtered quantities are identical.

A filtering operation as defined above has the effect of eliminating components rapidly varying in space from the filtered variables. Since in a turbulent flow, there is usually a high correlation between the high temporal frequency and the high spatial wave number components, application of a spatial low pass filtering eliminates high frequency turbulence structures.

After a filter has been applied to smoothen the flow field, one can employ a high order numerical discretization using grid sizes significantly smaller than the filter width to keep further discretization errors negligible small. From a theoretical viewpoint, we have a very attractive decoupling of physics and numerics. However it is usually not feasible in practice, since to resolve as many turbulent structures as possible with the available computational resources, the filter width usually cannot be chosen to be much larger than the grid size. Since the physical truncation errors associated with the unresolved scales are generally much larger than the truncation errors of the numerical scheme, such a maximum resolution becomes essential in large eddy simulation.

For the sharp cut-off filter, the grid and subgrid scales do not overlap in spectral space, i.e. they are represented by disjoint bands in Fourier space. A clear distinction

thus becomes possible between the two scales. Whenever a discrete approximation is used to treat a continuous problem, a cut-off filtering is implicitly applied (Nyquist theorem).

## C.4 Filtered Equations Of Motion

We now apply the above filtering operation to our governing equations, i.e. the incompressible Navier-Stokes equations. Upon applying a spatial filter to the equations 2.1 and 2.2 , assuming that the filter commutes with differentiation, we get the governing equations for large eddy simulations.

$$\overrightarrow{\nabla}.\overrightarrow{\overline{u}} = 0 \tag{C.7}$$

$$\frac{\partial \overrightarrow{\overline{u}}}{\partial t} + \overrightarrow{\overline{u}}.\overrightarrow{\nabla}\overrightarrow{\overline{u}} + \overrightarrow{\nabla}\overline{p} = \frac{1}{Re}\overrightarrow{\nabla}.\overrightarrow{\nabla}\overrightarrow{\overline{u}} + \overrightarrow{T}, \tag{C.8}$$

where the overbar denotes the filtering operation and $\overrightarrow{T} = -(\overline{\overrightarrow{u}.\overrightarrow{\nabla}\overrightarrow{u}} - \overrightarrow{\overline{u}}.\overrightarrow{\nabla}\overrightarrow{\overline{u}}) = -\overrightarrow{\nabla}.(\overline{\overrightarrow{u}\overrightarrow{u}} - \overrightarrow{\overline{u}}\overrightarrow{\overline{u}})$ is minus the divergence of the sub-grid scale (SGS) stress.

As we can see, the SGS stress is not a function of only the filtered velocity field. Computing the SGS stress also needs information about the unresolved part of the velocity field, which is not available to us. We thus have a "closure problem", i.e. the system of equations along with prescribed boundary conditions is not sufficient in itself. We need extra information to solve for the velocity field. This information is supplied with the help of a model for the SGS stress, known as the SGS model.

## C.5 Sub-Grid Scale Modeling

The task at hand is to model the subgrid scale tensor $\tau_{ij} = \overline{u_i u_j} - \overline{u}_i\overline{u}_j$ It is important to note that independent of the subgrid model chosen, if the flow parameters in the subgrid scales are unknown at the start of the simulation, the large eddy simulation problem is mathematically ill posed. Even if we have knowledge of the subgrid scales to start with, numerical errors will creep in as the simulation progresses. Uncertainty in the small wavelengths of the motion will contaminate the

larger scales through an "inverse error cascade" (Lesieur and Metais (1996)) up to the energy-containing range. Flows that differ only in the subgrid scales at the start of the simulation correspond to this error cascade. Hence, independent of the precision of the numerical scheme employed and the way in which the subgrid scales are dealt with, there will be decorrelation from reality as the simulation progresses. However, it is believed that the dynamics of the turbulence and the statistical quantities computed from the simulation are still representative of the true turbulence.

The meteorologist Smagorinski (1963) developed the first model for the SGS stress tensor for incompressible flows. This is an eddy-viscosity type model based on the assumption that the production and dissipation of small scale turbulent kinetic energy are equal,

$$\tau_{ij} - \frac{1}{3}\tau_{kk}\delta_{ij} = -2\nu_t \overline{S}_{ij} \tag{C.9}$$

where the eddy viscosity, $\nu_t$, is obtained algebraically from

$$\nu_t = C_s \Delta^2 \overline{S}_M \tag{C.10}$$

The proportionality factor, $C_s$, is known as the Smagorinski constant, $\Delta = (\Delta_1 \Delta_2 \Delta_3)^{1/3}$ is the effective filter width, and $\overline{S}_M = (2\overline{S}_{ij}\overline{S}_{ij})^{1/2}$. Since the isotropic part of the SGS stress tensor, $\frac{1}{3}\tau_{kk}$, can be absorbed into the pressure term, we need only compute

$$\tau_{ij} = -2\nu_t \overline{S}_{ij} \tag{C.11}$$

The Smagorinsky model, though easy to use, has some disadvantages. Firstly, the model constant is not universal. Also, it has to be specified apriori. This leads to non-robustness of the model. The model does not vanish for laminar flows, a requirement for any turbulence model. A phenomenon of importance, particularly for transitional flows, is backscatter of energy from small to large scales (Piomelli et al. (1991)). Being strictly dissipative in nature, the Smagorinsky model cannot account for this phenomenon.

Germano et al. (1991) introduced the idea of dynamic SGS modeling. The model constants are not specified apriori and do not remain the same throughout the simulation. They vary in space and time, and are computed dynamically with the help of information about the smaller resolved scales. This is accomplished by filtering the resolved scales using a second filter. This filter is known as a test filter, and has a filter width, $\widehat{\triangle}_i$, that is larger than the filter used to obtain the equations for LES. Application of the test filter results in the splitting of the scales into test scales and subtest scales (STS). The subtest scales include the unresolved subgrid scales (see figure 4.1). This second filtering of the LES equations results in the subtest scale stress given by

$$\zeta_{ij} = \widehat{\overline{u_i u_j}} - \widehat{\overline{u}}_i \widehat{\overline{u}}_j \tag{C.12}$$

Test filtering the subgrid scale stress tensor, $\tau_{ij} = \overline{u_i u_j} - \overline{u}_i \overline{u}_j$, and subtracting it from the above equation, we get the contribution of the smallest resolved scales to the subtest scale (STS) stress tensor

$$\zeta_{ij} - \widehat{\tau}_{ij} = \widehat{\overline{u}_i \overline{u}_j} - \widehat{\overline{u}}_i \widehat{\overline{u}}_j \tag{C.13}$$

If we assume that the energy transfer between the test and subtest scales happens in a manner similar to that between the grid and subgrid scales, we can use the same model to represent both the STS and SGS stresses. Hence we can write

$$\zeta_{ij} = -2(C_s \widehat{\Delta}^2 \widehat{\overline{S}}_M) \widehat{\overline{S}}_{ij} \tag{C.14}$$

$$\widehat{\tau}_{ij} = -2C_s \Delta^2 \widehat{\overline{S}_M \overline{S}_{ij}} \tag{C.15}$$

Substituting equations (4.14) and (4.15) in equation (4.13) we get

$$C_s(-2\widehat{\Delta}^2 \widehat{\overline{S}}_M \widehat{\overline{S}}_{ij} + 2\Delta^2 \widehat{\overline{S}_M \overline{S}_{ij}}) = \widehat{\overline{u}_i \overline{u}_j} - \widehat{\overline{u}}_i \widehat{\overline{u}}_j \tag{C.16}$$

This simplifies to

$$C_s = \frac{< (\widehat{\overline{u}_i \overline{u}_j} - \widehat{\overline{u}}_i \widehat{\overline{u}}_j) A_{ij} >}{< M_{ij} A_{ij} >} \tag{C.17}$$

where

$$M_{ij} = -2\widehat{\Delta}^2\widehat{\overline{S}}_M\widehat{\overline{S}}_{ij} + 2\Delta^2\widehat{\overline{S}_M\overline{S}_{ij}} \tag{C.18}$$

In equation 4.17, <> represents an ad-hoc average. This ad-hoc averaging procedure is performed on both sides of equation 4.16 to prevent any numerical difficulties that might arise from the left hand side becoming zero (or near zero) at some grid points. This procedure can be carried out only if we have at least one homogeneous direction, along which we perform spatial averaging. In the current work, the vortex is assumed to be homogeneous in the axial direction. Hence we can perform averaging in the axial ($z$) direction. Also, before averaging we contract both sides with a tensor $A_{ij}$ to ensure a unique solution for $C_s$. The current work uses the least squares approach to determine $C_s$ (Lilly (1992)). This results in choosing $A_{ij} = M_{ij}$. Hence

$$C_s = \frac{< (\widehat{\overline{u}_i\overline{u}_j} - \widehat{\overline{u}}_i\widehat{\overline{u}}_j)M_{ij} >}{< M_{ij}M_{ij} >} \tag{C.19}$$

Since averaging is carried out in the $z$ direction, $C_s$ is a function of $r$, $\theta$ and $t$ (note that we are working in the cylindrical coordinate system).

## C.6 Numerical Method

Proceeding exactly as in section 2.2, we obtain the weak form of the filtered Navier-Stokes equation

$$(\overrightarrow{\xi}, \frac{\partial \overrightarrow{\overline{v}}}{\partial t}) = \frac{1}{Re}(\overrightarrow{\xi}, (\overrightarrow{\nabla}.\overrightarrow{\nabla}\overrightarrow{\overline{v}})) + (\overrightarrow{\xi}, (\overrightarrow{\overline{v}} \times \overrightarrow{\overline{\omega}})) + (\overrightarrow{\xi}, \overrightarrow{T}), \tag{C.20}$$

where $\overrightarrow{\overline{v}}$ is the numerical approximation to $\overrightarrow{\overline{u}}$.

The formulation of the numerical method is exactly the same as in the Direct Numerical Simulations, except for the sub-grid stress which introduces a new non-linear term.

$$f^{\pm}_{nl_2} = \frac{1}{2\pi L_z}\int_0^{L_z}\int_0^{2\pi}\int_0^{R_2} \mathbf{w}^{\pm}_k.\overrightarrow{T}e^{-i(k'_\theta\theta + k'_z z)}rdrd\theta dz \tag{C.21}$$

This non-linear term, arising from using an SGS model as explained in section 4.5, cannot be evaluated in the same way as the non-linear term in the original DNS formulation. The eddy viscosity cannot be expressed in terms of the expansion of the velocity field as the vorticity can. One approach is to compute the eddy viscosity in physical space using a pseudo-spectral approach. Once defined in physical space, the eddy viscosity can be expanded in terms of b-spline functions, but with coefficients that are not directly related to the velocity field. Unfortunately, this leads to a large set of additional integrals involving triple products of b-spline functions, which would greatly increase the cost of the simulation.

An alternate approach is to compute the entire SGS term, $\overrightarrow{T}$, in physical space and to express this quantity in terms of a b-spline expansion. This leads to four integrals involving double products of b-splines. Two of these already are part of the formulation of the other terms in the weak form of the Navier-Stokes equation and are computed in the original code using Gaussian quadrature. This approach thus leads to only two additional integrations. This is the approach chosen, and is implemented in the following steps.

### C.6.1 Step 1

We start by computing the resolved strain rate tensor. In cylindrical coordinates this is given by

$$\begin{aligned} \overline{S}_{rr} &= \frac{\partial \overline{v}_r}{\partial r}, \quad \overline{S}_{r\theta} = \frac{1}{2}(\frac{1}{r}\frac{\partial \overline{v}_r}{\partial \theta} + \frac{\partial \overline{v}_\theta}{\partial r} - \frac{\overline{v}_\theta}{r}), \quad \overline{S}_{rz} = \frac{1}{2}(\frac{\partial \overline{v}_z}{\partial r} + \frac{\partial \overline{v}_r}{\partial z}) \\ \overline{S}_{\theta\theta} &= (\frac{1}{r}\frac{\partial \overline{v}_\theta}{\partial \theta} + \frac{\overline{v}_r}{r}), \quad \overline{S}_{\theta z} = \frac{1}{2}(\frac{\partial \overline{v}_\theta}{\partial z} + \frac{1}{r}\frac{\partial \overline{v}_z}{\partial \theta}), \quad \overline{S}_{zz} = \frac{\partial \overline{v}_z}{\partial z} \end{aligned} \tag{C.22}$$

The velocity components are computed as

$$\begin{aligned} \overline{v}_r(r,\theta,z,t) &= K_l g_l(r) \\ \overline{v}_\theta(r,\theta,z,t) &= J_l r g_l'(r) + I_l g_l(r) \\ \overline{v}_z(r,\theta,z,t) &= -G_l g_l'(r) - F_l \frac{g_l(r)}{r} \end{aligned} \tag{C.23}$$

where $g_l$ are the b-spline polynomials (see figure 2.2) and the summation convention is used for repeated indices. $K_l, J_l, I_l, G_l$ and $F_l$ are functions of $(\theta, z, t)$, and expressions for these are given in Appendix B. Expressions for the derivatives of the velocity components can be obtained by explicitly differentiating the relations given in (4.23). At the origin, a transformation to the Cartesian coordinate system is used to handle the singularity problems as follows

$$\begin{aligned} \overline{v}_x &= \overline{v}_r \cos\theta - \overline{v}_\theta \sin\theta \qquad \overline{v}_r = \overline{v}_x \cos\theta + \overline{v}_y \sin\theta \\ \overline{v}_y &= \overline{v}_r \sin\theta + \overline{v}_\theta \cos\theta \qquad \overline{v}_\theta = \overline{v}_y \cos\theta - \overline{v}_x \sin\theta \end{aligned} \tag{C.24}$$

Equations (4.24) along with the coordinate transformation $x = r\cos\theta$ and $y = r\sin\theta$ allow us to express $\overline{S}_{r\theta}$, $\overline{S}_{\theta\theta}$ and $\overline{S}_{\theta z}$ in the Cartesian coordinate system

$$\begin{aligned} \overline{S}_{r\theta} &= \frac{1}{2}(\cos 2\theta(\frac{\partial \overline{v}_x}{\partial y} + \frac{\partial \overline{v}_y}{\partial x}) - \sin 2\theta(\frac{\partial \overline{v}_x}{\partial x} - \frac{\partial \overline{v}_y}{\partial y})) \\ \overline{S}_{\theta\theta} &= (\sin^2\theta \frac{\partial \overline{v}_x}{\partial x} + cos^2\theta \frac{\partial \overline{v}_y}{\partial y} - \frac{\sin 2\theta}{2}(\frac{\partial \overline{v}_y}{\partial x} + \frac{\partial \overline{v}_x}{\partial y})) \\ \overline{S}_{\theta z} &= \frac{1}{2}(\cos\theta(\frac{\partial \overline{v}_y}{\partial z} + \frac{\partial \overline{v}_z}{\partial y}) - \sin\theta(\frac{\partial \overline{v}_x}{\partial z} + \frac{\partial \overline{v}_z}{\partial x})) \end{aligned} \tag{C.25}$$

These expressions can be re-written in terms of the derivatives of the velocity components in the cylindrical coordinates system, obtained by explicitly differentiating (4.23), thus giving us the following expressions for $\overline{S}_{r\theta}$, $\overline{S}_{\theta\theta}$ and $\overline{S}_{\theta z}$ at the origin

$$\begin{aligned} \overline{S}_{r\theta} &= \frac{1}{2}(\cos 2\theta(-\frac{\partial \overline{v}_\theta}{\partial r}|_{\theta=\pi/2} + \frac{\partial \overline{v}_\theta}{\partial r}|_{\theta=0}) - \sin 2\theta(\frac{\partial \overline{v}_r}{\partial r}|_{\theta=0} - \frac{\partial \overline{v}_r}{\partial r}|_{\theta=\pi/2})) \\ \overline{S}_{\theta\theta} &= (\sin^2\theta \frac{\partial \overline{v}_r}{\partial r}|_{\theta=0} + \cos^2\theta \frac{\partial \overline{v}_r}{\partial r}|_{\theta=\pi/2} - \frac{\sin 2\theta}{2}(\frac{\partial \overline{v}_\theta}{\partial r}|_{\theta=0} - \frac{\partial \overline{v}_\theta}{\partial r}|_{\theta=\pi/2})) \\ \overline{S}_{\theta z} &= \frac{1}{2}(\cos\theta(\frac{\partial \overline{v}_\theta}{\partial z}|_{\theta=0} + \frac{\partial \overline{v}_z}{\partial r}|_{\theta=\pi/2}) - \sin\theta(\frac{\partial \overline{v}_r}{\partial z}|_{\theta=0} + \frac{\partial \overline{v}_z}{\partial r}|_{\theta=0})) \end{aligned} \tag{C.26}$$

### C.6.2 Step 2

Next the eddy viscosity, $\nu_T$, is computed using the dynamic Smagorinsky model as explained in section 4.5. The filter width, $\triangle$, is chosen to be $(r\triangle\theta\triangle z)^{1/2}$ for $r \neq 0$, while it is set to $\triangle z$ at the origin. Note that the filtering operation is carried out only for the axial and azimuthal directions, thus resulting in a hybrid DNS-LES

formulation, with all the scales being resolved in the radial direction. This approach is analogous to large eddy simulations of channel flow, where the filtering operation is performed only along the two directions parallel to the walls. The test filter width, $\widehat{\triangle}$, is chosen to be twice the filter width.

### C.6.3 Step 3

The SGS stress tensor (here $T_{ij} = -\tau_{ij}$) is computed as

$$\begin{aligned} T_{rr} &= 2\nu_T \overline{S}_{rr}, \quad T_{r\theta} = 2\nu_T \overline{S}_{r\theta}, \quad T_{rz} = 2\nu_T \overline{S}_{rz} \\ T_{\theta\theta} &= 2\nu_T \overline{S}_{\theta\theta}, \quad T_{\theta z} = 2\nu_T \overline{S}_{\theta z}, \quad T_{zz} = 2\nu_T \overline{S}_{zz} \end{aligned} \tag{C.27}$$

where the resolved scale strain rates are given in equation (4.22) and $\nu_T$ is computed from equation (4.10). The isotropic part of the SGS stress tensor is absorbed in the modified pressure term.

### C.6.4 Step 4

The SGS term $\overrightarrow{T}$ is now put together as

$$\overrightarrow{T} = [T_\theta, T_r, T_z], \tag{C.28}$$

where

$$\begin{aligned} T_\theta &= \frac{\partial(T_{z\theta})}{\partial z} + \frac{1}{r}\frac{\partial(rT_{\theta r})}{\partial r} + \frac{1}{r}\frac{\partial(T_{\theta\theta})}{\partial \theta} + \frac{1}{r}(T_{r\theta}) \\ T_r &= \frac{\partial(T_{zr})}{\partial z} + \frac{1}{r}\frac{\partial(rT_{rr})}{\partial r} + \frac{1}{r}\frac{\partial(T_{r\theta})}{\partial \theta} - \frac{1}{r}(T_{\theta\theta}) \\ T_z &= \frac{\partial(T_{zz})}{\partial z} + \frac{1}{r}\frac{\partial(rT_{zr})}{\partial r} + \frac{1}{r}\frac{\partial(T_{z\theta})}{\partial \theta} \end{aligned} \tag{C.29}$$

Here derivatives in the $\theta$ and $z$ directions are evaluated using FFTs. To evaluate the derivative in the radial direction, the quantities of interest ($rT_{\theta r}$, $rT_{rr}$, and $rT_{zr}$) are first expressed in terms of b-splines. This is accomplished by solving a system of linear equations, $Ax = b$, for each ray emitting from the origin. Here $A$ is the b-spline matrix ($m^{th}$ row corresponds to the $m^{th}$ grid point along the ray and $n^{th}$ column corresponds to the value of the $n^{th}$ b-spline polynomial, $g_n(r)$, at the the $m^{th}$ grid

point), while $b$ is a column vector containing the values of the quantity of interest along the ray. The solution, $x$, gives us the coefficients for the b-spline expansion of the quantity along the ray. The derivative in the radial direction can then be obtained by performing the operation $Bx$, where $B$ is the b-spline derivative matrix (structure similar to A).

At the origin, a transformation to the Cartesian coordinate system is used to handle singularity problems. The approach is the same as that for the resolved strain rate tensor (see section 4.6.1), and results in the following expressions for $T_\theta$, $T_r$, and $T_z$ at the origin

$$\begin{aligned}
T_\theta &= -\left(\left.\frac{\partial(T_{rr})}{\partial r}\right|_{\theta=0} - \left.\frac{\partial(T_{r\theta})}{\partial r}\right|_{\theta=\pi/2} + \left.\frac{\partial(T_{rz})}{\partial z}\right|_{\theta=0}\right)\sin\theta \\
&+ \left(\left.\frac{\partial(T_{r\theta})}{\partial r}\right|_{\theta=0} + \left.\frac{\partial(T_{rr})}{\partial r}\right|_{\theta=\pi/2} + \left.\frac{\partial(T_{rz})}{\partial z}\right|_{\theta=\pi/2}\right)\cos\theta \\
T_r &= \left(\left.\frac{\partial(T_{rr})}{\partial r}\right|_{\theta=0} - \left.\frac{\partial(T_{r\theta})}{\partial r}\right|_{\theta=\pi/2} + \left.\frac{\partial(T_{rz})}{\partial z}\right|_{\theta=0}\right)\cos\theta \\
&+ \left(\left.\frac{\partial(T_{r\theta})}{\partial r}\right|_{\theta=0} + \left.\frac{\partial(T_{rr})}{\partial r}\right|_{\theta=\pi/2} + \left.\frac{\partial(T_{rz})}{\partial z}\right|_{\theta=\pi/2}\right)\sin\theta \\
T_z &= \left.\frac{\partial(T_{rz})}{\partial r}\right|_{\theta=0} + \left.\frac{\partial(T_{rz})}{\partial r}\right|_{\theta=\pi/2} + \frac{\partial(T_{zz})}{\partial z}
\end{aligned} \tag{C.30}$$

### C.6.5 Step 5

Using the approach described in Step 4 to express $rT_{\theta r}$, $rT_{rr}$, and $rT_{zr}$ in terms of b-splines, the SGS term is expanded in terms of b-splines as

$$\overrightarrow{T} = [T_\theta, T_r, T_z] = \sum_{k=1}^{N_r} [a_k, b_k, c_k] g_k(r) \tag{C.31}$$

Here $a_k$, $b_k$ and $c_k$ are functions of $\theta$ and $z$.

### C.6.6 Step 6

Upon performing the inner product operation on the b-spline representation of the SGS stress (see equation 4.21), we get the nonlinear term $f_{nl_2}^{\pm}$ as

For $k_z = k_\theta = 0$ :

$$\begin{aligned} f_{nl_2}^{+} &= \frac{1}{2\pi L_z}\int_0^{L_z}\int_0^{2\pi}\left[\sum_{k=1}^{N_r} b_k m_3\right] e^{-i(k'_\theta\theta + k'_z z)} d\theta dz \\ f_{nl_2}^{-} &= \frac{1}{2\pi L_z}\int_0^{L_z}\int_0^{2\pi}\left[\sum_{k=1}^{N_r} c_k m_{15}\right] e^{-i(k'_\theta\theta + k'_z z)} d\theta dz \end{aligned} \tag{C.32}$$

For $k_z = 0$, $k_\theta > 0$ :

$$\begin{aligned} f_{nl_2}^{+} &= ik_\theta \frac{1}{2\pi L_z}\int_0^{L_z}\int_0^{2\pi}\left[\sum_{k=1}^{N_r} a_k m_3\right] e^{-i(k'_\theta\theta + k'_z z)} d\theta dz \\ &\quad + \frac{1}{2\pi L_z}\int_0^{L_z}\int_0^{2\pi}\left[\sum_{k=1}^{N_r} b_k m_3\right] e^{-i(k'_\theta\theta + k'_z z)} d\theta dz \\ &\quad + \frac{1}{2\pi L_z}\int_0^{L_z}\int_0^{2\pi}\left[\sum_{k=1}^{N_r} b_k m_6\right] e^{-i(k'_\theta\theta + k'_z z)} d\theta dz \\ f_{nl_2}^{-} &= \frac{1}{2\pi L_z}\int_0^{L_z}\int_0^{2\pi}\left[\sum_{k=1}^{N_r} c_k m_{16}\right] e^{-i(k'_\theta\theta + k'_z z)} d\theta dz \\ &\quad + (1-k_\theta)\frac{1}{2\pi L_z}\int_0^{L_z}\int_0^{2\pi}\left[\sum_{k=1}^{N_r} c_k m_{15}\right] e^{-i(k'_\theta\theta + k'_z z)} d\theta dz \end{aligned} \tag{C.33}$$

For $k_z \neq 0$, $k_\theta = 0$ :

$$\begin{aligned}
f^+_{nl_2} &= k_z \frac{1}{2\pi L_z} \int_0^{L_z} \int_0^{2\pi} \left[ \sum_{k=1}^{N_r} b_k m_3 \right] e^{-i(k'_\theta \theta + k'_z z)} d\theta dz \\
f^-_{nl_2} &= ik_z \frac{1}{2\pi L_z} \int_0^{L_z} \int_0^{2\pi} \left[ \sum_{k=1}^{N_r} a_k m_3 \right] e^{-i(k'_\theta \theta + k'_z z)} d\theta dz \\
&\quad + k_z \frac{1}{2\pi L_z} \int_0^{L_z} \int_0^{2\pi} \left[ \sum_{k=1}^{N_r} b_k m_3 \right] e^{-i(k'_\theta \theta + k'_z z)} d\theta dz \\
&\quad + \frac{1}{2\pi L_z} \int_0^{L_z} \int_0^{2\pi} \left[ \sum_{k=1}^{N_r} c_k m_{15} \right] e^{-i(k'_\theta \theta + k'_z z)} d\theta dz \\
&\quad + \frac{1}{2\pi L_z} \int_0^{L_z} \int_0^{2\pi} \left[ \sum_{k=1}^{N_r} c_k m_{16} \right] e^{-i(k'_\theta \theta + k'_z z)} d\theta dz
\end{aligned} \tag{C.34}$$

For $k_z \neq 0$, $k_\theta > 0$ :

$$\begin{aligned}
f^+_{nl_2} &= ik_\theta k_z \frac{1}{2\pi L_z} \int_0^{L_z} \int_0^{2\pi} \left[ \sum_{k=1}^{N_r} a_k m_3 \right] e^{-i(k'_\theta \theta + k'_z z)} d\theta dz \\
&\quad + k_z \frac{1}{2\pi L_z} \int_0^{L_z} \int_0^{2\pi} \left[ \sum_{k=1}^{N_r} b_k m_3 \right] e^{-i(k'_\theta \theta + k'_z z)} d\theta dz \\
&\quad + k_z \frac{1}{2\pi L_z} \int_0^{L_z} \int_0^{2\pi} \left[ \sum_{k=1}^{N_r} b_k m_6 \right] e^{-i(k'_\theta \theta + k'_z z)} d\theta dz \\
f^-_{nl_2} &= ik_z \frac{1}{2\pi L_z} \int_0^{L_z} \int_0^{2\pi} \left[ \sum_{k=1}^{N_r} a_k m_3 \right] e^{-i(k'_\theta \theta + k'_z z)} d\theta dz \\
&\quad + k_z \frac{1}{2\pi L_z} \int_0^{L_z} \int_0^{2\pi} \left[ \sum_{k=1}^{N_r} b_k m_3 \right] e^{-i(k'_\theta \theta + k'_z z)} d\theta dz \\
&\quad + \frac{1}{2\pi L_z} \int_0^{L_z} \int_0^{2\pi} \left[ \sum_{k=1}^{N_r} c_k m_{16} \right] e^{-i(k'_\theta \theta + k'_z z)} d\theta dz \\
&\quad + (1 - k_\theta) \frac{1}{2\pi L_z} \int_0^{L_z} \int_0^{2\pi} \left[ \sum_{k=1}^{N_r} c_k m_{15} \right] e^{-i(k'_\theta \theta + k'_z z)} d\theta dz
\end{aligned} \tag{C.35}$$

Here $m_3, m_6, m_{15}$ and $m_{16}$ are elemental matrices defined as

$$\begin{aligned}
m_3 &= \int_0^R g_l g_k r dr, \quad m_6 = \int_0^R g'_l g_k r^2 dr \\
m_{15} &= \int_0^R g_l g_k dr, \quad m_{16} = \int_0^R g'_l g_k r dr
\end{aligned} \tag{C.36}$$

$m_3$ are $m_6$ are already being computed in the original code. $m_{15}$ and $m_{16}$ are the two additional integrations added into the code. These integrals are computed to machine accuracy using Gaussian quadrature. The following are computed in physical space

$$\begin{aligned} I_1 &= \sum_{k=1}^{N_r} a_k m_3, \quad I_2 = \sum_{k=1}^{N_r} b_k m_3, \quad I_3 = \sum_{k=1}^{N_r} c_k m_{15} \\ I_4 &= \sum_{k=1}^{N_r} c_k m_{16}, \quad I_5 = \sum_{k=1}^{N_r} b_k m_6 \end{aligned} \tag{C.37}$$

Now, since $\frac{1}{2\pi L_z}\int_0^{L_z}\int_0^{2\pi}(....)e^{-i(k'_\theta\theta+k'_z z)}$ is the definition of a Fourier transform, $I_1$ through $I_5$ are transformed to wave space using FFTs to obtain $\widehat{I}_1(k_\theta, k_z)$ through $\widehat{I}_5(k_\theta, k_z)$ and $f^{\pm}_{nl_2}$ is obtained in wave space as

For $k_z = k_\theta = 0$ :

$$\begin{aligned} f^{+}_{nl_2} &= \widehat{I}_2 \\ f^{-}_{nl_2} &= \widehat{I}_3 \end{aligned} \tag{C.38}$$

For $k_z = 0$, $k_\theta > 0$ :

$$\begin{aligned} f^{+}_{nl_2} &= ik_\theta \widehat{I}_1 + \widehat{I}_2 + \widehat{I}_5 \\ f^{-}_{nl_2} &= \widehat{I}_4 + (1 - k_\theta)\widehat{I}_3 \end{aligned} \tag{C.39}$$

For $k_z \neq 0$, $k_\theta = 0$ :

$$\begin{aligned} f^{+}_{nl_2} &= k_z \widehat{I}_2 \\ f^{-}_{nl_2} &= ik_z \widehat{I}_1 + k_z \widehat{I}_2 + \widehat{I}_3 + \widehat{I}_4 \end{aligned} \tag{C.40}$$

For $k_z \neq 0$, $k_\theta > 0$ :

$$\begin{aligned} f^{+}_{nl_2} &= ik_\theta k_z \widehat{I}_1 + k_z \widehat{I}_2 + k_z \widehat{I}_5 \\ f^{-}_{nl_2} &= ik_z \widehat{I}_1 + k_z \widehat{I}_2 + \widehat{I}_4 + (1 - k_\theta)\widehat{I}_3 \end{aligned} \tag{C.41}$$

This completes the LES formulation. The DNS code has been appropriately modified to perform LES. Once validated using the available DNS results, it shall be used to perform LES of the strained vortex at higher Reynolds numbers.

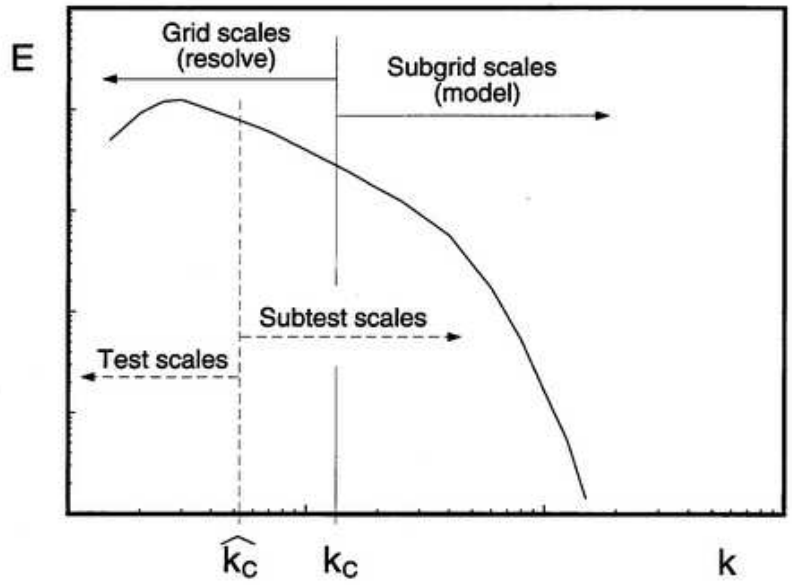


Figure C.1 Separation of scales for dynamic subgrid scale modeling (Spyropoulos (1996)).

# VITA

# VITA

Brijesh Eshpuniyani was born in Sri Ganganagar, Rajasthan, India, on 12th August 1974. He received his Bachelor of Technology (B.Tech.) degree in Civil Engineering from Indian Institute of Technology, Bombay (IIT-B) in July 1995. In August 1997, Brijesh obtained his Master of Science (M.S.) degree in Aerospace Engineering and Engineering Mechanics from University of Cincinnati. From August 1997 to December 2003 Brijesh attended the School of Aeronautics and Astronautics at Purdue University, West Lafayette, Indiana, as a PhD student. His PhD thesis title is "Flow Physics of Strained Turbulent Axial Vortices".